CIVIL ENGINEERING STUDIES
Illinois Center for Transportation Series No. 24-021
UILU-ENG-2024-2021
ISSN: 0197-9191

Utilizing a Particle-packing Approach for an Illinois-specific, Nonproprietary, Low-shrinkage UHPC

Prepared By
Bayezid Baten[1]
Matthew Gombeda[2]
Nishant Garg[1]
[1]University of Illinois Urbana-Champaign
[2]Illinois Institute of Technology

Research Report No. FHWA-ICT-24-018

A report of the findings of

ICT PROJECT R27-232
Utilizing a Particle Packing Approach for an Illinois-specific, Nonproprietary, Low-shrinkage UHPC

https://doi.org/10.36501/0197-9191/24-021

Illinois Center for Transportation

September 2024

TECHNICAL REPORT DOCUMENTATION PAGE

1. Report No.	2. Government Accession No.	3. Recipient's Catalog No.
FHWA-ICT-24-018	N/A	N/A

4. Title and Subtitle	5. Report Date
Utilizing a Particle-packing Approach for an Illinois-specific, Nonproprietary, Low-shrinkage UHPC	September 2024
	6. Performing Organization Code N/A

7. Authors	8. Performing Organization Report No.
Bayezid Baten (https://orcid.org/0000-0001-7107-9527), Matthew Gombeda, and Nishant Garg (https://orcid.org/0000-0001-9292-8364)	ICT-24-021 UILU-2024-2021

9. Performing Organization Name and Address	10. Work Unit No.
Illinois Center for Transportation Department of Civil and Environmental Engineering University of Illinois at Urbana-Champaign 205 North Mathews Avenue, MC-250 Urbana, IL 61801	N/A **11. Contract or Grant No.** R27-232

12. Sponsoring Agency Name and Address	13. Type of Report and Period Covered
Illinois Department of Transportation (SPR) Bureau of Research 126 East Ash Street Springfield, IL 62704	Final Report 7/1/21–9/30/24 **14. Sponsoring Agency Code**

15. Supplementary Notes

Conducted in cooperation with the U.S. Department of Transportation, Federal Highway Administration.
https://doi.org/10.36501/0197-9191/24-021

16. Abstract

Ultra-high-performance concrete (UHPC) represents the next generation of concrete, with a strength 3-4 times greater than traditional concrete (100-120 MPa as opposed to 30-40 MPa). However, most of the commercial UHPC mixes are proprietary and expensive. In this project, we document the development of nonproprietary, cost-effective UHPC mixes primarily using locally sourced or pre-qualified materials in Illinois. The research utilizes the modified Anderson and Andreasen packing model to establish a new parameter: "packing factor" that has a significant influence on the design and performance of multi-binder UHPC mixes. Initially, 19 UHPC mixes without fibers are analyzed for their rheological, mechanical, and durability properties, demonstrating promising results. Specifically, we obtain self-flowing capabilities with minimal HRWR usage (<1% by wt.%), a turnover time of 7–10 minutes, and a significant reduction in cement content (47% Type IL and the remaining 53% SCMs by volume) while maintaining superior compressive strengths (~120–150 MPa, 17.2–21.8 ksi @ 28 days). Then, optimal mixes, particularly M18 and M19, are evaluated with fibers, achieving compressive strengths exceeding 150 MPa (21.8 ksi) at 28 days and exhibiting open porosity under 2%, and have shrinkage rates below the target threshold (<800με @ 91 days). Finally, effective particle packing resulted in UHPC mixes costs of ~$400/m^3 (~$308/yd^3) without steel fibers and ~$590/m^3 (~$454/yd^3) with steel fibers, enabling cost-effective, optimal UHPC for deployment by the Illinois Department of Transportation.

17. Key Words	18. Distribution Statement
Packing Factor, Particle Packing, UHPC, Multi-Binder, Packing Models, Compressive Strength, Self-Flowability	No restrictions. This document is available through the National Technical Information Service, Springfield, VA 22161.

19. Security Classif. (of this report)	20. Security Classif. (of this page)	21. No. of Pages	22. Price
Unclassified	Unclassified	102+ appendices	N/A

ACKNOWLEDGMENT, DISCLAIMER, MANUFACTURERS' NAMES

This publication is based on the results of **ICT-R27-232: Utilizing a Particle Packing Approach for an Illinois-specific, Nonproprietary, Low-Shrinkage UHPC**. ICT-R27-232 was conducted in cooperation with the Illinois Center for Transportation; the Illinois Department of Transportation; and the U.S. Department of Transportation, Federal Highway Administration.

Members of the Technical Review Panel (TRP) were the following:

- James Krstulovich, TRP Chair, Illinois Department of Transportation
- Mark Shaffer, TRP Co-Chair, Illinois Department of Transportation
- Dan Gancarz, Illinois Tollway
- Ahmad Hammad, WSP
- Peter Pascua, Illinois Department of Transportation
- Kevin Riechers, Illinois Department of Transportation
- Frank Sharpe, Federal Highway Administration
- Dan Tobias, Illinois Department of Transportation

EXECUTIVE SUMMARY

Ultra-high-performance concrete (UHPC) is a state-of-the-art construction material known for its exceptional properties, including compressive strengths reaching up to 150 MPa (21.8 ksi), high ductility (~ 2%), superior impact resistance, and extended service life (> 100 years) compared to traditional concrete. These characteristics make UHPC highly desirable for critical applications where strength and durability are paramount. However, the proprietary nature of UHPC formulations has elevated the cost, up to $2,000 per cubic yard, which is 15–20 times the cost of conventional concrete. Despite the clear benefits of UHPC's longer service life, these high costs hinder its widespread use. Hence, it is crucial to develop cost-effective, nonproprietary UHPC solutions.

This project details a comprehensive study performed to develop nonproprietary UHPC mixes from local materials available in Illinois or pre-qualified by the Illinois Department of Transportation (IDOT). The primary objective of the project was to utilize the concept of particle-packing to formulate cost-effective UHPC mixes with adequate mechanical performance and high durability.

This study utilizes the modified Anderson and Andreasen packing model to formulate a new parameter: "packing factor." A simplex lattice design model has been used to design 19 different multi-binder UHPC mixes (M1–M19) with a range of packing factors (31.2 to 46.0) incorporating slag, ultra-fine fly ash, and silica fume as supplementary cementitious materials (SCMs). Later, the rheological, mechanical, and durability properties of the mixes were assessed at different ages of the samples and correlated to the packing factor.

The multi-binder UHPC mixes showed commendable self-flowing properties with varying high-range water reducer (HRWR) sensitivity based on the mix composition. In particular, we report the possibility of high mini-slump flow of 10–12 inches with less than 1% (by weight of binder) of HRWR requirement and a turnover time of 7–10 minutes for the optimum mixes (M18 and M19). Notably, through optimizing particle packing, the optimal mixes (M18 and M19) provide evidence of reducing cement content to 47% (Type IL by volume) while achieving compressive strength of more than 120 MPa (17.2 ksi) and open porosity lower than 2% at 28 days. The inclusion of 2% steel fibers in the same mixes elevated the 28-day strength to more than 150 MPa (21.8 ksi) at 28 days. With a lower open porosity (< 2%) and improved packing factor, the optimal mixes also exhibit a shrinkage rate lower than the target threshold of 800 μξ at 91 days. Finally, an optimized packing and lower cement content prove to be effective tools in ensuring cost-effective, optimal UHPC mixes with unit cost values of ~$400/$m^3$ (~$308/$yd^3$) without steel fibers and ~$590/$m^3$ (~$454/$yd^3$) with steel fibers.

Overall, in this study, the researchers have demonstrated a comprehensive mix design technique to develop nonproprietary UHPC mixes for IDOT with materials available locally or already pre-qualified by the department. The researchers show that although particle packing plays a key role in defining the UHPC mix design, an optimum blend of packing (physical) and hydration (chemical) characteristics is crucial in maximizing UHPC properties. Most importantly, this study shows the possibility of designing nonproprietary UHPC mixes with more than 150 MPa (21.8 ksi) by optimizing the properties of multiple binders. Hence, it provides immense potential for using UHPC for a wider implication and ensures stronger, durable, and sustainable infrastructural development in Illinois.

TABLE OF CONTENTS

LIST OF FIGURES

LIST OF TABLES

CHAPTER 1: INTRODUCTION

OVERVIEW OF UHPC

Ultra-high-performance concrete (UHPC) represents a significant advancement in the field of civil engineering and construction materials, driven by its exceptional mechanical properties and durability. UHPC's development has been guided by an acute need for more robust, long-lasting materials capable of enduring extreme environmental conditions and heavy loads without compromising structural integrity. This material is characterized by its exceedingly high compressive and tensile strengths, which far exceed those of standard concrete formulations. With considerably low water-to-binder (w/b) ratio (0.15–0.25), high particle-packing density (0.825–0.855), high volume of steel fibers (> 2% by volume), and chemical admixtures, UHPC possesses self-flowing properties and high mechanical properties (28-day compressive strength > 120 MPa [17.4 ksi] and tensile strength > 5 MPa) under standard curing.

Over the past 30 years, UHPC has been used in many diverse applications, including the construction of concrete piles, bridge connections, architectural building components, and blast-mitigating structures. Specifically, UHPC has been used by U.S. departments of transportation (DOTs) in numerous projects, including link slabs, shear keys, nosing for joints, overlays, and concrete bearing stiffeners for steel beams. Considering the high-speed construction, enhanced durability, reduced maintenance cost, decreased size and complexity of elements, and improved resiliency of UHPC, its rapid growth is expected in the state of Illinois. However, two major obstacles remain: (1) the proprietary nature and high cost (> \$2,000/yd^3) of commercially available UHPC (e.g., Ductal®, Steelike®, Cor-Tuf®), and (2) the requirement of high-shear mixers, which are specialized equipment with high capital and operating expenditures. To tackle these issues, researchers from several states such as, but not limited to, Arkansas, Arizona, Iowa, Michigan, and Florida have investigated nonproprietary UHPC mixtures from locally available materials. Hence, with the merging needs of high-performance materials and resilient infrastructure, it is crucial to develop and formulate Illinois-specific nonproprietary UHPC optimizing the local materials present here.

The distinguishing feature of UHPC is its ultra-dense microstructure, which is achieved through optimized particle packing and the addition of fibers—usually steel or polymeric—to improve its mechanical properties and ductility. In this study, the researchers propose a particle-packing approach to develop a range of UHPC mixes using blends of local SCMs, including silica fume, ultra-fine fly ash, and slag. The effect of packing on the rheological, mechanical, and durability properties of the designed UHPC has been evaluated for a long span of time. As shrinkage is a dominant problem associated with the high binder content of UHPC, the efficacy of the mix designs was tested on both early and long-term drying shrinkage.

In recent years, the focus has shifted toward sustainable practices in UHPC production, including the use of locally available materials and industrial by-products, to minimize the environmental impact of its use. This research also aimed at minimizing the cement content in the designed UHPC mixes, which has been evaluated through a comprehensive cost and environmental assessment. As a newly

developed material, the potential of scaling lab-based UHPC mixes to a larger scale has also been evaluated through designing and testing of larger structural members in shear and flexure.

Research and field applications have highlighted UHPC's potential in a variety of structures, particularly in the construction and repair of bridges, where its superior load-bearing capacity and resistance to environmental degradation make it an ideal choice. Developing nonproprietary UHPC mixtures is crucial to reduce dependency on costly, commercial mixes, enabling broader usage in public infrastructure projects. These advancements are crucial for the future of construction, potentially reducing life-cycle costs due to lower maintenance and longer service life of structures.

RESEARCH OBJECTIVES

The following objectives have been identified for the project:

- Review the existing literature to identify the potential material sources and the packing models suitable for designing UHPC systems with maximum particle packing.
- Conduct a broad survey on the availability of local and/or IDOT-qualified materials suitable as binders or fillers which can be used to design the nonproprietary UHPC mixes. This also includes assessing the physical and chemical characteristics of the materials to determine their suitability.
- Utilize a statistical mixture design method to formulate different combinations of the SCMs which can later be incorporated within the particle-packing models to design the packing factor of different UHPC mixes.
- Perform detailed testing on the rheological, mechanical, and durability properties of the designed UHPC mixes and correlate them to the packing factor of the mixes.
- Perform a comprehensive cost and feasibility analysis of the UHPC mixes, and apply environmental assessment to the mixes.
- Evaluate the large-scale mixing of the optimum mixes, and assess the shear and flexure behavior of the optimum mixes while testing structural members.

CHAPTER 2: LITERATURE REVIEW

OVERVIEW

This chapter details the background information on the development of UHPC mixes. It also describes the various models available for the efficient design of UHPC mixes and explains the basis of the packing model selection in this study.

BACKGROUND

Over several decades, researchers globally have endeavored to create cement-based materials that exemplify ultra-high performance. Early attempts included macro defect-free cement (Birchall et al., 1981) and densified small-particle concrete (Bache, 1981), which improved density and workability through innovations like superplasticizers and silica fume. The introduction of steel fibers addressed the brittleness associated with higher strengths, leading to developments like slurry infiltrated fiber concrete, which allowed for high-fiber volumes but was not workable enough for broader applications (Bache, 1981). This was followed by reactive powder concrete (Richard & Cheyrezy, 1995), a significant advancement in the 1990s, which utilized a very low water-to-binder (w/b) ratio and optimized particle packing to achieve compressive strengths up to 800 MPa (116 ksi). The term ultra-high-performance concrete (UHPC) emerged during this period, denoting mixtures with exceptional compressive and flexural strengths. Subsequently, the focus shifted toward making UHPC more sustainable and economical by reducing cement and silica fume content and incorporating alternative materials like fly ash. Despite these advancements, challenges such as high initial costs, complex production processes, and inconsistencies in raw material quality have limited UHPC's widespread industrial adoption, maintaining its application primarily in high-value, small-scale projects such as bridge joints and connections.

KEY PROPERTIES OF UHPC

Fresh Properties

UHPC develops superior mechanical properties due to its low w/b ratio and high packing density, with steel fibers enhancing tensile properties (ACI Committee 239, 2018; Meng & Khayat, 2017). High dosages of superplasticizers and other admixtures are used to achieve the desired fluidity and dispersion of the binder, impacting the rheology of UHPC mixes (Khayat et al., 2019). Factors such as sand ratio and binder content influence the rheology of UHPC mixes, with research showing an inverse correlation between plasticizer dosage and binder content for the same flow (Chen et al., 2022; Sharma et al., 2022).

Rheology is important in UHPC, as it determines fiber dispersion and mechanical properties. Meng et al. (2017) developed a rheological control method to control the distribution of fibers in UHPC. Teng et al. (2020) reported similar results: optimum rheology of UHPC leads to enhanced fiber distribution; see Figure 1. Despite the relatively lower fluidity of UHPC resisting fiber segregation, it is proportioned to be self-flowing and self-consolidating, requiring a high dosage of HRWR (Akhnoukh &

Buckhalter, 2021). The viscosity is adjusted considering the low yield stress of self-flowing UHPC to avoid fiber segregation and enhance fiber dispersion and orientation (Li et al., 2013).

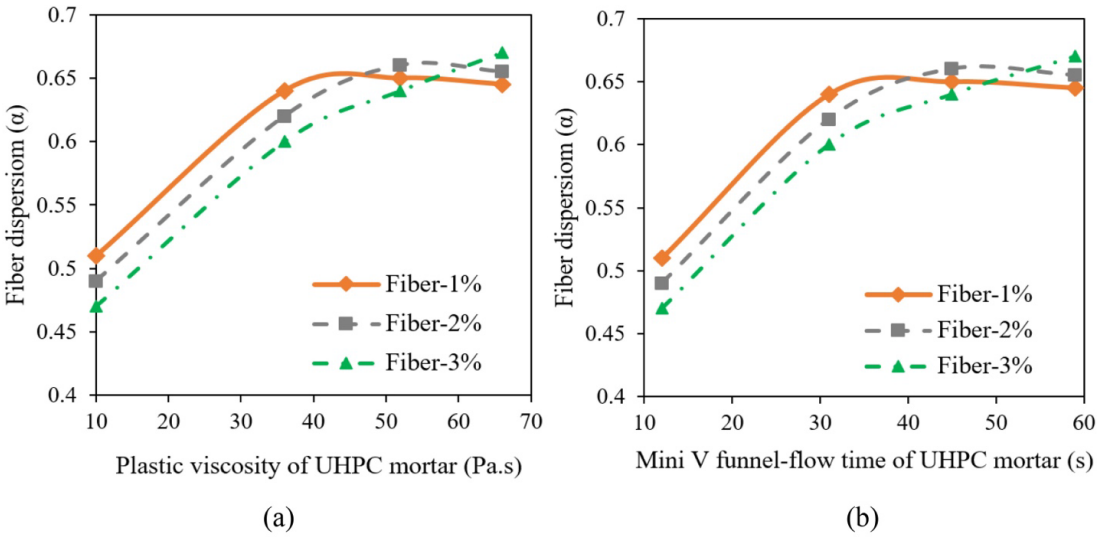

Figure 1. Graph. Relationships between (a) plastic viscosity of UHPC mortar and fiber dispersion and (b) mini V-funnel flow time of UHPC mortar and fiber dispersion (Teng et al., 2020).

In labs, rheometers are used to study UHPC paste flow; however, on construction sites, a mini-slump test per ASTM C1856 (2017) is used. The test is similar to ASTM C1437 (2020) but without dropping the flow table due to UHPC's flow range. Choi et al. (2016) showed that the flow table test correlates with a rheometer if the spread of UHPC is measured as a function of time and concluded that a rheometer can be replaced with a flow table test.

Rheological properties of UHPC mixes can be studied using rheometers due to small maximum aggregate size. Yahia and Khayat (2001) found a nonlinear relationship between shear stress and strain rate in UHPC paste, indicating changing viscosity with applied shear rate. This finding suggests that the Bingham linear model is unsuitable for UHPC paste, with modified Bingham and Herschel-Bulkley models being more appropriate (Atzeni et al., 1985). Arora et al. (2018) studied UHPC flow using a vane in-cup geometry rheometer and developed a database pairing rheological properties of UHPC paste with particle packing and mix constituents, useful for optimizing UHPC mix rheology.

Early-Age Setting and Strength Development

UHPC exhibits enhanced mechanical, durability, and rheological properties due to a low w/b ratio (~0.2), fine particles, and high admixture dosages. The high fineness and low w/b ratio can lead to rapid surface evaporation and condensation, causing an overestimation of setting time. To counter this, Yoo et al. (2013) applied paraffin oil to UHPC samples, enabling precise determination of setting times. Zhang et al. (2012) used an ultrasonic pulse velocity test to estimate the initial and final setting times of UHPC and reported that hydration is promoted by the curing temperature.

The strength development of UHPC has been extensively studied by Graybeal (2007) and Habel et al. (2006). Graybeal (2007) used the Weibull cumulative function to predict compressive strength

development after 0.9 days. Habel et al. (2006) found hydration begins 26 hours after water addition due to the high superplasticizer content in the mix, with strength development starting at a degree of reaction of 0.16 and reaching 0.99 after 90 days, indicating the end of UHPC hydration. See Figure 2.

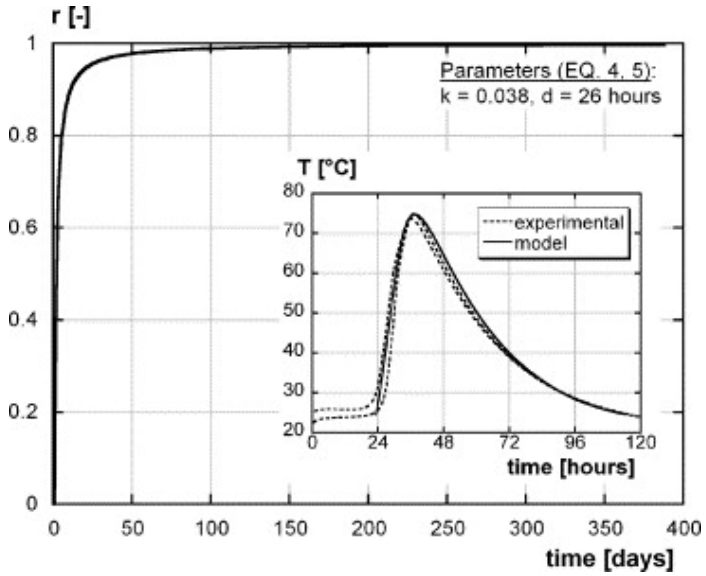

Figure 2. Graph. Development of the degree of reaction with time, detail: experimental results of the semi-adiabatic heat of hydration tests and modeling (Habel et al., 2006).

Different materials like slag, ultra-fine fly ash (UFFA), and silica fumes have varying effects on UHPC's mechanical properties. Slag improves workability but compromises early strength (Liu et al., 2018). UFFA jeopardizes early strength but increases compressive strength at later stages (Ferdosian & Camões, 2017). Silica fumes accelerate early cement hydration due to its finer average particle diameter and larger specific surface area (Oertel et al., 2014). However, Shi et al. (2015) found that silica fumes, owing to their ability to adhere to cement particles and limit their access to free water, can slow down early cement hydration.

Tensile Properties

Steel fibers are a key additive in UHPC, enhancing its ductility and tensile strength. UHPC exhibits high compressive and tensile strength due to particle packing, steel fibers, and a low w/b ratio. These fibers also enable UHPC to absorb energy and exhibit strain hardening after initial cracking (Larsen & Thorstensen, 2020).

Tensile strength in UHPC improves with increased fiber content, as fibers span more cracks (Figure 3) (Yoo et al., 2017). However, tensile strength does not continuously improve with fiber content. Higher fiber content (> 3%) can lead to fiber agglomeration, negatively affecting tensile properties (Meng & Khayat, 2018). At 6% fiber content, workability decreases but peak tensile strength significantly increases (Abbas et al., 2015). The effect of fiber content is influenced by constituents, rheology, and mix proportion of UHPC. Extended curing time densifies the microstructure and improves bond strength between the matrix and steel fibers (Abbas et al., 2015). Silica fume inclusion also enhances bond strength by creating more hydration products (Chan & Chu, 2004). Pre-cracking

strength improvement is not directly linked to increased fiber content, as it depends on the tensile properties of the cementitious materials (Yoo et al., 2017). However, some studies show that increased fiber content improves pre-cracking strength by delaying microcrack formation (Meng & Khayat, 2018).

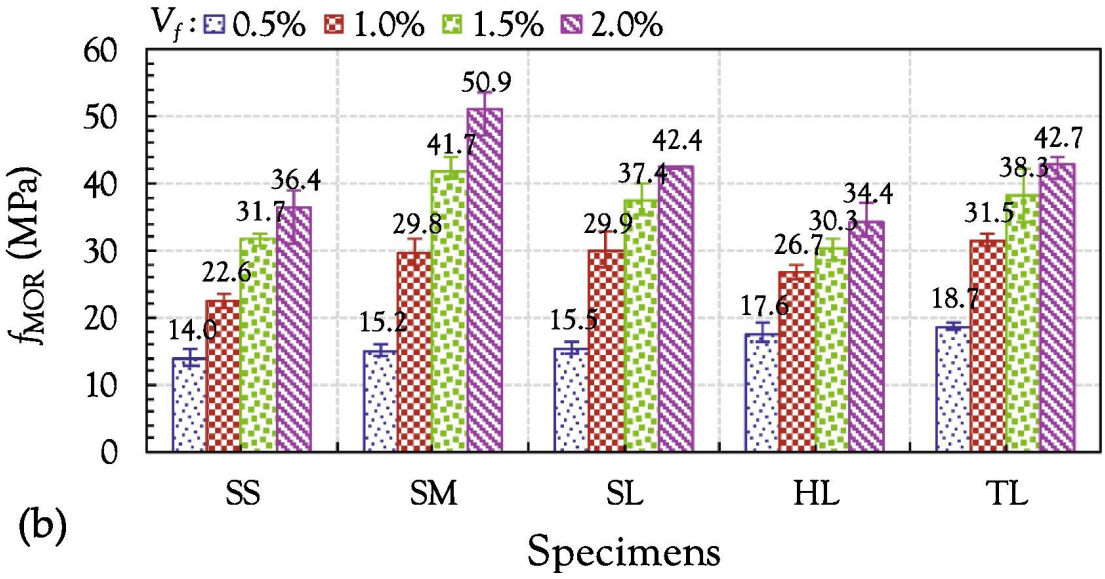

Figure 3. Graph. Effect of steel fibers on flexural properties of UHPC (Yoo et al., 2017).

In UHPC, the tensile strength can be increased up to 20% with an increase in fiber length. This improvement is attributed to the larger bonding area between the steel fibers and the matrix, which enhances the bridging capacity of the steel fibers (Yoo et al., 2017). However, note that the highest peak tensile strength is observed with smaller fibers. This is because the number of fibers available to bridge the cracks increases as fiber length decreases (Abbas et al., 2015). The shape of the fibers also plays a significant role in the tensile properties of UHPC. Deformed fibers, for instance, bond better with the matrix, leading to a higher pullout strength and more efficient crack bridging (Meng & Khayat, 2018). Despite these advantages, some studies have observed minimal effect on flexural properties with the use of deformed fibers (Yoo et al., 2017). At lower fiber content (< 1%), deformed fibers exhibit higher strength, while at higher fiber content (> 1.5%), straight microsteel fibers demonstrate the highest flexural strength (Yoo et al., 2017). This could be due to the formation of split cracks when deformed fibers are used. The number of these split cracks increases with an increase in the quantity of deformed fibers, which could potentially weaken the pullout strength of nearby fibers and consequently reduce the crack bridging capacity (Yoo et al., 2017). Hybrid fiber combination in UHPC can enhance its strength and reduce fiber content. Short fibers efficiently bridge microcracks, and long fibers prevent their propagation; however, results across studies may vary (Wu et al., 2017).

Shrinkage Behavior

UHPC exhibits exceptional strength due to high binder content and low w/b ratio. Higher binder and admixture content, low w/b ratio, and absence of coarse aggregate in UHPC are associated with

drying shrinkage of UHPC samples (Sun et al., 2022). Drying shrinkage is the contraction of hardened concrete due to the loss of capillary moisture, leading to the development of capillary tension inside the cement matrix's mesopore structure (Awoyera et al., 2022). Drying shrinkage is one of the reasons for cracking in UHPC, leading to a decrease in compressive strength (Wu et al., 2019). During the early stages of curing, because the fibers also provide restraint, high early-age shrinkage may result in even more cracking (Yoo et al., 2014).

The w/b ratio significantly impacts UHPC shrinkage. Increasing the w/b ratio increases drying shrinkage and lowers autogenous shrinkage, leading to higher total shrinkage; see Figure 4 (Fu et al., 2022). Superplasticizers are commonly used in UHPC due to the low w/b ratio. They reduce water demand and enhance performance, but their effect on shrinkage varies with composition (Li et al., 2017). Additionally, the binder composition affects UHPC shrinkage properties, making it essential to evaluate this impact (Li, 2016).

Silica fumes, owing to their fineness and large surface area, enhance UHPC's strength and durability but also cause shrinkage, especially as their quantity increases (Mazloom et al., 2004). Fly ash acts as a filler and pozzolan. Its impact on UHPC shrinkage is complex due to its varied particle size and composition (Termkhajornkit et al., 2005). Moderately fine fly ash can decrease UHPC shrinkage, while ultra-fine fly ash, similar to silica fumes, increases it. Substituting cement with slag increases drying shrinkage because slag reduces chemically bound water and promotes evaporation (Yalçınkaya & Yazıcı, 2017). Given the impact of these constituents on drying shrinkage, a combination of additives is often used to control drying shrinkage in UHPC (Park et al., 2013).

Steel fibers are added to UHPC to compensate for its low tensile strength. According to a previous study (Fu et al., 2022), the right amount of steel fibers can reduce UHPC's drying shrinkage by dispersing shrinkage stresses and resisting shrinkage crack formation. However, high fiber content can weaken the zones between fibers and matrix, making them prone to shrinkage cracking; see Figure 4.

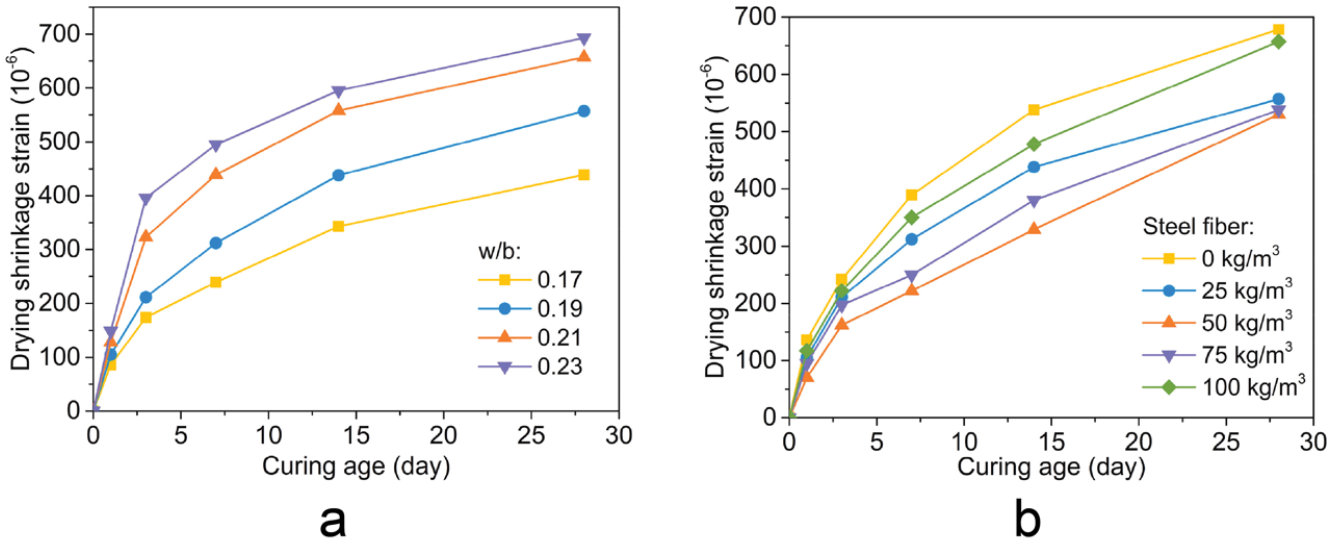

Figure 4. Graph. Effect of (a) w/b, (b) steel fibers on drying shrinkage of UHPC (Fu et al., 2022).

CONVENTIONAL MATERIALS FOR UHPC MIX DESIGN

UHPC mix designs primarily constitute ordinary Portland cement, fine aggregate, supplementary materials, high-range water reducer (HRWR), and steel fibers (Du et al., 2021). The constituents are usually proportioned to maximize the packing density of the resultant system. Conventional UHPC mixes usually incorporate a considerably high amount of binders, as shown in Figure 78 in Appendix A, for a wide range of mixes in the literature. Meanwhile, modern UHPC research works rely on the packing enhancement from SCMs and the pozzolanic reaction to optimize strength and durability performance.

MIX-DESIGN METHODS OF UHPC

UHPC mixes are designed with the aim of achieving a higher particle-packing density, which translates to higher mechanical performance with significantly lower porosity compared to regular concrete mixes (Wang et al., 2019). The conventional way of designing UHPC mixes involves optimizing dry powders to maximize the packing within the UHPC system for enhanced performance. In this regard, this section summarizes the various mix design techniques available in the literature for optimizing UHPC mix design and performance.

Close Packing Models

Packing models are conceptualized by enhancing the packing of the solid particles existing within a UHPC system. Packing models are either used in a dry system, considering the interactions between the particles, or in a wet state, taking water and superplasticizers into account.

Dry Packing Models

Over the years, various packing models have been proposed for customizing and estimating the packing state of dry powders with considering the structure and interaction effects, such as filling, wedging, loosening, and wall effects (Kwan et al., 2013; Mehdipour & Khayat, 2018a). This has been classified into discrete and continuous models based on the gradations involved in the cementitious systems.

The **discrete model** is based on the assumption that the particles can be fully compressed according to specific particle size [m]. Unlike the Furnas model (Furnas, 1931), which assumes non-interfering particles in a continuous particle size distribution (PSD), the discrete model acknowledges particle interaction and is more suitable for complex, multi-component mixtures like UHPC. Newer models like linear packing density model (LPDM), spherical square model (SSM), and compressible packing model (CPM) have transitioned from traditional to virtual packing techniques, addressing the limitations of wall and loosening effects in particle packing (De Larrard & Sedran, 1994; Glavind & Pedersen, 1999; Stovall et al., 1986). These models significantly enhance the prediction of dry packing density in UHPC and recognize the influence of particle surface forces, which were previously neglected.

Meanwhile, the **continuous model** assumes that the PSD is continuous and that all possible particle sizes can exist within the system. The initial concept of the grading curve, representing a continuous

system, was initially proposed as Fuller's curve (Fuller & Thompson, 1907), for optimizing the maximum density, as shown in Figure 5. The Fuller model has been modified by Shakhmenko and Birsh (1998) for further application to concrete mix design, as shown in Figure 6.

$$CPFT = \left(\frac{d}{D}\right)^n * 100$$

Figure 5. Equation. Initial conceptualization of the grading curve.

$$CPFT = T_n(d_i - d_0)^n$$

Figure 6. Equation. Continuous packing model from Fuller model.

where *CPFT* is the percentage of cumulative volume; *n* is the degree of curve equation, which is assumed to be 0.45; and *T* is a coefficient related to the maximum diameter of aggregate (unitless).

Later, Andreasen proposed an ideal packing model, assuming the smallest particle to be infinitesimal, which was later modified by Dinger and Funk as follows:

$$CPFT = \left(\frac{d - d_0}{D - d_0}\right)^q * 100$$

Figure 7. Equation. Modified Anderson and Andreasen continuous packing model.

where, *d* and *R* are the diameters of the particle (µm); d_0 and *D* are the minimum and maximum diameter of the particles (µm), respectively, and *q* is the distribution coefficient.

The continuous model is more applicable to a system like UHPC, as it usually consists of a wide range of particle sizes for maximizing packing density. The effect of different dry packing models on the overall packing is shown in Figure 8, where the continuous model shows a much higher packing density of the system compared to the discrete model of a binary system.

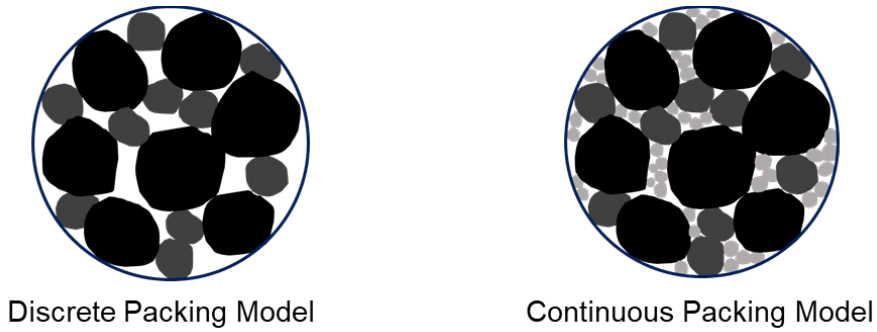

Figure 8. Photo. Discrete and continuous packing model in a multi-gradation particle system.

Wet Packing Models

The wet particle-packing method incorporates water and chemical additives to improve inter-particle movement and density, which are crucial for the structural integrity and performance of the concrete. When fine particles in UHPC are dry, their natural friction inhibits optimal packing. Introducing water into the mix reduces this friction by acting as a lubricant among the particles. This lubrication is most effective when particles reach a state of saturation, allowing them to pack more densely as frictional forces are minimized. Adding HRWRs further facilitates denser packing by altering the properties of the water film that coats the particles (Wong & Kwan, 2008). These additives decrease the water film's thickness, reducing the overall surface tension and enabling particles to slide past one another more easily, thus promoting a tighter packing configuration.

The wet packing density is usually assessed by evaluating the mass and volume of the paste for an initial w/b ratio. Later, the w/b ratio is reduced, and the density is measured at each modified w/b ratio until the point of maximum packing density [n]. For each mix, the solid concentration (ϕ) and void ratio (u) is measured for each mix as per Figure 9.

$$V_c = \frac{M}{\rho_w u_w + \rho_\alpha u_w + \rho_\beta R_\beta + \rho_\gamma R_\gamma}$$

$$\emptyset = V_c / V$$

$$u = (V - V_c)/V_c$$

Figure 9. Equation. Wet packing model for packing density.

Where, M and V represent the mass and volume of paste in the mold (62 mm × 60 mm in height); ρ_w is the density of water; ρ_α, ρ_β, and ρ_γ represent the solid densities; and R_α, R_β, and R_γ are the volumetric ratios of the cementitious materials.

Performance-based Design Methods

Performance-based design approaches have been recommended to formulate UHPC mixes aligning with specific application needs. For example, Meng et al. (2017) developed a method to optimize nonproprietary UHPC mixes through a detailed process, where the binder combinations are initially selected based on their flow characteristics. This selection is then refined by evaluating the particle packing, flowability, and mechanical performance. The choice is finalized based on rheological properties like plastic viscosity and yield stress. Following this, the w/b ratio is established to balance workability with 28-day compressive strength. The performance-based approach allows for precise and direct determination of mix design parameters, ensuring the UHPC mix achieves the intended performance characteristics.

CHAPTER 3: MATERIALS AND TEST METHODOLOGIES

OVERVIEW

The concept of enhancing particle packing using multiple binders has been used to design low-cement, nonproprietary UHPC mixes with the target performance. In this regard, the research team has mostly focused on using local materials for mix design and particle-packing optimization. For an efficient implementation, the mix design includes commonly used and available supplementary cementitious materials (SCMs) in Illinois, summarized in this chapter. This chapter also describes the optimized mixing regime incorporated to prepare the UHPC bases and details the test methodologies followed for the performance characterization.

MATERIAL CHARACTERIZATION

The researchers ensured the physical and chemical properties of the binders listed below conform to ASTM C150 (2001). The particle size distribution of the samples was measured by wet laser diffraction using a Malvern Mastersizer 3000 in accordance with ASTM C136 (2006) and is graphically represented in Figure 10. The target curve represents the ideal packing condition, based on the modified Anderson and Andreasen model, which is described in more detail in Chapter 5.

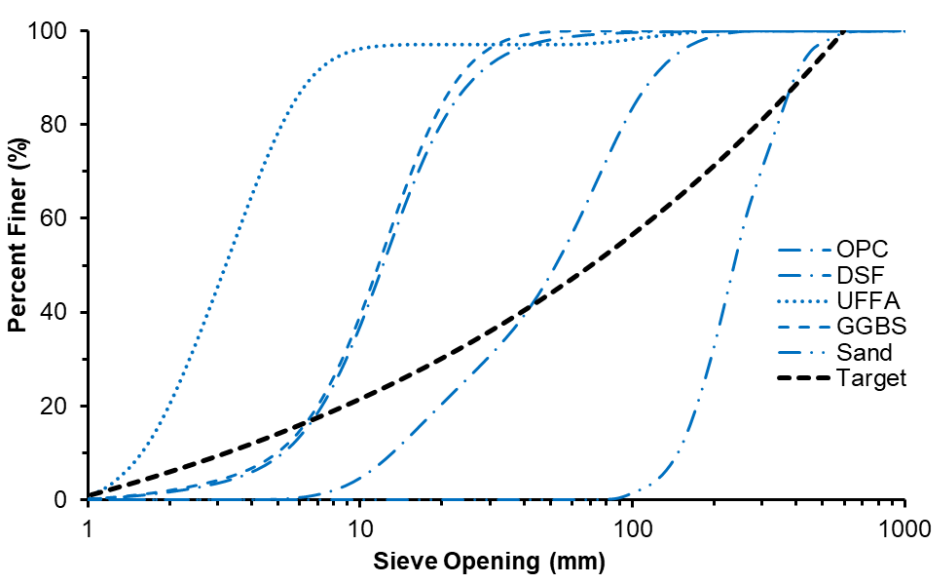

Figure 10. Graph. Particle size distribution of the sand and binders used in designing the UHPC mixes. The ideal target curve has been obtained from the modified Anderson and Andreasen model using a distribution modulus (q) of 0.23.

Cement

Type IL Portland Limestone Cement (PLC), in compliance with the IDOT-qualified list of approved cement producers, was used as the primary binder in the UHPC mix design. A low-alkali content was selected to prevent any future material deterioration, such as alkali-silica reaction. The chemical

composition of the cement, determined with a Shimadzu EDX-7000 X-ray fluorescence spectrometer, is tabulated in Table 15 of Appendix A.

Granulated Blast Furnace Slag

A commonly available Grade 100 slag was used with a moderate activity index. With a specific gravity of 2.95, the slag sample used had a median particle diameter of 11.6 μm, as evident in Figure 10. The slag sample conformed to the specifications of ASTM C989 (2022).

Ultra-Fine Fly Ash

A finer version (d_{50}: 3.4 μm) of Class F fly ash—namely, ultra-fine fly ash (UFFA)—conforming to ASTM C618 (2023), was used to increase the overall packing of the UHPC system. The chemical composition of the fly ash samples is summarized in Table 16 in Appendix A. Due to a higher (SiO_2 + Al_2O_3 + Fe_2O_3) content of 75.99%, fly ash samples can provide late-age pozzolanic activity, contributing to the late-age strength of the mixes.

Silica Fume

A dry densified silica fume powder was used in compliance with the specifications of ASTM C1240 (2020). In Figure 10, the particle size of the silica fume (SF) was higher than the other binders due to its densified state and agglomerating tendency. A specific gravity of 2.2 was used for the SF sample in the mix-design calculations.

Aggregate

Locally available fine masonry sand, complying to ASTM C144 (2024), was used as the aggregate. The masonry sand was chosen due to its fineness, availability, and favorable shape morphology, which would aid in designing cost-effective UHPC. Design for UHPC mixes requires finer gradation of sand for higher packing, so only sand finer than 600 μm was used in the mix designs.

High-Range Water Reducer

The high-range water reducer (HRWR) forms an essential constituent for UHPC mixes, to impact the workability of the mixes at an extremely low water-binder ratio. As a trial phase, different HRWR samples were tested from local suppliers and were compared with respect to the fluidity of the mixes. For the final set of UHPC mixes, a polycarboxylate ether-based (PCE) HRWR, AdvaCast 593, was used as the admixture, as it required a lower dosage for enhancing the fluidity of the mixes.

Steel Fibers

Steel fibers resist the development of post-cracking tensile stress through the composite action between the UHPC matrix and the fibers. In this study, striated steel fibers of 0.5 inch (13 mm) in length and 0.0078 inch (0.2 mm) in diameter with an aspect ratio of 65 were used for the UHPC mixes. Shear keys are formed in striated fiber as a result of paste hardening on the surface, which provides the initial pull-out resistance (Kim & Yoo, 2019; Park et al., 2014). After the initial resistance, the shear keys continue to provide frictional resistance, which enhances the bond between the UHPC matrix and the fibers (Xu et al., 2016). The striated surface of the steel fibers enhances the bond

strength between the UHPC matrix and the fibers, which prevents slipping and enhances the ductility of the UHPC mixes. The minimum tensile strength of the steel fibers was 285 ksi (1965 MPa).

TEST METHODOLOGIES

Mini-Slump Flow Test

The flow test for UHPC samples was conducted following ASTM C1856 (2017) using a brass cone mold set on a clean flat surface (see Figure 11). The mold, dimensions 2.75" top diameter by 2" height by 4" bottom diameter, was filled with a UHPC mix, and the surface was leveled without tamping or dropping the table. After lifting the mold vertically, the mix was allowed to spread for 2 minutes, and the spread diameter was measured across four lines to calculate the average flow diameter of the UHPC.

Figure 11. Photo. Mini-slump flow test used in measuring the rheological property (flow) of the fresh UHPC mixes.

Compressive Strength Test

The compression test for UHPC samples was carried out according to ASTM C1856 (2017), with samples cured for 1, 3, 14, and 28 days at 95% relative humidity. The flat end of each cube, free of projected fibers and without capping compounds, was positioned against the platen of the Forney compression testing machine. The cross-sectional area of each cube was measured before testing to ensure accuracy. During testing, the loading rate was maintained between 60,000 and 70,000 lb/minute until initial failure, with the maximum load recorded to calculate the compressive strength.

Open Porosity

The open porosity of UHPC samples was measured using an Accupyc II 1330 pycnometer (see Figure 12), with helium as the probe gas. The process involved introducing helium into a sample chamber (V_{sample}) at an initial pressure (P_i) of 19.5 psi, allowing it to expand into a reference chamber (V_{ref}), repeating this for 10 cycles to calculate average skeletal volume. The UHPC specimens were cast in 10 mm × 10 mm × 40 mm cuvettes, cured in a sealed environment for a day, and then cured in a curing

chamber until testing. Before measuring, samples were kept in a saturated surface dry condition, and excess moisture was wiped off. Their mass and volume were measured before and after oven drying at 105°C for 24 hours to calculate bulk (ρ_{bulk}) and true densities (ρ_{true}), respectively. Open porosity was then determined as the ratio of bulk to true density. This evaluation was performed at 3, 7, and 28 days to support strength assessments.

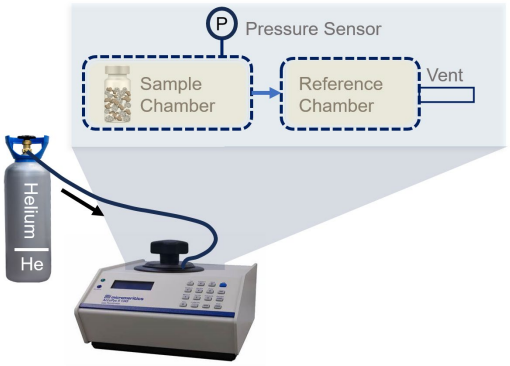

Figure 12. Photo. Methodology followed for measurement of the open porosity of UHPC specimens.

Drying Shrinkage

The shrinkage test for UHPC samples, adhering to ASTM C596 (2023) standards, involved using 1 inch × 1 inch × 11.25 inch prism molds with a 10-inch gauge length, as shown in Figure 13. Each mold was thoroughly cleaned with an oiled cloth to ensure no debris would affect the results and then filled with the UHPC mix without tamping for consistency. Post-casting, the molds were covered with plastic sheets to retain moisture and demolded after 24 hours before being placed in a moist curing room for 48 hours.

At 3 days of hydration, samples were removed from the curing room, and any surface moisture was wiped off. Initial length measurements were taken using a precise length comparator housed in a humidity chamber set at 50% relative humidity. Subsequent measurements were taken at 3-day intervals during air curing and the change in length, calculated by subtracting the initial measurement from each subsequent one, was expressed as microstrain.

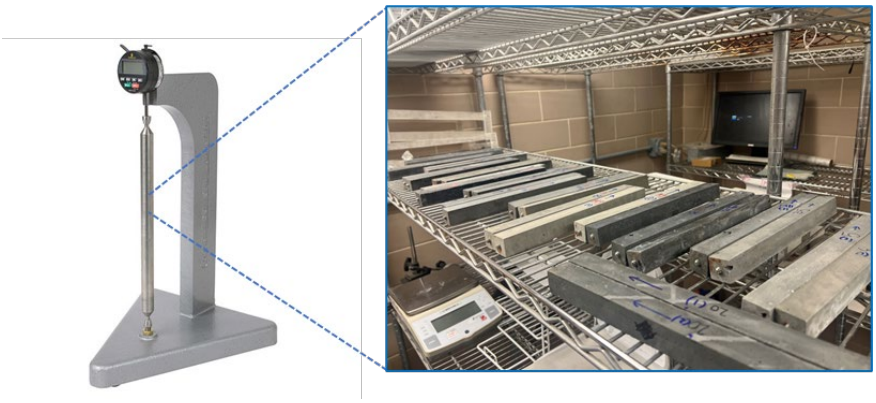

Figure 13. Photo. Length comparator used to measure the linear drying shrinkage of UHPC prisms.

MIXING REGIME AND SAMPLE STORAGE

UHPC mixes usually incorporate considerably higher amounts of binder compared to regular concrete. Hence, it is vital to ensure a high-shear energy input to the mix to achieve the desired consistency. It is also important because of the extremely low water-binder ratio of UHPC, which requires an optimized mixing strategy (mixing time, speed, and sequence) for efficient mixing of UHPC. The binder needs to be properly mixed so that the HRWR can effectively disperse the cement particles and attain the desired flow. In previous research by Wille et al. (2012) and the Federal Highway Administration (Graybeal, 2014), the ingredients were mixed together initially in a dry state before adding water and HRWR. Further, the researchers studied the influence of different HRWR addition times on UHPC properties, including direct and delayed addition. Note that increasing the mixing time and speed can result in an increased number of pores within the UHPC microstructure, which can impact the performance of UHPC.

In this study, a high-shear bench-top mixer was used to mix the UHPC mixes for small-scale batching. The researchers used the following mixing regime based on different preliminary trial mixing regimes to minimize turnover time and ensure the desired consistency:

- **Initial Dry Mixing**: Sand and silica fume were mixed dry for 5 minutes to break down agglomerates that can impact packing.
- **Addition of Dry Components**: Cement, fly ash, and slag were added and mixed for another 5 minutes to achieve uniform dispersion, with measures taken to prevent any loss of materials.
- **Wet Mixing**: Initial Phase—60% of the water combined with HRWR was introduced and mixed with the dry blend for 5 minutes to disperse PCE particles effectively.
- **Wet Mixing**: Final Phase—The remaining water and HRWR were added, continuing to mix until the mix reached the turnover time (i.e., conversion of the powders to a plastic state.)
- **Steel Fiber Addition**: At the plastic state, steel fibers were slowly incorporated, ensuring uniform dispersion and adjusting HRWR dosage as necessary for the target flow.
- **Final Mixing**: The mix underwent high-speed mixing for 2 minutes and then slowed down for an additional 1 minute before proceeding to further tests.

The optimized mixing regime is graphically represented in Figure 80 in Appendix A, describing the sequence of steps and time duration. The change in mix consistency was observed for each step, which marks the progression of the dry binder state to a paste consistency at the turnover time. The progression of the mix consistency is shown sequentially in Figure 14.

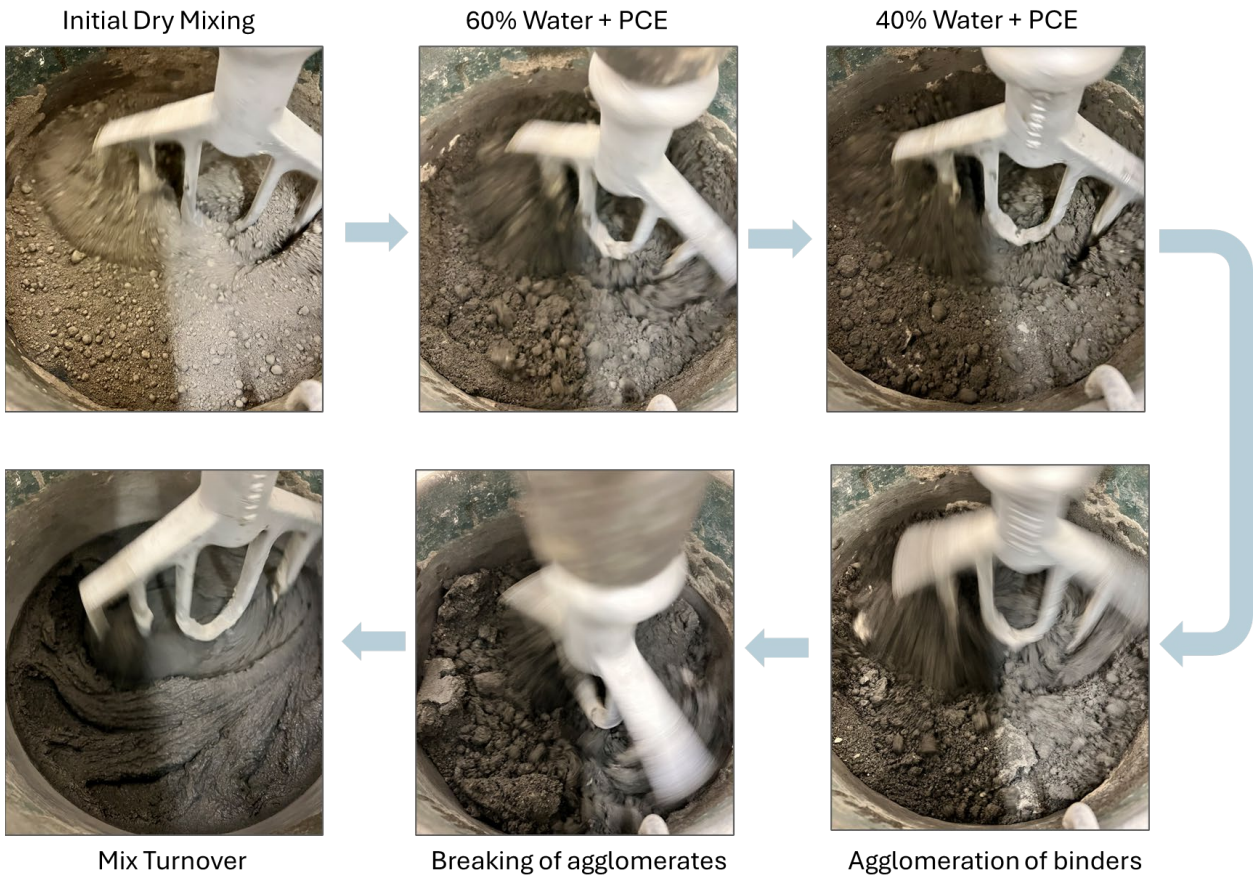

Figure 14. Photo. Progression of the mix consistency of a typical UHPC mix from dry mixing to the turnover time.

The mix was immediately transferred to the flow table for the mini-slump flow test and casting of the samples. The UHPC mixes were poured carefully into the cube molds to ensure uniform fiber dispersion. After casting, the samples were sealed for 24 hours to prevent any moisture changes with the environment. The samples were later demolded and stored in the curing chamber with a relative humidity of 95% and an ideal room temperature of 22°C before further tests.

CHAPTER 4: TRIAL MIX DESIGN AND MIX OPTIMIZATION

OVERVIEW

The formulation of multi-binder UHPC is a complex process that demands a meticulous selection and combination of materials, including cement, fine aggregates, fibers, and pozzolanic additives like fly ash and silica fume. Each component plays a pivotal role in defining the final properties of the concrete, such as its compressive strength, ductility, and permeability. Given the high-performance standards required from UHPC, traditional trial-and-error approaches to mix design are not only inefficient, but also economically unfeasible due to the high cost of UHPC materials. There is a pressing need for systematic approaches that can optimize these interactions and predict the outcomes effectively.

MIXTURE DESIGN

Mixture design is a specialized branch of statistical experimental design specifically tailored for scenarios where the experiment involves blending various components whose total must always sum to a fixed amount, usually 100%. This approach is ideal for UHPC, as it enables researchers to:

- Systematically investigate the impact of varying material proportions on concrete properties.
- Identify optimal combinations that deliver the desired balance of strength, durability, and cost-effectiveness.
- Explore the complex interactions between materials, which are pivotal in achieving the high-performance characteristics of UHPC.
- By implementing a mixture design, engineers and researchers can create more efficient, targeted experiments that accelerate the development process and enhance the performance of UHPC in practical applications.

MIX DESIGN MODEL USED FOR THE STUDY

This study used the simplex lattice design model to design the UHPC mixes. In a simplex lattice design with three components, the second-order model would include terms up to the quadratic interactions.

$$Y = \beta_0 + \beta_1 x_1 + \beta_2 x_2 + \beta_3 x_3 + \beta_{12} x_1 x_2 + \beta_{13} x_1 x_3 + \beta_{23} x_2 x_3 + \beta_{11} x_1^2 + \beta_{22} x_2^2 + \beta_{33} x_3^2$$

Figure 15. Equation. Simplex lattice design model for mixture design.

This model helps in understanding how individual components and their combinations influence the response. By fitting the above model to experimental data, coefficients can be estimated using least squares regression. Once the model is fitted, it can predict responses at any combination of component proportions within the experimental range. This predictive capability is crucial for

identifying optimal formulations in UHPC mix design, where the goal is to achieve a mix that optimizes desired properties such as strength and durability.

The research team used the commercial Minitab software to design 19 nonproprietary UHPC mixes, summarized in Table 1.

Table 1. Mix composition of the designed 19 mixes obtained from the mixture design method in Minitab software. The units are presented in kg/m^3 considering a volume of 0.04 m^3 in this study.

Mix ID	Cement	Silica Fume	Fly Ash	Slag	Total Binder	Sand
M1	1575	0	0	0	1575	1325
M2	1181.3	275	0	0	1456.3	1325
M3	1023.8	0	456.8	0	1480.5	1325
M4	630	275	456.8	0	1361.8	1325
M5	787.5	0	0	737.5	1525	1325
M6	630	110	0	737.5	1477.5	1325
M7	630	275	0	516.3	1421.3	1325
M8	630	0	130.5	737.5	1498	1325
M9	630	0	456.8	368.8	1455.5	1325
M10	857.5	103.9	166.8	344.2	1472.3	1325
M11	1216.3	51.9	83.4	172.1	1523.7	1325
M12	1019.4	189.4	83.4	172.1	1464.3	1325
M13	940.6	51.9	311.8	172.1	1476.4	1325
M14	743.8	189.4	311.8	172.1	1417	1325
M15	822.5	51.9	83.4	540.8	1498.7	1325
M16	743.8	106.9	83.4	540.8	1474.9	1325
M17	743.8	189.4	83.4	430.2	1446.8	1325
M18	743.8	51.9	148.6	540.8	1485.2	1325
M19	743.8	51.9	311.8	356.5	1463.9	1325

For generating the mix design, binders (cement, fly ash, silica fume, and slag) were considered as parameters, and the sum of the binders was equal to 1. Using the simplex lattice design ensures that the effect of the ternary binders can be evaluated for each corresponding cement component for optimizing the mixes. In this regard, a range of cement from 40%–100% was chosen as the primary binder along with an experimental range of 0%–25%, 0%–35%, and 0%–50% for silica fume, ultra-fine fly ash, and slag, respectively. The mix proportions obtained from the design of experiments analysis are summarized in Table 17 in Appendix B. While incorporating the aggregate skeleton, a sand-binder ratio of 1.0 was chosen for the mix design. Also, a water-binder ratio of 0.18 was chosen for the mixes based on the general water-binder ratio used in previous studies.

CHAPTER 5: PARTICLE-PACKING-BASED DESIGN OF UHPC MIXES

OVERVIEW

Ultra-high performance concrete mixtures are engineered to attain a high particle-packing density, significantly reducing porosity while enhancing strength and impermeability. The development of high-quality UHPC typically hinges on creating a dense particle assembly, which necessitates the use of packing models for systematic selection and design of binders.

Classical particle-packing theories have been instrumental in the precise formulation of UHPC. For instance, Larrard et al. (1994). pioneered the linear packing density model, which later incorporated the notion of virtual packing density (Roquier, 2019). This led to the development of the compressible packing model (CPM) to bridge the gap between actual and theoretical packing densities by introducing the compaction index. Arora et al. (2019) further expanded this approach by adapting the compressible packing model to select suitable aggregates for designing durable and sustainable UHPC mixtures. Conversely, Ji et al. (2011) explored the Aim and Goff model, which treats solid particles as distinct entities, though it lacks in representing the actual distribution of particles, complicating the calculation of fine particle metrics (Aim & Le Goff, 1968; Moini et al., 2019). To overcome the limitations inherent in discrete models, Fuller and Thomsen (2016) incorporated continuous grading of aggregates, which can enhance the overall properties of the concrete mix. Building on this foundation, Funk and Dinger (1994) introduced modifications to consider the smallest particle size in what is now referred to as the modified Anderson and Andreasen model (MAA).

In this study, the research team has leveraged existing knowledge of packing models to incorporate multiple models in characterizing the packing condition of the UHPC mixes. This chapter explores different packing models used in the literature to design UHPC and summarizes the different models used in this study to design the UHPC mixes with variable packing characteristics.

SYNOPSIS OF THE PACKING MODELS USED

Modified Anderson and Andreasen Model

The initial continuous model introduces the target particle size distribution, *P(D)*, to enhance optimal packing in the system, as follows:

$$P(D) = \left(\frac{D}{D_{max}}\right)^{q} X\ 100\%$$

Figure 16. Equation. Packing model from Fuller and Andersen.

where, *P(D)* denotes the fraction of the particles finer than the diameter *(D)*; *Dmax* is the maximum particle size within the system, and *q* represents the distribution modulus of the system.

Funk and Dinger introduced the minimum particle size, *(D_{min})*, into the model to consider the effect of minimum particle size on the packing state and instituted the MAA model as follows:

$$P(D) = \left(\frac{D^q - D_{min}^q}{D_{max}^q - D_{min}^q}\right) X\ 100\%$$

Figure 17. Equation. Modifications from Funk and Dinger to the packing model.

The distribution modulus *(q)* is a key parameter that dictates the proportion of finer and coarser particles within the system and significantly influences the overall properties and microstructure of the UHPC mixes. Ideally, for specific values of D_{min} and D_{max}, a lower value of *q* represents a finer particle distribution. Brouwers and Radix (2005) suggested a *q* value in the range of 0–0.25 for a cementitious system with a high amount of binder. Meanwhile, for UHPC mixes, a recommended range of 0.21–0.25 has been established in previous research works (Hunger, 2010; Mehdipour & Khayat, 2018b; Yu et al., 2015). Based on the recommended ranges and trial runs, a distribution modulus *(q)* of 0.23 was used to design the UHPC mixes in this study.

Compressible Packing Model

The compressible packing model (CPM) is integral in the formulation of concrete, especially for developing UHPC, by enhancing the arrangement of multi-sized particulate constituents to maximize the packing density, as shown in Figure 18. This model leverages a granular packing theory to strategically optimize the distribution and interaction of particles within the mix, reducing the porosity and enhancing the overall mechanical properties of the concrete. It takes into account complex particle interactions such as the loosening effect—where smaller particles disrupt the dense packing of larger ones—and the wall effect—where larger particles constrain the placement of smaller particles. Through precise control of particle size distribution and iterative adjustments based on CPM outputs, concrete mixes can achieve improved compressive strength and durability while using materials more efficiently. This scientifically informed method supports the creation of more sustainable concrete by minimizing the cement content required for strength and durability, leading to reduced environmental impact and enhanced economic feasibility. A comprehensive step-by-step conceptualization of the CPM model is provided in Appendix C for convenience.

$$\gamma_i = \frac{\beta_i}{1 - \sum_{j=1}^{i-1}[1 - \beta_i + b_{ij}\,\beta_i(1 - \frac{1}{\beta_j})]y_j - \sum_{j=i+1}^{n}[1 - a_{ij}\,\beta_i\,\beta_j]\,y_j}$$

$$K = \sum_{i=1}^{n} \frac{\frac{y_i}{\beta_i}}{\frac{1}{\phi} - \frac{1}{\gamma_i}}$$

Figure 18. Equation. Compressible packing model for packing estimation.

where,

- βi is the residual packing density of material size "i".
- yi represents the individual volume fraction of material size "i" in the mix.

- *n* is the number of different material sizes in the mix.
- wi and wj are the weight fractions of material sizes "i" and "j", respectively.
- ρi and ρj are the specific gravity values of material sizes "i" and "j", respectively.
- γi is the packing density of the material mix, considering material size "i" as the dominant.
- *K* is the compaction index. K = 9 is used when materials are vibrated and compacted and K = 4.75 only when vibration is used.

ESTIMATION OF PACKING FACTOR

The composite particle size distribution of each of the 19 finalized UHPC mixes is shown in Figure 20. The composite curves have been estimated based on the exact volumetric mix composition, where an equivalent weightage was assigned to the particle size distribution (PSD) of each binder. The resultant composite PSDs were compared with the ideal target curve (dotted line) for a distribution modulus of 0.23, which represents the optimum packing condition.

The aim of the MAA model is to ensure a customized mix composition to warrant that the composite PSD has a closer fit to the ideal target curve. Hence, to quantify the packing state of the UHPC mixes, the research team has formulated the "packing factor" as an effective measure of the deviation from the ideal packing condition. The deviation has been estimated per Figure 19 and represents the difference between the ideal state and an exemplary UHPC composite mix, as shown by green arrows in Figure 84 in Appendix C. The difference corresponds to the difference between the composite PSD of the UHPC binders and the target curve for each sieve opening, labelled "I."

$$\mathrm{PF} = \sqrt{\sum_{\mathrm{i}=1}^{\mathrm{n}} \left(\mathrm{P}_{\mathrm{UHPC}}\left(\mathrm{D}_{\mathrm{i}}^{\mathrm{i}+1}\right) - \mathrm{P}_{\mathrm{tar.}}\left(\mathrm{D}_{\mathrm{i}}^{\mathrm{i}+1}\right) \right)^2}$$

Figure 19. Equation. Estimation of packing factor.

The packing factor (PF) of each UHPC mix (M1–M19), corresponding to different mix compositions, is shown in Figure 21. Each bar corresponds to the mix composition of each mix, and the bars are arranged in ascending order of the packing factors. Note that a lower PF represents a UHPC mix with lower deviation from the ideal packing state, indicating a dry powder system with higher inherent packing. In this regard, the mix M4 exhibited the lowest packing factor (31.33) even at a significantly lower cement content of 40% by volume. The observed trend also highlights that UHPC systems with an inclusion of a higher number of binder types aid in lowering the packing factors, as evident for M14 (PF: 32.50), M10 (PF: 37.58), and M12 (PF: 38.03). This is due to particles of different sizes, which can fit the gaps more effectively, leading to higher packing. The aforementioned conclusion is also supported by the higher packing factors for unary UHPC M1 (PF: 46.0) and binary mixes M2 (PF:

42.90) and M5 (PF: 47.13), which exhibited much lower packing because of lower variation in particle size.

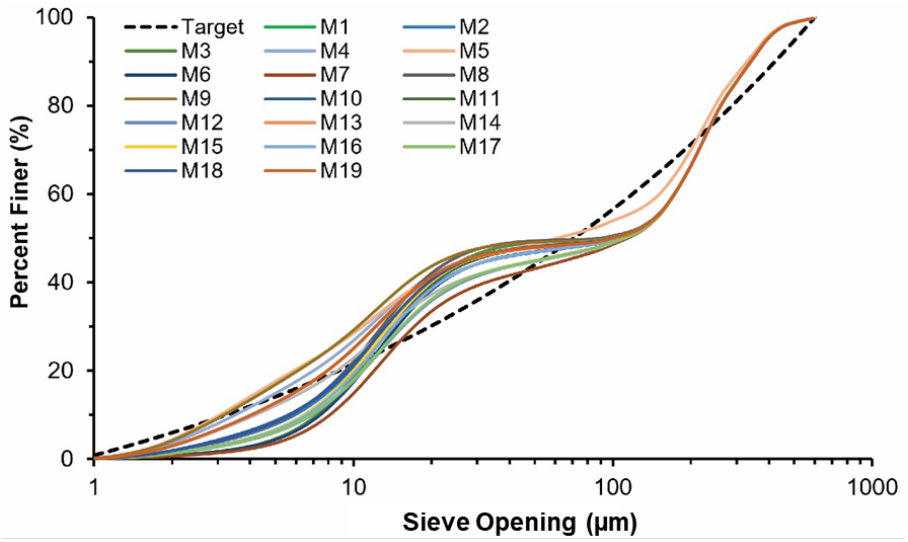

Figure 20. Graph. Composite particle size distribution of the developed 19 UHPC mixes compared to the ideal target curve for distribution modulus (q) of 0.23.

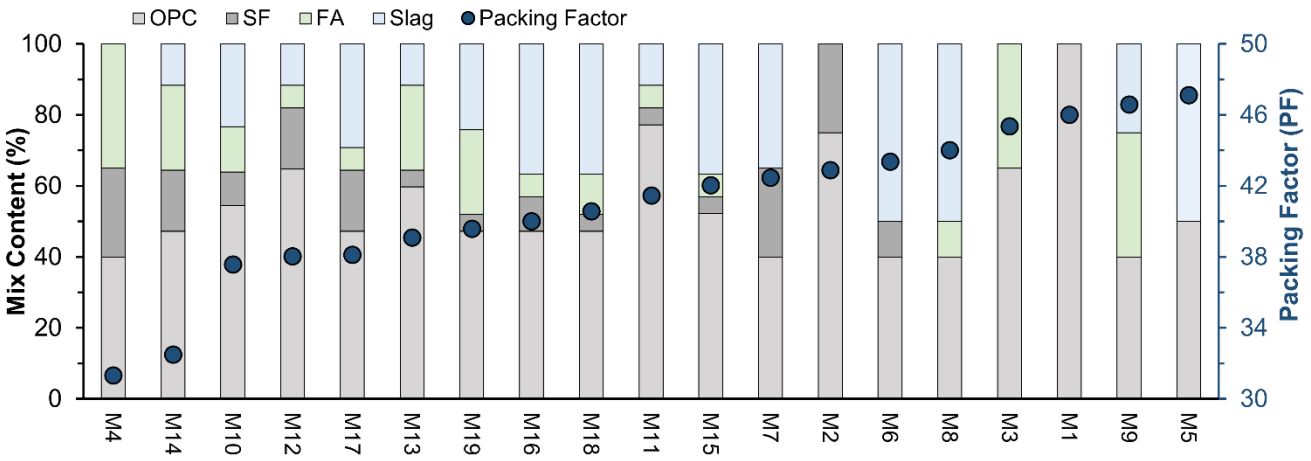

Figure 21. Graph. Summary of the packing factor (PF) for the 19 mixes designed in this study from the mixture method.

SENSITIVITY OF PACKING FACTOR TO BINDER COMPOSITION

Variations in packing factor highlight the importance of using binders with different particle sizes to optimize the UHPC mix, which in turn influences its rheological, mechanical, and durability properties. The sensitivity of PFs to each binder type is depicted in the Cox response trace plot (Figure 22) based on a reference blend composition (Cem: 54.4%; Slag: 23.33%; UFFA: 12.78%; SF: 9.44%). The plot shows that both cement and slag lead to a decrease in packing factor with increased content, suggesting lower packing efficiency. Conversely, UFFA, due to its finer particle size, initially decreases

the packing factor below around 20% before contributing to an increase, likely due to a loosening effect that impacts overall packing at higher volumes.

Aiming to reduce the cement content in the UHPC mixes, the correlations for each binder in the previous section have been utilized in developing the response surface plot in Figure 23. The ternary response plot reflects the influence of each SCM type on the packing factor at a definite cement content. An example of interpreting the ternary plot is shown in Figure 85 in Appendix C. The response of the SCMs on packing is represented in Figure 23 for different cement contents, ranging from 40% to 90% in Figure 23. The grey-dotted zone denotes the domain within the experimental range of the binder composition, while the exterior regions represent the extrapolated behavior based on the regression analysis.

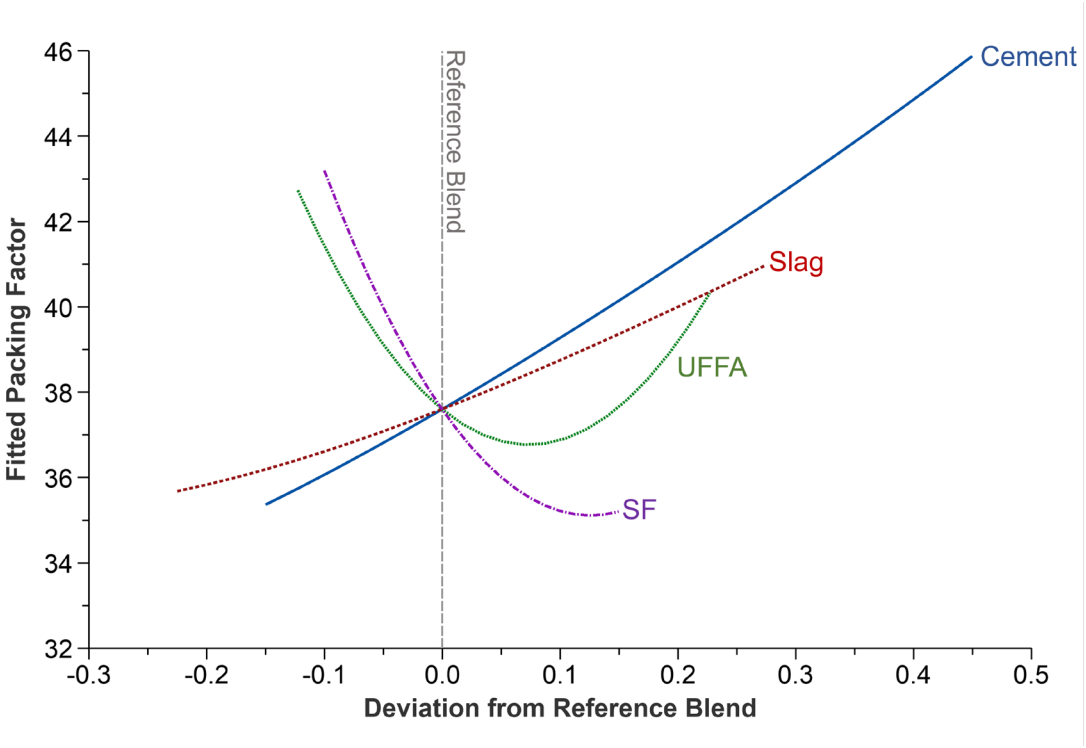

Figure 22. Graph. Sensitivity of packing factor of the designed UHPC mixes for unit variation of different binder constituents.

Based on the overall performance mapping in Figure 23, the research team confirmed some key observations. First, regardless of the cement content, the UHPC mixes exhibited lower packing (higher packing factors) at the corners of the ternary plots, referring to a high volume of a single SCM. This validates the necessity of having multiple binders to ensure a higher packing density in UHPC mixes. Second, the zone with higher packing (lower PF values), represented by the dark blue zone, became less prominent with an increase in cement content (minimum for cement content of 90%). This confirms the trend in Figure 23 (c) that it is possible to enhance UHPC mixes with a minimum cement content through optimization of particle packing. Third, the dark blue zone, signifying the higher packed regime, is more prominent with a nearly equivalent proportion of ultra-fine fly ash and

silica fume, which is more evident at higher SCM content. Finally, the response maps hold immense potential in customizing the binder type and composition to tailor the packing factor of the UHPC mixes while safeguarding the sustainability of the mixes.

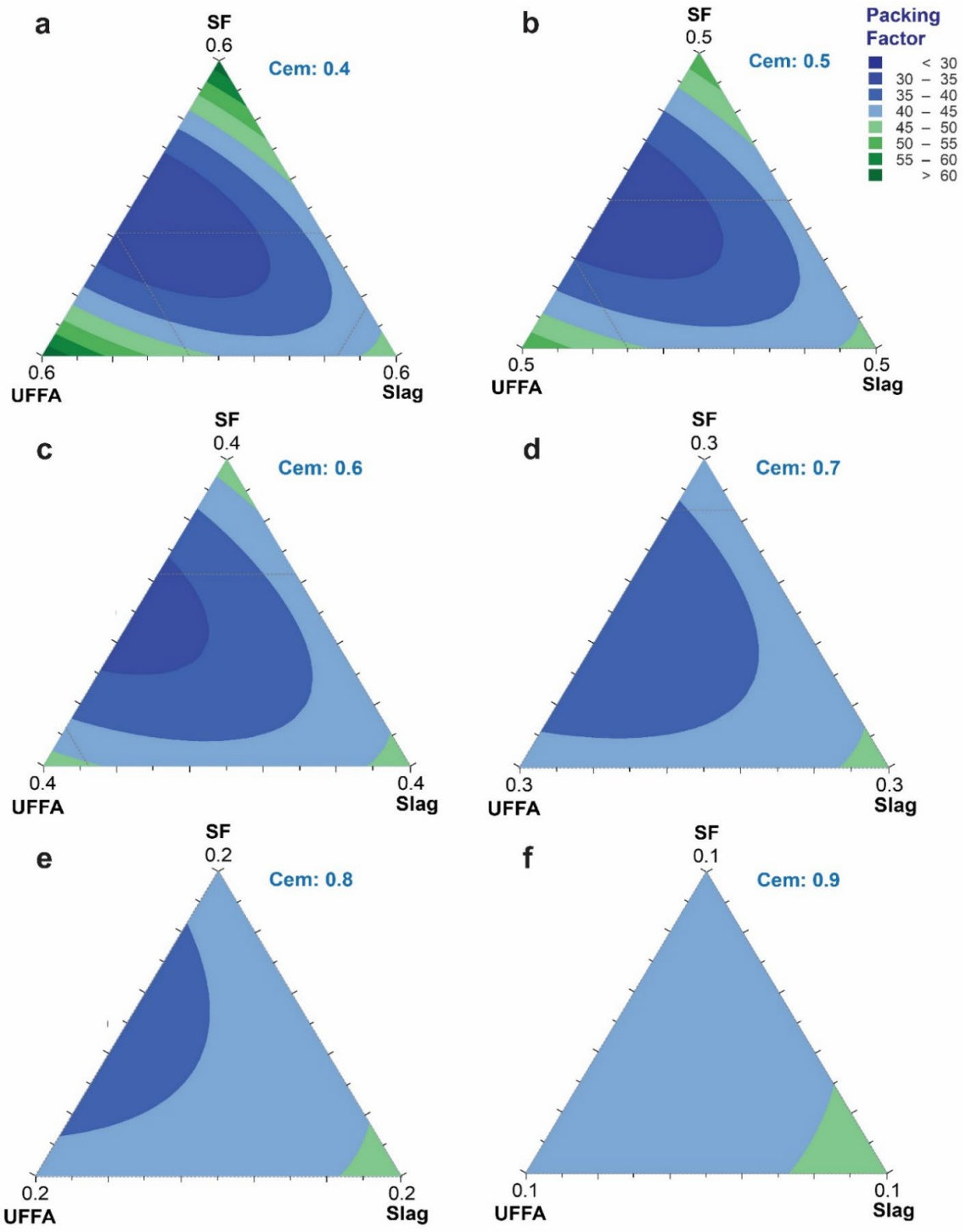

Figure 23. Graph. Ternary response plot showing the packing factor of the UHPC mixes for compositional variation of the binder constituents used in the study for 40%–90% of binder.

COMPARISON OF THE PACKING MODELS

The packing factors obtained through the continuous model (MAA) were validated by comparing them with the virtual packing coefficients obtained from the discrete CPM model. Based on the individual packing density of the individual binder and the fine aggregate, the virtual packing densities obtained from the CPM model were evaluated for the 19 UHPC mixes. The correlation between the packing factor and the packing coefficients is represented in Figure 24. The trend in Figure 21 shows an overall inverse correlation between the two packing parameters. This confirms that the MAA model can effectively characterize the packing state of the UHPC mixes. Note that the correlation between the two coefficients shows a very strong correlation, which justifies the use of the MAA model in characterizing the packing of the granular binders and aggregate.

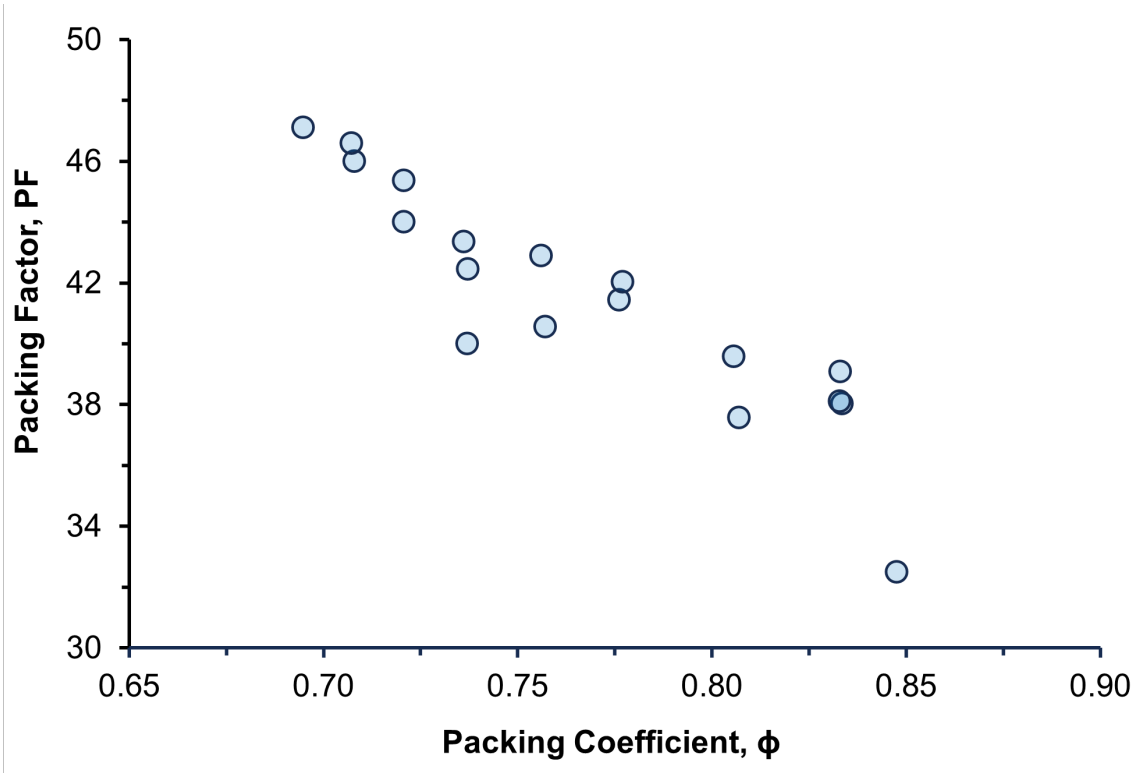

Figure 24. Graph. Comparison of the packing factor obtained from the modified Anderson and Andreasen model with the packing coefficient (ϕ) obtained using the CPM model.

CHAPTER 6: RHEOLOGICAL PROPERTIES OF THE OPTIMIZED UHPC MIXES

OVERVIEW

The unique composition of UHPC, which includes fine particles and high fiber content, necessitates a delicate balance of the rheological properties to ensure optimal flow without segregation or excessive bleeding. Scientifically adjusting the rheological parameters allows for the enhancement of particle-packing density and fiber distribution, which is critical for achieving the high compressive and tensile strengths characteristic of UHPC. This section summarizes the rheological properties of the UHPC mixes and correlates the rheological behavior to the HRWR fluidity of different binder compositions. Finally, this chapter describes the contribution of particle packing in influencing the rheological parameters and provides response models for the effective design of multi-binder UHPC mixes with optimum rheological properties.

RHEOLOGICAL SIGNATURE OF THE UHPC MIXES

The flow of the UHPC mixes obtained from the mini-slump flow test are summarized in Figure 25-A along with the HRWR dosage for each mix. The HRWR dosage required to achieve the self-flowing state varied considerably for the mixes, which also resulted in a wider variation in the final flow. This finding indicates the role of the binders, and the resultant physical and chemical aspects, in influencing the rheological properties of the multi-binder UHPC systems. Hence, the research team emphasized evaluating the flow/HRWR as a more effective measure for UHPC mixes with varying binder types and compositions. Most importantly, as silica fume drastically impacts the rheological properties, the mixes have been categorized into three separate zones with varying content of silica fume (Zone A: 4.7%–10%, Zone B: 17.2%–25.0%, and Zone C: 0%) to segregate the influence of different binders on the rheological properties.

In Figure 25-B, the UHPC mixes exhibited a wide variation in the flow/HRWR values from 2.43 to 10.76, confirming the role of different binder compositions on the HRWR effectiveness and overall rheology. Correlating to the mini-slump flow of 8–11 inches, as recommended by AASHTO, most of the UHPC mixes satisfied the slump range and, hence, can be considered self-flowable UHPC. Meanwhile, the variation of flow and flow/HRWR values within the recommended zone is due to the multi-binder interaction. For example, in Zone A corresponding to moderate silica fume content, M19 (flow/HRWR: 7.3) showed a higher rheology compared to M13 (flow/HRWR: 6.94), which is attributed to the cement dilution with slag. A similar trend was observed for M15, which exhibited a stronger flow/HRWR (5.18) compared to M11 with higher cement content (77.2%). The role of multiple binders is also evident in Figure 87, where a wide variation in flow/HRWR was observed for a variation in SCM composition even for a similar content.

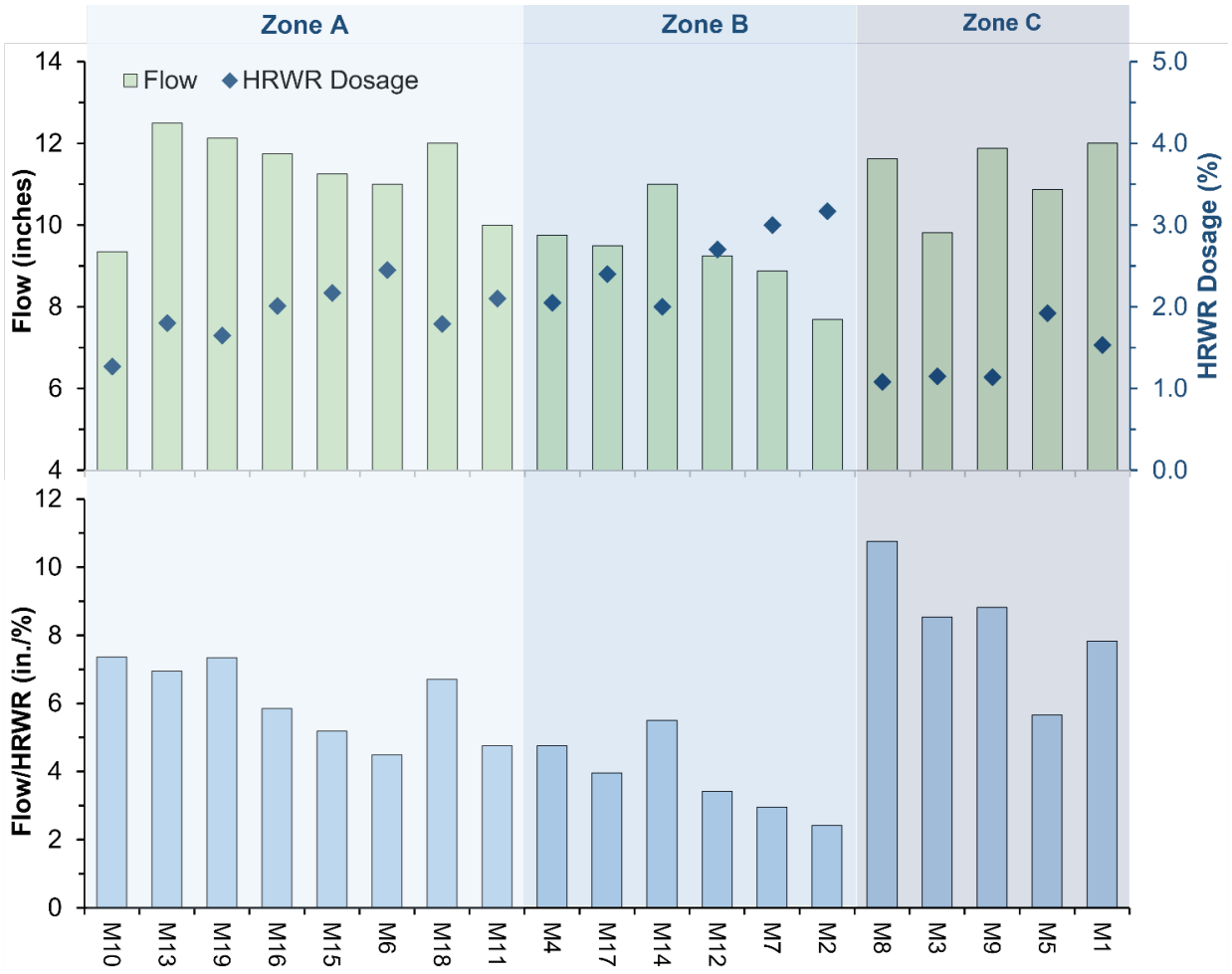

Figure 25. Graph. Summary of flow and flow/HRWR ratio of the designed UHPC mixes. The mixes have been classified into three different zones (Zone A–Zone C) based on different slag content.

The effect of silica fume on the fluidizing effect of HRWR was more prominent in mixes within Zone B with a higher amount of silica fume. M2, with a binary binder composition of 25% silica fume and 75% cement, showed a minimum flow/HRWR value of 2.43. This is due to the high water demand of the silica fume particles (Zain et al., 2000) and preferential adsorption to the PCE molecules (Schröfl et al., 2012), which impacts the mixes' overall rheology. Also, as the silica fume particles agglomerate (as evident through a larger particle size distribution in the PSD curve analysis), the clumps can hold water within the agglomerate, resulting in a lower amount of free water for lubrication of the mixes. Meanwhile, dilution of the cement with slag in M7 resulted in a moderate gain in the flow/HRWR value by 21.8% (2.43 to 2.96), despite having similar silica fume content. However, the most significant enhancement in flow/HRWR values was noted with the inclusion of ultra-fine fly ash into the UHPC system, such as M4 (4.76) or M14 (5.50). The increase in rheological properties with UFFA is due to the spherical morphology of the fly ash particles which, by rolling action, enhance lubrication and increase the fluidity of the mixes. Also, the finer particle size of UFFA filled up the pores, resulting in a better-packed microstructure, as evident from the low packing factor for M4 (31.3) and M14 (32.5). Focusing on the contrasting influence of UFFA and SF particles on the packing

morphology and rheological properties, understanding the variation of the flow properties for different SF/UFFA ratios would be substantial in interpreting the dual effect, as shown in Figure 26. Based on the general trend, the researchers demonstrate an exponential decay of the flow/HRWR index with an increase in the SF/UFFA ratio. As explained earlier, higher SF/UFFA ratios would increase the overall water demand of the UHPC mix, resulting in a reduced flow. Note that the variation at any individual SF/UFFA ratio accounts for the role of other binders in multi-binder UHPC mixes.

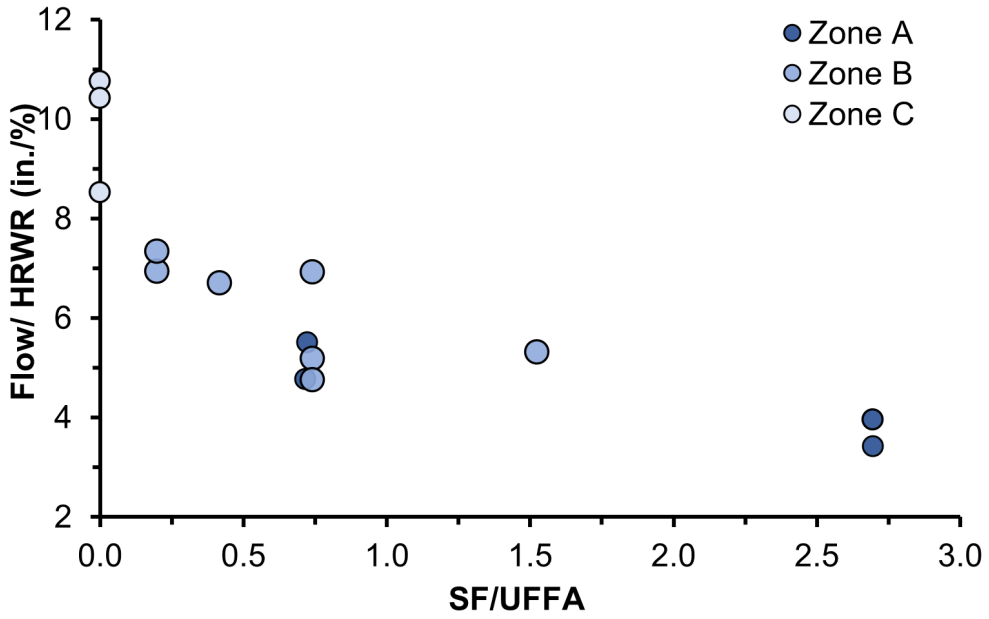

Figure 26. Graph. Effect of silica fume to ultra-fine fly ash ratio on the flow/HRWR ratio of the UHPC mixes.

IMPACT OF PARTICLE PACKING ON RHEOLOGICAL PROPERTIES

In a multi-binder UHPC system, the inclusion of binders of different particle sizes influences the overall packing, which defines the overall UHPC properties, as observed in the previous chapter. Hence, in this section, the rheological properties of the UHPC mixes were evaluated on the ground of their packing state (i.e., packing factor).

The mini-slump flow of the UHPC mixes was correlated to the packing factor (PF) of the mixes, as shown in Figure 86 in Appendix D. There is no definite trend between the two parameters, which reinstates the fact that flow alone might not be adequate to infer the role of multiple binders on the mixes' rheological properties, as the HRWR requirement varies corresponding to any changes in the mix composition. Hence, the correlation has been refined by comparing the packing factor with flow/HRWR in Figure 27, which demonstrates a definite correlation between the two for each zone of the UHPC considered in this section. This also validates the advantage of using flow/HRWR as a more reliable parameter to assess the rheological properties and superplasticizer efficiency in multi-binder UHPC.

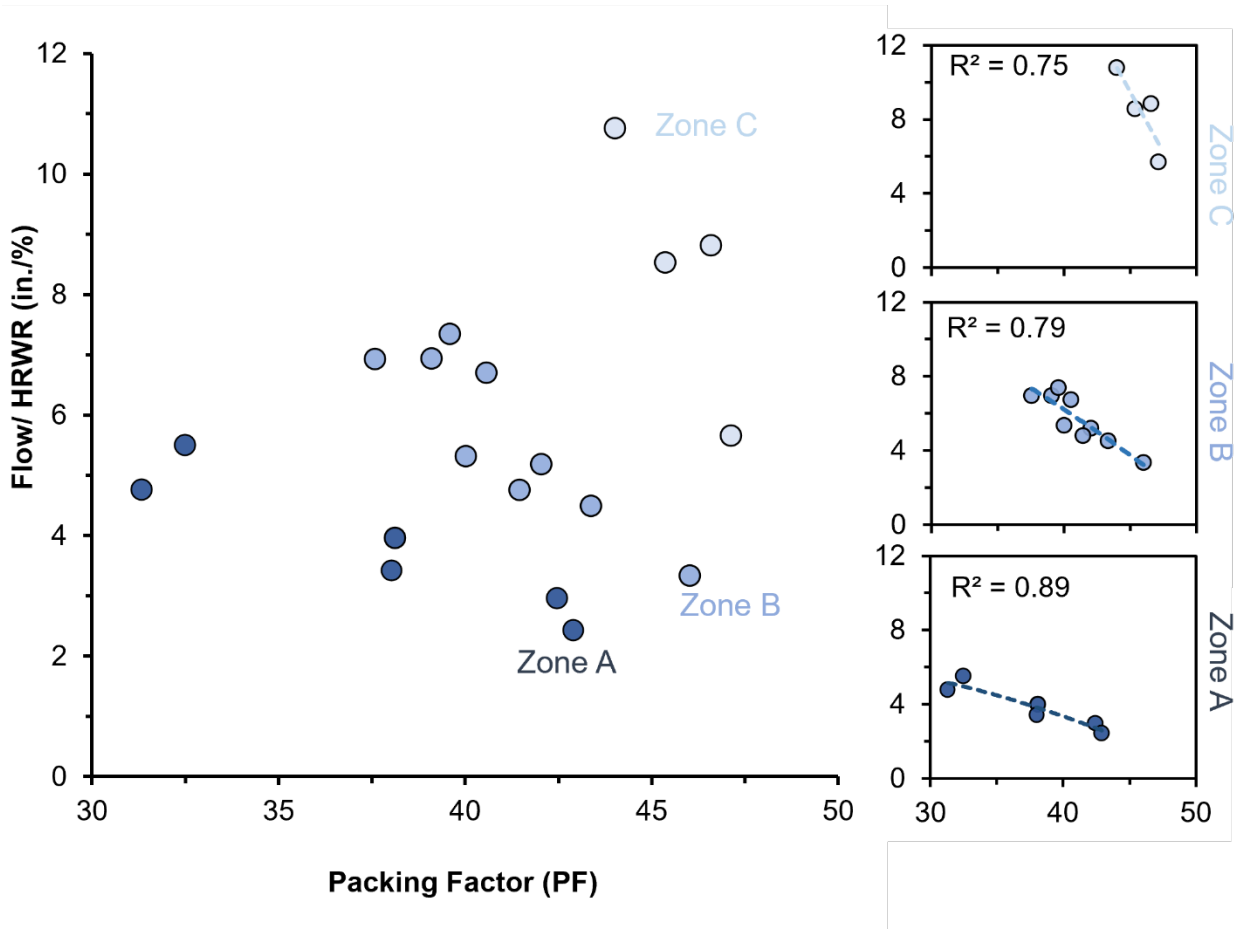

Figure 27. Graph. Correlation between the packing factor and the flow/HRWR ratio for the designed UHPC mixes.

In Figure 27, different mix zones show varying correlations, highlighting the complex role of binders in UHPC systems. Correlations for each zone are displayed separately for clarity. Notably, mixes in Zone C (0% SF) exhibit a significant correlation between a higher packing factor and enhanced rheological properties, with the steepest relationship between flow/HRWR and packing factor in this zone. This finding suggests that without the influence of silica fume, other binders' contribution to packing significantly affects rheology. Conversely, as SF content increases, its impact on rheology becomes more pronounced due to factors like water demand and selective PCE adsorption, lessening the dominance of the packing factor. This trend is evident in Zone A (moderate SF content) and extends to Zone B (17.2%–25.0% SF), where despite lower overall flow/HRWR values, a strong correlation (R2: 0.89) between packing factor and rheological properties persists across a broader PF range.

BINDER-BASED CHARACTERIZATION OF RHEOLOGICAL PROPERTIES

The variation in rheological properties across different mix zones underscores the need for binder-specific evaluation. The sensitivity of these properties, specifically flow and flow/HRWR, to changes in binder composition, is detailed in Cox response plots in Figure 28 and Figure 88 (Appendix D). Figure 28 illustrates how increasing cement content initially decreases flow but then increases it beyond a

20% deviation from the reference blend, likely due to higher paste volume enhancing flow. However, this also necessitates increased HRWR dosage for effective particle dispersion, leading to a continuous decline in flow/HRWR values at higher cement levels. Similarly, an increase in silica fume sharply reduces both flow and flow/HRWR, reflecting its significant impact on rheology. In contrast, UFFA consistently improves flow properties across varying proportions, highlighting its beneficial effect. The influence of slag becomes more pronounced at higher proportions due to cement dilution. Slag particles, carrying a negative charge from deprotonated silanol groups, attract Ca^{2+} ions, forming a stern layer that enhances PCE adsorption and particle dispersion (Flatt et al., 2023). This effect is more marked at higher slag contents, where cement dilution leads to significantly improved flow properties.

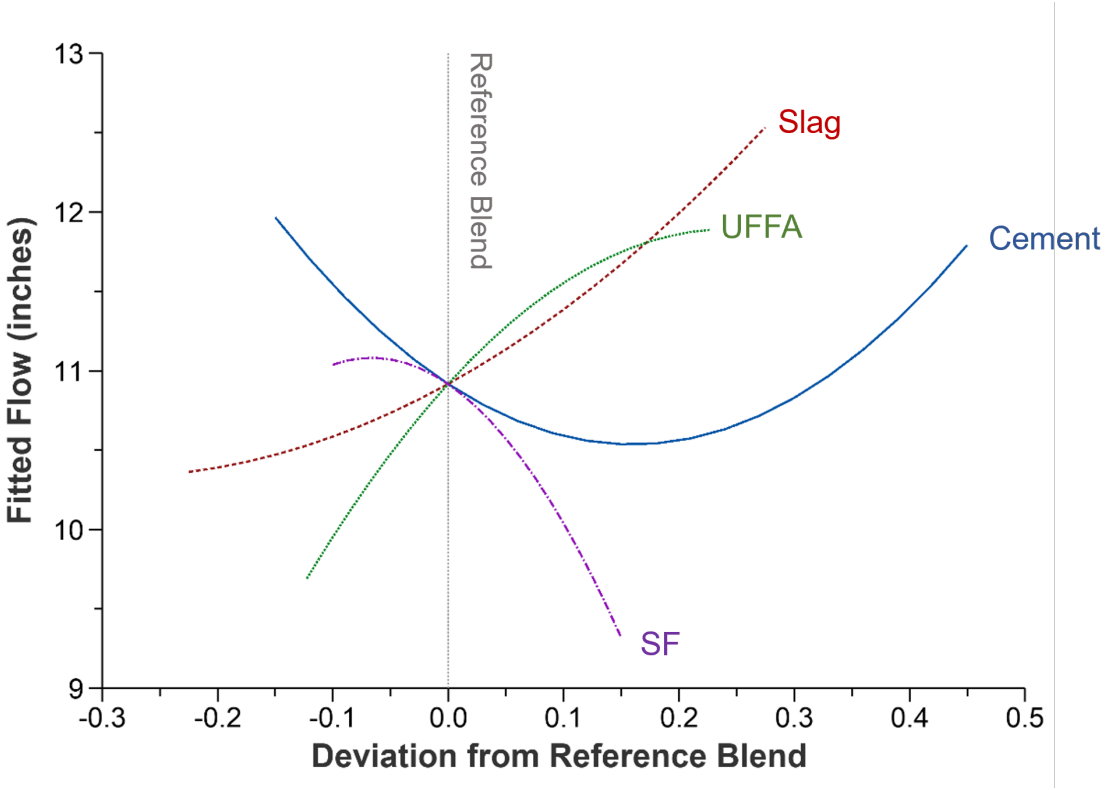

Figure 28. Graph. Sensitivity of flow of the UHPC mixes at (a) 3 days and (b) 28 days of hydration for unit variation of different binder constituents.

The sensitivity of the rheological properties was used to generate the response ternary plots defining the flow corresponding to different binder compositions. The ternary plots in Figure 89 (Appendix D) and Figure 29 were developed to predict the flow and the flow/HRWR ratio to have an overall idea of the flow and HRWR requirement for any binder composition.

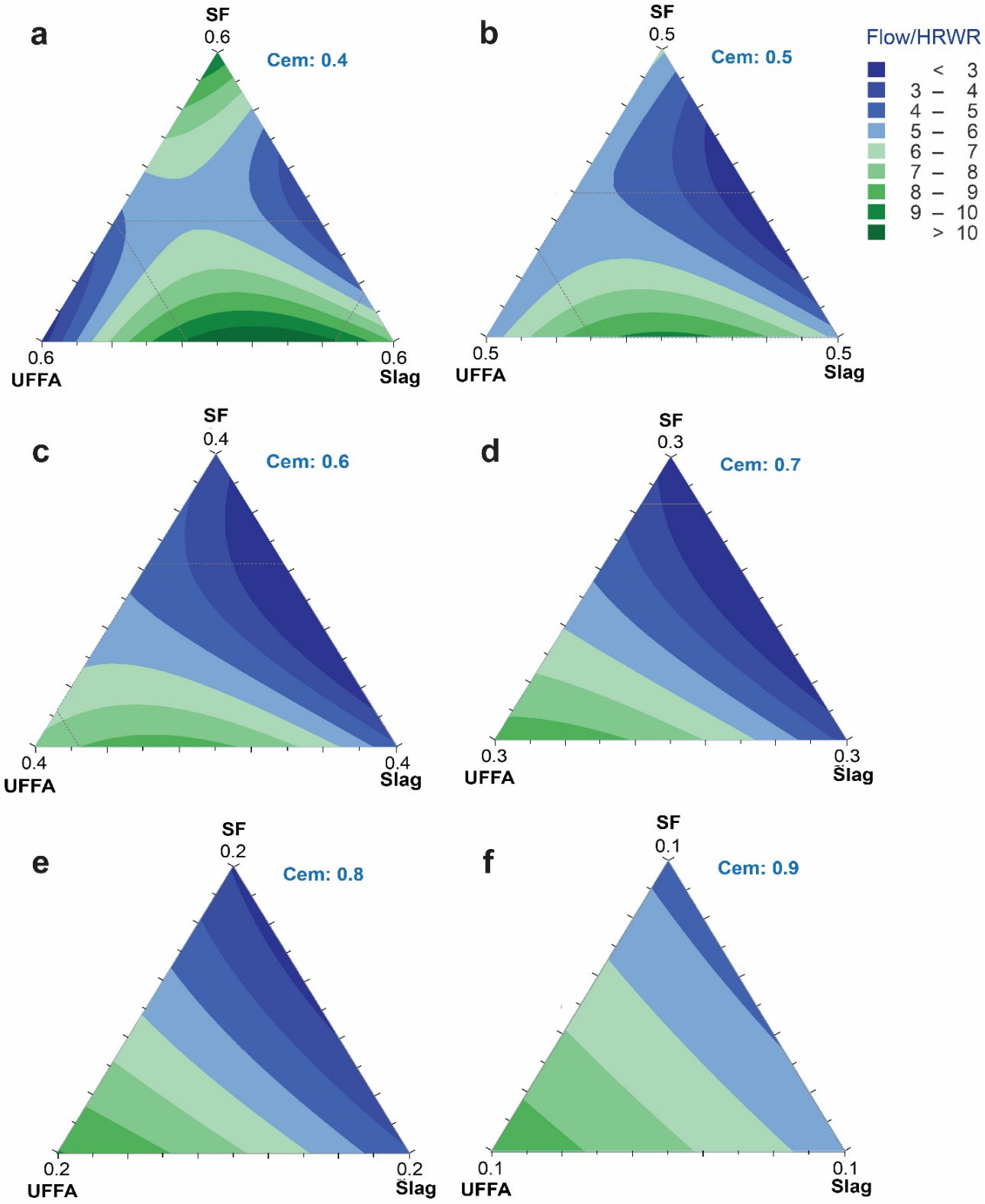

Figure 29. Graph. Ternary response plot for flow/HRWR of the UHPC mixes at 3 days for compositional variation of the binder constituents used in the study.

Figure 89 (Appendix D) shows that the inclusion of silica fume reduces the flow of the UHPC mixes, especially in mixes with lower cement content. A higher cement content compensates for the effect of silica fume by generating more paste for lubrication, which contributes to higher flow. However, the inclusion of either fly ash or slag resulted in higher flow, mostly at a lower cement content. Meanwhile, with an increase in the cement content, fly ash plays a more dominant role in enhancing the rheology of the UHPC systems which was evident in the mixes with higher UFFA content.

A similar trend was evident in Figure 29: higher flow/HRWR values (green zones) are evident at a higher blend of fly ash and slag. However, mixes with a blend of silica fume and slag exhibited significantly higher HRWR demand owing to their higher HRWR adsorption. A comprehensive idea of flow and flow/HRWR would aid in designing UHPC mixes with optimum rheological performance.

CHAPTER 7: PERFORMANCE EVALUATION OF THE OPTIMUM UHPC MIXES

As a state-of-the-art construction material, UHPC holds its significance by ensuring compressive strength of at least 17.4 ksi (120 MPa) as per AASHTO requirements. Based on previous literature (Alkaysi et al., 2016), researchers have focused on enhancing the particle packing of the UHPC system, both in dry and wet states, to ensure a well-packed system with an extraordinary load-bearing capacity. This also complies with an extremely low water-binder ratio, which results in a significant quantity of unhydrated cement and thereby provides the scope to utilize different alternate binders in the system (Du et al., 2021). Consequently, in a multi-binder system, it is also crucial to ensure optimum hydration of the system for a sufficient amount of hydration product to enhance the microstructure. Hence, in this research work, the research team has investigated the importance of packing (i.e., packing factor and the chemical aspect of the binders) and emphasized the consideration of the dual role in designing sustainable UHPC mixes.

This section underlines the mechanical performance of the optimized UHPC mixes at different ages of the specimens. Also, the role of packing factor and different binder compositions have been investigated to quantify the overall effect on strength development. Likewise, a binder-based characterization of the strength development has been explained to aid in customizing future UHPC mix designs based on different target strengths.

COMPRESSIVE STRENGTH OF THE UHPC MIXES

Figure 30 summarizes the compressive strength of the 19 optimized UHPC mixes for ages of 3, 7, 14, and 28 days. Based on existing literature, blast furnace slag plays a major role in influencing both early- and late-age strength of UHPC mixes. Hence, this section categorized the UHPC mixes into three different zones based on slag content: Zone A (0%), Zone B (11.7%–29.2%) and Zone C (35.0%–50.0%). Figure 30 represents the strength gain of the mixes from 0–3 days and 4–28 days to infer the early- and late-age strength properties of the mixes, respectively.

Referring to the overall trend in Figure 30, most mixes achieve more than 10 ksi (69.0 MPa) within 3 days of hydration. This finding signifies that the mixes possess a well-compacted microstructure, owing to a multi-binder composition, which resulted in high early strength. Note that the mixes have varying early- (0–3 days) and late-age strength (4–28 days), which denotes the role of both packing and chemical aspects at different stages of hydration in UHPC systems. For Zone A in Figure 30, corresponding to mostly binary mixes, the early strength is typically lower at 3 days, particularly for mixes with low cement content (e.g., M4). This finding shows the potential of slag's hydraulic activity in complementing early-age hydration of a cementitious system. This is also exemplified by M3 with a higher 3-day strength (11.5 ksi), which has moderately higher cement content. Meanwhile, there is considerable strength gain (> 8.2 ksi) for M4 at a later age of 28 days, which accounts for the higher UFFA content (35%) in the mixes, resulting in a late-age pozzolanic reaction.

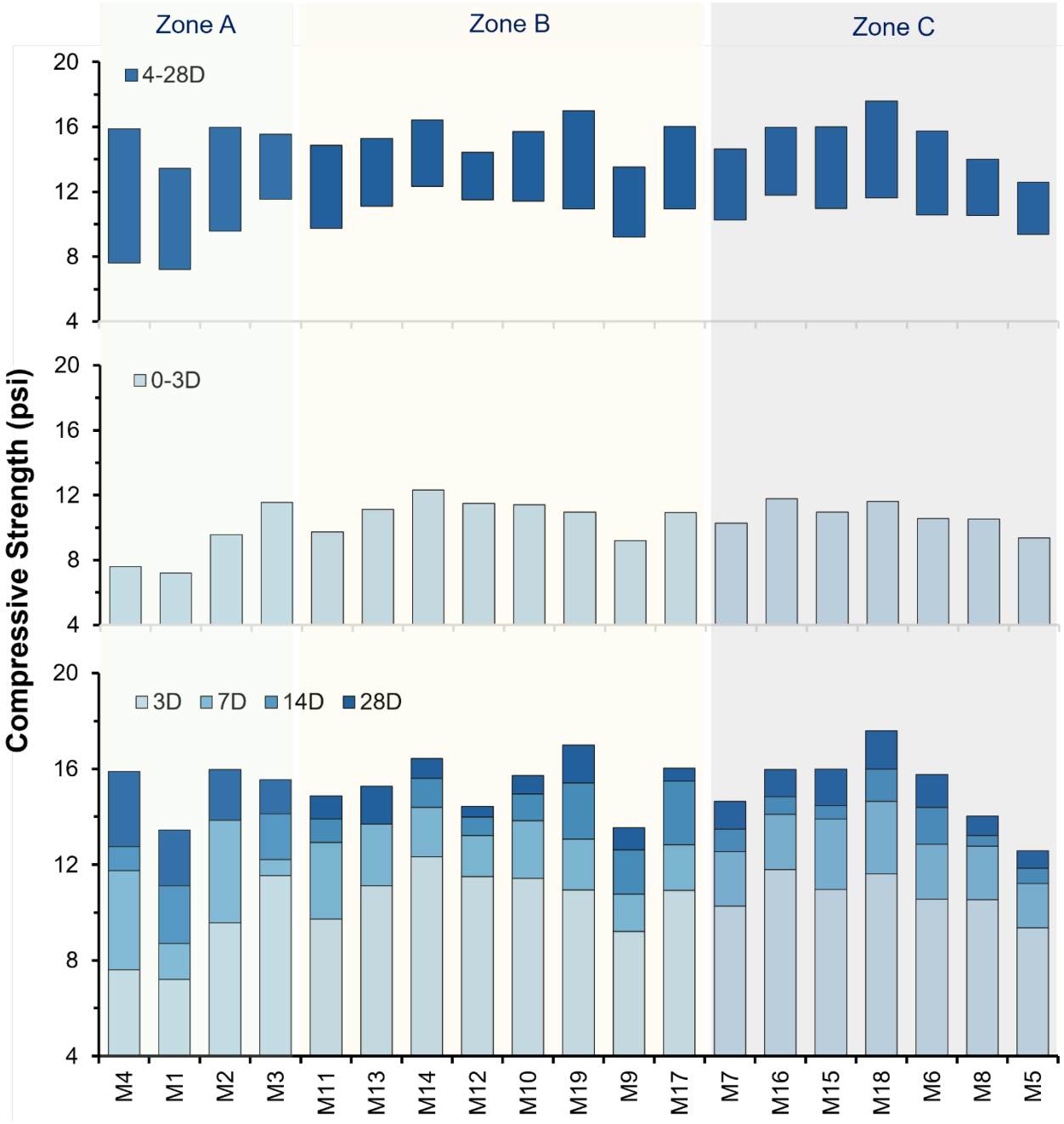

Figure 30. Chart. Compressive strength of the UHPC mixes separated into different ages of hydration and strength gain from days 0 to 3 and from days 4 to 28 of hydration for the designed multi-binder UHPC mixes.

For mixes with moderate slag content (Zone B), the early strength is notably higher even with lower cement content, demonstrating blast furnace slag's potential to reduce cement use without sacrificing early strength. For instance, M11, despite its higher cement volume (77.2%), shows a lower early strength (9.7 ksi) compared to M12, which achieves a higher early strength (11.5 ksi) with only 64.7% cement, thanks to added silica fume. This finding highlights the importance of particle packing

in enhancing early strength, as evidenced by M19, which achieves a balance of good packing (PF: 39.6) and a 3-day strength of 10.9 ksi with minimal cement (47.2%) and moderate slag (24.2%) contents. This mix also benefits from UFFA content (23.9%), boosting strength by over 6.1 ksi after 28 days. These findings, detailed in Figure 91 in Appendix E, underscore the significance of binder composition and mix design in optimizing compressive strength and reducing cement use.

In high slag mixes (Zone C), the presence of multiple binders leads to superior early strengths, aided by the hydraulic reactivity of slag and its synergy with fly ash. This is exemplified by M18, which shows the highest compressive strength at both early (11.6 ksi) and late (17.6 ksi) stages. However, in mixes like M5, where slag and cement have similar particle sizes, the packing is less effective (PF: 47.1), highlighting the need for a careful balance in particle size and binder chemistry to achieve optimal mechanical performance. The next section explores the impact of packing properties on mix performance.

IMPACT OF PARTICLE PACKING ON COMPRESSIVE STRENGTH

In this section, the researchers evaluate the compressive strength of UHPC mixes based on the packing factors (PF) established in Chapter 5, with data presented in Figure 90 (Appendix E) spanning Zones A through C over hydration ages of 3, 7, 14, and 28 days. The inverse correlation observed across the data indicates that lower PF values, suggesting denser packing, correlate to higher compressive strengths. This relationship is most pronounced in multi-binder UHPC systems, where enhanced packing results in lower void content and more effective load transfer, increasing strength. The trend suggests that meticulous packing, facilitated by the inclusion of multiple binders, significantly boosts early strength, particularly in mixes with moderate to high slag content.

For mixes with moderate and high slag content (Zones B and C), the correlation between PF and compressive strength at different hydration ages is illustrated in Figure 90 (A–D) in Appendix E. The data underscore how slag not only reduces water demand and improves microstructure through hydraulic reactivity, but also how its effectiveness depends on the packing state of the mixes (Liu et al., 2018). The correlations, detailed in Figure 31-A and Figure 31-C, show that better packing significantly influences early-age strength development, with R2 values of 0.91 and 0.90 for Zones B and C, respectively. This finding confirms that the physical configuration of the binders—specifically their tight packing—plays a crucial role in microstructural development, leading to higher strengths in mixes with optimal dry packing (Baten & Garg, 2024).

As hydration progresses, the influence of binder chemistry becomes more prominent, which is reflected by a decrease in R2 values: from 0.91 to 0.62 and 0.47 in Zone B and from 0.90 to 0.81 and 0.77 in Zone C over 14 and 28 days, respectively. This shift indicates an increasing dominance of the chemical aspects of hydration, particularly in mixes with higher slag content, which initially benefit from higher initial packing and more available water for effective hydration and pozzolanic reactions (Yu et al., 2015). Moreover, the similar particle size of slag and cement leads to heightened sensitivity to packing in these mixes, as evidenced by the stronger correlation between strength and packing in Zone C over time.

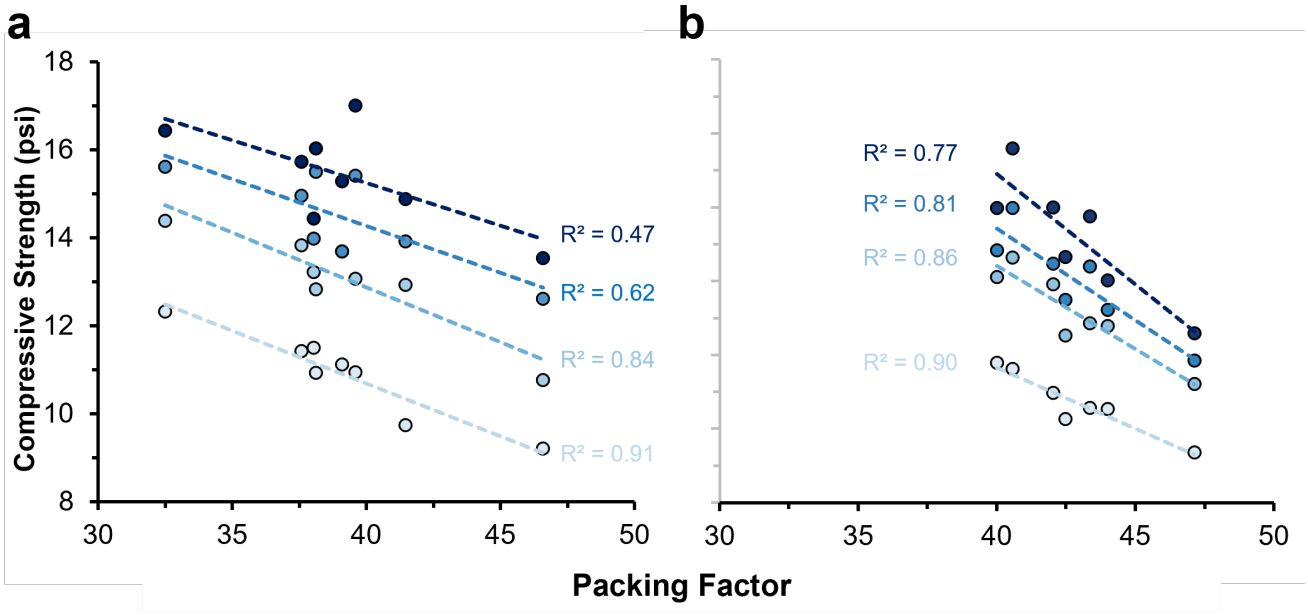

Figure 31. Graph. Correlation between the compressive strength and the packing factor for the UHPC mixes within (a) Zone B and (b) Zone C at different ages of hydration.

BINDER-BASED CHARACTERIZATION OF COMPRESSIVE STRENGTH

To incorporate the role of both physical and chemical aspects of the binders within the UHPC system, the sensitivity of the UHPC mixes' strength at both the early age (3 days) and late age (28 days) is represented in Figure 32-A and Figure 32-B, respectively, for variation in each binder used in this study. The sensitivity was evaluated with respect to the reference blend (Cem: 54.4%; Slag: 23.33%; UFFA: 12.78%; SF: 9.44%). Similar to the previous trend, Figure 32-A and Figure 32-B show that increasing cement content has an inverse impact on the strength of the UHPC mixes, with a more prominent effect on early-age strength (Figure 32-A). The higher impact at an early age is due to a greater reliance on packing (physical aspect), which is impacted by a higher amount of cement content. Similarly, the inclusion of fly ash and silica fume of different particle sizes also enhances packing up to a certain proportion, beyond which the wall and loosening effect disrupts the packing state, which refers to the dip of the response line in Figure 32-A and Figure 32-B after the optimum content. A similar pattern is evident for the strength response plots generated for 7 and 14 days, represented in Figure 92 and Figure 93 in Appendix E.

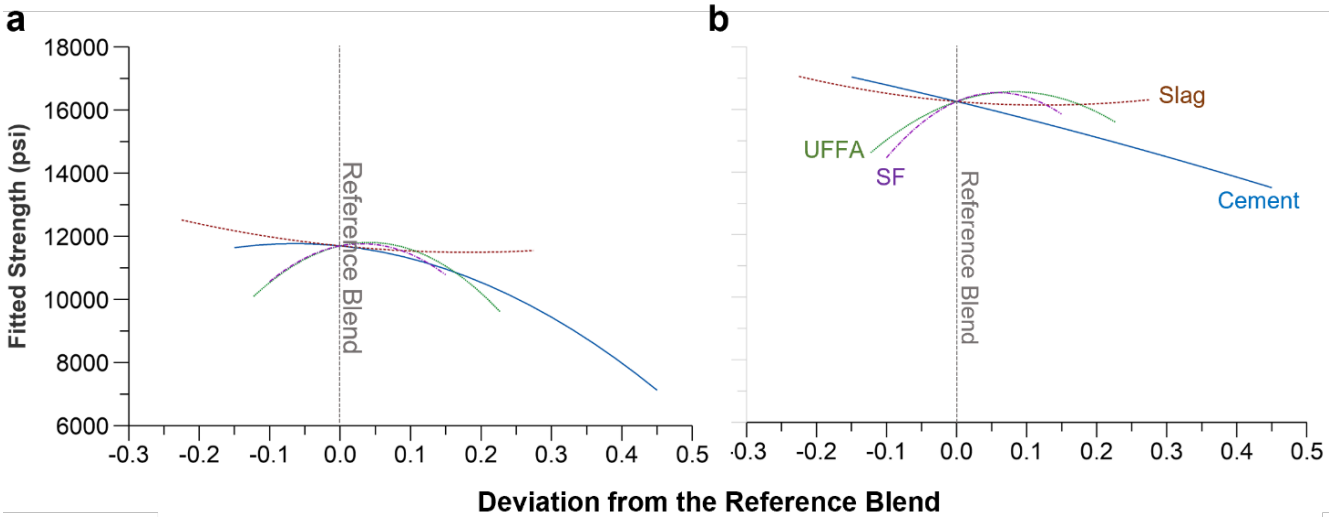

Figure 32. Chart. Sensitivity of the compressive strength of the UHPC mixes at (a) 3 days and (b) 28 days of hydration for unit variation of different binder constituents.

The sensitivity of the mixes was used to generate ternary plots as a tool for mix design optimization, as shown in Figure 33 and Figure 34 for samples of 3 and 28 days of hydration, respectively. Based on the response at an early age, it requires a certain amount of cement for higher strength, which is reflected by the green zones for cement content of 60% or 70% by volume of binder. Meanwhile, at a later age, it was possible to achieve higher strength at a lower cement content. This trend shows the potential of a multi-binder system in ensuring an adequate blend of packing, hydration, and pozzolanic activity to ensure higher strength even with fewer cement particles in the system. The trend is evident through darker green zones in the ternary plots for lower cement content at an early age. The ternary plots for other ages of hydration are shown in Figure 94 and Figure 95 in Appendix E.

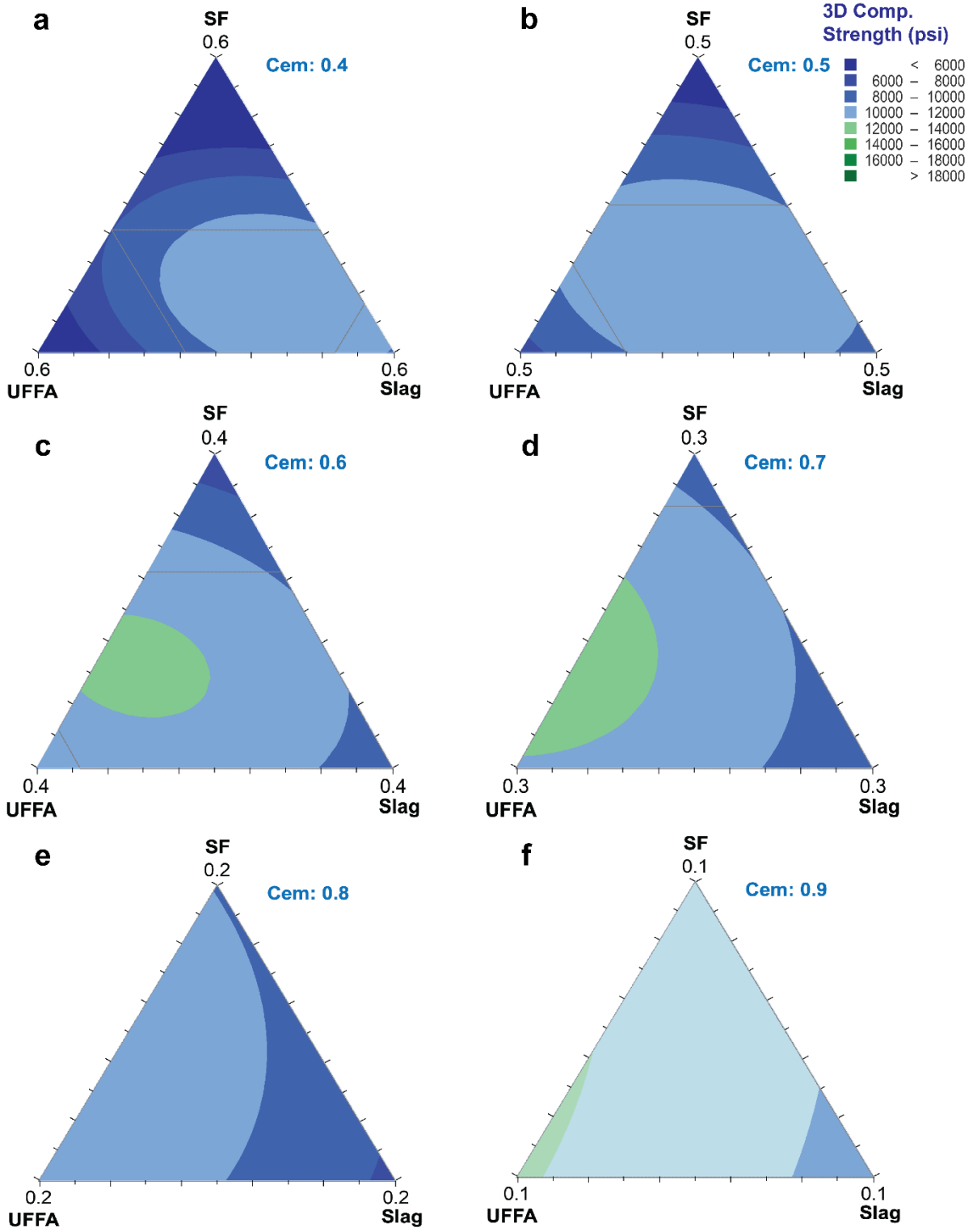

Figure 33. Graphs. Ternary response plot for compressive strength development of the UHPC mixes at 3 days for compositional variation of the binder constituents used in the study.

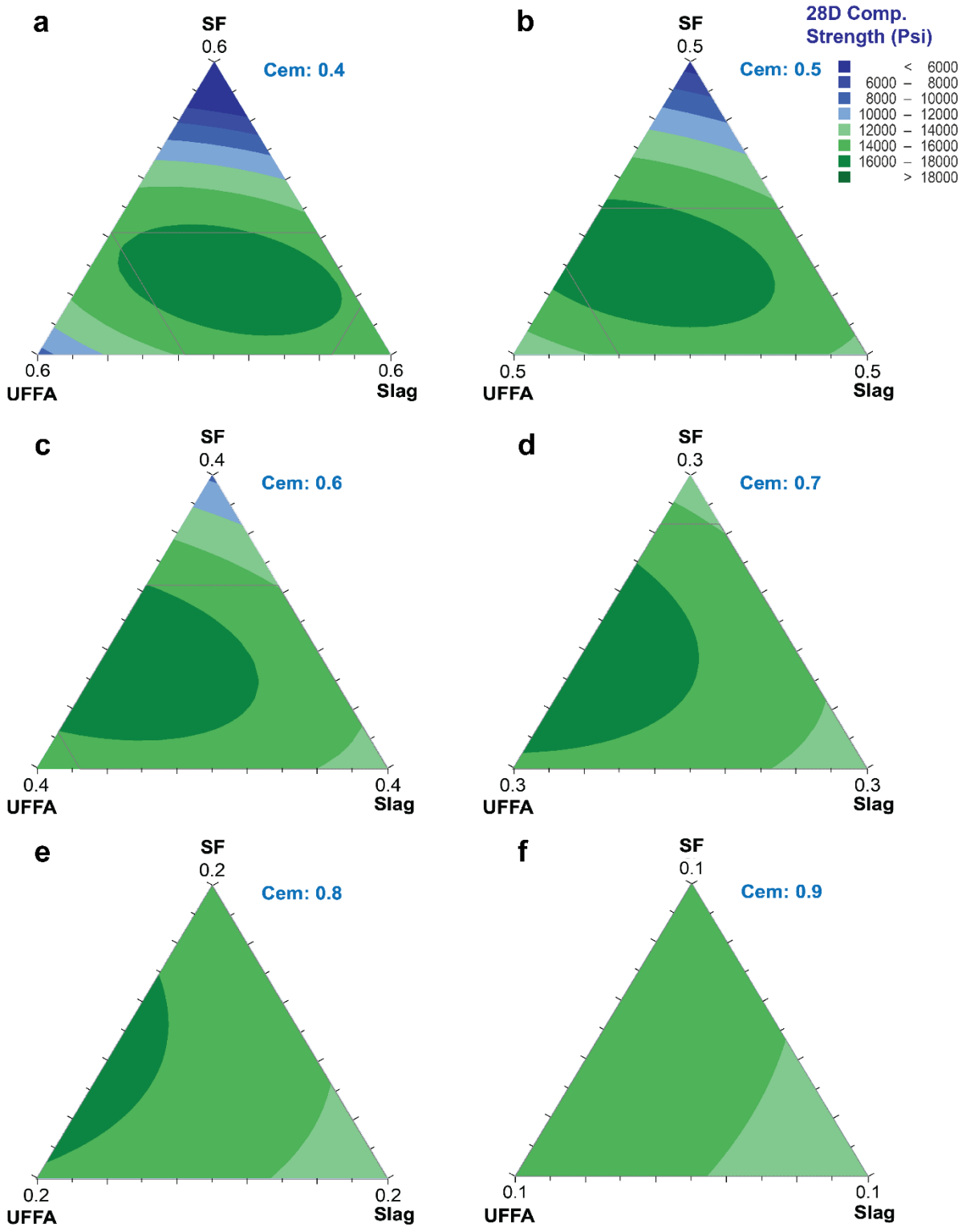

Figure 34. Graph. Ternary response plot for compressive strength development of the UHPC mixes at 28 days for compositional variation of the binder constituents used in the study.

OPEN POROSITY AT DIFFERENT AGES

The UHPC mixes' strength development in previous sections is significantly influenced by physical (packing) and chemical (hydration) aspects of the UHPC matrix, which also impacts microstructure refinement. Hence, the microstructural development of the UHPC mixes was investigated in this section through analysis of the open porosity of the mixes at different ages. Figure 35 shows the open porosity of the UHPC mixes, corresponding to different zones with varying slag content (Zone A: 0%, Zone B: 11.7%–29.2%, Zone C: 35.0%–50.0%). The top of the bar represents the initial porosity at 3 days of hydration and the bottom of the bar denotes the final open porosity after 28 days of hydration. For an effective comparison, the grey bars in Figure 35 display the change in porosity over the later age of hydration (4–28 days).

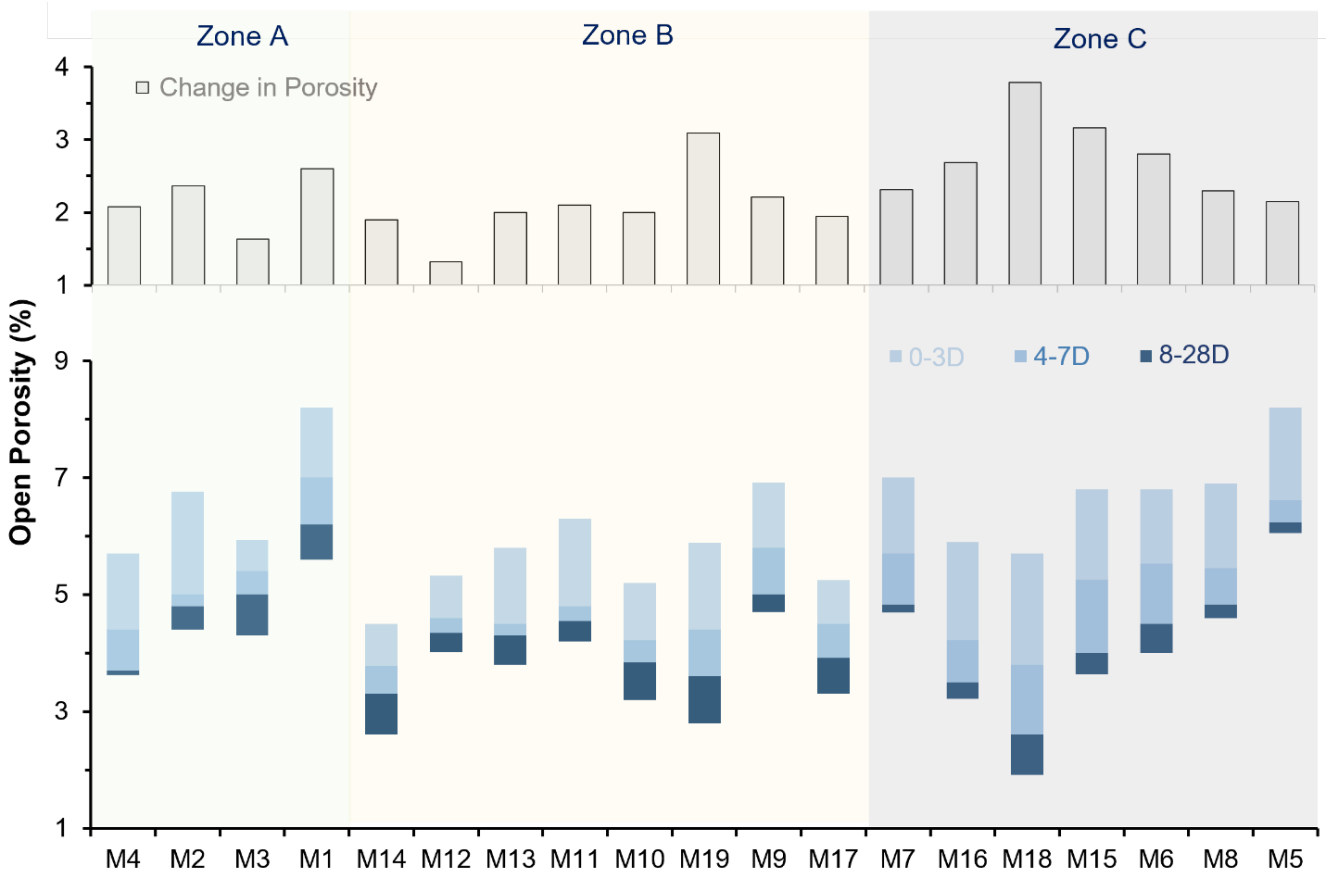

Figure 35. Chart. Open porosity of the designed UHPC systems at different hydration ages of the samples.

Referring to Zone A, mixes with unary (M1) and binary (M2 and M3) binder composition exhibited higher porosity at the early age (3 days), which refers to inadequate packing of the dry UHPC mix. Meanwhile, M4, with a multi-binder UHPC mix, shows the lowest 3-day porosity (5.7%) in the zone due to the higher packing of the binders (PF: 31.3). It also shows the importance of a multi-binder UHPC system to ensure a hydrated system with low porosity, which can safeguard the mechanical and durability performance of the UHPC mixes. Meanwhile, the inclusion of moderate slag content in

the mixes (Zone B) aided in reducing the overall initial porosity of the mixes in Zone B, which is also attributed to a lower packing factor, as observed in previous chapters. Similarly, mixes with higher cement content (M11) imply a lower packing state that increases the initial pores (6.3%) within the system. Notably, M19, with a varying composition of different SCMs, ensured a lower initial porosity (5.9%) while also facilitating a higher long-term porosity reduction (5.9% to 2.8% at 28 days). This confirms the combined role of enhanced packing and hydration in M19 with optimum performance. A similar trend is observed in UHPC mixes with higher slag content (Zone C), where mixes M15, M6, and M8 exhibited similar early-age porosity while the porosity reduction (3.2%) in M15 was the highest due to its multi-binder composition. Most importantly, M18 showed evidence of optimized packing and late-age pozzolanic activity. Hence, the mix exhibited the lowest initial (5.7%) and final (1.9%) porosity, which complements the highest 28-day compressive strength (17.9 ksi), as discussed in the previous section.

In order to assess the overall change on the microstructure of the UHPC samples, the compressive strength and porosity of the mixes at different ages are combined to infer the relationship between the two in Figure 36. There is a strong overall correlation between strength and porosity of the UHPC mixes. This confirms that the overall microstructure refinement, corresponding to different mix compositions, primarily governs the strength development and porosity changes in the UHPC specimens. To investigate the phenomenon at different temporal points, the strength–porosity correlations have been evaluated and represented separately in Figure 36. Interestingly, although there is a linear correlation at all ages, the correlation strengthened with age of the UHPC mixes. The R2 value increased from 0.42 at 3 days to 0.89 at 28 days. This increase is attributed to the fact that at the early age of hydration, the strength of the UHPC systems relies on effective load transfer through the points of contact, which depend more on the packing of the binders and might not impact porosity in a similar way. Meanwhile, at a later age with an increased degree of hydration, the microstructure is more refined, which impacts strength and porosity more significantly.

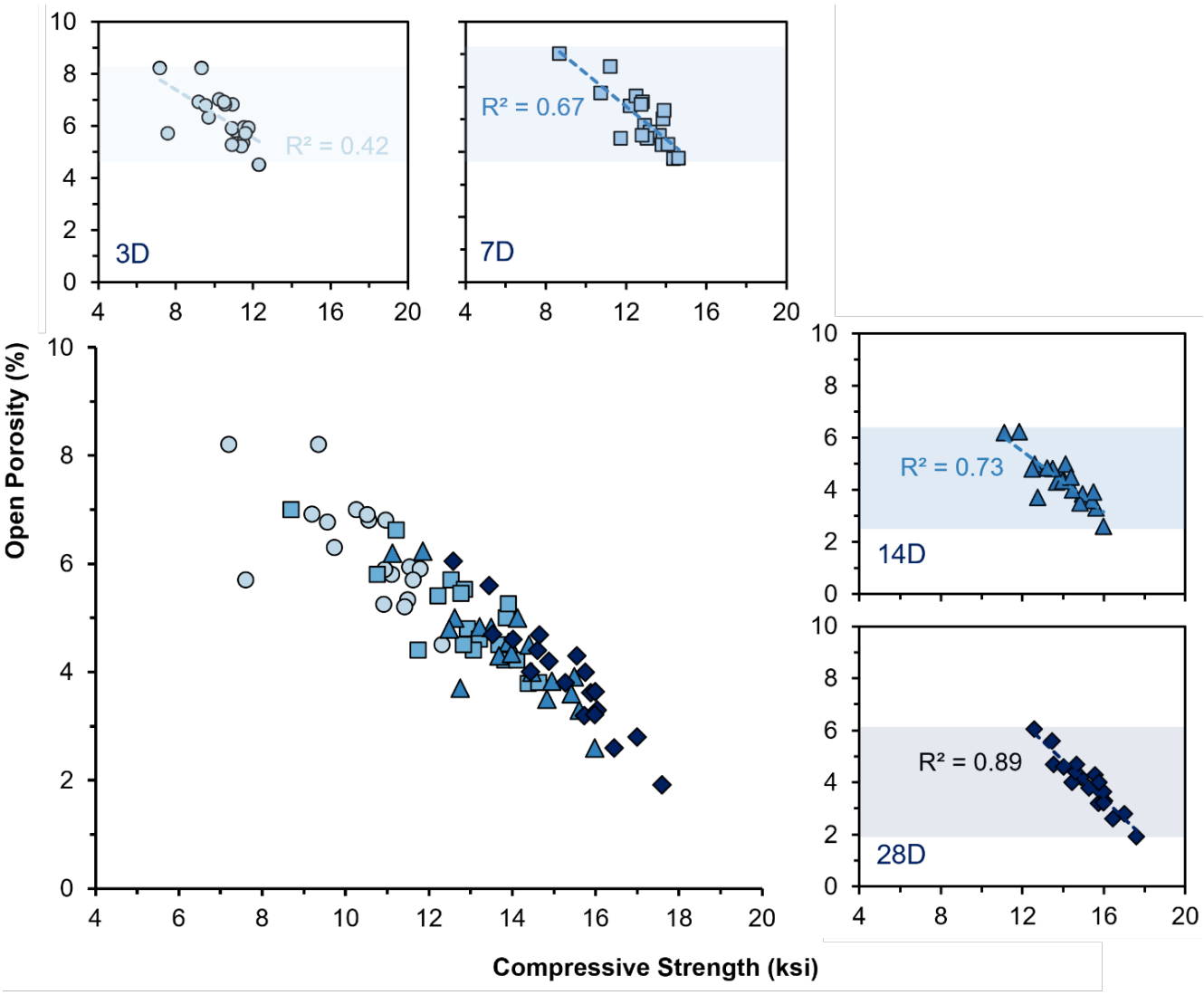

Figure 36. Graph. Correlation between strength and open porosity of the UHPC mixes.

IMPACT OF PARTICLE PACKING ON OPEN POROSITY DEVELOPMENT

Based on the previous sections, the properties of UHPC depend significantly on the packing of binders and aggregate within the system. The initial porosity and pore refinement is dependent on the voids created within the arrangement of the binder particles in addition to the role of hydration products in filling up the voids. The role of particle packing is thereby evaluated by establishing the correlation between the open porosity of the UHPC samples with the packing factor of the dry binder blends. The correlation between the two is represented in Figure 37 for the mixes within the mix zones (Zone A–Zone C) at different ages of hydration.

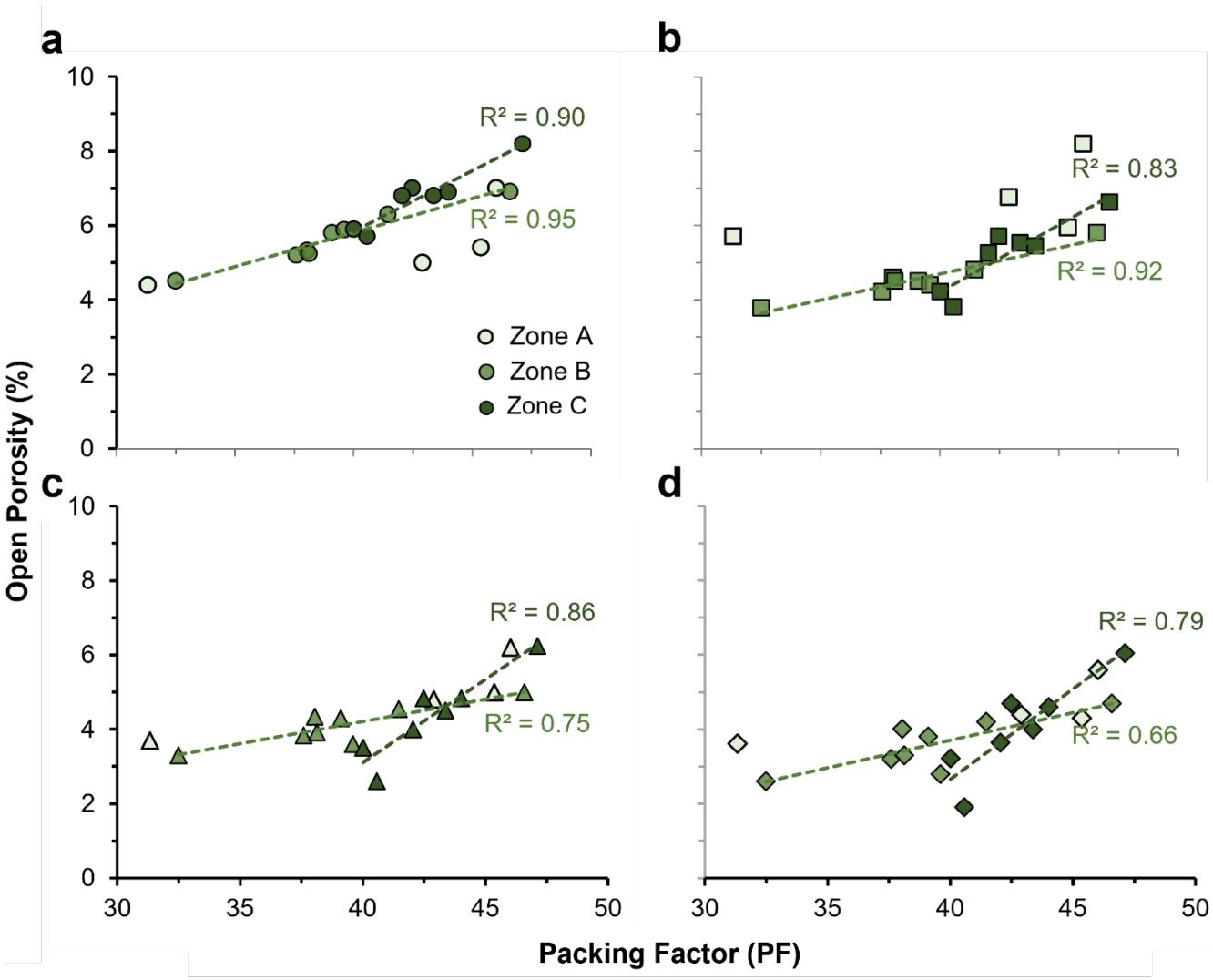

Figure 37. Graph. Correlation between open porosity with the packing factor for sample age of (a) 3 days, (b) 7 days, (c) 14 days, and (d) 28 days.

The trends in Figure 37 show a strong positive correlation between particle packing (PF values) and the open porosity of the UHPC samples at different ages. Note that the values of the correlation coefficients (R2) are higher at an early age of 3 days (R2: 0.90–0.95) compared to a later age of 28 days (R2: 0.66–0.79). This shows a more significant role of packing on the porosity within the system at an earlier stage of hydration in UHPC mixes. Hence, the observed trend indicates that at an initial stage of hydration, the degree of hydration is limited due to a significantly lower water-binder ratio (0.18). Consequently, the interlocking of the particles, governed by particle packing, plays a more dominant role in defining the microstructure and overall open porosity. This is also reflected in lower R2 values at a later age when the hydration production fills up the generated voids and affects the overall porosity. The importance of analyzing the trend by classifying the mixes into three different zones is also reflected in Figure 96 (Appendix E), where the correlation conceits are much lower compared to the individual zones observed in the section.

BINDER-BASED CHARACTERIZATION OF OPEN POROSITY

In order to assess the porosity development from a compositional point of view, the sensitivity of open porosity is assessed with unit change of each constituent in the UHPC mix design. Figure 38 reports the sensitivity analysis with respect to a reference UHPC mix with a binder composition of Cem (54.4%), Slag (23.33%), UFFA (12.78%), and SF (9.44%) using the Minitab software. The analysis is shown for both early age (3 days) and late age (28 days) of the samples in part (a) and (b) of Figure 38, respectively.

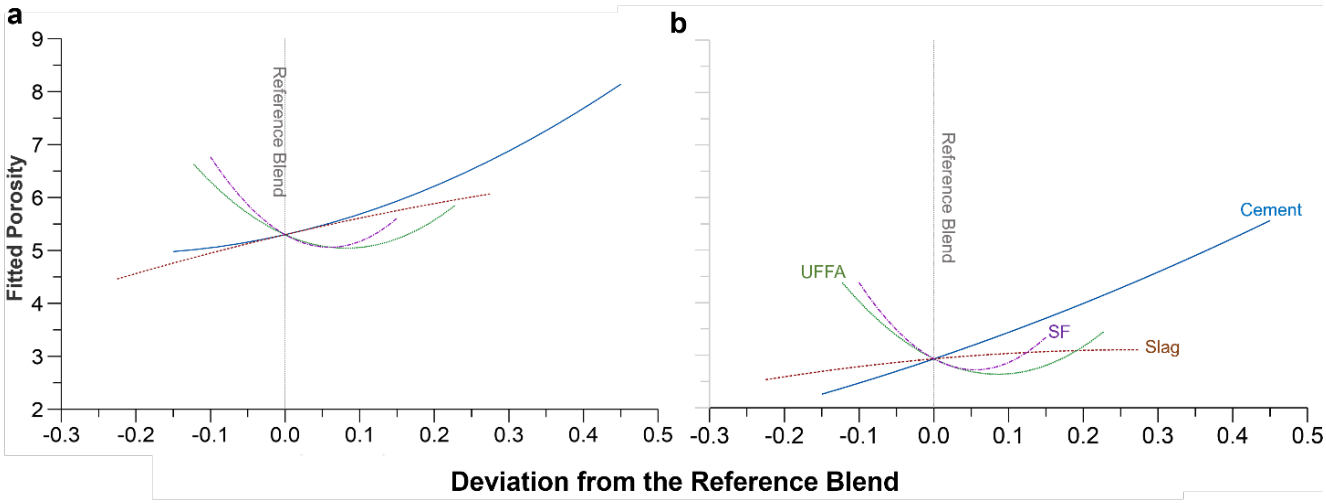

Figure 38. Graph. Sensitivity of open porosity of the designed UHPC mixes at (a) 3 days and (b) 28 days of hydration for unit variation of different binder constituents.

Based on the trend in Figure 38, the cement content in the mix shows a significantly strong correlation with the open porosity with a higher impact at an earlier age of the samples. This validates the role of cement particles on the packing of the UHPC system, as reported in previous sections. Meanwhile, a nearly linear correlation at a later age for cement shows again the importance of a multi-binder system in reducing the overall porosity of UHPC mixes. Slag shows a tendency to increase the porosity at an earlier age, which is attributed to a similar particle size of the slag particles, which results in a higher porosity when packing governs the overall microstructure. This is confirmed by a stable correlation of slag with open porosity at a later age (28 days) of the samples. Meanwhile, silica fume and fly ash particles play a positive role in reducing the porosity up to a certain amount which in excess can deteriorate the packing state of the UHPC mixes, impacting the overall porosity.

The sensitivity of open porosity has been translated to response models for a wider variation of the binder compositions in terms of ternary plots. The response plots for early age (3 days) and late age (28 days) are represented in Figure 39 and Figure 40, respectively, as a function of the SCMs used in designing the UHPC mixes for variable cement contents.

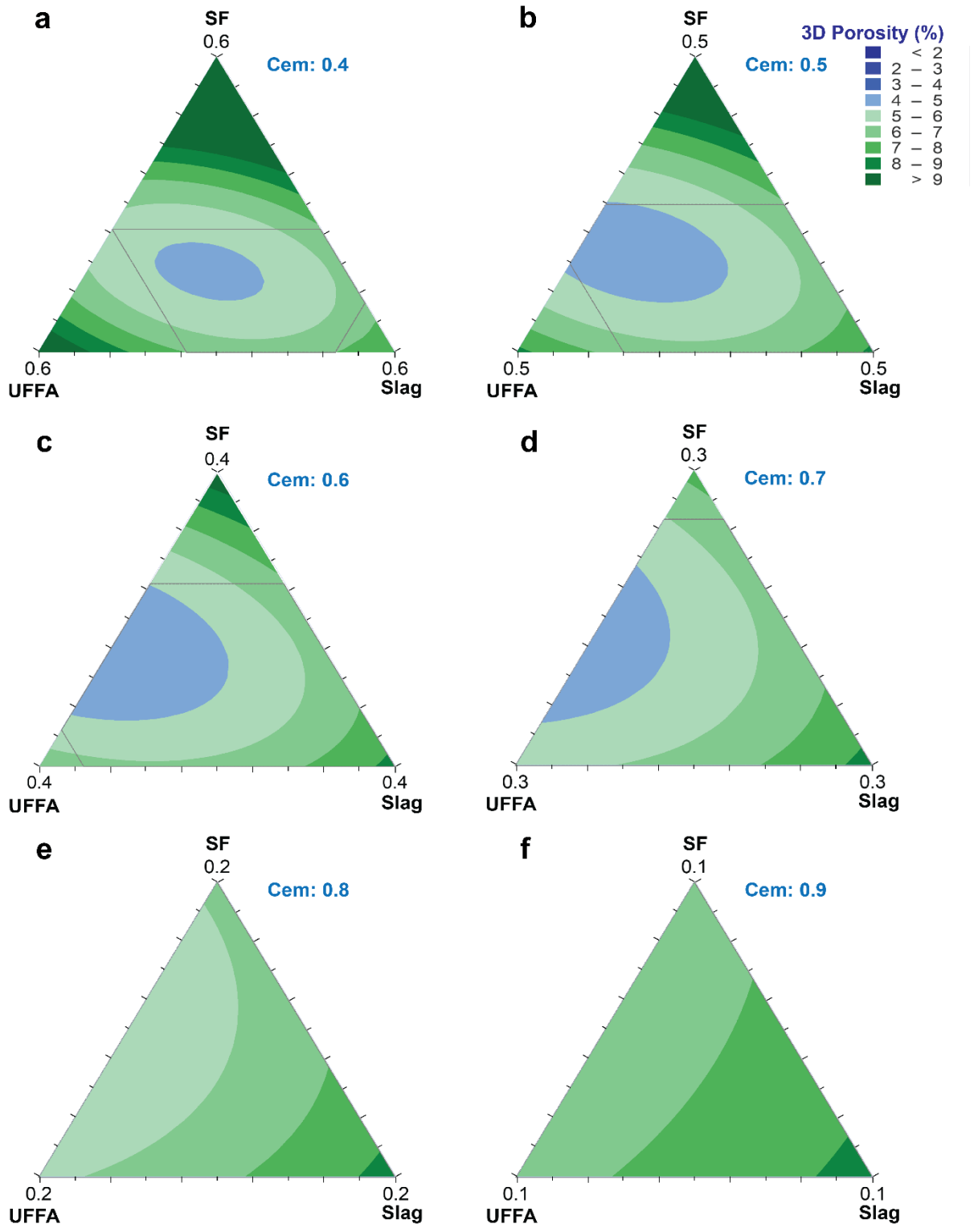

Figure 39. Graph. Ternary response plot showing the 3-day open porosity of the UHPC mixes for compositional variation of the binder constituents used in the study.

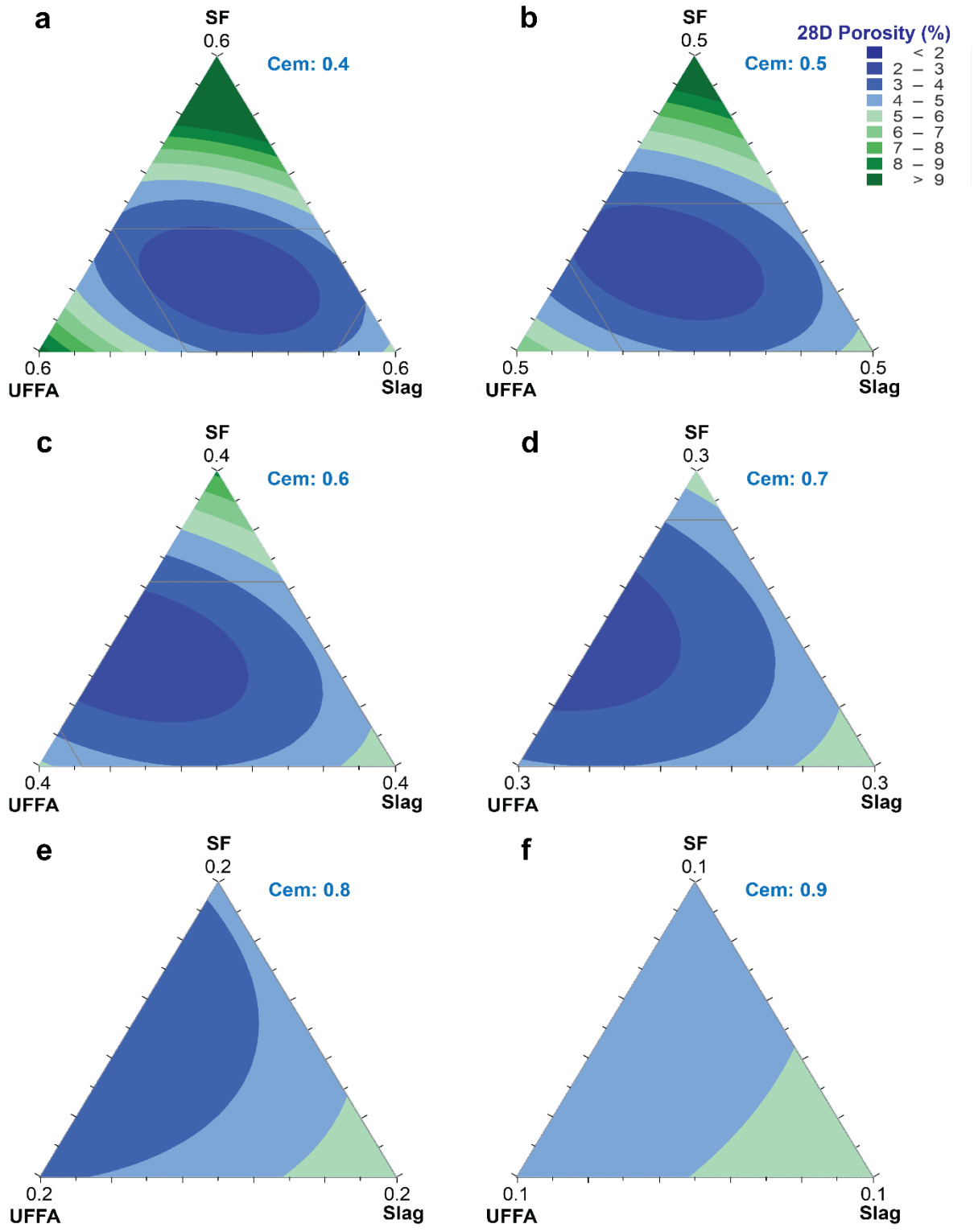

Figure 40. Graph. Ternary response plot showing the 28-day open porosity of the UHPC mixes for compositional variation of the binder constituents used in the study.

Conforming to previous observations, ternary plots at any age show a higher open porosity close to corners of the plots, indicating a unary binder system is highly associated with more pores within the system, which would hamper the strength and durability properties of UHPC mixes. At an earlier age of 3 days, Figure 39 shows a gradual absence of the blue zone at a higher cement content, which confirms the role of cement in inducing high porosity to UHPC mixes. Meanwhile, at a much lower cement content of around 40% by volume, the zone of lower porosity highlights an equal blend of all SCMs for minimizing porosity. This signifies that particle packing using a multi-binder blend at lower cement content can lower overall porosity within the UHPC system.

At a later age (28 days), Figure 40 shows much lower open porosity for blends at all cement content. The importance of a multi-binder system in UHPC mix design is clearly shown or reflected, especially for lower cement content of 40%–60%. For example, the response model shows the possibility of lowering open porosity to less than 2% by optimizing the content of silica fume, fly ash, and slag content even at a cement content of 40% to 50%. The porosity of mixes at intermediate ages of 7 days and 14 days of hydration is shown in Figure 91 and Figure 92 in Appendix E.

CHAPTER 8: LONG-TERM DRYING SHRINKAGE

This chapter summarizes the drying shrinkage behavior of designed UHPC mixes over a span of 91 days. The drying shrinkage behavior is detailed for different mix regimes, zoned by the slag content of the mixes. Moreover, this section describes the analysis of drying shrinkage with the open porosity of the mixes. The role of packing factor is investigated on the mixes' drying shrinkage behavior. Last, a response pattern of drying shrinkage of UHPC mixes is developed for different cement and SCM contents.

DRYING SHRINKAGE OF UHPC MIXES AT DIFFERENT AGES

The long-term drying shrinkage behavior of UHPC mixes across different zones (A to C) and slag contents are depicted in Figure 41. Early-age shrinkage within 10–15 days post-demolding is significant, largely due to early cement hydration in a water-restricted environment. Zone A mixes, with no slag and higher cement content, generally exceed the target shrinkage strain of −800μξ. However, the inclusion of supplementary cementitious materials (SCMs) like fly ash and slag in Zones B and C substantially reduces shrinkage, keeping most mixes, except M9, within the desired limits. This reduction is attributed to improved packing and pore structure from pozzolanic reactions, which minimize internal water reorganization and, hence, shrinkage. Notably, optimized mixes M18 and M19 in Zone C also achieve shrinkage values below the −800μξ threshold, highlighting the effectiveness of multi-binder systems in producing UHPC mixes with controlled shrinkage and robust mechanical properties.

The drying shrinkage of 19 optimized UHPC mixes was investigated at an early age of 28 days (light blue) and a long-term span of 91 days (dark blue), which are summarized in Figure 42. The mixes were classified into similar zones, based on the slag content (Zone A: 0%, Zone B: 11.7%–29.2%, Zone C: 35.0%–50.0%) to correlate to the previous observations on packing, strength, and porosity development.

In previous sections, the researchers have emphasized the significance of a multi-binder system in enhancing the physical (packing factor) and mechanical (strength and porosity) properties of a UHPC system. A similar characteristic is also evident for the shrinkage behavior of the mixes, as mixes in Zone A with unary (M1) and binary (M2 and M3) binder composition exhibited much higher overall drying shrinkage. As the overall binder content in UHPC mixes is usually higher than regular concrete mixes, M1 and M2 show that cement content in UHPC can lead to a higher early-age and long-term drying shrinkage when subjected to lower relative humidity. High cement content usually results in an increased amount of cement paste with curing age, which is also associated with a higher amount of capillary pores, accounting for a higher amount of shrinkage. It is also complemented by higher porosity of the mixes that resulted from a lower packing state (higher packing factor), as explained in previous sections. Contrarily, higher SCM content in M4 with a much lower cement content (40%) drastically lowered the drying shrinkage of the mixes.

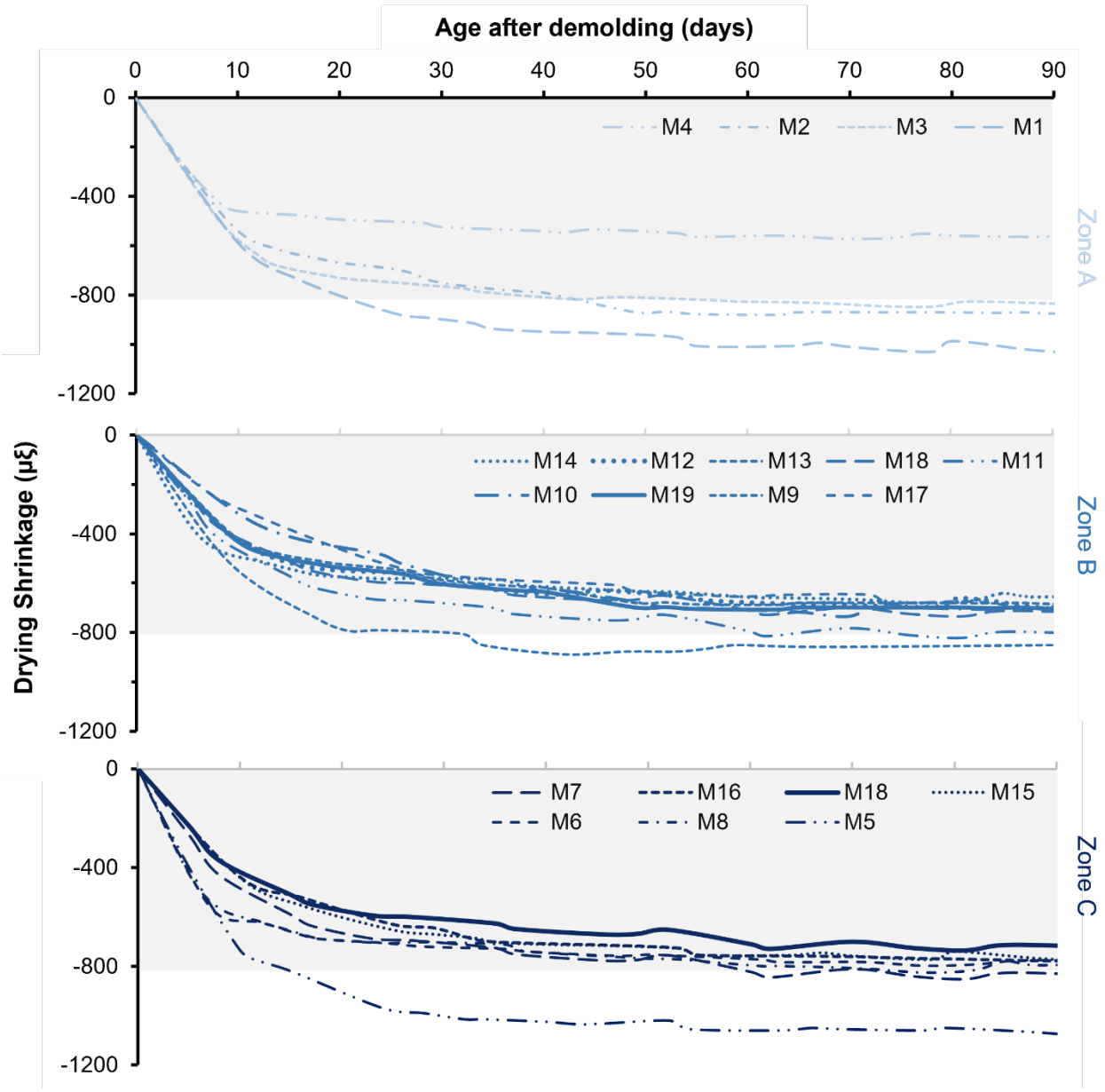

Figure 41. Graph. Drying shrinkage behavior of the designed UHPC mixes with the age of the samples. The grey zone represents the target shrinkage limits considered for the study.

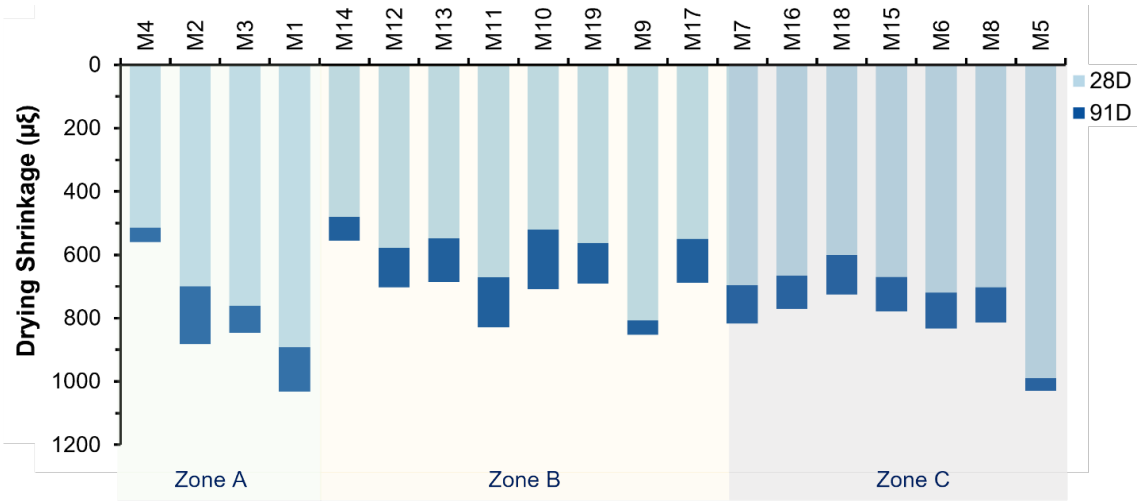

Figure 42. Chart. Summary of cumulative drying shrinkage values of the designed UHPC mixes at 28 days and 91 days of hydration.

The inclusion of alternative binders, specifically slag and fly ash, significantly influences the drying shrinkage of mixes in Zones B and C. Notably, Zone B mixes demonstrate lower shrinkage at both early and late stages. The cement content and packing factor are key determinants of shrinkage behavior. For example, M11 experiences higher shrinkage (day 28: −671με and day 91: −829 με) due to its higher cement content, which increases capillary porosity and subsequent shrinkage. Conversely, M9, despite its lower cement and higher SCM content, still shows considerable shrinkage at both early (−807 με) and later stages (−852 με). M13 and M14 show moderate shrinkage improvements by substituting cement with UFFA and slag; particularly, M14 exhibits lower shrinkage (day 91: −555 με) due to a reduced packing factor (PF: 32.5). M19, with an optimized blend of fly ash and slag, achieves moderate early and long-term shrinkage. The slag enhances early-age hydration, impacting early shrinkage, while fly ash's late-age pozzolanic activity contributes to controlling long-term drying shrinkage.

In Zone C, where slag content is higher, the overall shrinkage tends to be greater than in Zone B, particularly at early ages due to the enhanced hydraulic activity of slag, which accelerates early hydration. For instance, M18, which has the highest compressive strength and lowest porosity in Zone C, also exhibits the lowest shrinkage (day 28: −600 με and day 91: −725 με). Conversely, M5, despite containing the highest slag content at 50%, shows significant early and long-term drying shrinkage, a result of poor packing in the UHPC system. These observations underscore the critical influence of packing factor on porosity development and shrinkage behavior, a theme further explored in subsequent sections.

INFLUENCE OF OPEN POROSITY ON DRYING SHRINKAGE

As the drying shrinkage of a cementitious system enroots to the internal redistribution of water within the mesopores of microstructure, drying shrinkage behavior is expected to be influenced by porosity within the hardened UHPC system. Hence, the drying shrinkage of UHPC specimens was evaluated with the open porosity of the samples, which is summarized in Figure 43.

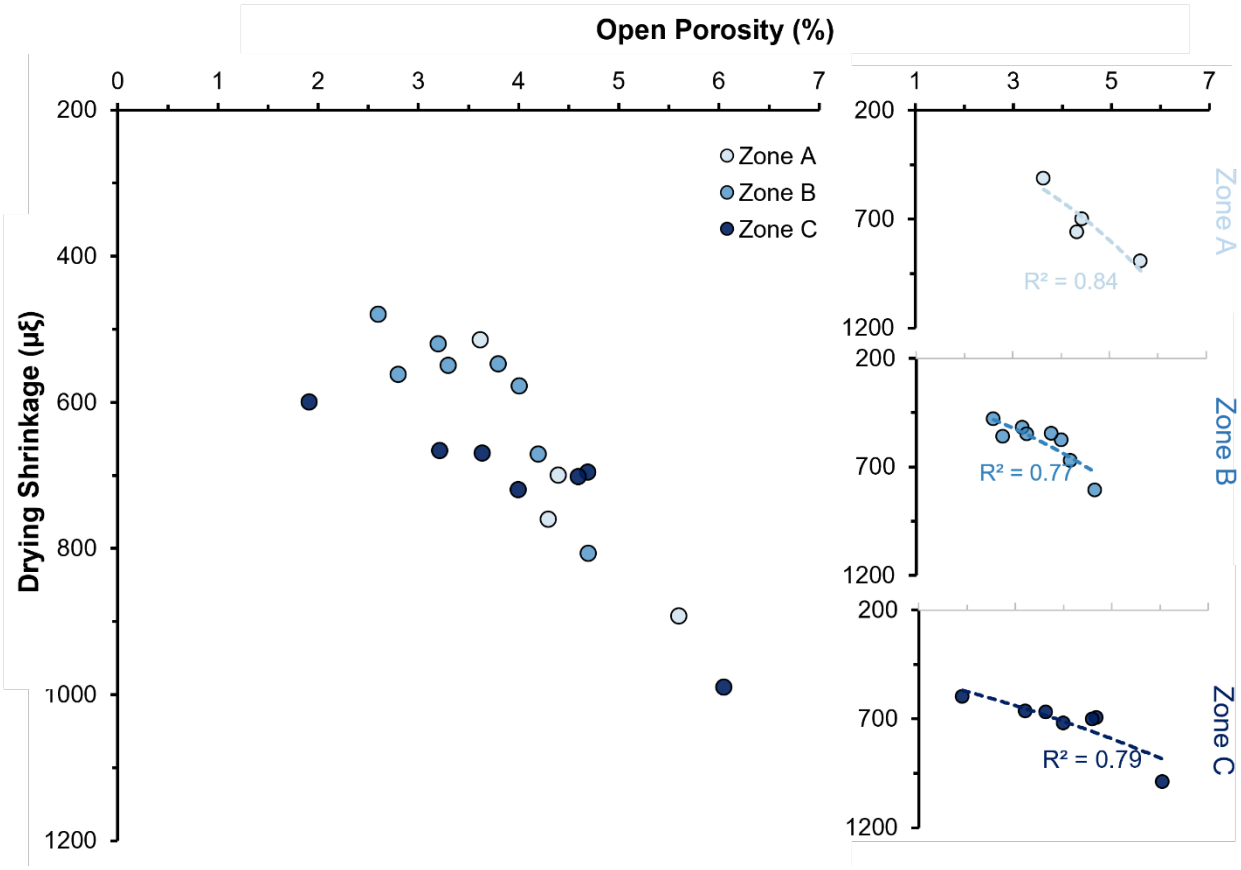

Figure 43. Graph. Correlation of 91-day drying shrinkage with the open porosity of UHPC mixes.

As the open porosity was evaluated at 28 days, early drying shrinkage of mixes at 28 days is represented here with respect to porosity of the samples at a similar age. Correlations were developed for mixes with a similar classification into different zones (Zone A–Zone C), as discussed in previous sections. In Figure 43, there is an overall significant correlation between the shrinkage behavior of UHPC mixes with the change in open porosity of the UHPC matrix. This is due to higher porosity, offering more accessible routes for the internal water to redistribute within the microstructure when subjected to lower relative humidity (50% in this study). The transportation of water and subsequent removal from the capillary pores resulted in a higher drying shrinkage strain in mixes with higher porosity. Mixes with open porosity have only exceeded the shrinkage limit of −800 με. A general correlation, with similar R2 values, is observed within mixes of different zones, which signifies that the porosity of mixtures plays a significant role in influencing the overall shrinkage behavior regardless of the physical and chemical efficiency of the UHPC mix. Similar correlations are observed at a later age of 91 days, as shown in Figure 99 in Appendix F.

IMPACT OF PARTICLE PACKING ON DRYING SHRINKAGE OF UHPC MIXES

In a typical UHPC system with a significantly lower degree of hydration, the microstructure and the resultant drying shrinkage is governed by the packing state of system. Hence, early-age and long-term drying shrinkage of UHPC mixes were compared to the mixes' packing factor, graphically represented

in Figure 44. The early-age shrinkage at 28 days of hydration is represented as faded circles to emphasize the late-age shrinkage strain of UHPC mixes, corresponding to Zone A–Zone C.

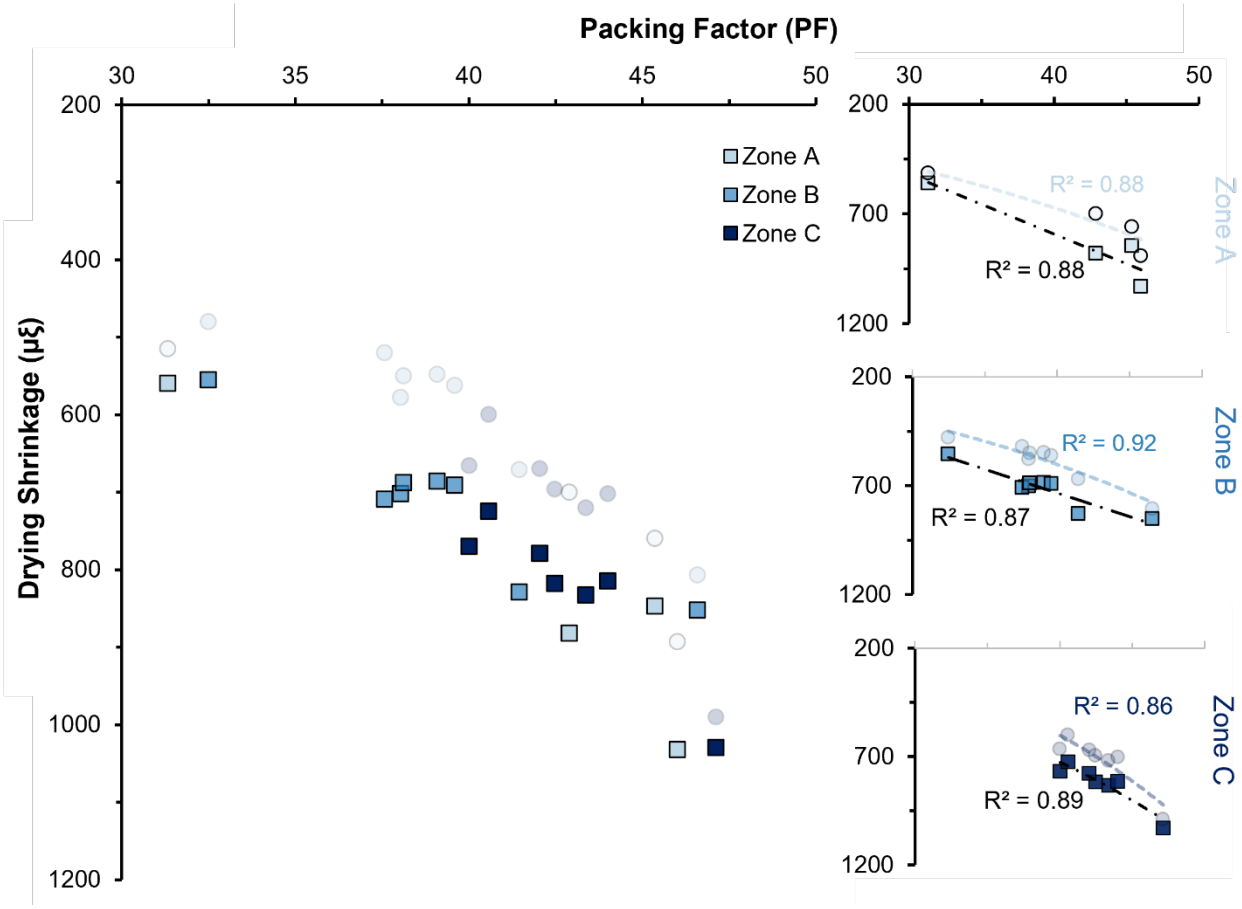

Figure 44. Graph. Correlation of drying shrinkage with the packing factor of UHPC mixes. The faded markers correspond to the shrinkage values at 28 days while the darker markers represent the shrinkage values at 91 days.

As an overall trend, the packing factor showed a strong correlation with the drying shrinkage of UHPC mixes at both ages considered. This trend is due to the significant role of packing factor (PF) of the multi-binder UHPC systems on governing the resultant porosity of the systems. A highly packed system usually provides lower connectivity and provides resistance to the redistribution of water within the hydrated system. Hence, a lower PF resulted in an overall lower drying shrinkage of UHPC mixes. As a quantitative guideline for aligning the packing regime for shrinkage optimization, mixes with a PF higher than 41 exhibited drying shrinkage strain of more than the limit of −800 με considered for this study. Meanwhile, the packing factor of the mixes contributed similarly to the drying shrinkage regardless of the slag proportion, as observed by strong R2 values (0.88, 0.87–0.92, and 0.86–0.89 for Zone A, Zone B, and Zone C, respectively). Generally, the packing factor also combatively contributes more to the early-age properties of UHPC mixes through a well-packed microstructure with limited chemical effects.

BINDER-BASED CHARACTERIZATION OF DRYING SHRINKAGE

A highly packed system usually alters the evaporation route of water within the system. In addition, as hydration progresses within the UHPC system, hydration products also contribute to refining the pores and thereby impact the overall shrinkage behavior. At the same time, this also signifies that determination of the mix composition is crucial to maintain a well-packed microstructure and provide enough space for the initial and long-term shrinkage measurement. Hence, in this study, the sensitivity of UHPC mixes at 91 days in the humidity chamber was correlated to all binders based on the response surface model (Figure 45). The response analysis for the early-age drying shrinkage is also represented in Figure 100 (Appendix F).

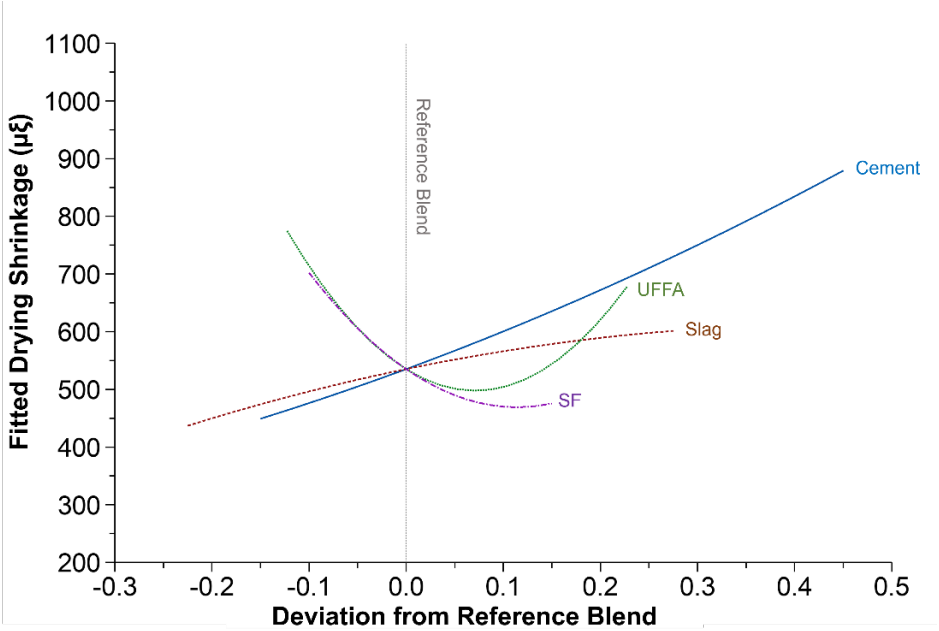

Figure 45. Graph. Sensitivity of the drying shrinkage of UHPC mixes at 91 days of hydration for unit variation of different binder constituents.

Corresponding to the reference blend (Cem: 54.4%; Slag: 23.33%; UFFA: 12.78%; SF: 9.44%), increasing cement content increases the shrinkage behavior of the mixes (Figure 45). Based on earlier observations, increasing cement content leads to a higher amount of cement paste production, which primarily acts as a source of shrinkage in a drying environment. Meanwhile, slag also showed a similar but less drastic correlation with the drying shrinkage at both early and long-term age of curing. The observed behavior is due to the hydraulic reactivity of slag particles, which generates more hydration products. Notably, fly ash showed a dual role in governing the drying shrinkage in Figure 45. At a lower dosage, fly ash usually fills up the gaps within the larger solid grains, which reduces the overall shrinkage. Contrarily, at a higher dosage, mixes with fly ash exhibit long-term pozzolanic reactions and hydration products. Summarizing the observed trends on the effect of different binders in the early-age and long-term drying shrinkage behavior, binder-specific response maps have also been generated, as shown in Figure 46.

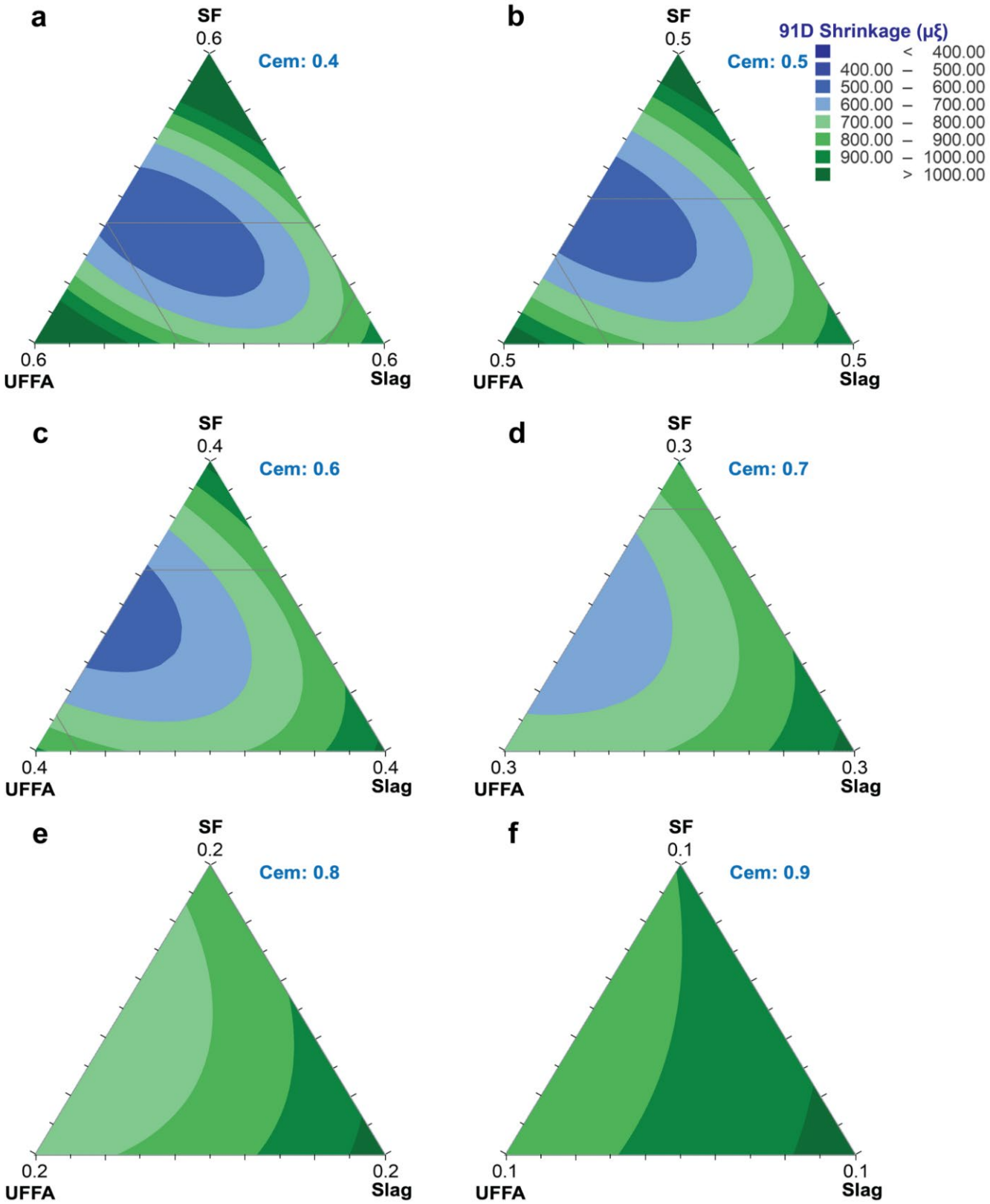

Figure 46. Graph. Ternary response plot showing the 91-day shrinkage of UHPC mixes for compositional variation of the binder constituents used in the study.

The binder-specific ternary plots align with the observed behavior and performance trends, as observed in earlier sections. The blue zones with lower shrinkage values are mostly concentrated near the blend of ultra-fine fly ash and silica fume at a cement content of 40%–90%. Meanwhile, a higher slag content exhibited higher slag values, with an increasing intensity of the green zone with an increase in the cement content. The response plots show the role of higher cement and slag content in inducing long-term drying shrinkage of UHPC mixes, which correlates to an increased hydration and pozzolanic reaction.

The shrinkage behavior at a relatively shorter time scale of 28 days is represented in Figure 101 in Appendix F for UHPC mixes. A similar trend is observed for the UHPC mixes at 28 days with an increased contribution of slag and cement in inducing higher shrinkage values. Overall, the response models can be used to design the binder compositions for UHPC mixes with minimal short- and long-term drying shrinkage.

CHAPTER 9: SENSITIVITY ANALYSIS AND MODIFICATION OF OPTIMUM UHPC MIXES

OVERVIEW

The optimum mixes obtained from previous chapters were modified by adding different fiber quantities, and several sensitivity analyses were performed on the same mixes for different parameters. This section covers the performance of UHPC mixes for different fiber additions as well as covers the optimization of effective fiber quantity for the next phases. This chapter also explains the performance analysis (rheology and mechanical properties) of the optimum mixes for different cement quantities, types of silica fume, and water-binder ratios.

EFFECT OF FIBER ADDITION

Fibers form an essential part of UHPC mixes to enhance tensile properties. Hence, the optimized mixes in previous sections were tested with different amounts of steel fibers to determine the optimum fiber quantity. In this regard, a wide range of fiber quantities from 1%–6% was added to mix M18, which are labeled M18-A to M18-D. The cement quantity was also increased to 60% for a separate mix (M18-E), as a higher paste content is required to cover the extra surface area of the fibers. The summary of mix regime with different fiber contents is summarized in Figure 47.

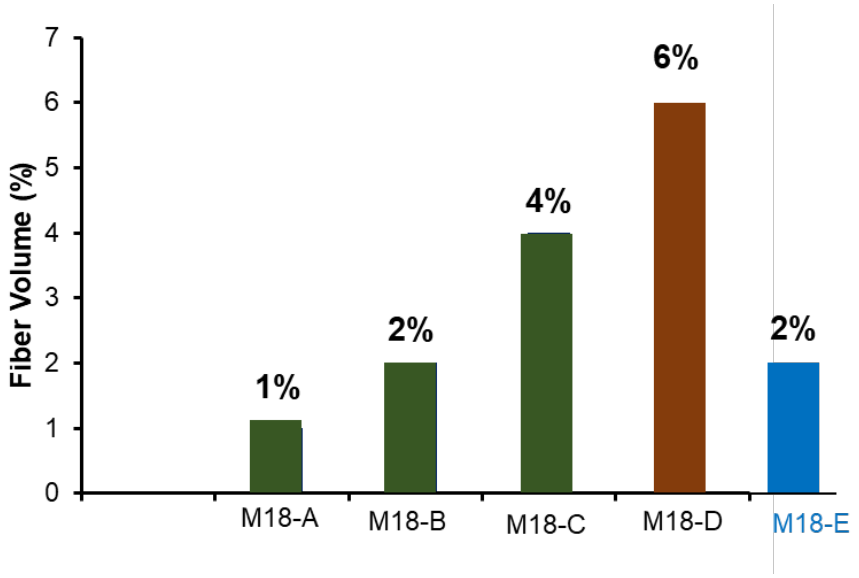

Figure 47. Chart. Summary of mix regime with different steel fiber contents. The steel fiber considered in the study varies from 1%–6%, as represented by mix M18-A to M18-D.

The effect of different fiber contents on the rheological properties of UHPC mixes (M18 A–E) is represented in Figure 48. The inclusion of steel fibers resulted in a reduction of the flow of UHPC mixes, evident from a reduction in flow from 12 inches to almost 7 inches from Mix M18-A to M18-D. This is also evident from a significant reduction in the flow/HRWR ratio for the mixes. In particular, in

mixes with a higher amount of steel fibers, fibers have a high tendency to agglomerate, which results in a considerable amount of segregation. Hence, based on the rheological aspects of the mixes, it is recommended to use a maximum fiber content of 4% or less.

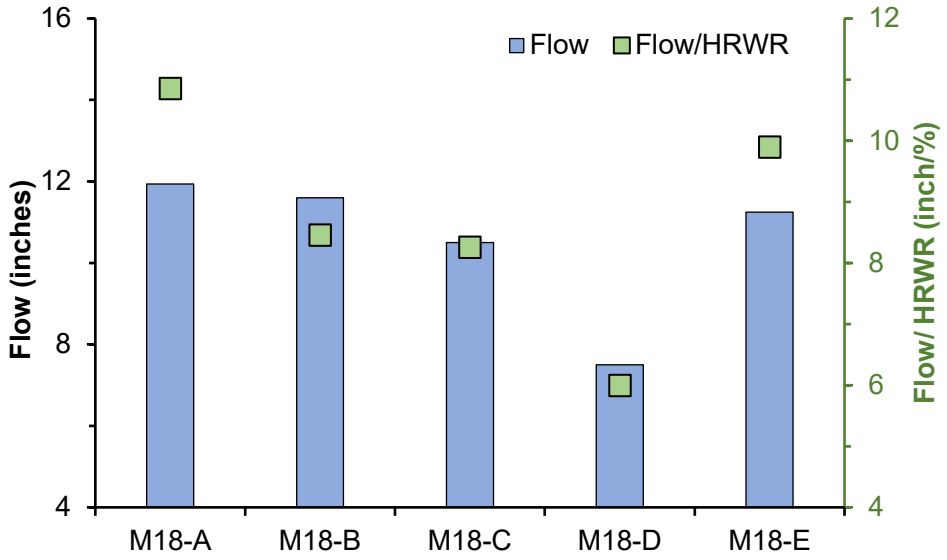

Figure 48. Chart. The rheological performance of UHPC mixes with different steel fiber content. The blue bars represent the flow of UHPC mixes obtained from the mini-slump flow test.

M18-E, which included an additional 10% of cement, achieved similar flow characteristics as M18-A, but with a higher flow/HRWR ratio, suggesting the increased paste content helps coat the additional surface area from the fibers. The reduction in flow (workability) with more fibers can be linked to their physical interference and network formation within the cementitious matrix. Fibers raise the mix's viscosity and impede its movement, reducing flowability. This is consistent with rheological principles, where increased solid volume (fibers, in this case) heightens flow resistance. Additionally, while fibers bridge microcracks to boost tensile and flexural strength, this also increases internal friction and interlocking, reducing flowability. Managing this trade-off between mechanical properties and workability is crucial in UHPC design.

To assess the impact of varying steel fiber contents on UHPC mixes, the strength development of M18 with steel fibers ranging from 0% (control) to 6% is detailed in Figure 49. The inclusion of steel fibers notably enhances the compressive strength by improving matrix integrity and bridging microcracks, which helps distribute stresses more uniformly and prevent crack formation and propagation. This increases both the load-bearing capacity and the concrete's resistance to crushing. Fiber contents at 4% yielded the highest strength gain (over 3.5 ksi), enhancing ductility and fracture resistance under high stress. However, at 6% fiber content, the compressive strength decreased due to reduced workability and fiber clumping, which led to defects. Figure 50 shows that while 4% fiber content provided the maximum strength gain, the high cost of steel fibers—constituting over 50% of UHPC's total cost—makes 2% the optimal content for future phases based on cost-effectiveness and performance enhancement.

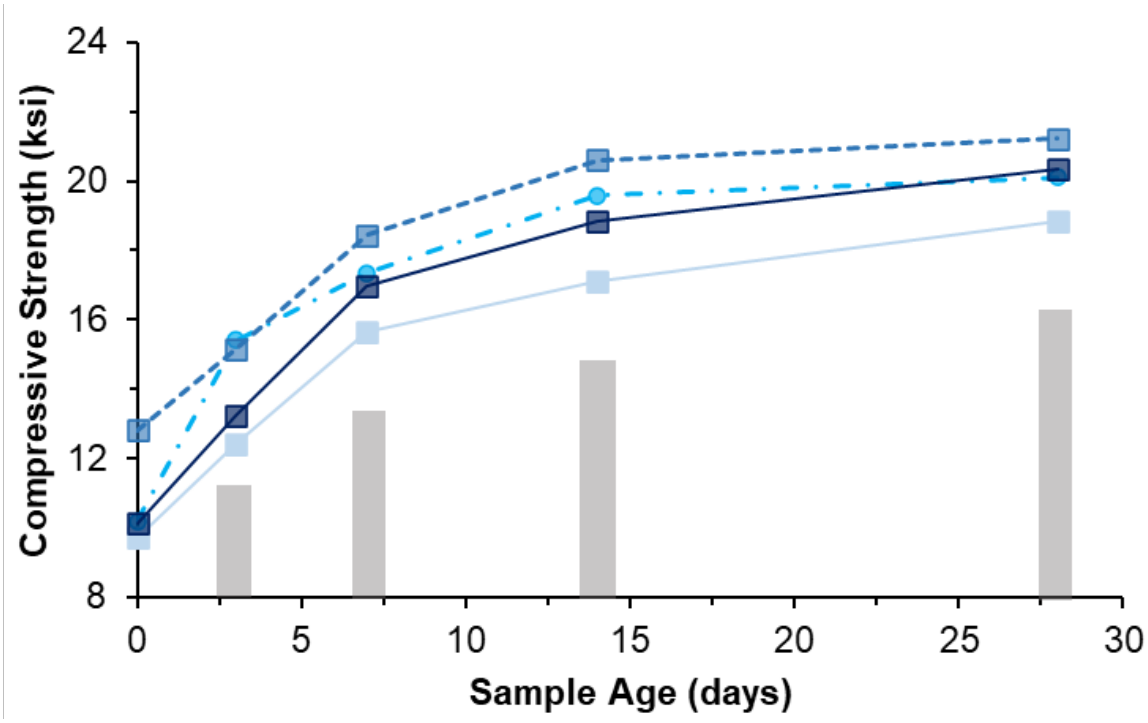

Figure 49. Chart. Effect of different steel fiber content on the strength gain of UHPC mixes at different ages of hydration.

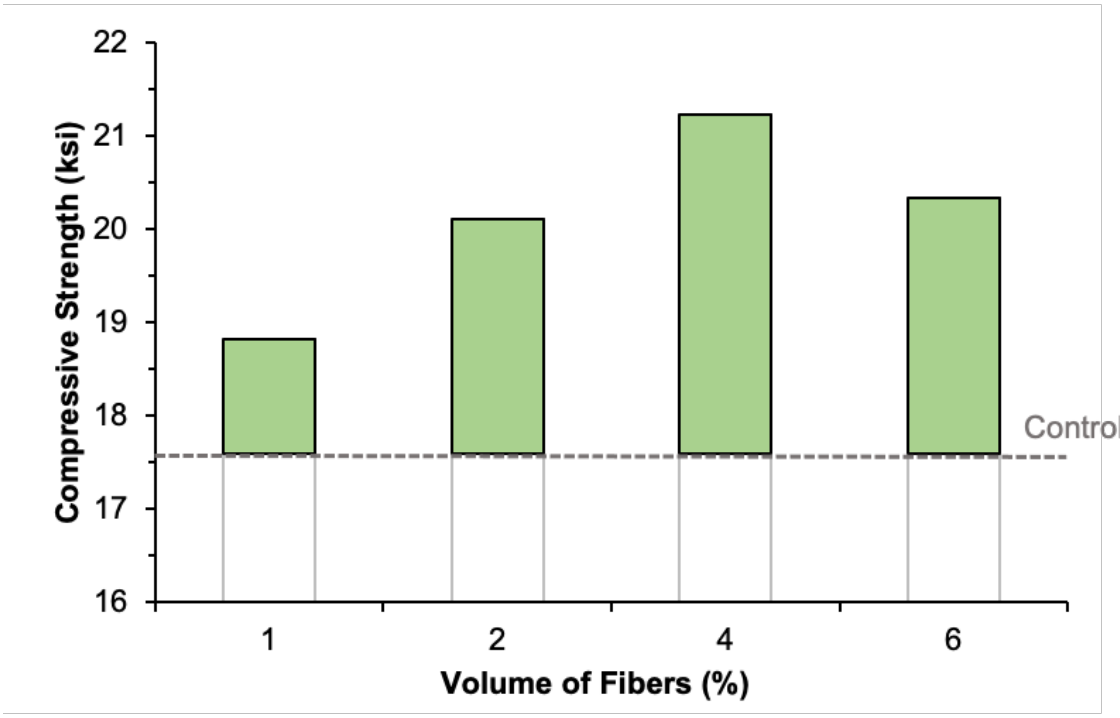

Figure 50. Chart. Summary of net increase in compressive strength of the optimum UHPC mix (M18) for different fiber contents at 28 days of the sample age.

The effect of 2% fiber content on the strength development of both optimum mixes M18 and M19 is shown in Figure 51. The strength values of base mixes without fibers are shown as green and blue bars at ages of 3, 7, 14, and 28 days. As a comparison to the control mix, the strength development of M1 is also represented in Figure 51. Based on the trend, both M18 and M19 showed a significant increase in strength gain compared to the base mixes without fibers. M18 showed the highest increase in strength, although M19 showed higher strength gain at a later age. As a comparative measure, M18 and M19 attained a strength of 16 ksi at 4 days and 10 days, respectively, which can be crucial in applications when early strength is a key. M18 and M19 also reached the ACI strength requirement of 120 MPa (17.4 ksi) at the age of 7 and 14 days, respectively.

Later, the effect of fiber addition was also validated on a range of other UHPC mixes, which is shown in Figure 52. The dotted bars represent UHPC mixes without any fibers. The inclusion of fibers exhibited a significant increase in strength for all mixes. Even in the control mixes (M1) with 100% cement, inclusion of 2% fiber content resulted in an almost 3 ksi increase in strength to the final strength of almost 16.5 ksi at 28 days. Meanwhile, M10 and M15 also showed a significant strength increase at 28 days to almost 18 ksi. The strength increase from fiber inclusion was more evident for M18 and M19, which also validates the optimum performance of these mixes for further implementation.

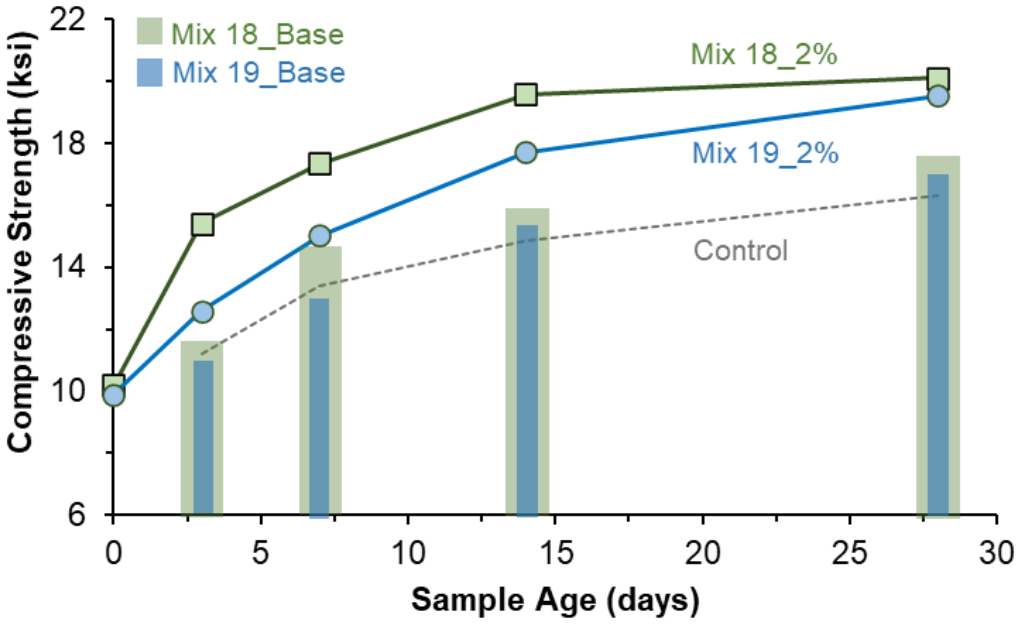

Figure 51. Chart. Strength development of the optimum mixes M18 and M19 with 2% steel fibers.

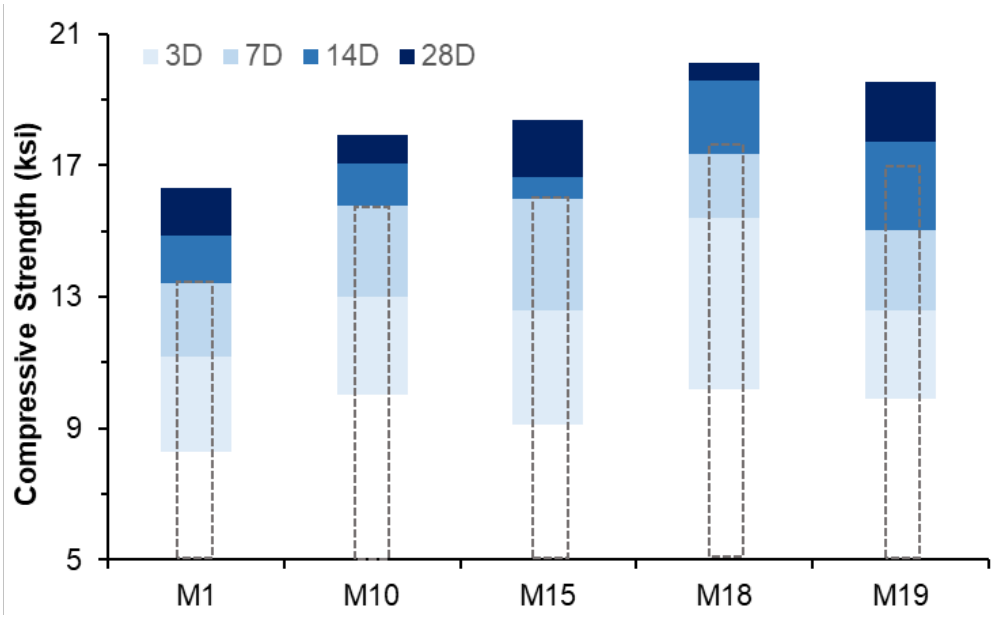

Figure 52. Chart. Strength enhancement of different UHPC mixes with the inclusion of 2% steel fibers. The blue zones correspond to the strength increase at each test duration.

Steel fibers in UHPC have the ability to bridge cracks, which results in high ductility and capacity to carry loads even after the initiation of cracks. Hence, in order to test the capacity of UHPC mixes, the UHPC sample cubes were subjected to compressive loading after the initial failures and the process is repeated in successive cycles. The capacity of UHPC mixes after each cycle was measured till the moment the samples were crushed. The capacity of the optimum mix M18 at each cycle of load application after 7 days of hydration is shown in Figure 53 along with the sample appearance at different stages of load application. The samples cast had 2% steel fiber content, as found to be optimal in the last section. Based on the results of a single sample of M18 with 2% fiber content in Figure 53, the sample had a significant residual strength capacity of more than 80% at the second cycle compared to the initial strength at the first cycle (15.2 ksi). Interestingly, the sample also showed a strength capacity of more than 5 ksi even after five cycles of load application with the sample exhibiting minor chipping of the UHPC matrix. Notably, an increase in strength at the seventh cycle was observed, which is mainly attributed to the core of steel fibers in the sample taking the load. This also explains the deformation of the sample prior to being completely crushed at Stage VI in Figure 53. The same phenomenon is observed at other early and late ages of the M18 samples, which is presented in Figure 102 in Appendix G.

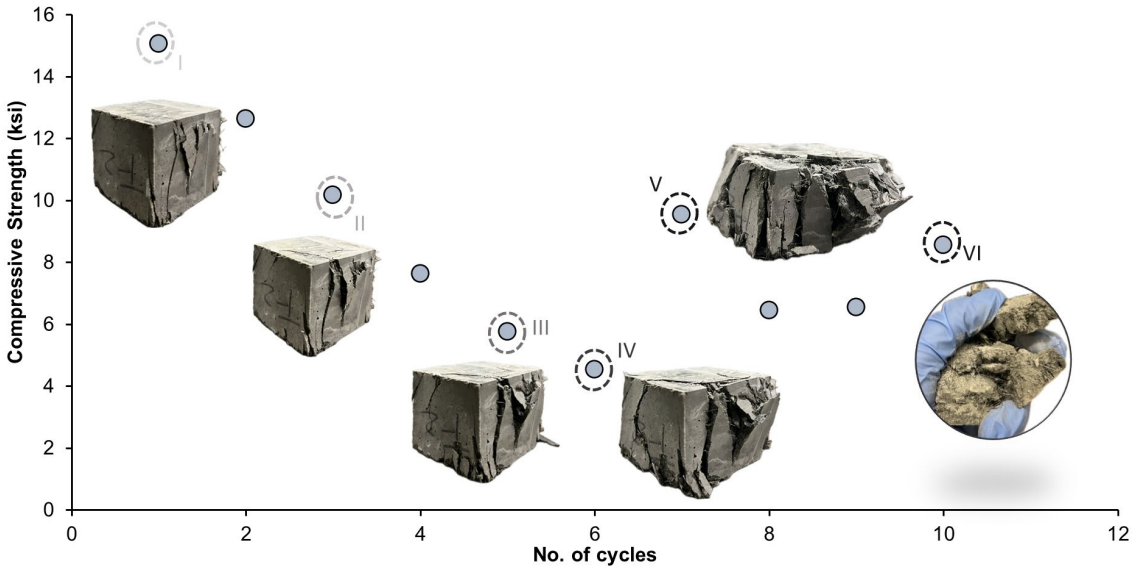

Figure 53. Graph. Strength capacity of M18 with 2% steel fiber at each cycle of load application.

EFFECT OF CEMENT CONTENT

The optimum mixes from previous sections had a cement content of around 50%. In this section, a sensitivity analysis was performed to investigate the role of cement content on the performance of optimum mixes to further enhance the performance of well-performing mixes. Hence, the cement content varied from 40% to 70% of the total binder content, and the effect on mechanical performance was investigated. The strength performance of the mixes at different ages is represented in Figure 54 for different cement contents, where the digits after C (Cxx) refer to the volumetric percentage of cement.

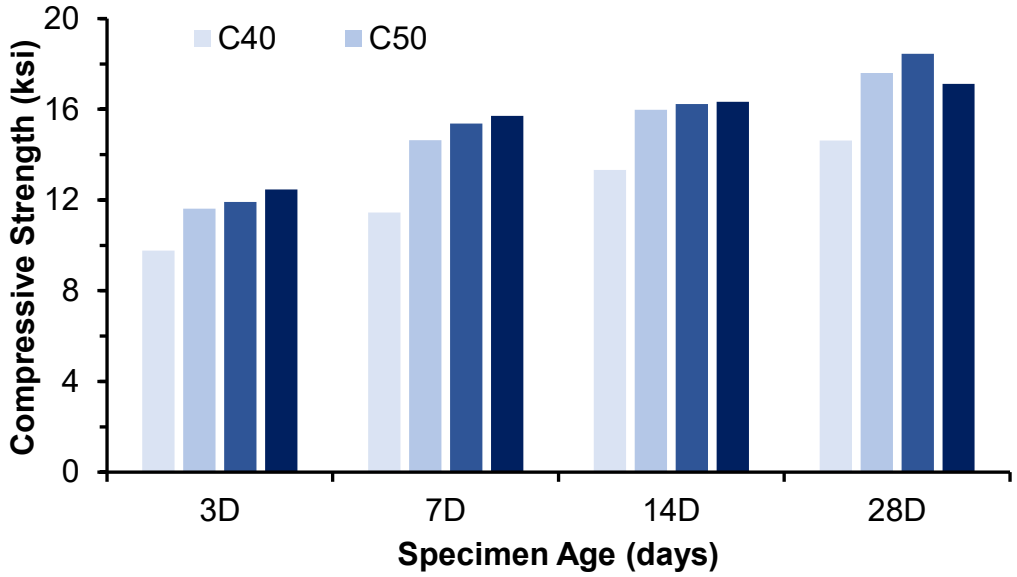

Figure 54. Chart. Effect of different cement content (40%–70%) on strength development of UHPC mixes at sample ages of 3, 7, 14, and 28 days.

The water-binder ratio in UHPC mixes is notably low at 0.18, resulting in a significant amount of unreacted cement. This highlights the dual role of cement particles in both packing and hydration within the UHPC systems. At an early age (3 days), mixes with a higher cement content of 70% show the greatest strength, due to more cement particles facilitating increased hydration. Conversely, mixes with only 40% cement content display the lowest strength at all ages, due to minimal hydration from the limited amount of primary binder. Over time, the strength differences between mixes C50, C60, and C70 decrease, indicating a plateau in cement hydration caused by water constraints within the system. Additionally, the reduced strength of mix C90 at later ages illustrates the dual impact of excessive cement, which, while initially boosting hydration potential, adversely affects packing and overall strength. Therefore, a cement content of around 50%–60% is optimal for achieving robust UHPC strength both early and late in the process. Given the limited variance in strength due to water constraints, lower cement content is also advocated to enhance the mix's sustainability and environmental friendliness.

EFFECT OF SILICA FUME TYPE

In previous sections, UHPC mixes were designed using densified silica fume (DSF). However, a switch to undensified silica fume (USF) was explored to assess its effects on the mixes' rheological and mechanical properties. USF, with its finer particle size compared to DSF, was tested in six UHPC mixes, significantly impacting their flow and strength. The rheological changes, particularly in mixes with high silica fume content like M2 and M4, showed a dramatic reduction in flow due to the increased HRWR demand from the finer USF particles, as detailed in Figure 55 and Figure 103 in Appendix G. For example, mix M4's flow decreased from 9.75 inches to 5.0 inches. In mixes with moderate silica fume content, the impact on HRWR/flow ratio was less pronounced.

In terms of strength development, as shown in Figure 56, the inclusion of USF led to higher early strength gains, particularly in M2 and M4, where the finer USF replaced larger DSF particles, enhancing packing density. However, the long-term strength gains (28-day strength shown in Figure 104) were less significant, with mixes like M18 and M19 experiencing only a marginal decrease in compressive strength. Despite their lower silica fume content, the finer particle size of USF still significantly influenced the mixes' packing and water demand, affecting overall strength development.

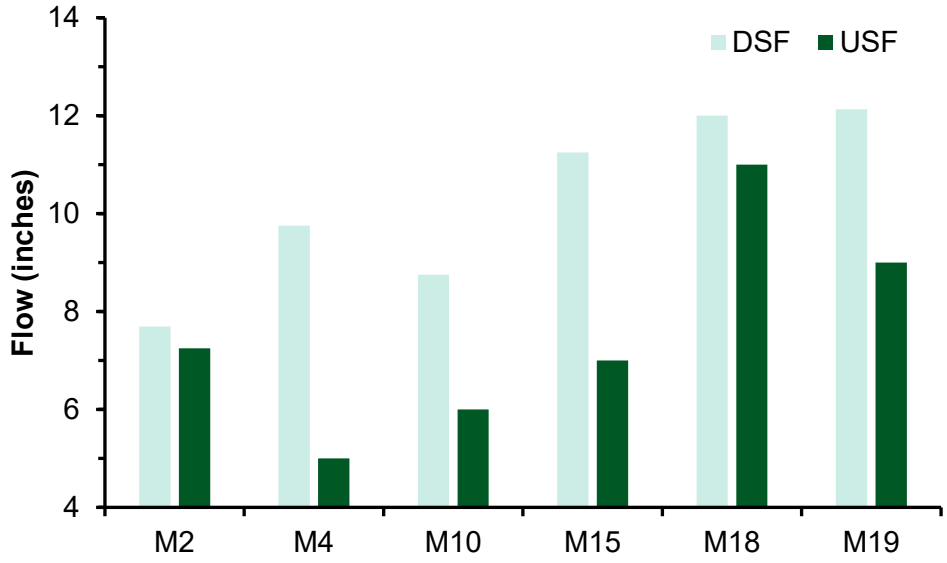

Figure 55. Chart. Effect of silica fume type on the flow of UHPC mixes.

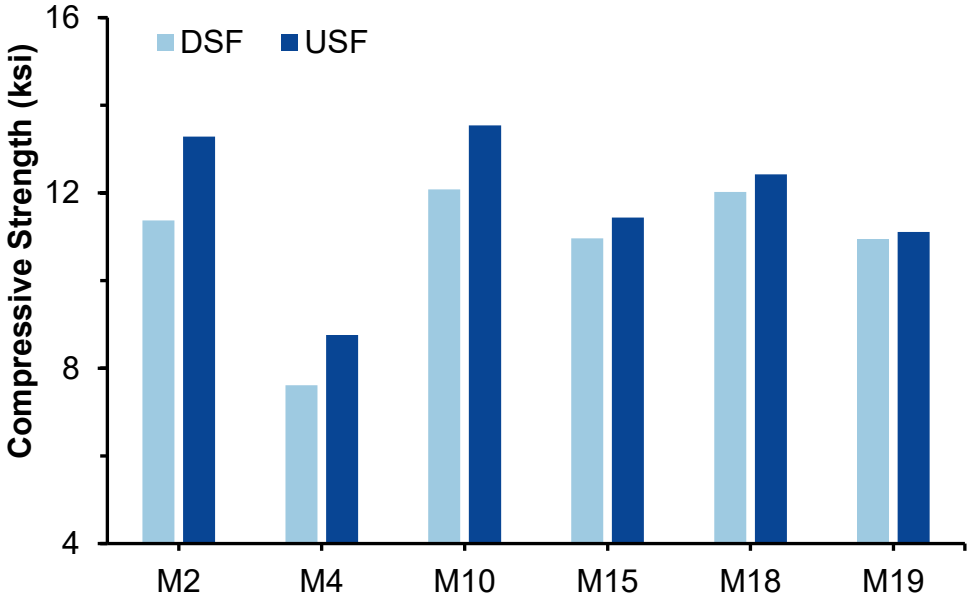

Figure 56. Chart. Effect of silica fume type on early-age (3 days) compressive strength of UHPC mixes.

EFFECT OF WATER-BINDER RATIO ON UHPC PERFORMANCE

The performance of UHPC mixes (M18) without fibers was tested for different water-binder ratios (Figure 57). A sensitivity analysis was performed on four UHPC mixes (M4, M5, M18, and M19) to analyze the effect on mixes with compositional variation. Based on the observed result, a lower water-binder ratio of 0.18 exhibited the highest strength for the mixes. Mixes at lower water-binder ratios (0.14 and 0.16) showed strength lower than 16 ksi even after 28 days of hydration. This is accountable to the limited degree of hydration due to a significantly lower water content in these

mixes for the cement particles to hydrate. This is also confirmed from a lower difference in strength at an early age of mixes, as particle packing plays a key role at that stage. The strength gain at a later age, accountable to a higher degree of cement hydration and pozzolanic reaction, is evident in a higher increase in strength for the mixes, especially for M18 and M19, at 28 days in Figure 57. Based on the overall performance, an optimum water-binder ratio of 0.18 was used for the next phases of the study and further implementation.

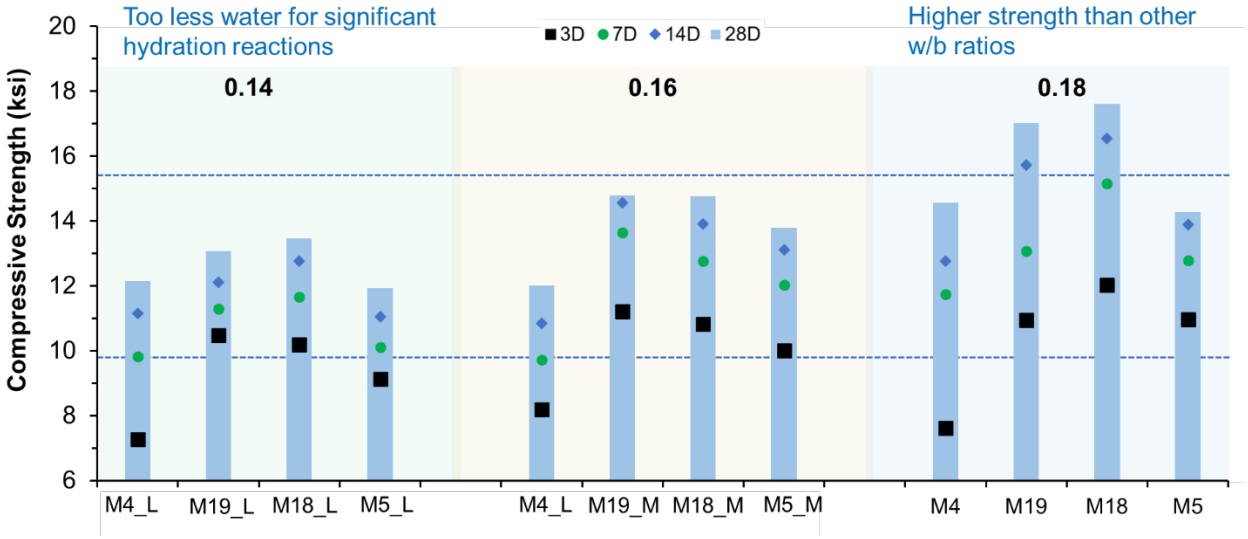

Figure 57. Chart. Sensitivity analysis of the strength enhancement of UHPC mixes (M4, M5, M18, and M19) due to change in water-binder ratio.

CHAPTER 10: COST AND ENVIRONMENTAL ANALYSIS OF THE OPTIMIZED UHPC MIXES

OVERVIEW

This section covers the detailed cost analysis of 19 optimized UHPC mixes based on the cost structure of local materials. A strength-normalized cost parameter was formulated to compare the efficiency of the mixes with respect to both the mechanical and cost point of view. Later, a comprehensive cradle-to-gate life-cycle analysis (LCA) was performed on 19 UHPC mixes to determine the extent of environmental emissions associated with each constituent of the mixes. These steps are fundamental in designing sustainable and low-cost nonproprietary UHPC mixes while safeguarding their performance.

CONSTITUENT-BASED COST ANALYSIS OF UHPC MIXES

One of the key milestones considered for developing the nonproprietary UHPC mixes in this study was to minimize the overall cost to make it feasible for implementation. It stems from the expensive nature of commercial proprietary UHPC mixes, which puts constraints on the overall budget for its mass adoption. Hence, a survey of the cost structure for each local ingredient was performed, summarized in Table 2. The material costs were compared with other states to ensure a reasonable cost framework for further studies.

Table 2. Cost structure of each constituent used for designing nonproprietary UHPC mixes

Cost	$/ton
Cement	140
FA	75
Slag	135
SF	525
Sand	25
HRWR	3800
Water	–
Fibers	1000

Based on the aforementioned cost structure, the overall cost of UHPC mixes was evaluated with and without fibers. The overall cost was segregated for contribution corresponding to each binder in the mixes to aid in mix optimization from a financial perspective. The cost of UHPC mixes is arranged in ascending order in Figure 58 for clarity. From the figure, cement and silica fume contribute to a major share of the overall UHPC costs among the binders considered in the study. This is attributed to the higher per-unit cost of cement and silica fume in Table 2. Note that an increase in binder content has a higher stress on the overall cost of UHPC compared to the aggregates within UHPC mixes. Hence, a higher sand-to-cement ratio would aid in further reducing the overall costs although the effect on other properties needs to be assessed as well. It is striking that high-range water reducers (PCE based

in this study) also have a manifold higher unit cost compared to other constituents. This is particularly crucial in low water-to-binder (w/b) systems such as UHPC, which usually require a higher dosage of HRWR to attain the required flow. As a result, the contribution toward the cost for both cement and HRWR was plotted separately in Figure 58. The cost of fibers corresponds to a volumetric ratio of 2%, which exhibited the highest strength enhancement with optimum rheology in previous chapters.

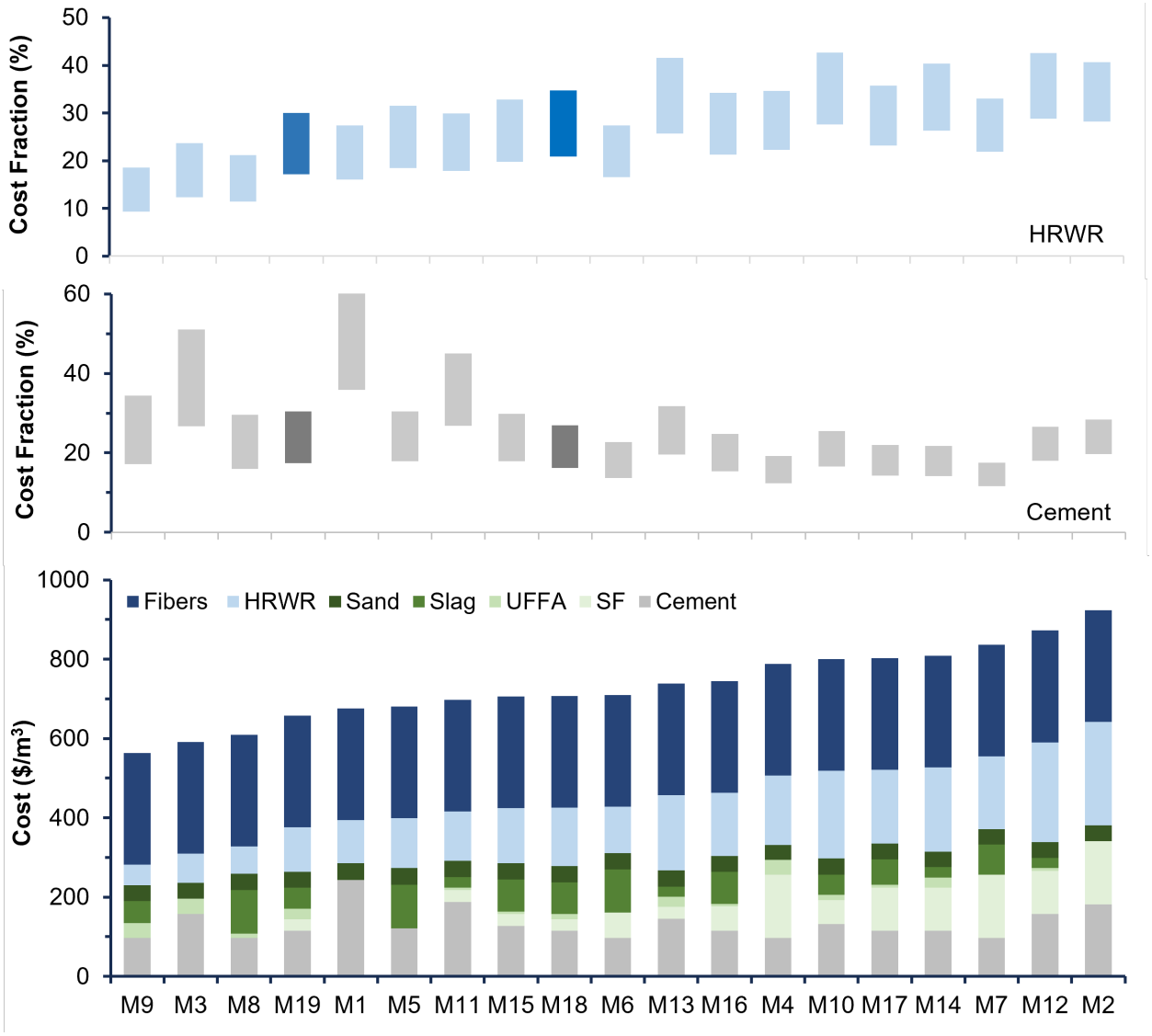

Figure 58. Chart. Cost structure of UHPC mixes developed in the study based on the unit cost in Table 2.

Figure 58 illustrates that UHPC can be designed with varying costs, ranging from \$282/m^3 (\$564/m^3 with fibers) to \$641/m^3 (\$923/m^3 with fibers), by optimizing binder type and composition through a multi-binder approach. This approach aims to balance cost with required rheological, mechanical, and durability performance. For example, M9 achieved the lowest cost due to a low cement content of 40% and a high amount of UFFA (35%), which enhanced rheology and reduced HRWR demand, accounting for only 18% (10% of the total cost with fibers) of its overall cost. In contrast, M2 was the

most expensive at \$923/m^3, due to high proportions of costly binders (75% cement and 25% SF) and a significant HRWR requirement, making up 40.6% (28.2% with fibers) of its total cost.

M1 and M3 had higher cement contributions (62% and 51%, respectively) but lower mechanical performance, highlighting the importance of optimizing binder design for cost-effectiveness and performance. Optimally designed mixes like M18 and M19 showed significantly lower costs of \$426/m^3 (\$707/m^3 with fibers) and \$377/m^3 (\$658/m^3 with fibers), respectively, which are 33% and 41% lower than M2. The study also evaluated UHPC cost relative to mechanical performance, with results detailed in Figure 59, showing costs normalized to strength at 3 and 28 days. This emphasizes the critical balance between minimizing costs and achieving desired UHPC strength.

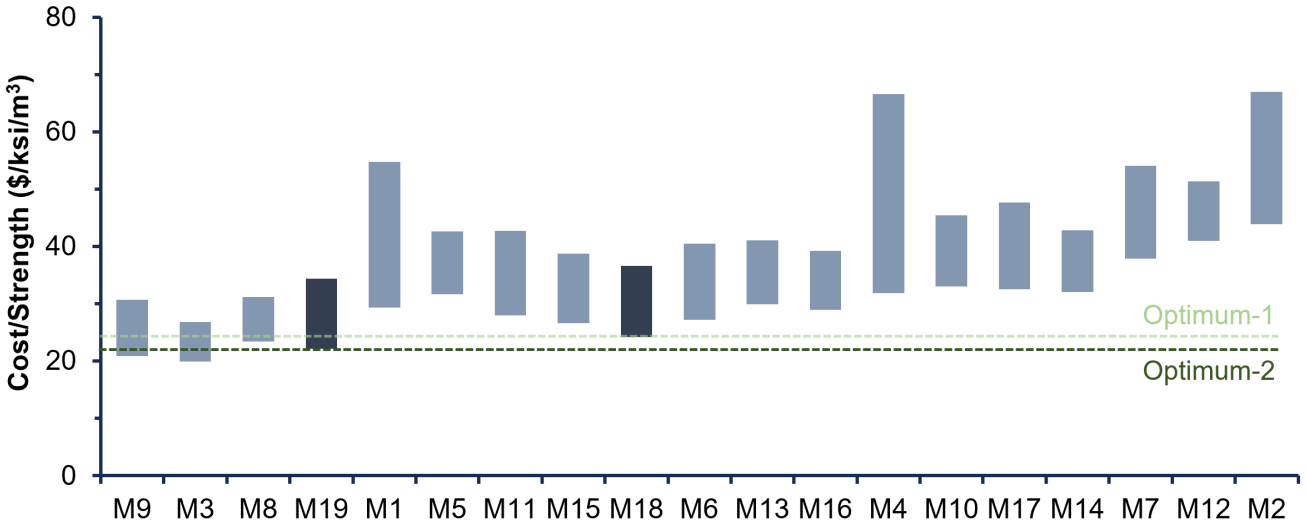

Figure 59. Chart. Cost estimation of UHPC mixes per unit of mechanical property (strength). The top and bottom of the bar represent the cost of the UHPC mixes normalized to 3- and 28-day strength.

The distribution of strength-normalized cost shows a similar pattern as in Figure 59. M3 exhibited the lowest cost/strength ratio of \$26.8/MPa/m^3, which shows the role of better strength values compared to M9 with the highest cost (Figure 59). M2 also showed the highest normalized cost of \$67/MPa/m^3 and 43.9/MPa/m^3 due to a much higher contribution of HRWR in addition to the lower strength gain. Interestingly, M1 with a 100% cement content shows a significant drop in cost/strength values from early age to long-term age of the samples. This is attributed to the long-term hydration of unreacted cement grains when subjected to continuous curing. Meanwhile, M4 exhibited the maximum drop (\$34.7/MPa/m^3) in normalized cost, highlighting the effect of maximum packing state and long-term strength gain. The optimum mixes M18 and M19 showed a considerably lower normalized cost of only \$24.2/MPa/m^3 (optimum-1) and \$21.1/MPa/m^3 (optimum-2), which confirms the optimization of both the cost and mechanical properties of UHPC mixes utilizing multi-binders.

BINDER-BASED MAPPING OF COST FOR UHPC MIXES

As a general guideline to design UHPC mixes based on the cost criteria, it is essential to properly understand the sensitivity to the cost corresponding to each binder. Hence, the response of the cost

sensitivity was compared to a new reference blend of 100% OPC to understand the role of each binder on overall cost. In Figure 60, with respect to the reference blend, an increase in silica fume content had the highest sensitivity to the overall cost, which is justified by the high cost associated with processing silica fume from silicon-based industries. Meanwhile, slag yielded a minimal change in the increase in the cost initially while leading to an overall cost decrease at a volume proportion in excess of 15%–20%. Meanwhile, fly ash was the most probable option if reducing the overall cost of UHPC mixes with an overall decrease in the fitted cost. This is also complemented by a lower HRWR demand, which can further lead to an overall decrease in UHPC cost.

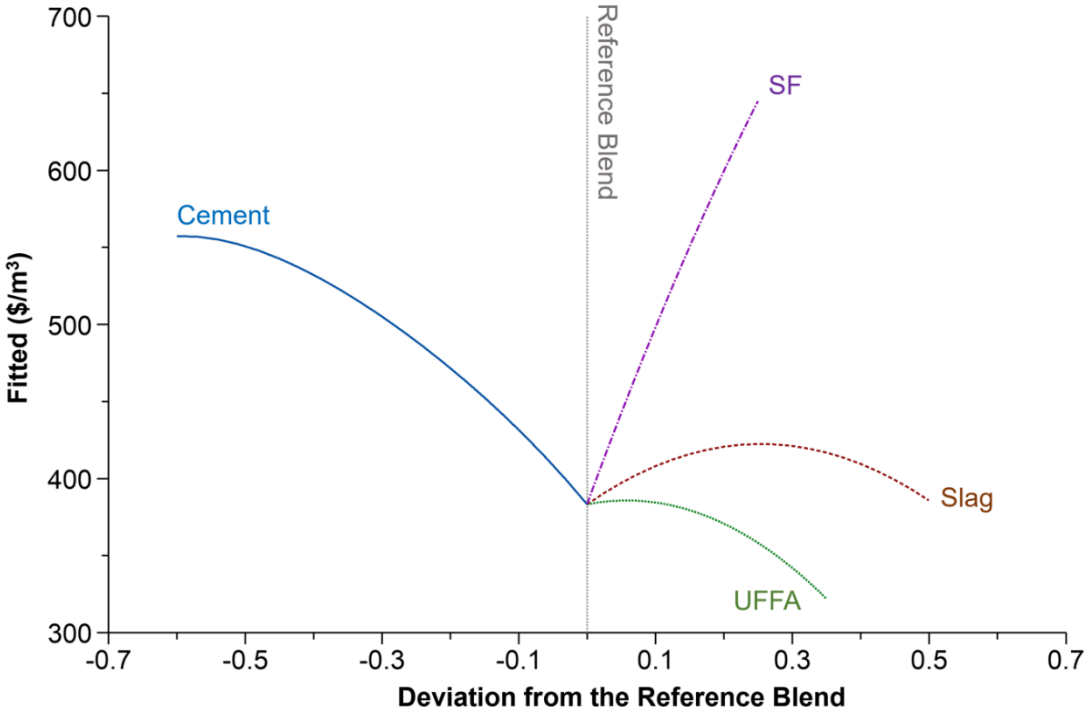

Figure 60. Graph. Sensitivity of the strength-normalized cost of UHPC mixes for unit variation of different binder constituents.

As an attempt to establish a binder-based guideline for mix design, ternary plots (SF, UFFA, and slag) corresponding to different cements were plotted in Figure 61 for further optimization of UHPC mixes. Similar to the sensitivity response of binders in Figure 60, the ternary plots exhibit regions of higher cost closer to the edges of silica fume. This is more prevalent in mixes with lower cement content with a higher amount of alternate binders. The regions of lower cost (blue shades) are more concentrated near the edges of slag and UFFA with darker blue regions (lower cost) closer to the UFFA corner. Last, a significant shift from the green to blue region is observed with a gradual increase in the cement content of UHPC mixes. The generated ternary plots will aid practitioners in customizing UHPC mixes with binder composition even beyond the range covered by this study.

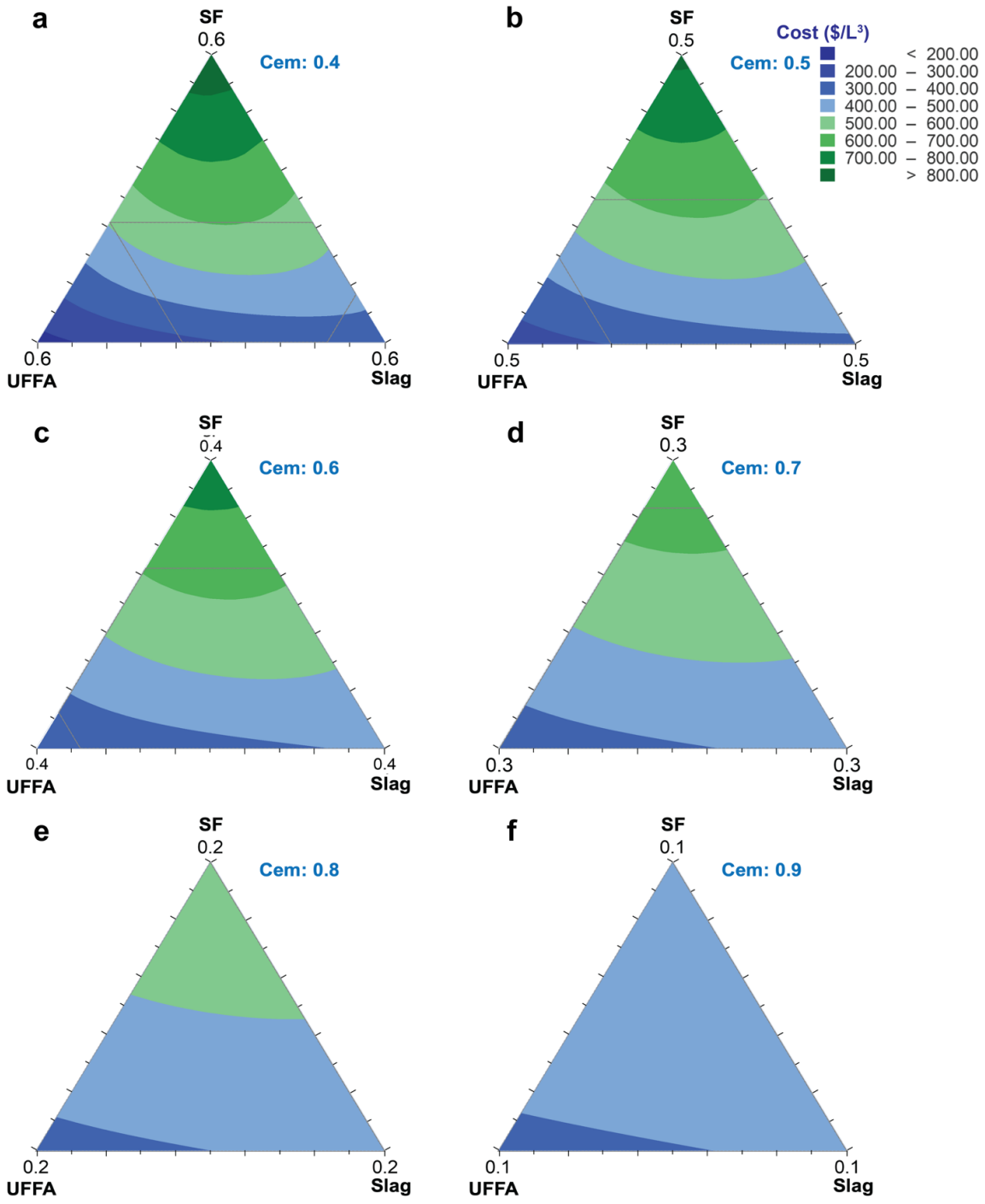

Figure 61. Graph. Ternary plot showing the cost of UHPC mixes for a wide range of binder constituents used in the study.

CONSTITUENT-BASED GREENHOUSE GAS EMISSIONS

UHPC is usually perceived as a carbon-intensive construction material due to its higher cement content, which also prevents its wider adoption or implementation. In this regard, SCMs are usually used to lower cement content while ensuring adequate strength and long-term durability. As SCMs,

such as fly ash and slag, are usually biproducts of different industries, they play a significant role in making concrete greener. In this study, the research team aimed to develop a range of sustainable multi-binder UHPC mixes with lower cement content but competitive strength and performance. Hence, in this step, a detailed LCA was performed on the optimized mixes to assess the reduction on environmental impacts from the sustainable mix design.

A comprehensive LCA tool, OpenConcrete software, originally developed by Kim et. al. (2022), was used to compare the environmental impact of UHPC mixes. Generally, the global warming potential is used as the reference metric within the environmental product declaration. However, other environmental indicators such as nitrous- (NOx) and sulfur-based (SOx) oxides along with particulate matters (PM) are equally important, which can impact health and the environment. Hence, in this study, a range of 11 environmental indicators were evaluated for each constituent of UHPC mixes. This is vital in customizing the UHPC mix design from a sustainable standpoint.

OpenConcrete has been used for constituent life-cycle inventories and impact modelling. Hence, a cradle-to-gate approach was implemented while considering the impact from constituent production to the point of UHPC casting. The processes, from material acquisition to UHPC casting, which have been considered for LCA inventories, are mapped in Figure 62. The batching location was Newmark Civil Engineering Laboratory at the University of Illinois, while most of the material were locally sourced with a transportation distance of 20 km from the analysis. However, silica fume and HRWR were transported from San Francisco and Indiana, respectively, which contributed to the transportation distance in accordance with the inventory of the Portland Cement Association.

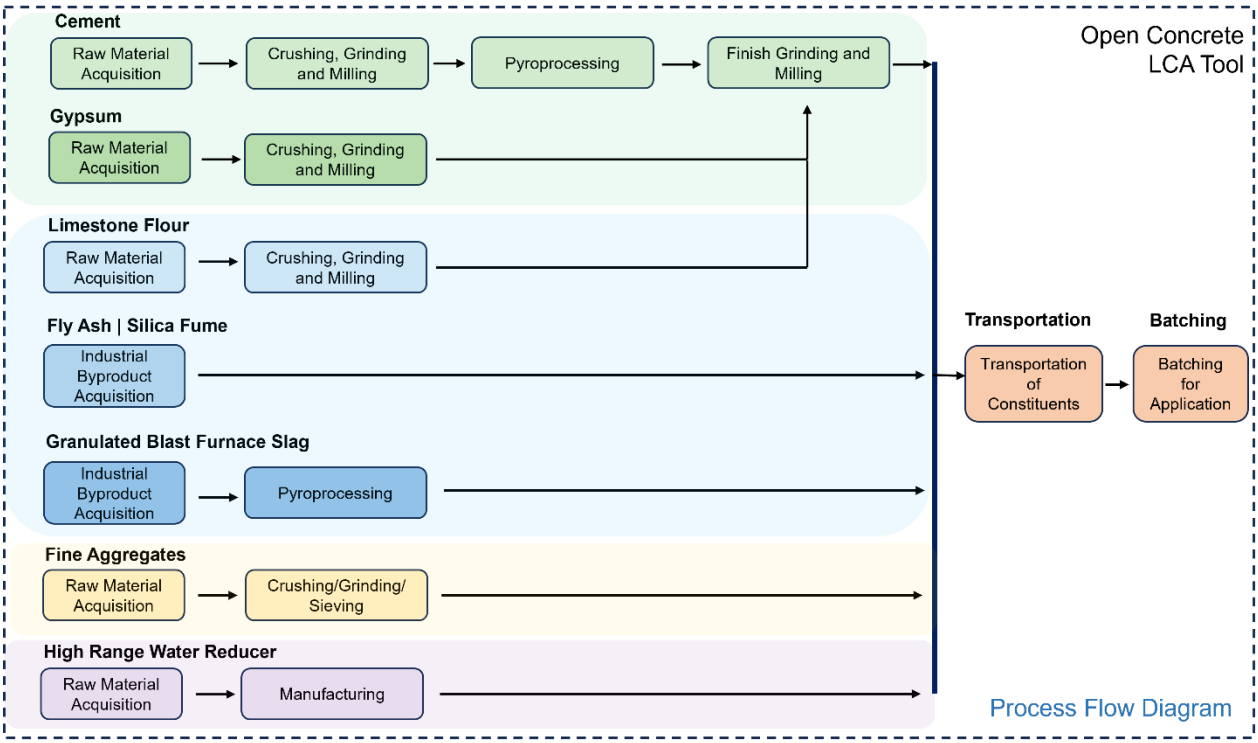

Figure 62. Graph. Energy process flow diagram considered for the cradle-to-gate life-cycle analysis of UHPC mixes.

Based on the model's output, the environmental impact of each UHPC mix was analyzed while also estimating the contribution from each constituent. Summaries for optimum mixes M18 and M19 are graphically represented in Figure 63 and Figure 105 (Appendix H), respectively, for all 11 environmental parameters. Cement contributes the most significant share of most of the environmental indicators. This is attributed to the energy-intensive and environmentally impactful calcination process involved in cement production. Meanwhile, HRWR also contributes to a considerable proportion of most of the environmental impact. Notably, aggregate contributes significantly to both PM2.5 and P.M10 due to the aggregate crushing and processing zone, which release particulate matter into the air.

Figure 63 summarizes different environmental parameters for all designed multi-binder mixes and provides a detailed assessment of each mix constituent separately. There is a general trend of an overall increase in greenhouse gas (GHG) emissions for an increase in the cement content in UHPC mixes. This is evident from a higher GHG contribution for M2, M11, and M12. Also, as seen in Figure 62, HRWR contributes significantly to GHG emissions, which also contributes considerably to the higher GHG emissions of M2 and M12 associated with a high silica fume content in the mixes. Meanwhile, alternate SCMs such as slag and fly ash have insignificant GHG emissions so they contribute minimally to overall GHG emissions along with a low demand for HRWR. Hence, a multi-binder UHPC blend with high slag and fly ash content in the optimum mixes M18 and M19 also showed considerably low GHG emissions.

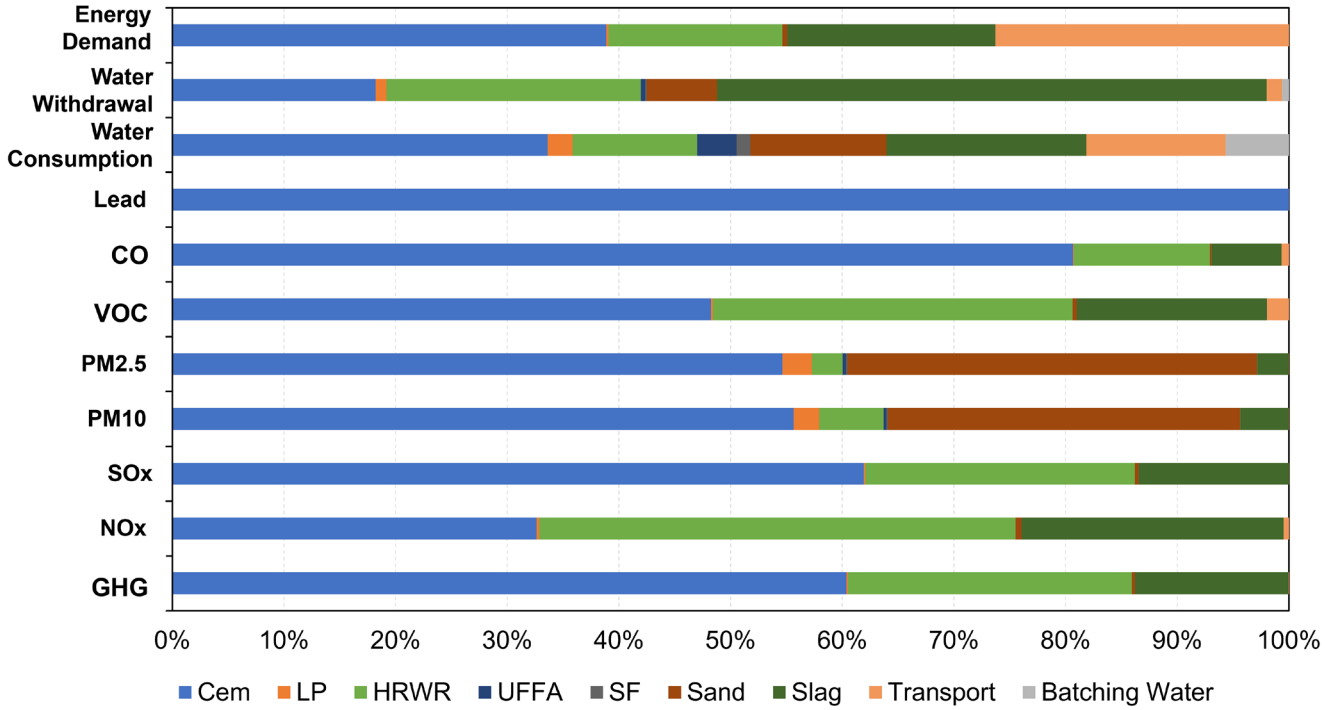

Figure 63. Chart. Environmental emissions for different contaminants for M18 obtained from the cradle-to-gate analysis using the Open Concrete LCA software.

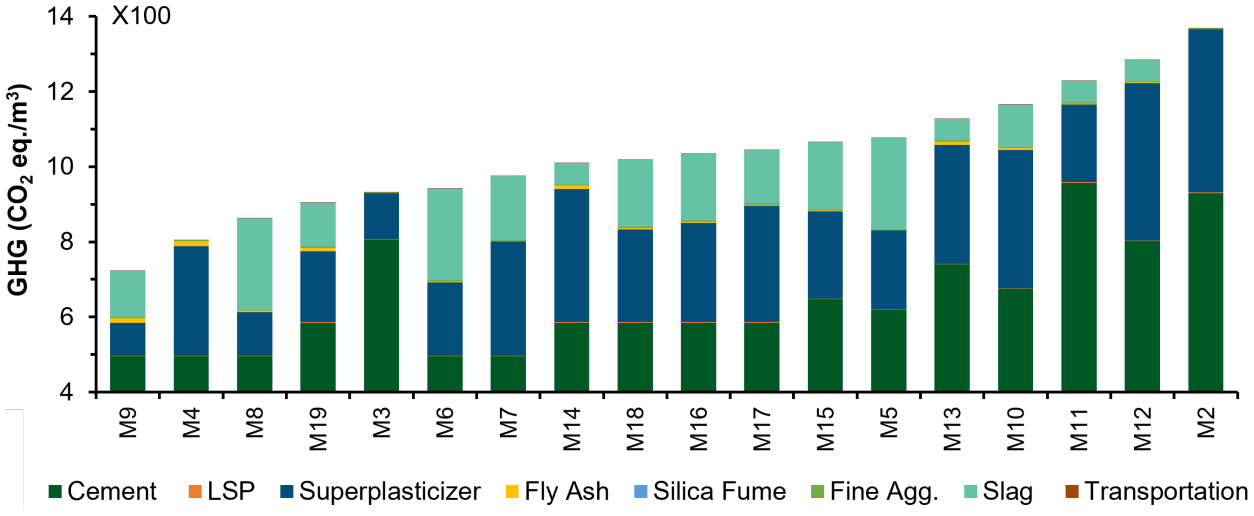
X100
GHG (CO_2 eq./m^3)
14
12
10
8
6
4
M9 M4 M8 M19 M3 M6 M7 M14 M18 M16 M17 M15 M5 M13 M10 M11 M12 M2
Cement
LSP
Superplasticizer
Fly Ash
Silica Fume
Fine Agg.
Slag
Transportation

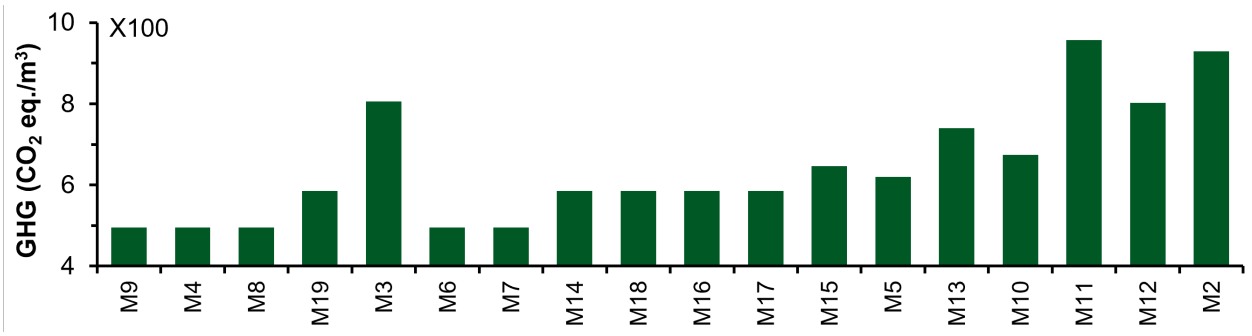
X100
GHG (CO_2 eq./m^3)
10
8
6
4
M9 M4 M8 M19 M3 M6 M7 M14 M18 M16 M17 M15 M5 M13 M10 M11 M12 M2

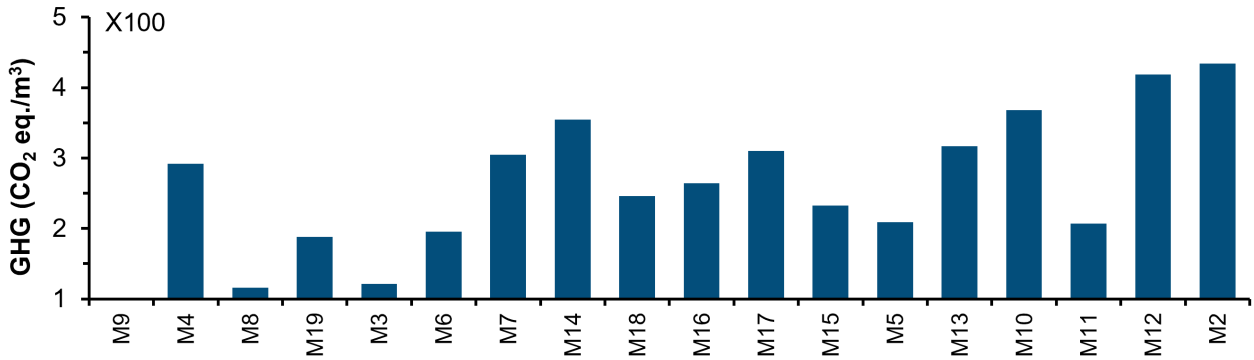
X100
GHG (CO_2 eq./m^3)
5
4
3
2
1
M9 M4 M8 M19 M3 M6 M7 M14 M18 M16 M17 M15 M5 M13 M10 M11 M12 M2


X100
GHG (CO_2 eq./m^3)
3
2
1
0
M9 M4 M8 M19 M3 M6 M7 M14 M18 M16 M17 M15 M5 M13 M10 M11 M12 M2

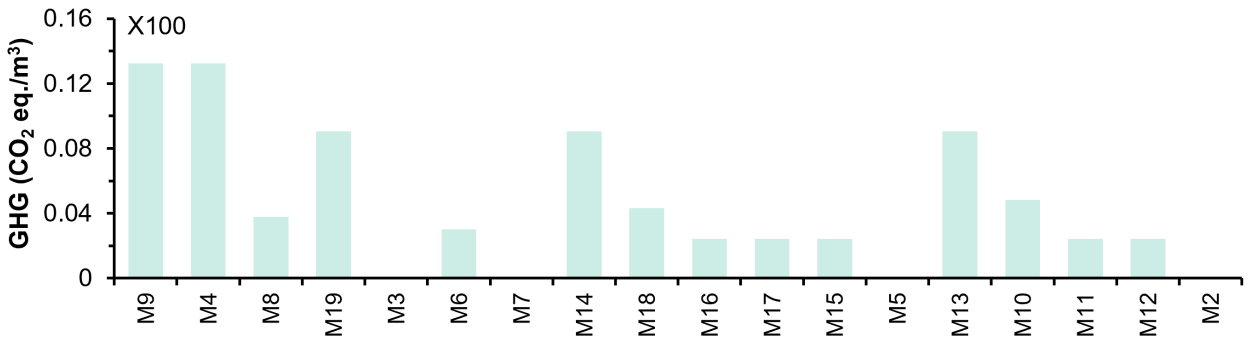

Figure 64. Chart. Summary of greenhouse gas emissions for the optimized mixes in a (a) combined form and relative contribution of (b) cement, (c) HRWR, (d) slag, and (e) fly ash.

For an overall comparison of the mechanical and sustainability perspective, it is crucial to consider the strength unit per unit of cement used for the sustainable UHPC mixes. Hence, the GHG emissions were compared with the strength of the mixes per unit of binder in Figure 65. The correlations provide evidence that it is possible to significantly reduce GHG emissions while ensuring higher mechanical performance per unit of cement used by using multi-binder blends in UHPC mix design. A similar trend is observed for mixes with different slag content represented by Zone A–Zone C. Notably, the inclusion of moderate or high slag content can reduce GHG emissions significantly by almost 50% (1,250 kg to 640 kg eq. CO_2) while ensuring higher strength to cement (strength/cem) ratios of almost 0.17 MPa/kgm^3. Hence, the correlation can be crucial in ensuring sustainable UHPC with adequate mechanical performance.

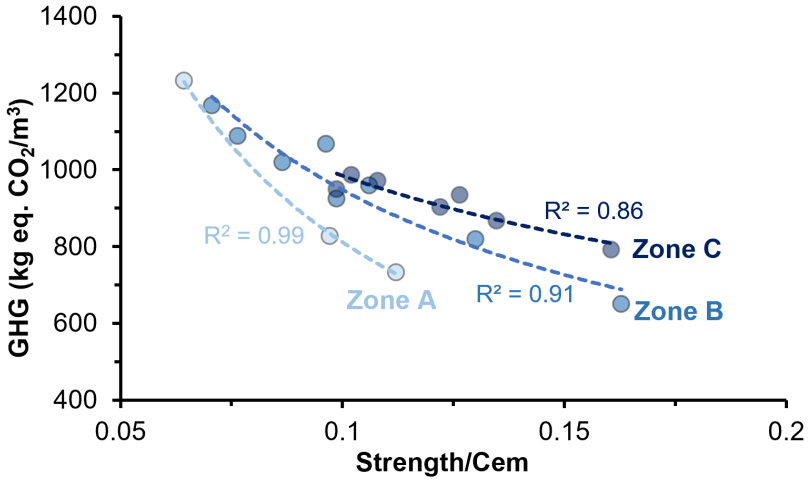

Figure 65. Graph. Correlation between greenhouse gas emissions and the cement normalized strength of the UHPC mixes.

CHAPTER 11: INTERLABORATORY REPEATABILITY AND SCALABILITY OF UHPC MIXES

REPEATABILITY OF SMALL-SCALE OPTIMUM UHPC PERFORMANCE

Following the completion of the initial round of binder development and testing, several of the most promising mix formulations were transferred to the partner research team with an initial goal of reproducing consistency and strength performance in a different laboratory setting. This repeatability-focused effort will help to promote confidence that a given nonproprietary, ultra-high performance concrete mix can achieve its target performance metrics, such as compressive strength at a given concrete age, given the possibility for slight variations or substitutions of local materials, varying types of mixing equipment, varying levels of experience for laboratory personnel, and ambient conditions of the facility in which the concrete is produced.

The most promising mix formulations identified from the larger test matrix described in the previous section of this report were M18 and M19. After receiving the mix formulations, the partner research team first made small amendments to the mix designs, such as adjusting for the moisture content of concrete sand and replacing ultra-fine fly ash (UFFA) with a conventional fresh Class F fly ash meeting ASTM C618 (2023) requirements. (Therefore, the modified M18 and M19 mixes in Table 3 contain unsieved conventional fresh Class F fly ash.) Class F fly ash was chosen as a potential substitute as it would not have to be processed to reach an ultra-fine state and, thus, its production would likely generate less CO_2 emissions. Additionally, UFFA is generally a specialty material that may be difficult to procure and, thus, may inhibit more widespread use. The partner research team also developed variants of the original M18 and M19 mixes with fresh Class F fly ash passing through a no. 200 (75µm) sieve to verify that using sieved conventional fly ash as a substitute for UFFA would yield comparable (or better) performance with other variables held constant. Those particular mixes were labeled with "U," as shown in Table 3. Complete mix designs for the benchtop mixer are also provided in Table 3. Additional minor adjustments were made to ensure the sand-to-binder ratio remained one as the specific gravity for each material was updated—a necessary step when using locally available materials as opposed to a pre-bagged proprietary mix. Relative cementitious volumes were maintained from the mixture design formulations. (See the previous section of this report.) An initial amount of a high-range water reducer (HRWR) admixture was initially recommended but a larger dosage was needed to ensure satisfactory flow performance was met.

Table 3. Nonproprietary UHPC mix design matrix for repeatability study

Mix ID	Type IL Cem.	Silica Fume	Fly Ash (Class F)	Slag	Fine Agg.	Water	HRWR
	kg/m³ (lbm/yd³)						mL/cwt (fl. oz/cwt)
M18/ M18U*	738 (1244)	54 (91)	116 (196)	503 (848)	1411 (2378)	254 (428)	887 (30.0)
M19/ M19U*	738 (1244)	54 (91)	231 (389)	359 (605)	1383 (2331)	254 (428)	887 (30.0)

*Note: Mix identifiers ending with "U" used Class F fly ash passing through a No. 200 sieve.

A benchtop mortar mixer (see Figure 66) with three speeds—low (130 RPM), medium (233 RPM), and high (415 RPM)—and a maximum fill capacity of 14 liters (0.5 ft^3) was used to batch these mixes. The aforementioned batch volume was sufficient enough to perform a flow test (in accordance with ASTM C1856 [2017]) and subsequently produce 15 5 cm (2 in.) cubes for compressive strength testing. Cubes were fabricated by filling the molds (each mold set produced three cubes) from one corner and allowing the concrete to flow into the remainder of the cavity to minimize entrapped air, followed by lightly tapping each cube five times on each side to further promote proper consolidation. A glass plate was then placed on top of each mold group before the whole assembly was placed in its respective curing environment within 1 minute of finishing the surface of the cubes. Curing methods were based on ASTM C511 (2021) provisions, and specimens labeled with -W (see Table 4) were placed in a digitally controlled chamber that maintained a temperature of 23.0 ± 2.0°C and 95% relative humidity. These -W specimens were then demolded at an age of 24 hours and subsequently placed in a water bath with a lime solution (3 g/L of calcium hydroxide) that held a constant temperature of 23.0 ± 1.0°C, which was controlled by a heating element connected to a temperature sensor. Specimens labeled with -A (see Table 4) were ambient cured in the laboratory where the average temperature was 26.7± 3.0°C and with a range of 30%–50% relative humidity. The ambient specimens were used for two reasons: (1) to examine the effect of the curing environment on the strength development of the nonproprietary UHPC binders and (2) to more closely emulate realistic curing conditions, such as in a precast facility or on a jobsite. Both justifications should help to facilitate more widespread use of the novel nonproprietary UHPC formulations by demonstrating that their strength performance is achievable across multiple types of curing conditions (an objective that will be further examined later in this report).

Figure 66. Photo. Benchtop mortar mixer used in the repeatability study.

The batching sequence used in this repeatability study was developed with guidance from the research team that created the original mix formulations and supplemented by further information from the Precast/Prestressed Concrete Institute (PCI) Phase II UHPC Report that focused on the implementation of UHPC mixes for precast construction (Kurt, 2021) and other publications documenting recent research on UHPC applications for transportation structures (Mendonca et al., 2019; Mendonca et al., 2020). The resulting batch sequence for the benchtop small mixer is detailed in the flowchart in Figure 67.

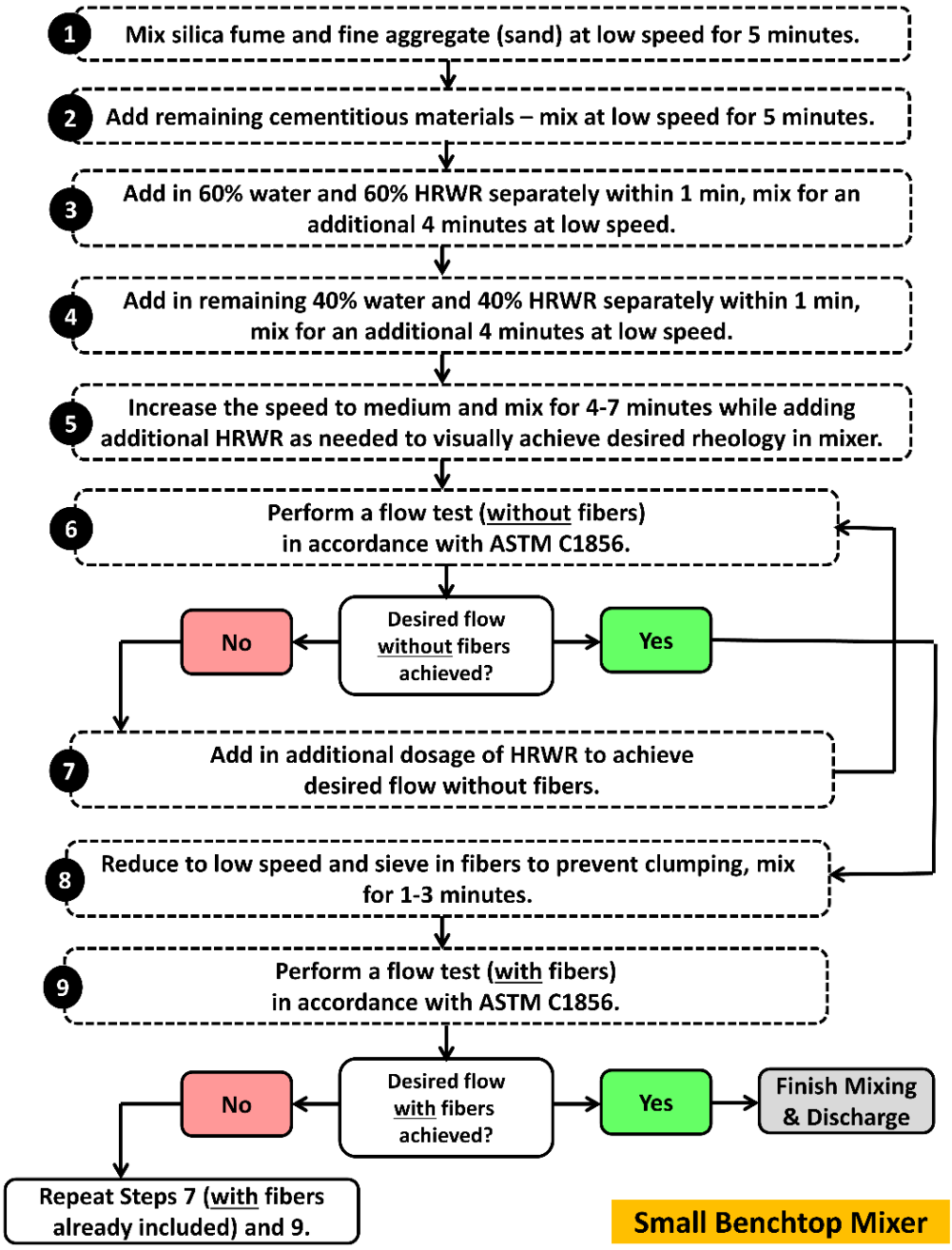

Figure 67. Illustration. Batching sequence for small benchtop mixer used in repeatability study.

Flow and compressive strength test results for the reproduced mixes are displayed in Table 4. The results show that the partner research team was able to exceed the cube compression strength achieved during the original development of the mix formulations in all cases—which promotes confidence in the ability to satisfactorily reproduce these nonproprietary UHPC mixes with slight variations in local materials (including without using UFFA), mixing equipment, and experience level of the technicians/operators. Furthermore, the majority of M18 and M19 mixes using conventional Class F fly ash relative to the sieved Class F fly ash showed no less than a 6% reduction in compressive strength, with the majority of the M1U-W and M2U-W results exceeding those for the M18-W and M19-W mixes. Last, the ambient cured cube specimens achieved an average compression strength of 92% and 93% of the corresponding specimens cured in the chamber/water bath conditions at ages of 3 and 7 days, respectively. These specific results provide further confidence toward implementation of these mixes at larger scales, where providing a controlled curing environment is not feasible, and will be compared with the results of larger ambient cured cylinder samples later in this report.

Table 4. Small batch flow and cube average compressive strength results

Mix ID	Flow cm (in)	Cube Compressive Strength, f_m			
		3 Day	7 Day	14 Day	28 Day
M18-W	26.67 (10.50)	89.83 MPa (13029 psi)	114.05 MPa (16542 psi)	135.00 MPa (19580 psi)	147.29 MPa (21363 psi)
M18U-W	26.03 (10.25)	87.47 MPa (12686 psi)	118.03 MPa (17119 psi)	114.18 MPa (16560 psi)	141.40 MPa (20508 psi)
M18-W/M18U-W	n/a	1.03	0.97	1.18	1.04
M18-O	n/a	76.93 MPa (11158 psi)	90.34 MPa (13103 psi)	104.67 MPa (15181 psi)	108.42 MPa (15725 psi)
M18-W/M18-O	n/a	1.17	1.26	1.29	1.36
M18U-W/M18-O	n/a	1.14	1.31	1.09	1.30
M19-W	25.40 (10.00)	82.53 MPa (11970 psi)	114.18 MPa (16560 psi)	131.28 MPa (19041 psi)	142.15 MPa (20617 psi)
M19U-W	27.94 (11.00)	87.53 MPa (12695 psi)	112.64 MPa (16337 psi)	130.94 MPa (18991 psi)	141.98 MPa (20592 psi)
M19-W/M19U-W	n/a	0.94	1.01	1.00	1.00
M19-O	n/a	68.56 MPa (9944 psi)	76.38 MPa (11078 psi)	91.27 MPa (13238 psi)	107.35 MPa (15570 psi)
M19-W/M19-O	n/a	1.20	1.49	1.44	1.32
M19U-W/M19-O	n/a	1.28	1.47	1.43	1.32
M18-A	26.67 (10.5)	82.00 MPa (11893 psi)	106.22 MPa (15406 psi)	n.d.	n.d.
M18-A/M18-W	n/a	0.92	0.93	n/a	n/a

SCALABILITY OF THE OPTIMUM UHPC MIXES

Following the previously examined efforts to demonstrate satisfactory repeatability of the underlying optimum UHPC binder formulations, the next step toward facilitating adoption of the novel mix designs in realistic construction applications is to showcase the scalability of the technology. More

specifically, the scaling up efforts within the scope of this study include increasing the batch quantity using a significantly larger laboratory-scale concrete mixer, assessing the effect of longer batching times (since larger volumes of mix ingredients must be sequentially introduced to mixer), observing the effects of varying mixer shearing action on larger batch quantities, evaluating the implications for turnaround time so another similar UHPC batch can be produced in a reasonable time frame following a previous one, and mitigating premature setting on the exposed surface of a UHPC member if more than one batch is needed to fabricate a large structural member. The following section will examine select and noteworthy qualitative phenomena associated with these objectives, followed by a more quantitative-focused discussion of concrete mixing logistics and concrete performance.

QUALITATIVE OBSERVATIONS OF OPTIMUM UHPC PHENOMENA

Mitigating Clumping of Steel Fibers

Steel fibers are often a key component of UHPC mixes to enhance tensile ductility after crack initiation and to prolong substantial crack localization in a structural member. This ductility is generally a function of the fiber dosage with respect to the other mix constituents and, thus, is often specified in terms of a percentage of the mix volume or mass of other mix ingredients. As the total quantity of fibers increases with the batch size, the likelihood of fibers clumping together during dispersal in the mixer or during the subsequent mixing action also increases. Therefore, the larger batch mixing procedure outlined later in this report was developed to minimize fiber clumping/balling and promote an even distribution of fibers through the concrete mix volume. Before fibers were added to the mixer in this study, the mix needed to reach an appropriate UHPC consistency, demonstrated by performing a flow test in accordance with ASTM C1856 (2017) and achieving a minimum flow of 20.3 cm (8 in.). Once satisfactory flow was confirmed, fibers were then added using several strategies aimed at mitigating clumping or balling of the fibers. These strategies include pre-sieving fibers before batching to remove any clumps or balls that may have formed during shipping/handling, sieving fibers directly into the mixer, reducing the mixer speed during the addition of fibers, and optimizing the mixing time between the final addition of fibers and discharge of the optimum UHPC from the mixer. After performing micro-tests for each strategy, an approach with the combination thereof was adopted as part of the larger-scale batching sequence, as will be shown later in this report.

Primed Concrete Mixer

Because realistic concrete production usually requires a rapid turnaround time prior to introducing the ingredients for the following batch, the effect of utilizing a primed or “buttered” concrete mixer was also evaluated. While leaving the mixer primed/buttered in between batches will reduce turnaround time (which can be critical for UHPC mixes that often have relatively faster set times or are prone to the formation of skins on the exposed concrete surface, as will be discussed in the next subsection) by not having to thoroughly clean or stop the mixer, concrete that sets on the mixing barrel or paddles may result in more difficult long-term cleaning of the mixer or damage if not assessed and managed properly. Therefore, the researchers monitored the conditions of the mixer’s interior throughout the batching process, often doing three or more batches in sequence to fully

observe the buttered effect. Additional batches after the first often required less HRWR, and hardened concrete properties between the first and second batches showed no significant differences. The researchers ultimately concluded that the mixes presented in this report generally did not cause any problems with regards to keeping the mixer primed; however, their general recommendation is to execute trials to monitor this specific phenomenon as each mixer and mix design are different—as well as the number of mix cycles a given mixer performs within a given time frame.

Skin Formation During Optimum UHPC Mix Setting

The last noteworthy qualitative phenomenon examined herein is a premature skin that can form on the exposed surface of a UHPC specimen or member if proper precautions are not employed. This aspect, also known as "elephant skin" due to its similar resemblance, can form as a crust of dehydrated concrete as the concrete rapidly dries and prematurely sets. Per ASTM C1856 (2017), this occurrence can be regulated by either finishing the surface or placing a cover on the exposed surface of the specimen/member within approximately 1 minute after a fresh concrete placement event. This effect is increasingly important for larger UHPC concrete pours that may require more than one batch to fill a given mold such as for a structural member. If the skin forms between concrete placements, it could result in a discontinuity, which if severe enough, may impact the assumption of strain compatibility through a cross-section for the purposes of structural concrete design or increase the likelihood of a premature structural failure, such as loss of development of a reinforcing bar embedded in a region where the skin is present. The researchers found that placing a large plastic sheet, ideally directly on the concrete surface or alternatively as a tent over the formwork, was an effective strategy to minimize premature skin formation. Curing an entire member in a regulated moisture/humidity environment is also likely an effective strategy to reduce moisture loss in the concrete, but the researchers did not have access to such equipment on a large scale for this study and realize that achieving such an environment in a realistic application might not be feasible.

Larger-Scale Nonproprietary UHPC Production

After demonstrating the repeatability of the novel nonproprietary UHPC formulations in the small benchtop mixer, the next phase of experimental research focused on scaling up the batch quantities to several cubic feet in a mixer that emulates those commonly found in ready-mix or precast production. More specifically, a planetary concrete mixer with a maximum concrete yield of approximately 4.5 cubic feet (for conventional concretes) was used in this scaling effort, compared with the recommended maximum filling capacity of approximately 0.5 cubic feet for the benchtop mixer described in a previous section of this report. Due to the viscosity of the nonproprietary UHPC in comparison to conventional concretes, the maximum mix volume was capped at approximately 2.5 cubic feet to account for the additional mixing power required to produce the proper shearing action during mixing. The particular larger-scale laboratory mixer used in this study is equipped with a variable frequency drive to control the main and planetary rotor speeds, ranging between 0–26 rpm and 0–64 rpm, respectively, where the upper limits coincide with the throttle set at 100%. Table 5 shows the updated M1 mix design variants to reflect the larger batch quantity, and the updated batching sequence is shown in the flowchart in Figure 68. Table 6 shows the gradation results from the sieve analysis performed on the fine aggregate (i.e., sand) used in this study; the resulting

fineness modulus was 2.73 and the specific gravity was 2.66 on average. Please recall that these metrics will change slightly between different material sources and therefore should be evaluated before commencing concrete mixing efforts. Noteworthy adjustments relative to the procedure for the smaller benchtop mixer (see Figure 67) include adjustments to mixer speed to ensure a sustained level of high shearing action for the duration of mixing and reducing the speed following the addition of steel fibers. The set retarder admixture was also strategically added to help mitigate the development of the aforementioned "elephant skin" on the surface of exposed concrete during specimen preparation/fabrication. A viscosity modifying admixture (VMA) was also added for the larger batches to help mitigate segregation of fine aggregates and steel fibers given the relatively higher mixing shear needed to produce the larger batch quantities. Table 7 shows the results of flow tests with and without fibers for the larger batch mixes provided in Table 5. The results show that achieving desirable workability (a slump flow in excess of 20.3 cm [8 in.] prior to the addition of fibers in this case) is feasible at larger scales with careful adjustment of HRWR dosage. Furthermore, the addition of 2% by volume of steel fibers for the M18-2 mixes resulted in slump flow losses of 21.3% and 27.7% for batches M18-2A and M18-2B, respectively. Please note that M18-2A and M18-2B have the same mix design and were duplicate batches for the purposes of gathering additional experimental test data across multiple batches. The researchers found the residual workability with the fibers to still be sufficient for preparation of mechanical test specimens (see the following sections of this report) and fabricating structural members, the latter of which will be discussed in a future publication by several of the authors of this report.

Table 5. Larger batch UHPC mix designs

Mix ID	Type IL Cement	Fly Ash (Class F)	Slag	SF	Fine Agg.	Water	HRWR	VMA	RA	Steel Fibers
	kg/m³ (lbm/ft³)						(mL/cwt)			kg/m³ (lbm/ft³)
M18-0 (0% F)	738 (1244)	116 (196)	503 (848)	54 (91)	1411 (2378)	254 (428)	887 (1495)	0	104 (175)	0
M18-2 (2% F)	738 (1244)	116 (196)	503 (848)	54 (91)	1411 (2378)	254 (428)	444 (748)	118 (199)	0	157 (265)

Note: F = fibers, SF = silica fume, RA = retarder liquid admixture.

Table 6. Gradation results for fine aggregate used in this study

Sieve Size	% Passing
4	100.00
8	90.91
16	72.73
30	54.55
50	9.09
100	0.00
Pan	0.00

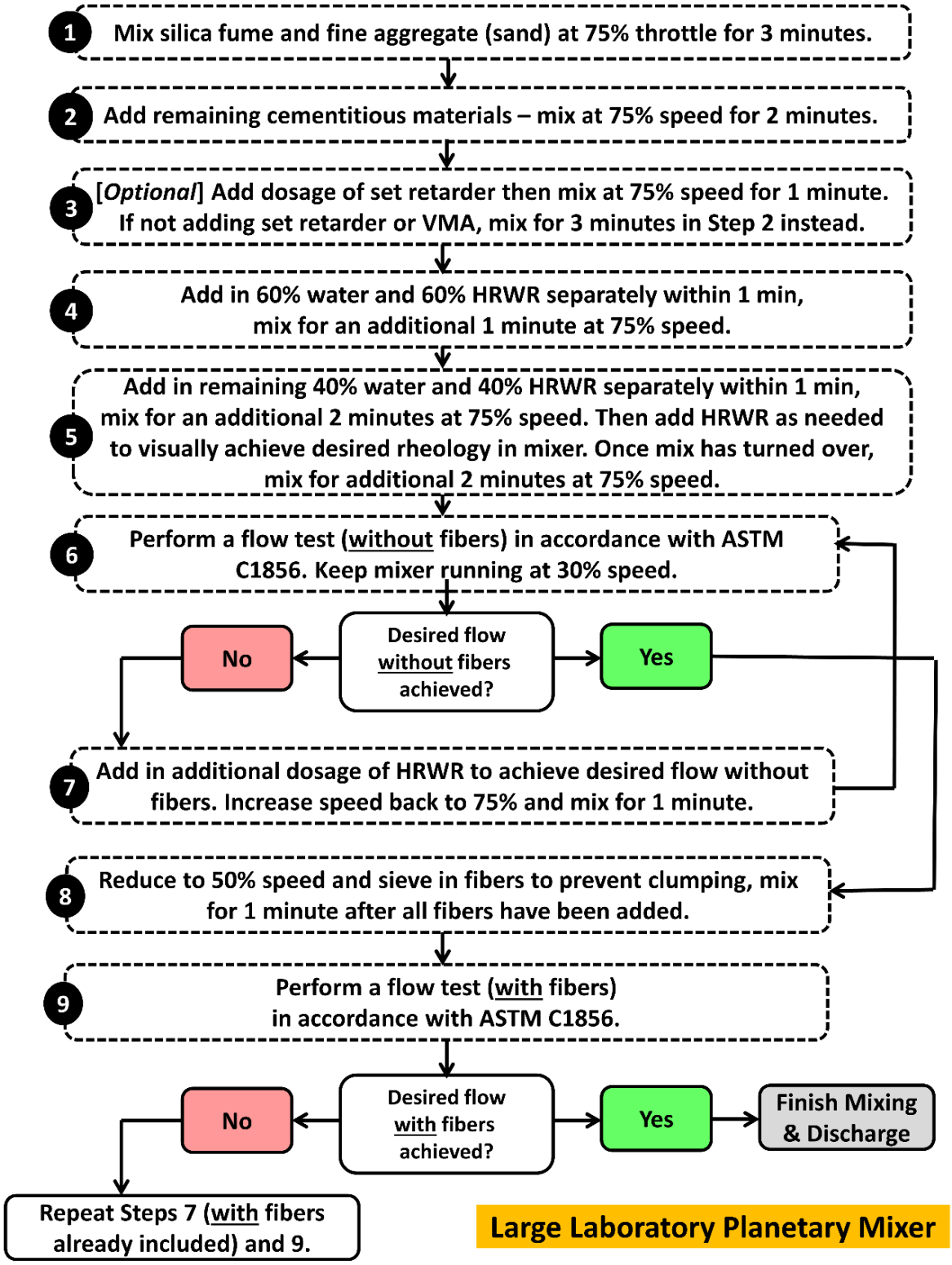

Figure 68. Illustration. Batching sequence for large laboratory planetary mixer.

Table 7. Average fresh properties of larger UHPC batches

Batch ID	Batch Size	Slump Flow w/o Fibers	Slump Flow w/ Fibers	% Slump Flow Loss w/ Fibers
	L (ft^3)	cm (in.)	cm (in.)	%
M18-0	34.69 (1.23)	28.58 (11.25)	n/a	n/a
M18-2A	64.4 (2.27)	24.87 (9.79)	19.58 (7.71)	21.3%
M18-2B	65.0 (2.30)	27.94 (11.00)	20.21 (7.96)	27.7%

Mechanical Testing of Larger Batch Specimens

In addition to demonstrating the scalability of the optimum UHPC mixes, another motivation for producing larger quantities of these materials is to prepare several types of specimens for mechanical testing of hardened concrete performance beyond just cubes. The following sections will provide more specific information on the types of mechanical tests performed in this study and the corresponding results.

Compressive Strength

Based on the provisions of ASTM C1856-17 (2017), 75 mm × 150 mm (3 in. × 6 in.) cylinders were prepared to evaluate compressive strength at an age of 7 days. The age of 7 days was chosen, rather than a more conventional age of 28 days, in the event that future applications for the nonproprietary UHPC formulations would necessitate more rapid strength development and due to limitations on how much concrete could be produced from a single batch in the laboratory planetary mixer. Please note that mechanical test specimens (including cylinders and tension prisms—the latter will be discussed later in this report) were subjected to ambient conditions in the laboratory to facilitate extrapolation of mechanical test results to estimate the behavior of UHPC structural members fabricated in a precast facility or in situ on a jobsite. Table 8 highlights the average compressive strengths (minimum of three tests performed for each mix) of the 75 × 150 cylinders for larger batches with (M18-0) and without fibers (M18-2 series), which do not show a discernible difference relative to each other in most cases. Additionally, no discernible difference in compressive strength between the cylinder specimens from batch M1-0 and the corresponding strength of the cubes when batched in the smaller benchtop mixer was present, further providing confidence of the scalability of these mix designs.

Table 8. Average 7-day compressive strength test results

Batch ID	f_{cm} [3×6 cyl.] MPa (psi)	f_m [2×2 cube] MPa* (psi)	f_{cm}/f_m
M18-0	106.25 (15410)	106.22 (15406)	1.00
M18-2A	107.58 (15603)		
M18-2B	108.55 (15744)		

*Note: 7-day cube compressive strength from test results of M1-A (see Table 4).

Modulus of Elasticity in Compression

ASTM C1856-17 (2017) states that the modulus of elasticity in compression (MOE-C) specimens be 75 mm × 150 mm (3 in. × 6 in.) cylinders. However, the research team chose to slightly modify the MOE-C test program in this study using 100 mm × 200 mm (4 in. × 8 in.) cylinders. The researchers made this change because access to the instrumentation needed to perform this test in accordance with ASTM C469-22 (2014) is generally more common for larger cylinders, as they are generally the standard for testing conventional concrete specimens. Table 9 shows the average results of the MOE-C tests (minimum of four tests performed for each mix) and provides comparisons to equation 1.4.2.3-1 as specified in the guidelines for structural design of UHPC issued by the Federal Highway Administration (Graybeal & El-Helou, 2023). The results generally compare well with this particular design equation, as the average MOE-C test result for each batch was within 90% of the design value calculated as a function of the corresponding compressive strength. Note that the FHWA equation overpredicted the test results in these cases, which is unconservative for the purposes of ensuring a safe structural design. This conclusion may be the result of variations in the fine aggregate type used in this study, relative to proprietary or other similar mixes used by FHWA when developing the provision. Therefore, the authors recommend that laboratory MOE-C testing be performed on newly developed nonproprietary UHPC mix designs whenever possible to facilitate more accurate and safe design of nonproprietary UHPC structures, especially in applications where deflections or other limit states driven by the elastic stiffness (and thus a function of the MOE-C) are of particular importance.

Table 9. Average 7-day modulus of elasticity (compression) test results

Batch ID	f_{cm} [4 × 8 cyl.]	Avg. MoE-C	Avg. MoE-C /sqrt(f_{cm})	FHWA Eq.	Avg. MoE-C/ FHWA Eq.
	MPa (psi)	GPa (ksi)	–	GPa (ksi)	–
M18-0	106.01 (15375)	40.05 (5809)	3890	42.45 (6157)	0.943
M18-2A	107.20 (15548)	38.50 (5584)	3718	42.61 (6180)	0.903
M18-2B	109.92 (15943)	38.84 (5633)	3705	42.96 (6231)	0.904

Tensile Performance

Evaluating the tensile behavior of UHPC formulations is more imperative relative to conventional concrete mixes because it generally exhibits relatively higher peak tensile strength coupled with enhanced tensile ductility with the use of steel fibers. A standard method of assessing the tension performance of UHPC test specimens was published by AASHTO (2022) and will be followed in this study. A minimum of 10 rectangular UHPC prisms measuring 5.08 cm (2 in.) × 5.08 cm (2 in.) × 43.18 cm (17 in.) were fabricated with each of the M1-2 batches (i.e., the mix designs containing the 2% fiber dosage) and allowed to cure under ambient laboratory conditions until the desired testing age of 7 days was reached. The mold for the prisms was also capped with an acrylic sheet that served to prevent the development of “elephant skin” on the top (i.e., exposed) surface of the specimens. Hardened prisms were then tested for 7-day tensile performance using a universal testing machine equipped with a manual, flat grip apparatus as shown in Figure 69-A. This type of grip setup was recommended in Section X2.2.2 of the AASHTO T 397-22 standard (2022) for laboratories that do not have the capabilities to test 5.08 cm (2 in.) wide specimens using a machine with hydraulic grips. Aluminum transfer plates with a thickness of 3.175 mm (0.125 in.) and plan dimensions in accordance with Section 7.4 of the AASHTO T 397-22 standard (2022) were glued to opposite sides of the prism that were to contact the surface of the grips at either end using a quick-set epoxy rated with a tensile strength of 26 MPa (3770 psi) with a set time of 15 minutes and a fully cure time of 30 minutes. The plates were clamped while the epoxy set and cured to ensure full contact with the surface of the prism. After the epoxy was fully cured, the prism was installed in the grip apparatus and the row of two bolts closest to the center of the prism on both grip plates (i.e., top and bottom plates, as shown in Figure 69-A) were tightened to 40.68 N-m (30 lbf-ft) using a manual torque wrench. During the test, force was applied to the specimen to produce a constant stress rate of 6.90 MPa/min (1000 psi/min) in accordance with Section 8.7 of the AASHTO T 397-22 standard (2022). The testing program was designed to allow the post-peak behavior to be captured, which in turn will facilitate assessments of tensile ductility. Force was measured using a pressure transducer installed in the universal testing machine, and strain was calculated using displacement acquired via a transducer mounted to the prism, as shown in Figure 69-A. A photograph showing an example of a broken specimen following satisfactory completion of the testing procedure is shown in Figure 69-B.

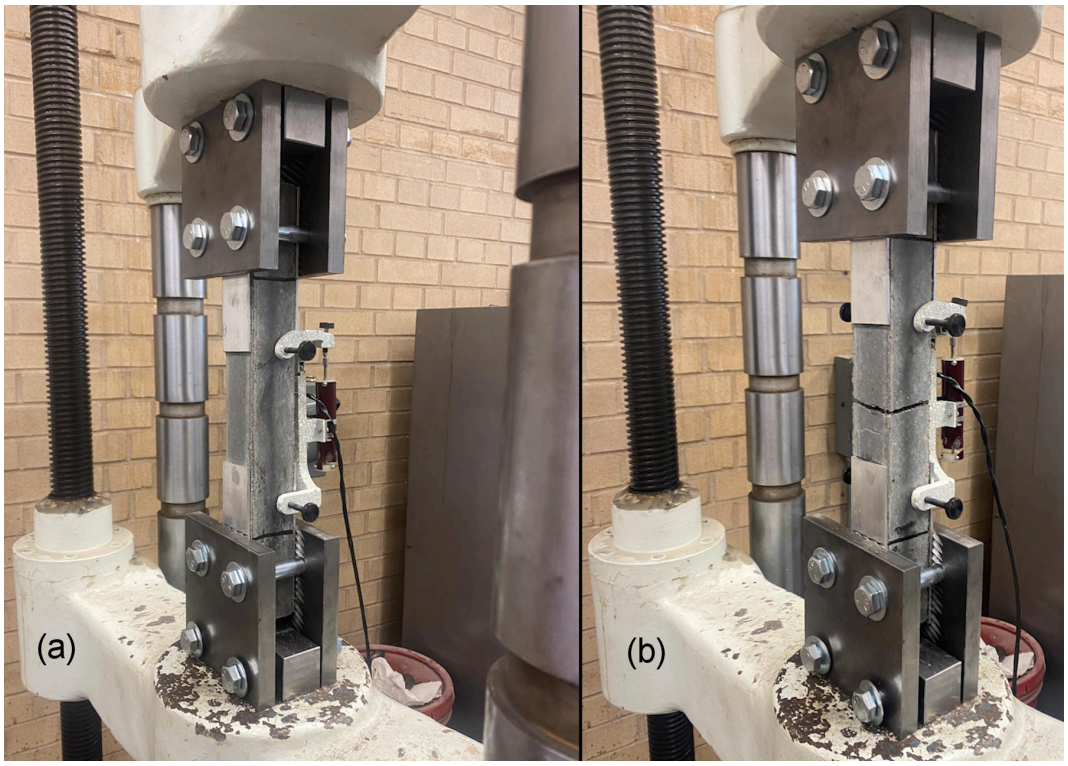

Figure 69. Photo. Manual grip apparatus for direct tension testing: (a) prior to a test and (b) following completion of a test.

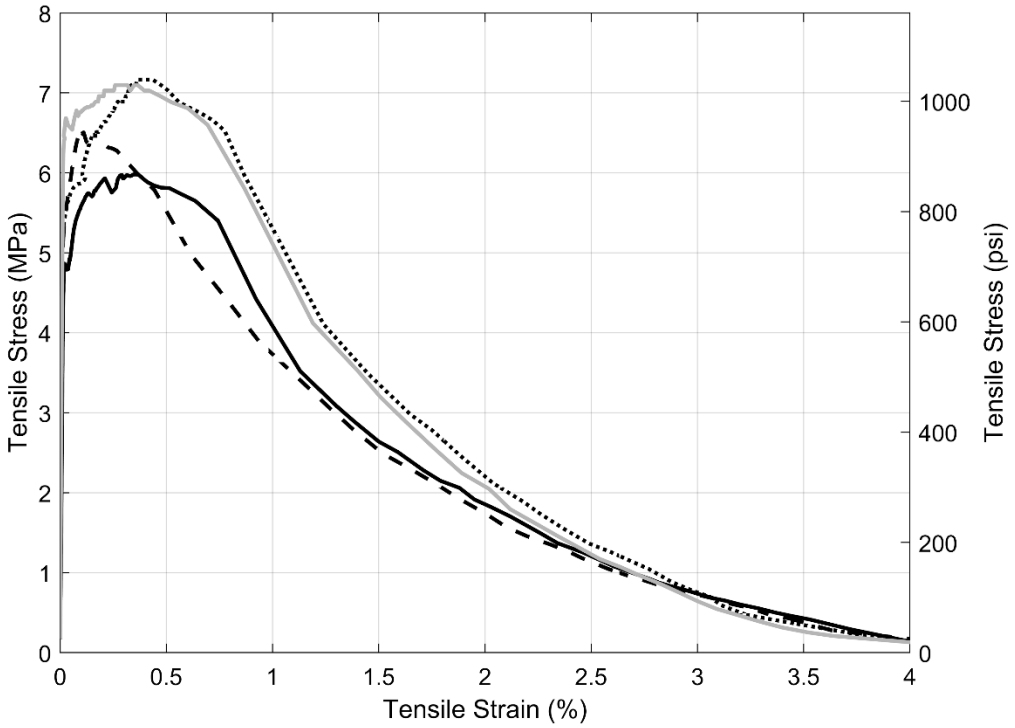

Figure 70. Graph. Plot of tensile stress-strain data acquired from M1-2 specimens.

Table 10 highlights the critical tensile performance parameters extracted from the tension stress versus strain relationships plotted in Figure 70. The procedure to determine the effective cracking strength, $f_{t,cr}$, approximately an equivalent metric to yield strength in metals, was based on the provisions of Section 10.3.5 of the AASHTO T 397-22 standard (2022). This procedure specifies using a 0.02% offset line parallel to the elastic response region with a slope equal to the modulus of elasticity in tension, MOE-T (determined using a best-fit regression line with the elastic portion of the data) and starting at the origin of the data plot. Comparisons between the moduli of elasticity determined using the protocols for compression and tension are also shown in Table 10, and the results are within approximately 22% of each other for both batches, with the tension prisms exhibiting a greater average modulus of elasticity in each case. Further research is likely needed to more closely examine this observation and determine sources of error that influenced this outcome. The corresponding stress and strain at the location where the offset line intersects the experimental data are then recorded as the effective cracking strength, $f_{t,cr}$, and the strain at effective cracking strength, $\varepsilon_{t,cr}$, respectively. Calculation of the crack localization strength, $f_{t,loc}$, and corresponding strain, $\varepsilon_{t,loc}$, relies on a visual interpretation of the test data to determine the point after which the strength continuously decreases thereafter. These two points can then be used to construct a simplified backbone curve to be used to characterize the tension behavior for the purposes of UHPC structural design, as outlined in Chapter B3 of the FHWA report on UHPC structural design (Graybeal & El-Helou, 2023). The results from this study show good agreement across multiple batching events and, thus, promote further confidence in the repeatability of the novel nonproprietary UHPC mixes developed as part of this study. The implications of the mechanical performance assessed herein on the structural design and behavior of nonproprietary UHPC beams will be discussed later in this report.

Table 10. Average direct tension test results

Batch ID	MOE-T	MOE-T/ MOE-C	$f_{t,cr}$	$\varepsilon_{t,cr}$	$f_{t,loc}$	$\varepsilon_{t,loc}$
	GPa (ksi)	–	MPa (psi)	%	MPa (psi)	%
M18-2A	47.00 (6817)	1.221	6.63 (962)	0.034	6.60 (957)	0.694
M18-2B	46.67 (6869)	1.202	5.33 (773)	0.032	6.12 (888)	0.570

EXPERIMENTAL TESTING OF THE OPTIMUM UHPC BEAMS

Design of Experimental Program

To assess a structural application for the novel UHPC formulations, an experimental testing program was designed with the following objectives: (1) further demonstrate the scalability of the mixes to facilitate ease of implementation with successively larger concrete placements, (2) evaluate flexure- and shear-driven failure modes and the influence of transverse reinforcement on the controlling limit state, and (3) determine if UHPC structural design guidelines published by FHWA (Graybeal & El-Helou, 2023) are reasonable for structural members fabricated using a nonproprietary UHPC mix design. In order to best highlight the effect of the steel fiber content and transverse reinforcement,

the rectangular cross-section, including the longitudinal reinforcement configuration, as shown in Figure 71, was held constant across all beam tests discussed in this report. Each beam was fabricated with an overall length of 2.95 m (116 in.) and tested with a simply supported span length of 2.74 m (108 in.). The member was loaded in three-point bending using a large-format universal testing machine—a photo showing the complete test setup is shown in Figure 72. During the test, the crosshead, to which a steel cylinder is mounted to simulate a point load, is locked while the bottom platform, on which the two supports rest, is raised using an automatic displacement-controlled profile. Two distinct displacement rates (note that for the purposes of test control the reference displacement was the travel of the universal testing machine platform) were specified for two regions on the load versus displacement relationship of the beam. First, a displacement rate of 2.54 mm/min (0.1 in./min) was used from the onset of the test to the approximate yield point (i.e., the point where the load begins to plateau in this case) to ensure proper capturing of the elastic response, including initial development of cracking. For the remainder of the test, the displacement rate was set to 6.35 mm/min (0.25 in./min) if no significant diagonal tension cracking had formed, and the flexural crack localization mechanism became more prevalent to manifest (in the case of a flexural failure). If a significant shear failure appeared imminent, the displacement rate was not increased beyond its original value. Force was recorded using a 222.4 kN (50 kip) pancake load cell bolted directly above the center point roller and midspan deflection was acquired using a string potentiometer secured to a rigid assembly that was mounted directly to the two support pedestals which ensured that any small deflections of the steel beams underneath did not influence the actual deflection of the optimum UHPC beams.

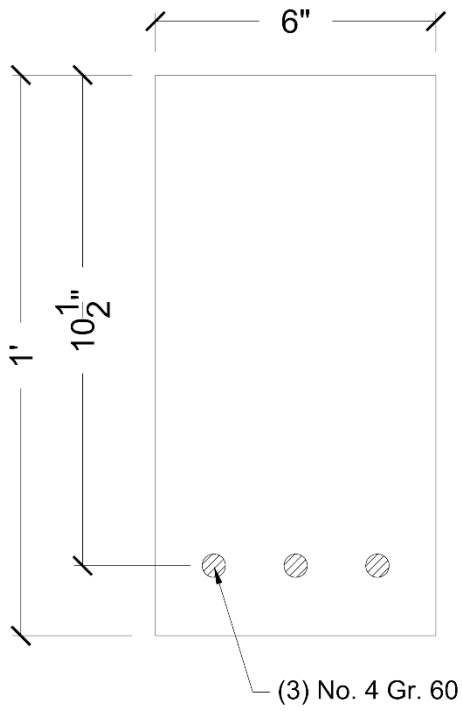

Figure 71. Illustration. Typical beam cross-section with longitudinal reinforcement layout.

Figure 72. Photo. Beam test setup.

A total of three UHPC beams, made of the optimum mixes, were tested in this study, one with 0% steel fibers and without transverse reinforcement (TR), a second with 2% steel fibers (by volume) and without transverse reinforcement, and a third also with 2% steel fibers but with transverse reinforcement. A major objective for choosing these three configurations was to determine the significance of the transverse reinforcement as the steel fiber dosage was increased. More specifically, would the additional tensile ductility provided by the steel fibers prevent further development of diagonal tension cracks and thus mitigate a shear-controlled failure mechanism? Two additional "control" beams were fabricated using a conventional, high-strength self-consolidating concrete mix to serve as approximate comparisons to assess the performance of the novel UHPC members. Table 11 provides additional details for the complete beam test matrix. Mix designs for each member are in reference to Table 5 for the optimum UHPC mixes and Table 12 for the control mixes. Each beam was fabricated in a structural testing laboratory setting using multiple concrete batches, as the capacity of the laboratory-scale planetary concrete mixer used in this study was not large enough to place the entire member at one time. The need to use multiple successive batches is one of the main motivators for closely examining the primed concrete mixer and "elephant skin" phenomena as discussed previously in this report. Table 13 summarizes results of mechanical testing on specimens prepared during fabrication of the beams.

Table 11. Beam test matrix

Beam ID	Beam Description	Mix Design	Unit Batch QTY L (ft^3)	No. of Batches Reqd.
CNTR-0	Control without TR – 0% fibers	CM-0 (See Table 12)	113.8 (4.02)	2
CYTR-0	Control with TR – 0% fibers	CM-0 (See Table 12)	113.8 (4.02)	2
NNTR-0	NP-UHPC without TR – 0% fibers	M18-0	63.4 (2.24)	3
NNTR-2	NP-UHPC without TR – 2% fibers	M18-2	65.1 (2.30)	3
NYTR-2	NP-UHPC with TR – 2% fibers	M18-2	64.6 (2.28)	3

Note: TR = transverse reinforcement.

Table 12. Concrete mix design for control beams

Mix ID	Type IL Cement	Fly Ash (Class F)	Slag	Silica Fume	No. 8 Stone	Sand	Water	HRWR	Retarder
	kg/m^3 (lbm/yd^3)							mL/cwt (fl. oz/cwt)	
CM-0 (0% fibers)	248.2 (418.3)	39.2 (66.0)	169.3 (285.4)	18.0 (30.3)	810.8 (1366.6)	918.4 (1548.0)	166.7 (280.9)	325.6 (11.01)	103.5 (3.50)

Table 13. Average mechanical testing results corresponding to beam tests

Beam ID	f_{cm} MPa (psi)	MOE-C GPa (ksi)
CNTR-0$^+$	58.3 (8465)	34.6 (5025)
CYTR-0$^+$	62.8 (9115)	36.1 (5247)
NNTR-0	110.8 (16083)	42.8 (6213)
NNTR-2*	108.6 (15755)	38.8 (5637)
NYTR-2^	107.6 (15614)	38.5 (5587)

Notes: *Tension results for beam NNTR-2 corresponds to Batch ID M1-2B (see Table 7), ^Tension results for beam NYTR-2 corresponds to Batch ID M1-2A (see Table 7), $^+$4 × 8 cylinders were used for compressive strength testing for control beams (3 × 6 cylinders were used for nonproprietary UHPC beams and 4 × 8 cylinders were used for MOE-C in all cases).

SUMMARY OF BEAM TEST RESULTS

When comparing the structural performance of the UHPC beams of the optimum mixes to those fabricated with a conventional self-consolidating high-strength concrete, there is a clear improvement to the overall capacity of the section, as expected (see Figure 73 and Table 14). Interestingly, the addition of transverse reinforcement largely did not impact the performance of the UHPC members; however, there is a marked increase in the overall load capacity with the introduction of steel fibers as the member failed in flexure. Additionally, without steel fibers nor

transverse reinforcement, beam NNTR-0 failed in shear (see Figure 74), whereas the NYTR-2 and NNTR-2 beams with 2% fibers, regardless of the presence of transverse reinforcement, failed in flexure (see Figure 75 and Figure 76, respectively). The addition of steel fibers improved the ductility response and failure mode of the UHPC beams, which is supported by the literature (Luo et al., 2024). The literature also found that fiber content improves the shear capacity to drive flexure failure where a conventional concrete section would fail in shear (Bermudez & Hung, 2019; Frank et al., 2024; Kodur et al., 2018), a phenomenon that was also confirmed in this study. While stirrups negatively impacted the ultimate load of the conventional concrete sections, transverse reinforcement allowed for the controlled failure of the section rather than the brittle shear failure observed for the conventional section without transverse reinforcement. It was anticipated that the UHPC section would exhibit a similar effect; however, the response of beams NNTR-2 and NYTR-2 were very similar. Transverse reinforcement was observed to improve the ultimate capacity by approximately 4.45 kN (1000 lbf) and marginally extend the ductility by 1.27 mm (0.05 in.) with beam NYTR-2, relative to beam NNTR-2. Without steel fibers, beam NNTR-0 behaved similarly to beam CNTR-0 made with the conventional concrete, affirming that most of UHPC improvements for the purposes of this study were the result of the addition of steel fibers. Fibers work to strengthen the section and improve resistance to crack development. Without fiber reinforcement, the majority of the tensile capacity comes from additional reinforcement (most commonly steel). Furthermore, in UHPC without any fiber reinforcement, there is a smaller range of aggregate gradation, limiting the extent to which aggregate interlock is able to resist loading.

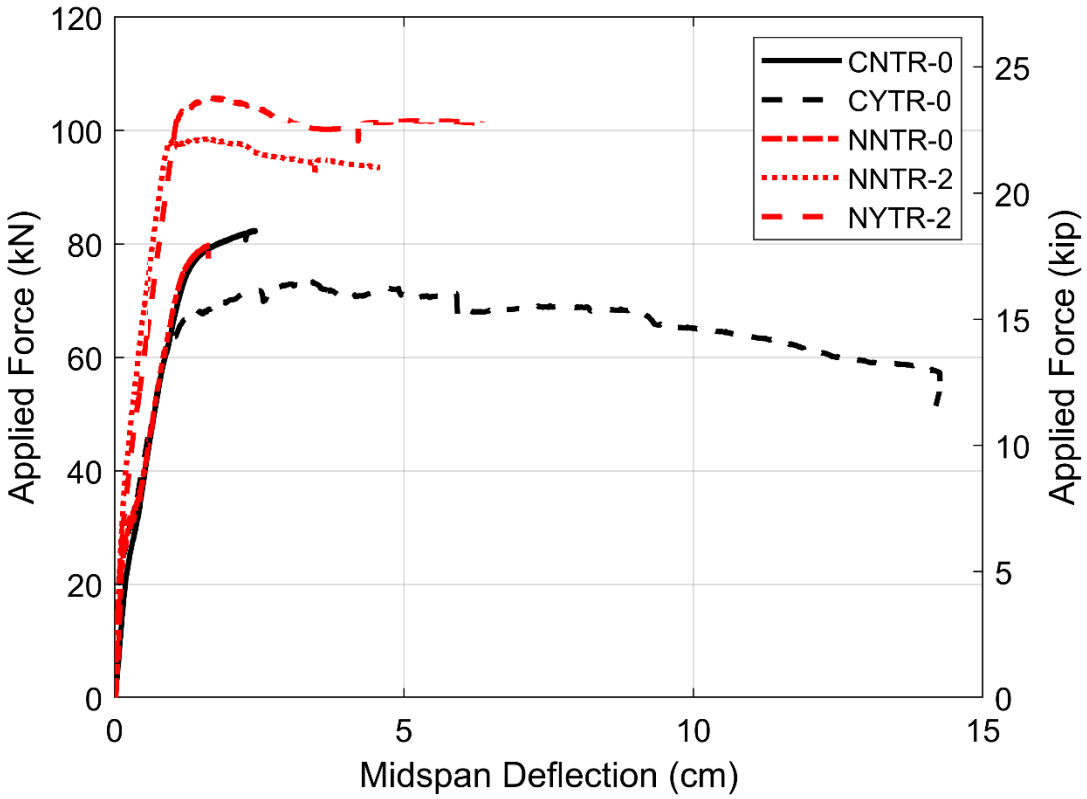

Figure 73. Photo. Plots of load versus displacement response for the beams.

Table 14. Summary of beam test results

Beam ID	Deflection at Peak Load mm (in.)	Peak Load kN (kip)	Failure Mode
CNTR-0	24.00 (0.945)	82.38 (18.52)	Shear
CYTR-0	34.11 (1.343)	73.31 (16.48)	Flexure
NNTR-0	16.15 (0.636)	79.76 (17.93)	Shear
NNTR-2	16.05 (0.632)	98.66 (22.18)	Flexure
NYTR-2	17.15 (0.675)	105.78 (23.78)	Flexure

Figure 74. Photo. Shear failure mode of beam NNTR-0.

Figure 75. Photo. Flexural failure mode of beam NYTR-2.

Figure 76. Photo. Flexural failure mode of beam NNTR-2.

CHAPTER 12: CONCLUSION AND FUTURE RESEARCH NEEDS

CONCLUSIONS

This study used a modified Anderson and Andreasen (MAA) model as the basis to design a range of 19 nonproprietary multi-binder UHPC mixes (M1-19) using locally available materials in Illinois. Based on the rheological, mechanical, and durability property assessment of the UHPC mixes, the major conclusions inferred from the study are described below:

- The packing model was used to design 19 multi-binder UHPC systems (cement, slag, ultra-fine fly ash, and silica fume) with a wide variation in the formulated packing factor (31.6 to 46.7). The packing factors from the MAA model show a strong correlation to the packing coefficient obtained from discrete packing models, such as the compressible packing model (CPM).

- The study shows the potential of effectively packed multi-binder UHPC systems to have shorter turnover time (7–10 minutes for the optimum mixes, M18 and M19) at a much lower HRWR requirement (<1 % by wt.% of binders). The designed mix composition exhibited a wide range of flow variation (7.75–12.5 inches) showing the role of binder selection and composition on rheological properties. In particular, the flow/HRWR ratio was determined as a more effective parameter to characterize the binder composition and mix parameters on rheological parameters. A decrease in packing factor (i.e., improved packing) generally led to a higher flow/HRWR ratio sensitivity with higher workability.

- The newly defined “packing factor” exhibited a significant impact on the compressive strength of the UHPC mixes, mostly at an earlier age. In general, multi-binder UHPC systems showed potential of achieving higher early strength (> 10 ksi @ 3 days). Particularly, the variation in PF value from 31.6 to 46.7 exhibited 3-day strength variation from 7.1–12.0 ksi. Multi-binder UHPC system with higher slag content (35%–50% by volume, expressed by Zone C) exhibited higher early-age strength development (9.2–12.0 ksi @ 3 days) compared to other mixes. This observation has also been translated at strength values over 17.4 ksi (120 MPa) at 28 days for optimum mixes, M18 and M19, without fibers. The same systems also exhibited highly packed microstructure with open porosity of less than 2% at 28 days of hydration.

- Fiber content of 2% by volume of the binders is suggested as the optimum content for maximized UHPC performance. The optimum mixes (M18 and M19) exhibited compressive strength of more than 21.7 ksi (150 MPa) at 28 days of hydration with the inclusion of steel fibers. Meanwhile, this study also emphasizes that an optimum balance of both physical (packing) and chemical (hydration) phenomena is the key to maximizing long-term UHPC performance.

- This study also highlights the combined role of packing factor and open porosity in governing drying shrinkage at both early and long-term ages of the samples. The optimum

mixes (M18 and M19) exhibited lower shrinkage (−725 με and −702με, respectively) than the established limit of −800 με at 91 days of hydration.

- Optimizing particle packing in a multi-binder UHPC system unveiled the potential of reducing the cement content to 47% (Type IL by volume) in the optimum mixes with a significantly lower cost structure of $426/m^3 ($327.7/yd^3) and $377/m^3 ($290/yd^3) for M18 and M19, respectively, without fibers. This shows promise to a low-cost and sustainable UHPC system with adequate performance, which can be implemented for wider adoption and enhanced performance.

FUTURE RESEARCH NEEDS

In this study, a comprehensive evaluation and characterization was performed on 19 multi-binder UHPC mixes to select the optimum two mixes (M18 and M19). One of the best features of the mixes is that both constitute local materials and require very low HRWR requirements with a low turnover time of 7–10 minutes, which shows immense potential for future studies. Hence, in consideration of the potential variation in the discrepancy between lab and field conditions, it is crucial to test the feasibility of scaling it up for a large sample size and wide-scale field implementation. In this regard, this study highlights the following promising research aspects to further optimize and implement the IDOT UHPC mixes (Figure 77).

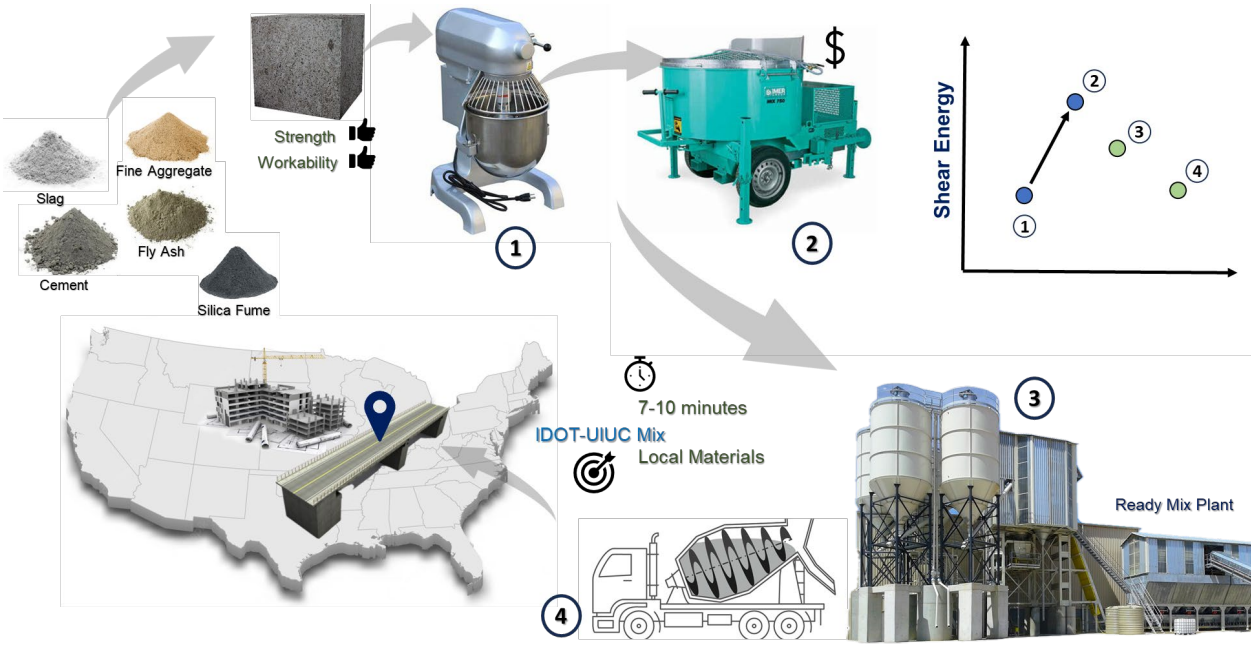

Figure 77. Photo. Future prospects of the optimum UHPC mixes (M18 and M19) developed in this study.

MIXING EQUIPMENT

Due to a higher binder content, UHPC mixes usually require higher shear energy for mixing and attaining the turnover. Hence, while scaling up the optimum mixes (M18 and M19), it is highly important to assess the turnover time and mixing regime for different volumes and shear conditions,

including high-shear mixer (Figure 77, marked as 2) and ready-mix plant (marked as 3). Hence, in the next phase, the optimum mixes should be cast in a precaster or a ready-mix plant in Illinois to investigate the shear requirement at different scales of mix production. Having a much lower turnover time in the lab scale, M18 and M19 can be really effective in scaling up in a ready-mix facility for a wider application.

FIELD IMPLEMENTATION

Extending the optimum performance of the mixes (M18 and M19) at a lab scale, the mixes should be used for a pilot mock-up batching and casting at a field condition. Also, the performance of the mixes should be assessed in the field condition by comparing the results of the field cylinders with the lab samples.

MIX CUSTOMIZATION FOR FIELD CONDITION

The field conditions usually result in higher evaporation of water from the mixes, which results in faster slump and moisture loss. This is highly important for a high-volume casting, which requires the mix to retain workability for a certain duration for placement and finishing. Hence, in the next phase, it is key to investigate the modified HRWR dosage and a probable change in the binder composition, which can reduce the slump loss and aid in maintaining the adequate rheology. Also, the role of retarders and hydration stabilizers on UHPC performance should also be analyzed in future studies.

INCLUSION OF ALTERNATE BINDER SOURCES

It is important to take the shortage of fly ash and wide variation in fly ash composition into account, especially in designing multi-binder UHPC. This was evident in the wide variation seen in the cumulative heat of hydration generated from various quarterly fly ash samples collected from the IDOT lab (see Figure 110 in Appendix H). Hence, for future mix improvisation, the UHPC mix design should be refined based on the compositional variation of the ashes so that the hydration and overall performance of the UHPC mixes can be enhanced. Moreover, this would also open up the opportunity to use other alternate SCMs, such as reclaimed ashes and natural pozzolans, provided chemical composition has been taken into account. This would be fundamental in addressing FHWA's recent emphasis on promoting low-carbon materials in construction. Using such an approach would give the IDOT UHPC a competitive advantage to ensure durable and sustainable infrastructural development.

REFERENCES

AASHTO T 397-22. (2022). *Standard method of test for uniaxial tensile response of ultra-high performance concrete*. American Association of State and Highway Transportation Officials.

Abbas, S., Soliman, A. M., & Nehdi, M. L. (2015). Exploring mechanical and durability properties of ultra-high performance concrete incorporating various steel fiber lengths and dosages. *Construction and Building Materials*, *75*, 429–441. https://doi.org/10.1016/j.conbuildmat.2014.11.017

ACI Committee 239. (2018). *ACI PRC-239-18: Ultra-High Performance Concrete: An Emerging Technology Report*.

Aim, R. Ben, & Le Goff, P. (1968). Effet de paroi dans les empilements désordonnés de sphères et application à la porosité de mélanges binaires. *Powder Technology*, *1*(5), 281–290.

Akhnoukh, A. K., & Buckhalter, C. (2021). Ultra-high-performance concrete: Constituents, mechanical properties, applications and current challenges. *Case Studies in Construction Materials*, *15*, e00559. https://doi.org/10.1016/j.cscm.2021.e00559

Alkaysi, M., El-Tawil, S., Liu, Z., & Hansen, W. (2016). Effects of silica powder and cement type on durability of ultra high performance concrete (UHPC). *Cement and Concrete Composites*, *66*, 47–56. https://doi.org/10.1016/j.cemconcomp.2015.11.005

Arora, A., Aguayo, M., Hansen, H., Castro, C., Federspiel, E., Mobasher, B., & Neithalath, N. (2018). Microstructural packing- and rheology-based binder selection and characterization for ultra-high performance concrete (UHPC). *Cement and Concrete Research*, *103*, 179–190. https://doi.org/10.1016/j.cemconres.2017.10.013

Arora, A., Almujaddidi, A., Kianmofrad, F., Mobasher, B., & Neithalath, N. (2019). Material design of economical ultra-high performance concrete (UHPC) and evaluation of their properties. *Cement and Concrete Composites*, *104*, 103346.

ASTM C136. (2006). Standard test method for sieve analysis of fine and coarse aggregates.

ASTM C144. (2024). Standard Specification for Aggregate for Masonry Mortar.

ASTM C150. (2001). ASTM C150: Standard specification for Portland cement.

ASTM C511. (2021). Standard Specification for Mixing Rooms, Moist Cabinets, Moist Rooms, and Water Storage Tanks Used in the Testing of Hydraulic Cements and Concretes.

ASTM C596. (2023). Standard Test Method for Drying Shrinkage of Mortar Containing Hydraulic Cement.

ASTM C618. (2023). Standard Specification for Coal Fly Ash and Raw or Calcined Natural Pozzolan for Use in Concrete.

ASTM C989. (2022). Standard Specification for Slag Cement for Use in Concrete and Mortars.

ASTM C1240. (2020). Standard Specification for Silica Fume Used in Cementitious Mixtures.

ASTM C1437. (2020). Standard Test Method for Flow of Hydraulic Cement Mortar.

https://doi.org/10.1520/C1437-20

ASTM C1856. (2017). Standard Practice for Fabricating and Testing Specimens of Ultra-High Performance Concrete 1. https://doi.org/10.1520/C1856_C1856M-17

ASTM-C618-19. (n.d.). Standard Specification for Coal Fly Ash and Raw or Calcined Natural Pozzolan for Use in Concrete 1. https://doi.org/10.1520/C0618-1

Atzeni, C., Massidda, L., & Sanna, U. (1985). Comparison between rheological models for portland cement pastes. *Cement and Concrete Research*, *15*(3), 511–519. https://doi.org/10.1016/0008-8846(85)90125-5

Awoyera, P. O., Babalola, O. E., & Aluko, O. G. (2022). The use of slags in recycled aggregate concrete. In *The Structural Integrity of Recycled Aggregate Concrete Produced with Fillers and Pozzolans* (pp. 145–170). Elsevier. https://doi.org/10.1016/B978-0-12-824105-9.00009-3

Bache, H. H. (1981). *Densified cement ultra-fine particle-based materials*.

Baten, B., & Garg, N. (2024). Introducing Particle Shape Metric (PSM): A fundamental parameter that encapsulates role of aggregate shape in enhancing packing and performance. *Cement and Concrete Research*, *182*, 107558. https://doi.org/10.1016/j.cemconres.2024.107558

Bermudez, M., & Hung, C.-C. (2019). Shear behavior of ultra-high performance hybrid fiber reinforced concrete beams. *International Interactive Symposium on Ultra-High Performance Concrete*, *2*(1).

Birchall, J. D., Howard, A. J., & Kendall, K. (1981). Flexural strength and porosity of cements. *Nature*, *289*(5796), 388–390.

Brouwers, H. J. H., & Radix, H. J. (2005). Self-compacting concrete: Theoretical and experimental study. *Cement and Concrete Research*, *35*(11), 2116–2136.

Chan, Y.-W., & Chu, S.-H. (2004). Effect of silica fume on steel fiber bond characteristics in reactive powder concrete. *Cement and Concrete Research*, *34*(7), 1167–1172. https://doi.org/10.1016/j.cemconres.2003.12.023

Chen, Y., Liu, P., Sha, F., Yin, J., He, S., Li, Q., Yu, Z., & Chen, H. (2022). Study on the mechanical and rheological properties of ultra-high performance concrete. *Journal of Materials Research and Technology*, *17*, 111–124. https://doi.org/10.1016/j.jmrt.2021.12.139

Choi, M. S., Lee, J. S., Ryu, K. S., Koh, K.-T., & Kwon, S. H. (2016). Estimation of rheological properties of UHPC using mini slump test. *Construction and Building Materials*, *106*, 632–639. https://doi.org/10.1016/j.conbuildmat.2015.12.106

De Larrard, F., & Sedran, T. (1994). Optimization of ultra-high-performance concrete by the use of a packing model. *Cement and Concrete Research*, *24*(6), 997–1009.

Du, J., Meng, W., Khayat, K. H., Bao, Y., Guo, P., Lyu, Z., Abu-obeidah, A., Nassif, H., & Wang, H. (2021). New development of ultra-high-performance concrete (UHPC). Composites Part B: Engineering, 224, 109220. https://doi.org/10.1016/j.compositesb.2021.109220

Estrada, N. (2016). Effects of grain size distribution on the packing fraction and shear strength of frictionless disk packings. *Physical Review E*, *94*(6), 062903.

Ferdosian, I., & Camões, A. (2017). Eco-efficient ultra-high performance concrete development by means of response surface methodology. *Cement and Concrete Composites*, *84*, 146–156. https://doi.org/10.1016/j.cemconcomp.2017.08.019

Flatt, R. J., Roussel, N., Bessaies-Bey, H., Caneda-Martínez, L., Palacios, M., & Zunino, F. (2023). From physics to chemistry of fresh blended cements. *Cement and Concrete Research*, *172*, 107243.

Frank, T., Amaddio, P., Landes, C., Farrell, D., Decko, E., & Tri, A. (2024). Investigation of shear response due to variation of fiber volume fraction, transverse steel, and placement method on short span R/UHPC beams. *Advances in Structural Engineering*. https://doi.org/10.1177/13694332241237586

Fu, D., Xia, C., Xu, S., Zhang, C., & Jia, X. (2022). Effect of concrete composition on drying shrinkage behavior of ultra-high performance concrete. *Journal of Building Engineering*, *62*, 105333. https://doi.org/10.1016/j.jobe.2022.105333

Fuller, W. B., & Thompson, S. E. (1907). The laws of proportioning concrete. *Transactions of the American Society of Civil Engineers*, *59*(2), 67–143.

Funk, J. E., & Dinger, D. R. (1994). Particle packing. VI: Applications of particle size distribution concepts. Interceram, 43(5), 350–353.

Furnas, C. C. (1931). Grading aggregates-I.-Mathematical relations for beds of broken solids of maximum density. *Industrial & Engineering Chemistry*, *23*(9), 1052–1058.

Glavind, M., & Pedersen, E. (1999). Packing calcuations applied for concrete mix design. *Utilizing Ready Mix Concrete and Mortar*, 121–130.

Graybeal, B. A. (2007). Compressive Behavior of Ultra-High-Performance Fiber-Reinforced Concrete. *ACI Materials Journal*.

Graybeal, B. (2014). *Design and construction of field-cast UHPC connections.* Federal Highway Administration.

Graybeal, B. A., & El-Helou, R. (2023). *Structural design with ultra-high performance concrete*. United States Department of Transportation, Federal Highway Administration.

Habel, K., Viviani, M., Denarié, E., & Brühwiler, E. (2006). Development of the mechanical properties of an ultra-high performance fiber reinforced concrete (UHPFRC). *Cement and Concrete Research*, *36*(7), 1362–1370. https://doi.org/10.1016/j.cemconres.2006.03.009

Hunger, M. (2010). *An integral design concept for ecological self-compacting concrete*.

Ji, T., Chen, B. C., Li, F., Zhuang, Y. Z., Huang, Z. Bin, & Liang, Y. N. (2011). Effects of packing density and calcium-silicon ratio of ternary cementitious material system on strength of reactive powder concrete. *Advanced Materials Research*, 261, 197–201.

Khayat, K. H., Meng, W., Vallurupalli, K., & Teng, L. (2019). Rheological properties of ultra-high-performance concrete — An overview. *Cement and Concrete Research*, *124*, 105828. https://doi.org/10.1016/j.cemconres.2019.105828

Kim, A., Cunningham, P. R., Kamau-Devers, K., & Miller, S. A. (2022). OpenConcrete: A tool for estimating the environmental impacts from concrete production. *Environmental Research:*

Infrastructure and Sustainability, *2*(4), 041001. https://doi.org/10.1088/2634-4505/ac8a6d

Kim, J.-J., & Yoo, D.-Y. (2019). Effects of fiber shape and distance on the pullout behavior of steel fibers embedded in ultra-high-performance concrete. *Cement and Concrete Composites*, *103*, 213–223.

Kodur, V., Solhmirzaei, R., Agrawal, A., Aziz, E. M., & Soroushian, P. (2018). Analysis of flexural and shear resistance of ultra high performance fiber reinforced concrete beams without stirrups. *Engineering Structures*, *174*, 873–884.

Kurt, A. (2021). *Implementation of Ultra-High Performance Concrete in Long-Span Precast Pretensioned Structural Elements for Buildings*. North Carolina State University.

Kwan, A. K. H., Chan, K. W., & Wong, V. (2013). A 3-parameter particle packing model incorporating the wedging effect. *Powder Technology*, *237*, 172–179.

Larsen, I. L., & Thorstensen, R. T. (2020). The influence of steel fibres on compressive and tensile strength of ultra high performance concrete: A review. *Construction and Building Materials*, *256*, 119459. https://doi.org/10.1016/j.conbuildmat.2020.119459

Li, M., & Li, V. C. (2013). Rheology, fiber dispersion, and robust properties of Engineered Cementitious Composites. *Materials and Structures*, *46*(3), 405–420. https://doi.org/10.1617/s11527-012-9909-z

Li, P. P., Yu, Q. L., & Brouwers, H. J. H. (2017). Effect of PCE-type superplasticizer on early-age behaviour of ultra-high performance concrete (UHPC). *Construction and Building Materials*, *153*, 740–750. https://doi.org/10.1016/j.conbuildmat.2017.07.145

Li, Z. (2016). Drying shrinkage prediction of paste containing meta-kaolin and ultrafine fly ash for developing ultra-high performance concrete. *Materials Today Communications*, *6*, 74–80. https://doi.org/10.1016/j.mtcomm.2016.01.001

Liu, Z., El-Tawil, S., Hansen, W., & Wang, F. (2018). Effect of slag cement on the properties of ultra-high performance concrete. *Construction and Building Materials*, *190*, 830–837. https://doi.org/10.1016/j.conbuildmat.2018.09.173

Luo, X., Zhang, S., Li, A., Zhang, C., & Zhang, Y. (2024). Reinforcement effects on tensile behavior of ultra-high-performance concrete (UHPC) with low steel fiber volume fractions. *Materials*, *17*(10), 2418. https://doi.org/10.3390/ma17102418

Mazloom, M., Ramezanianpour, A. A., & Brooks, J. J. (2004). Effect of silica fume on mechanical properties of high-strength concrete. *Cement and Concrete Composites*, *26*(4), 347–357. https://doi.org/10.1016/S0958-9465(03)00017-9

Mehdipour, I., & Khayat, K. H. (2018a). Understanding the role of particle packing characteristics in rheo-physical properties of cementitious suspensions: A literature review. *Construction and Building Materials*, *161*, 340–353.

Mehdipour, I., & Khayat, K. H. (2018b). Understanding the role of particle packing characteristics in rheo-physical properties of cementitious suspensions: A literature review. *Construction and Building Materials*, *161*, 340–353.

Mendonca, F., Hu, J., & Morcous, G. (2019). Fresh and hardened behavior of UHPC prepared with different mix design parameters. *International Interactive Symposium on Ultra-High Performance Concrete*, *2*(1).

Mendonca, F., El-Khier, M. A., Morcous, G., & Hu, J. (2020). *Feasibility study of development of ultra-high performance concrete (UHPC) for highway bridge applications in Nebraska*. University of Nebraska--Lincoln.

Meng, W., & Khayat, K. H. (2017). Improving flexural performance of ultra-high-performance concrete by rheology control of suspending mortar. *Composites Part B: Engineering*, *117*, 26–34. https://doi.org/10.1016/j.compositesb.2017.02.019

Meng, W., & Khayat, K. H. (2018). Effect of hybrid fibers on fresh properties, mechanical properties, and autogenous shrinkage of cost-effective UHPC. *Journal of Materials in Civil Engineering*, *30*(4). https://doi.org/10.1061/(ASCE)MT.1943-5533.0002212

Meng, W., Valipour, M., & Khayat, K. H. (2017a). Optimization and performance of cost-effective ultra-high performance concrete. *Materials and Structures*, *50*(1), 29. https://doi.org/10.1617/s11527-016-0896-3

Meng, W., Valipour, M., & Khayat, K. H. (2017b). Optimization and performance of cost-effective ultra-high performance concrete. *Materials and Structures*, *50*, 1–16.

Moini, M., Sobolev, K., Flores-Vivian, I., & Amirjanov, A. (2019). Modeling and experimental evaluation of aggregate packing for effective application in concrete. *Journal of Materials in Civil Engineering*, *31*(3), 04019001.

Oertel, T., Helbig, U., Hutter, F., Kletti, H., & Sextl, G. (2014). Influence of amorphous silica on the hydration in ultra-high performance concrete. *Cement and Concrete Research*, *58*, 121–130. https://doi.org/10.1016/j.cemconres.2014.01.006

Park, J.-J., Yoo, D.-Y., Kim, S.-W., & Yoon, Y.-S. (2013). Drying shrinkage cracking characteristics of ultra-high-performance fibre reinforced concrete with expansive and shrinkage reducing agents. *Magazine of Concrete Research*, *65*(4), 248–256. https://doi.org/10.1680/macr.12.00069

Park, S. H., Ryu, G. S., Koh, K. T., & Kim, D. J. (2014). Effect of shrinkage reducing agent on pullout resistance of high-strength steel fibers embedded in ultra-high-performance concrete. *Cement and Concrete Composites*, *49*, 59–69.

Richard, P., & Cheyrezy, M. (1995). Composition of reactive powder concretes. *Cement and Concrete Research*, *25*(7), 1501–1511.

Roquier, G. (2019). A Theoretical Packing Density Model (TPDM) for ordered and disordered packings. *Powder Technology*, *344*, 343–362.

Schröfl, C., Gruber, M., & Plank, J. (2012). Preferential adsorption of polycarboxylate superplasticizers on cement and silica fume in ultra-high performance concrete (UHPC). *Cement and Concrete Research*, *42*(11), 1401–1408.

Shakhmenko, G., & Birsh, J. (1998). Concrete mix design and optimization. *Proceedings of the 2nd International Symposium in Civil Engineering*, 1–8.

Sharma, R., Jang, J. G., & Bansal, P. P. (2022). A comprehensive review on effects of mineral admixtures and fibers on engineering properties of ultra-high-performance concrete. *Journal of Building Engineering*, *45*, 103314. https://doi.org/10.1016/j.jobe.2021.103314

Shi, C., Wang, D., Wu, L., & Wu, Z. (2015). The hydration and microstructure of ultra high-strength concrete with cement–silica fume–slag binder. *Cement and Concrete Composites*, *61*, 44–52. https://doi.org/10.1016/j.cemconcomp.2015.04.013

Stovall, T., De Larrard, F., & Buil, M. (1986). Linear packing density model of grain mixtures. *Powder Technology*, *48*(1), 1–12.

Sun, Z., Yang, S., Hang, M., Wang, J., & Yang, T. (2022). Optimization design of ultrahigh-performance concrete based on interaction analysis of multiple factors. *Case Studies in Construction Materials*, *16*, e00858. https://doi.org/10.1016/j.cscm.2021.e00858

Teng, L., Meng, W., & Khayat, K. H. (2020). Rheology control of ultra-high-performance concrete made with different fiber contents. *Cement and Concrete Research*, *138*, 106222. https://doi.org/10.1016/j.cemconres.2020.106222

Termkhajornkit, P., Nawa, T., Nakai, M., & Saito, T. (2005). Effect of fly ash on autogenous shrinkage. *Cement and Concrete Research*, *35*(3), 473–482. https://doi.org/10.1016/j.cemconres.2004.07.010

Wang, X., Yu, R., Song, Q., Shui, Z., Liu, Z., Wu, S., & Hou, D. (2019). Optimized design of ultra-high performance concrete (UHPC) with a high wet packing density. *Cement and Concrete Research*, *126*, 105921.

Wille, K., Naaman, A. E., El-Tawil, S., & Parra-Montesinos, G. J. (2012). Ultra-high performance concrete and fiber reinforced concrete: achieving strength and ductility without heat curing. *Materials and Structures*, *45*, 309–324.

Wong, H. H. C., & Kwan, A. K. H. (2008). Packing density of cementitious materials: Part 1—measurement using a wet packing method. *Materials and Structures*, *41*, 689–701.

Wu, Z., Shi, C., He, W., & Wang, D. (2017). Static and dynamic compressive properties of ultra-high performance concrete (UHPC) with hybrid steel fiber reinforcements. *Cement and Concrete Composites*, *79*, 148–157. https://doi.org/10.1016/j.cemconcomp.2017.02.010

Wu, Z., Shi, C., & Khayat, K. H. (2019). Investigation of mechanical properties and shrinkage of ultra-high performance concrete: Influence of steel fiber content and shape. *Composites Part B: Engineering*, *174*, 107021. https://doi.org/10.1016/j.compositesb.2019.107021

Xu, M., Hallinan, B., & Wille, K. (2016). Effect of loading rates on pullout behavior of high strength steel fibers embedded in ultra-high performance concrete. *Cement and Concrete Composites*, *70*, 98–109.

Yahia, A., & Khayat, K. H. (2001). Analytical models for estimating yield stress of high-performance pseudoplastic grout. *Cement and Concrete Research*, *31*(5), 731–738. https://doi.org/10.1016/S0008-8846(01)00476-8

Yalçınkaya, Ç., & Yazıcı, H. (2017). Effects of ambient temperature and relative humidity on early-age

shrinkage of UHPC with high-volume mineral admixtures. *Construction and Building Materials*, *144*, 252–259. https://doi.org/10.1016/j.conbuildmat.2017.03.198

Yoo, D.-Y., Kim, S., Park, G.-J., Park, J.-J., & Kim, S.-W. (2017). Effects of fiber shape, aspect ratio, and volume fraction on flexural behavior of ultra-high-performance fiber-reinforced cement composites. *Composite Structures*, *174*, 375–388. https://doi.org/10.1016/j.compstruct.2017.04.069

Yoo, D.-Y., Kim, S.-W., & Park, J.-J. (2017). Comparative flexural behavior of ultra-high-performance concrete reinforced with hybrid straight steel fibers. *Construction and Building Materials*, *132*, 219–229. https://doi.org/10.1016/j.conbuildmat.2016.11.104

Yoo, D.-Y., Park, J.-J., Kim, S.-W., & Yoon, Y.-S. (2013). Early age setting, shrinkage and tensile characteristics of ultra high performance fiber reinforced concrete. *Construction and Building Materials*, *41*, 427–438. https://doi.org/10.1016/j.conbuildmat.2012.12.015

Yoo, D.-Y., Park, J.-J., Kim, S.-W., & Yoon, Y.-S. (2014). Influence of reinforcing bar type on autogenous shrinkage stress and bond behavior of ultra high performance fiber reinforced concrete. *Cement and Concrete Composites*, *48*, 150–161. https://doi.org/10.1016/j.cemconcomp.2013.11.014

Yu, R., Spiesz, P., & Brouwers, H. J. H. (2015). Development of an eco-friendly ultra-high performance concrete (UHPC) with efficient cement and mineral admixtures uses. *Cement and Concrete Composites*, *55*, 383–394. https://doi.org/10.1016/j.cemconcomp.2014.09.024

Zain, M. F. M., Safiuddin, M., & Mahmud, H. (2000). Development of high performance concrete using silica fume at relatively high water–binder ratios. *Cement and Concrete Research*, *30*(9), 1501–1505.

Zhang, Y., Zhang, W., She, W., Ma, L., & Zhu, W. (2012). Ultrasound monitoring of setting and hardening process of ultra-high performance cementitious materials. *NDT & E International*, *47*, 177–184. https://doi.org/10.1016/j.ndteint.2009.10.006

APPENDIX A: MATERIAL CHARACTERISTICS

Average Cement Content of 1000-1500 lb/yd^3

Designation formulation (kg/m^3)

Code	Premix	Cement	SF	QP	Sand	AC	HRWR	Water	Steel fiber
Ductal®	–	712	231	211	1020	30	31	109	156
BSI®	–	1114	169	–	1072	–	40	209	234
CEMTEC®	–	1050	268	–	514	–	44	180	470
CRC®	930	–	–	–	1300	–	–	150	225
BCV®	2136	–	–	–	–	–	21.5	–	156
Cor-Tuf®	–	758	497	295	733	–	13	158	140

Figure 78. Chart. Summary of the binder content of conventional UHPC mixes developed in the literature.

Table 15. Chemical composition of low alkali Type-I cement determined using X-ray fluorescence

Oxide	Percentage Composition (%)
CaO	68.15
SiO_2	18.1
Al_2O_3	2.66
Fe_2O_3	4.11
MgO	1.43
SO_3	4.32
K_2O	0.71

Table 16. Chemical composition of ultra-fine fly ash determined using X-ray fluorescence

Oxide	Percentage Composition (%)
SiO_2	53.64
Al_2O_3	16.95
Fe_2O_3	5.40
Sum (SiO_2 + Al_2O_3 + Fe_2O_3)	75.99
SO_3	1.41
CaO	9.48
MgO	3.61
Na_2O	4.62
K_2O	2.89
Moisture	0.08
Loss on Ignition	0.30

Figure 79. Photo. Striated steel fibers (0.2 mm × 13 mm) from HiPer Fibers used in the development of UHPC mix designs.

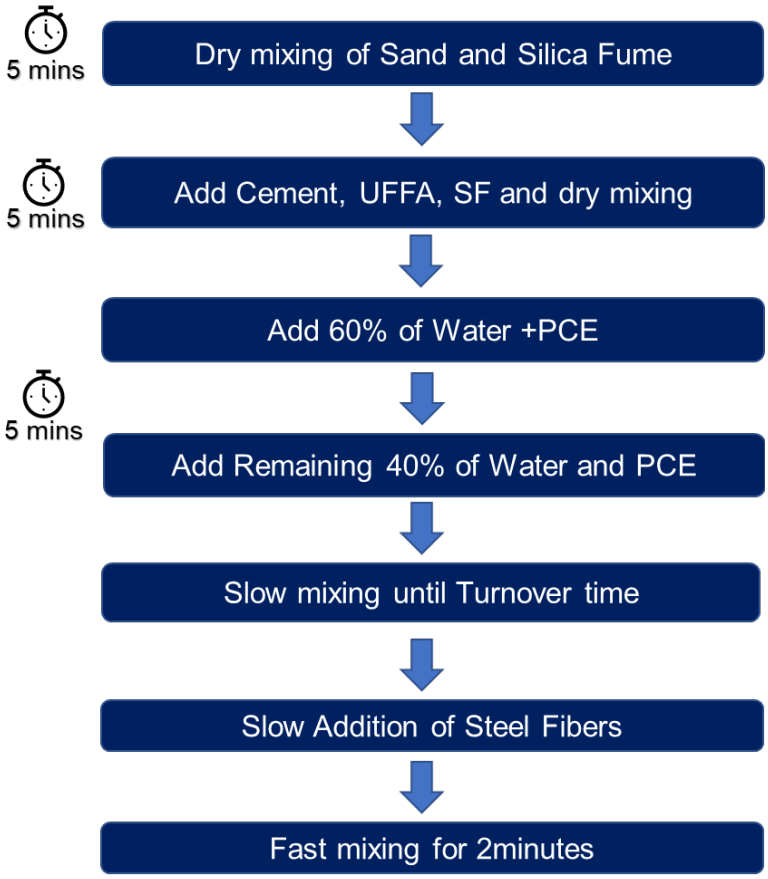

Figure 80. Chart. Optimized mixing regime incorporated to prepare the UHPC mixes in the lab. The mixing regime has been used for smaller-scale mixes for binder optimization.

APPENDIX B: MIX DESIGN

TYPES OF MIXTURE DESIGNS

In mixture experiments, the response Y is modeled as a function of the proportions of the components. Considering a mixture with p components where x_1, x_2, and x_p represent the proportions of each component which satisfy the following constraint:

$$x_1 + x_2 + \cdots + x_p = 1$$

The general polynomial model for a mixture design can be expressed as:

$$Y = \beta_0 + \sum_{i=1}^{p} \beta_i x_i + \sum_{i=1}^{p} \sum_{j=i}^{p} \beta_{ij} x_i x_j + \sum_{i=1}^{p} \sum_{j=i}^{p} \sum_{k=j}^{p} \beta_{ijk} x_i x_j x_k + \cdots$$

where,

- β_0 is the intercept
- β_i are the coefficients for the linear terms (representing the main effects of each component)
- β_{ij} are the coefficients for the interaction terms (representing the interaction effects between two components)
- β_{ijk} are the coefficients for the higher order interactions and so on.

Mixture designs are characterized by different types based on the experimental objectives and the number of components involved. The key types include the Simplex Lattice Design, Simplex Centroid Design, and Extreme Vertices Design.

- **Simplex Lattice Design:** This design includes a set of formulations that vary systematically across all components, providing a structured approach to explore the entire composition space. It is particularly useful when the number of components is high.
- **Simplex Centroid Design:** Each point in this design represents the centroid of a subset of the full set of components, useful for preliminary screening studies.
- **Extreme Vertices Design:** Optimized for situations where the response is expected to be optimal at the extreme combinations of the components.

Table 17. Mix design output from the mixture design optimization technique from Minitab software

StdOrder	RunOrder	PtType	Blocks	Cem	Slag	UFFA	SF
14	1	-1	1	0.47222	0.116667	0.238889	0.172222
15	2	-1	1	0.52222	0.366667	0.063889	0.047222
1	3	1	1	1	0	0	0
18	4	-1	1	0.47222	0.366667	0.113889	0.047222
11	5	-1	1	0.77222	0.116667	0.063889	0.047222
12	6	-1	1	0.64722	0.116667	0.063889	0.172222
2	7	1	1	0.75	0	0	0.25
10	8	0	1	0.54444	0.233333	0.127778	0.094444
4	9	1	1	0.4	0	0.35	0.25
8	10	1	1	0.4	0.5	0.1	0
13	11	-1	1	0.59722	0.116667	0.238889	0.047222
17	12	-1	1	0.47222	0.291667	0.063889	0.172222
19	13	-1	1	0.47222	0.241667	0.238889	0.047222
16	14	-1	1	0.47222	0.366667	0.063889	0.097222
5	15	1	1	0.5	0.5	0	0
6	16	1	1	0.4	0.5	0	0.1
9	17	1	1	0.4	0.25	0.35	0
7	18	1	1	0.4	0.35	0	0.25
3	19	1	1	0.65	0	0.35	0

APPENDIX C: PACKING MODELS USED FOR MIX OPTIMIZATION

COMPRESSIBLE PACKING MODEL

The Compressible Packing Model (CPM) is a tool to compute the packing density of mixes containing binders and materials of varying sizes. To grasp the concept of CPM, let's consider a straightforward scenario with two material sizes, denoted as d_1 and d_2, where $d_1 >> d_2$. The addition of d_2 does not disturb the packing of d_1. Assuming the random packing densities of d_1 and d_2 are β_1 and β_2 respectively, the researchers can determine the packing density of a mix comprising these materials, with y_1% of d_1 and y_2% of d_2. Here "y_1" and "y_2" represent the relative volume fractions of d_1 and d_2 (See Figure 81). When these materials are packed within a unit volume, "ϕ_1" and "ϕ_2" denote the volume fractions occupied by d_1 and d_2 in the overall volume. Therefore, Eqn. 3 and 4 establish the relationship between relative volume fractions (y_1 and y_2) and packing density (γ).

$$y_1 = \frac{\phi_1}{\phi_1+\phi_2} \; and \; y_2 = \frac{\phi_2}{\phi_1+\phi_2} \qquad \text{Equation 3}$$

$$\gamma = \phi_1 + \phi_2 \text{ where } 1 > \gamma > 0 \qquad \text{Equation 4}$$

When d_1 has a higher volume fraction, d_1 will occupy all the available space as if no materials were present. In that case, $\phi_1 = \beta_1$, and the packing density (γ_1) can be calculated using Eqn. 5.

$$\gamma = \gamma_1 = \frac{\beta_1}{1-y_2} \qquad \text{Equation 5}$$

Similarly, when d_2 has a higher volume fraction, d_2 will occupy all the available porosity between d_1 materials. In that case, $\phi_2 = \beta_2(1 - \phi_1)$, and packing density γ_2 can be calculated using Eqn. 6.

$$\gamma = \gamma_2 = \frac{\beta_2}{1-(1-\beta_2)y_1} \qquad \text{Equation 6}$$

Therefore, for any mix of d_1 and d_2 materials, the researchers can write the packing density (γ) as $\gamma \leq \min(\gamma_1,\gamma_2)$.

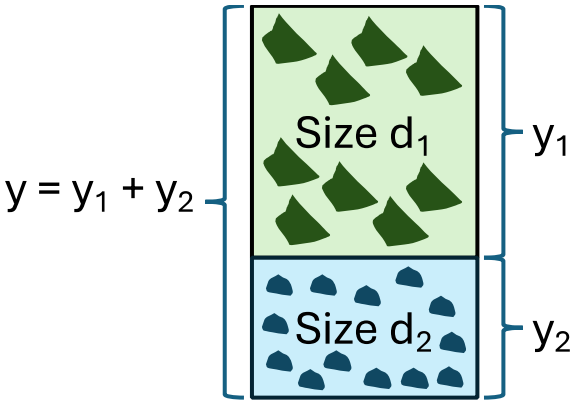

Figure 81. Illustration. Binary system used as the basis for modeling the theoretical packing using the compressible packing model (CPM).

In the previous example, it has been assumed that the packing of one material size remained unaffected by the presence of another. However, in practice, the interaction between different material sizes leads to what's known as the loosening and wall effects. The loosening effect occurs when fine materials are added to a coarse mix, disrupting its original packing []. Conversely, the wall effect arises when coarse material is introduced to a fine mix []. Both effects result in a reduction of the original mix's packing density.

For two material sizes, denoted as "i" and "j", the coefficients "a_{ij}" and "b_{ij}" represent the loosening and wall effect coefficients for material size i influenced by material size j. These coefficients can be calculated using Eqn. 7 and 8.

$$a_{ij} = \sqrt{1 - \left(1 - \frac{d_j}{d_i}\right)^{1.02}} \; ; d_j > d_i$$

Equation 7

$$b_{ij} = 1 - \left(1 - \frac{d_i}{d_j}\right)^{1.50} \; ; d_i > d_j$$

Equation 8

where,

- "i" and "j" refer to i^{th} and j^{th} material sizes in the mix.
- a_{ij} is the loosening effect coefficient for material size "i" due to the influence of material size "j".
- b_{ij} is the wall effect coefficient for material size "i" due to the influence of material size "j".
- d_i is the average diameter for material size "i".
- d_j is the average diameter for material size "j".

For a mix of three materials, the coefficients for the loosening and wall effects can be computed in a matrix format, as illustrated in Table 18. This same methodology can be extended to mixes containing "n" different sizes of materials.

Table 18. Matrix of loosening and wall effect coefficient used for a system of three materials

	i	j	k
i	a_{ii}, b_{ii}	a_{ij}, b_{ij}	a_{ik}, b_{ik}
j	a_{ji}, b_{ji}	a_{jj}, b_{jj}	a_{jk}, b_{jk}
k	a_{ki}, b_{ki}	a_{kj}, b_{kj}	a_{kk}, b_{kk}

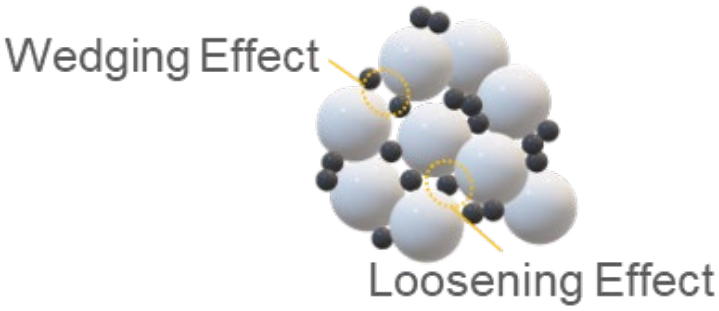

Figure 82. Illustration. Loosening effect in a binary system due to the influence of the finer aggregate on the coarser gradation.

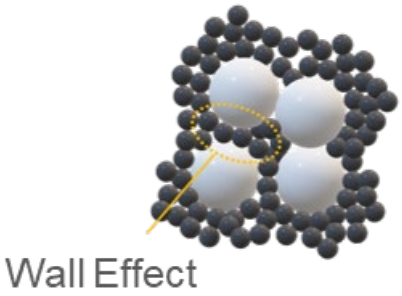

Figure 83. Illustration. Wall effect in a binary system due to the influence of the coarser aggregate on the finer gradation.

Considering the loosening and the wall effect, the individual virtual packing density (γi) is defined as the theoretical value of packing density of the materials mix when class "i" is dominant. It can be calculated using Equations 7, 8, and 9. Once all the parameters are determined, the mix's packing density (ϕ) can be determined using Newton's iteration method using Eqn. 12.

$$\beta_i = \frac{\frac{\text{Mass of the material}}{\text{Volume of the container}}}{\text{Solid density of the material}} \qquad \text{Equation 9}$$

$$y_i = \frac{\frac{w_i}{\rho_i}}{\sum_{j=1}^{n} \frac{w_j}{\rho_j}} \qquad \text{Equation 10}$$

$$\gamma_i = \frac{\beta_i}{1 - \sum_{j=1}^{i-1}[\,1 - \beta_i + b_{ij}\,\beta_i(\,1 - \frac{1}{\beta_j})]y_j - \sum_{j=i+1}^{n}[1 - a_{ij}\,\beta_i\,\beta_j\,]y_j} \qquad \text{Equation 11}$$

$$K = \sum_{i=1}^{n} \frac{\frac{y_i}{\beta_i}}{\frac{1}{\phi} - \frac{1}{\gamma_i}} \qquad \text{Equation 12}$$

where,

- β_i is the residual packing density of material size "i".
- y_i represents the individual volume fraction of material size "i" in the mix.
- n is the number of different material sizes in the mix.
- w_i and w_j are the weight fractions of material sizes "i" and "j", respectively.
- ρ_i and ρ_j are the specific gravity values of material sizes "i" and "j", respectively.
- γ_i is the packing density of the material mix, considering material size "i" as the dominant.
- K is the compaction index; K = 9 is used when materials are vibrated and compacted, and K=4.75 is used when only vibration is used.

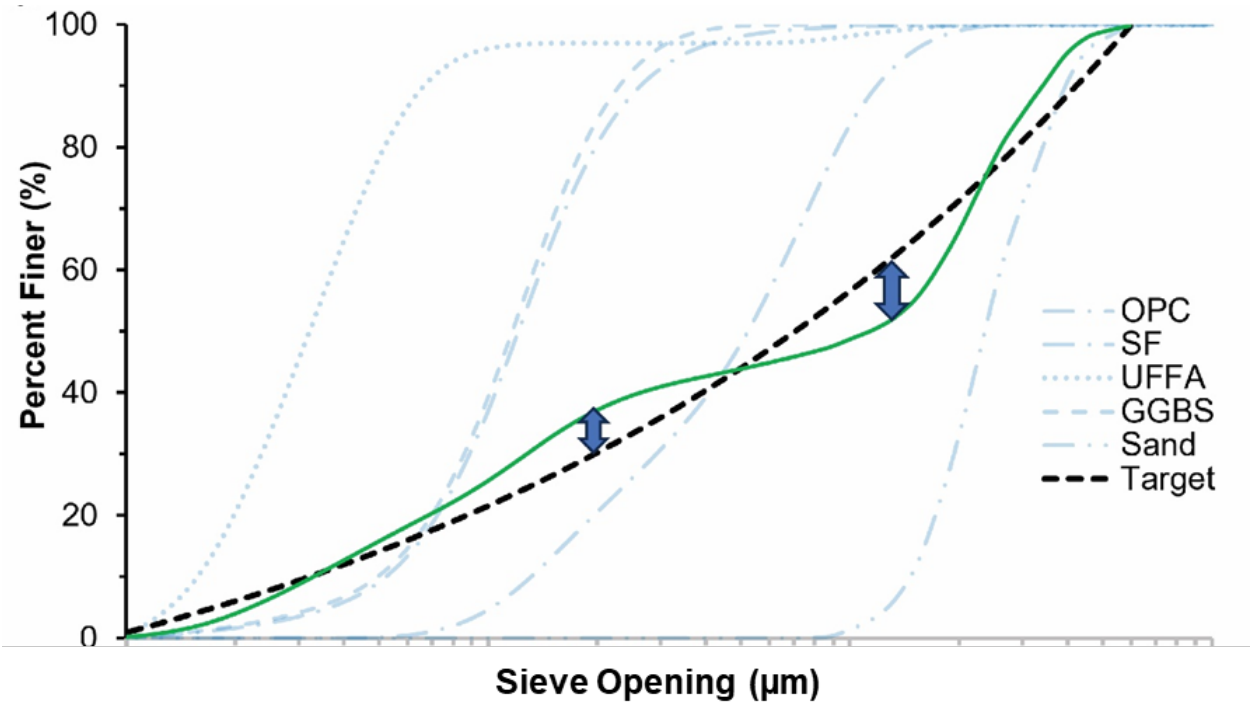

Figure 84. Graph. Estimation of the packing factor as the discrepancy between the composite particle size distribution and the ideal packing curve.

INTERPRETATION OF THE TERNARY RESPONSE PLOT FOR PACKING FACTOR ESTIMATION

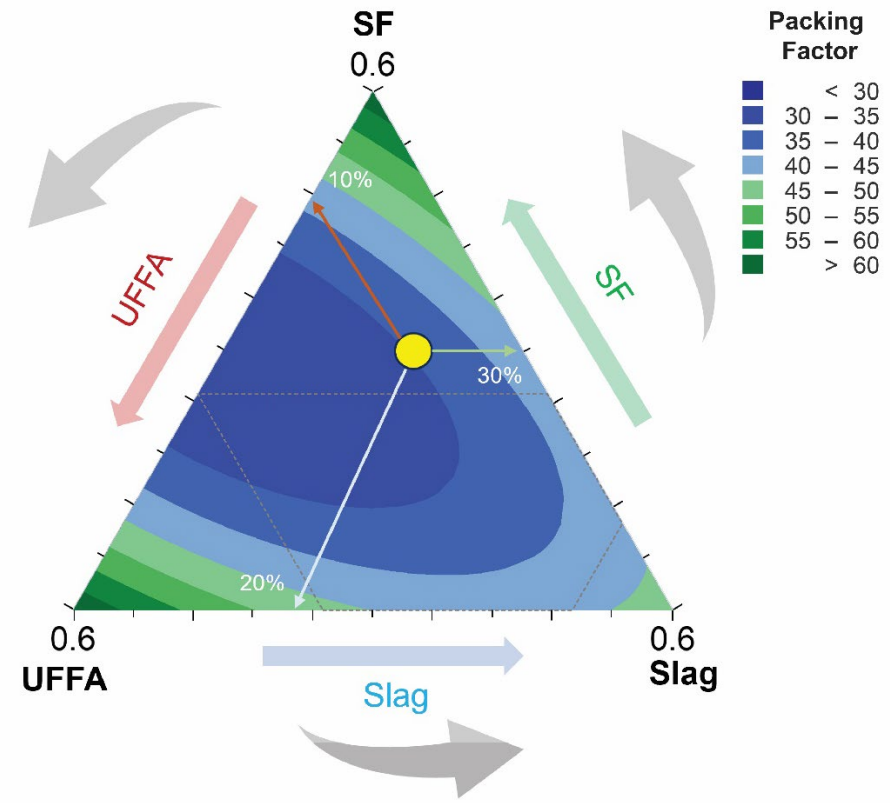

Figure 85. Graph. A typical ternary plot showing the response of packing factor (PF) for different compositions of silica fume (SF), ultra fine fly ash (UFFA), and slag.

This ternary plot illustrates the relationships between three components (SF, UFFA, Slag) used in a specific formulation. The following enlists several aspects of interpretation of the ternary plots:

Understanding the Axes

The axes of a ternary plot represent the proportions of three components that sum to 100%. Each axis starts from 0 at the vertex opposite it and increases to 100% at the vertex it originates from. The bottom axis represents the proportion of UFFA (Ultra Fine Fly Ash), ranging from 0 at the left vertex to 60% at the bottom right corner. The left axis shows the proportion of Slag, ranging from 0 at the bottom right to 60% at the top vertex. The right axis depicts the proportion of SF (Silica Fume), from 0 at the top vertex to 60% at the bottom right corner.

Reading the Composition

The yellow dot marks a specific mixture, showing the percentages of each component. Lines drawn parallel to the axes intersect them at the respective percentages. For instance, follow the line parallel to the Slag-UFFA edge to read the percentage of SF, and similarly for the other two components. This particular mixture contains approximately 10% SF, 30% Slag, and 60% UFFA.

Packing Factor

The color coding shows the packing factor, a measure typically indicating how densely the particles pack together, affecting the mixture's properties like strength and durability. Darker shades represent a higher packing factor. In this plot, the blue shades transition from light (less than 30%) to dark blue and green (>60%).

Directional Arrows

The arrows suggest trends or the impact of increasing each component. For example, the arrow along the SF axis implies that increasing SF will likely move the composition within the indicated packing factor range. Similarly, arrows for UFFA and Slag show how increases in these components shift the mixture within the plot.

APPENDIX D: RHEOLOGICAL PROPERTIES

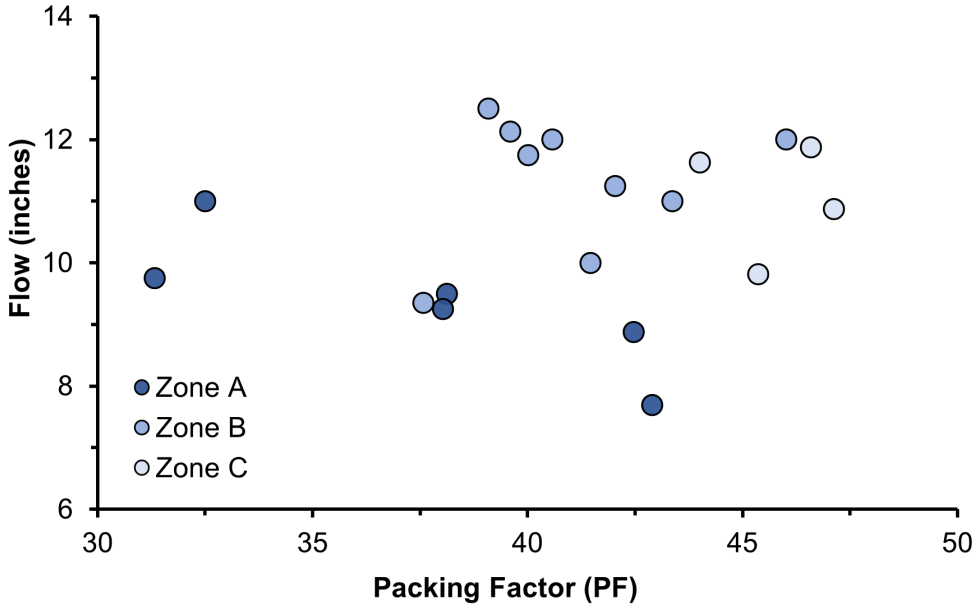

Figure 86. Graph. Correlation between packing factor and flow of the UHPC mixes. The mixes, corresponding to different zones, are marked with different shades.

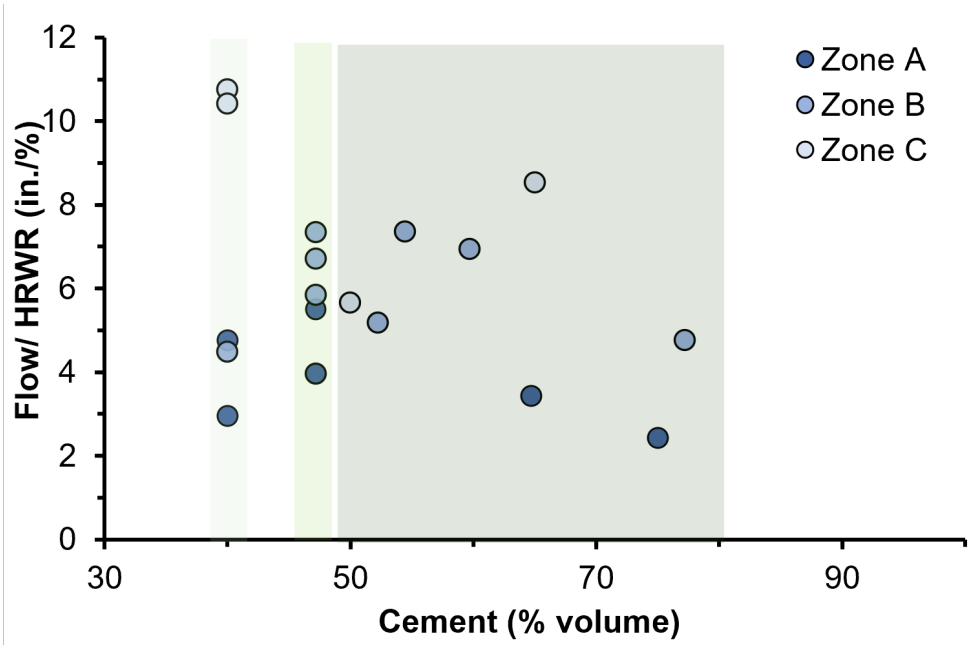

Figure 87. Graph. Variation of flow of the UHPC mixes for an increase in cement content within the UHPC mix design.

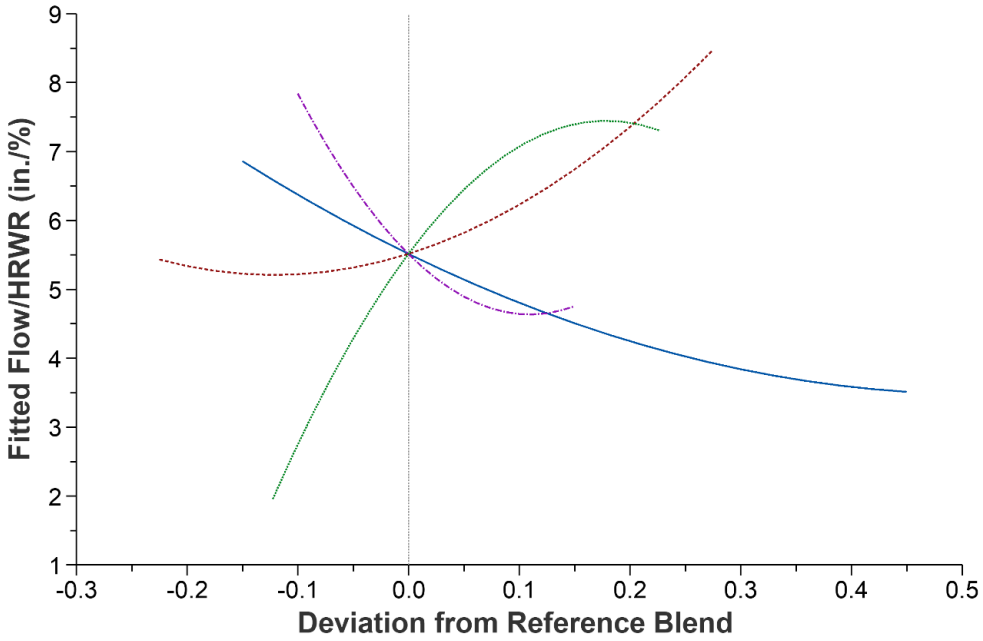

Figure 88. Graph. Sensitivity of flow of the UHPC mixes for unit variation of different binder constituents.

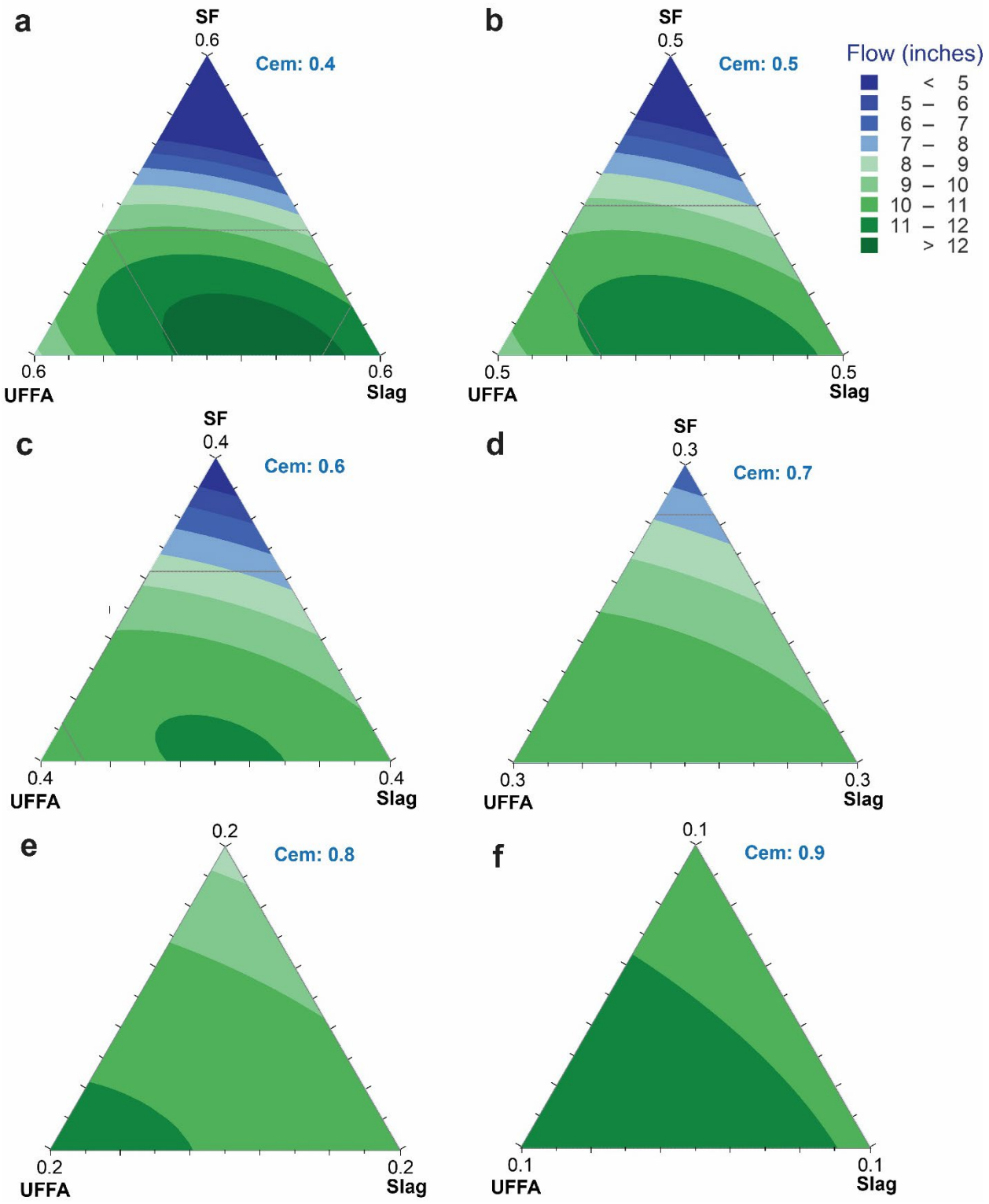

Figure 89. Graph. Ternary response plot for flow of the UHPC mixes at 3 days for compositional variation of the binder constituents used in the study.

APPENDIX E: MECHANICAL PROPERTIES OF THE UHPC MIXES

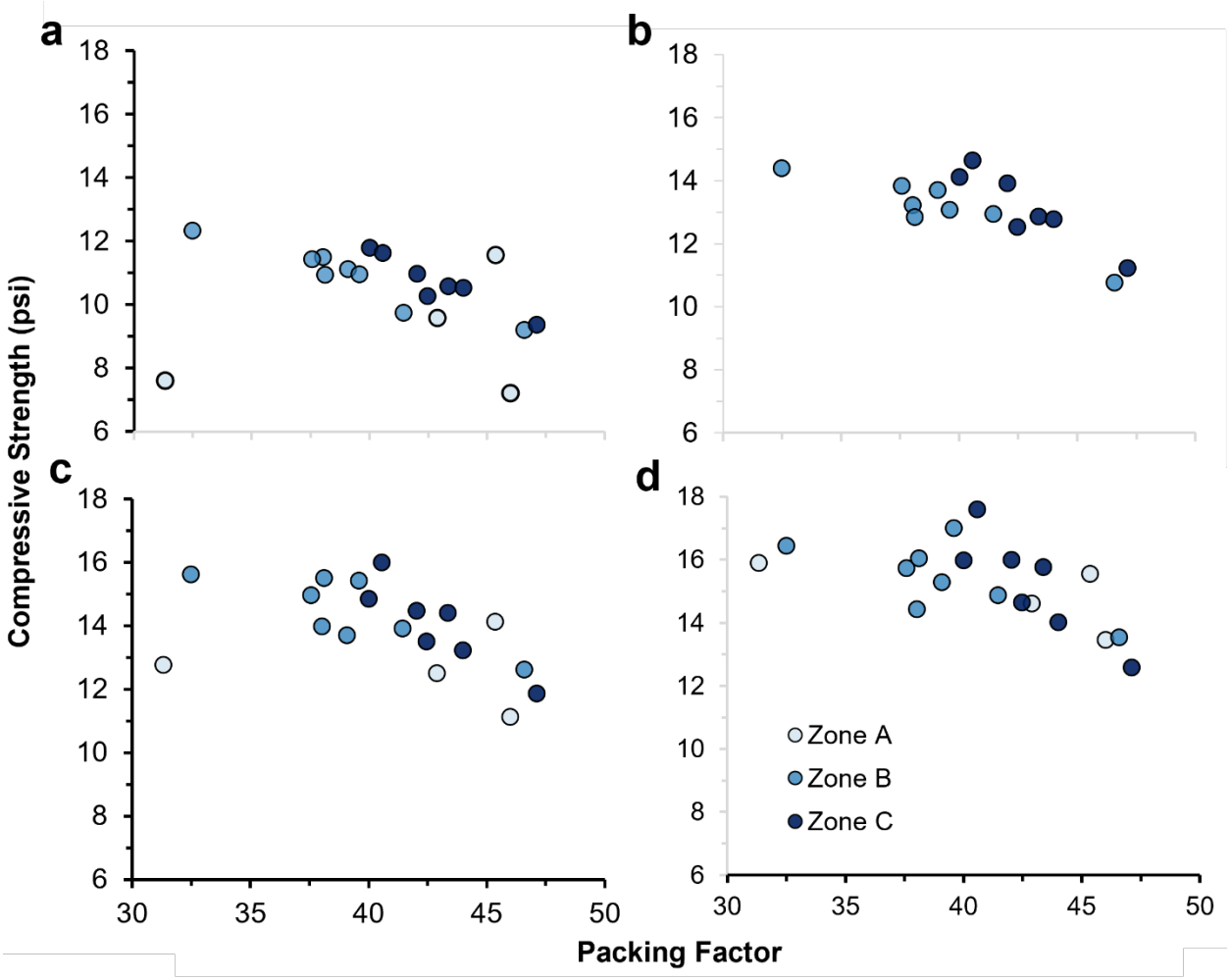

Figure 90. Graph. Correlation between the compressive strength development and the packing factor for the designed UHPC mixes. The relationship between the two is presented at (a) 3, (b) 7, (c) 14, and (d) 28 days of hydration.

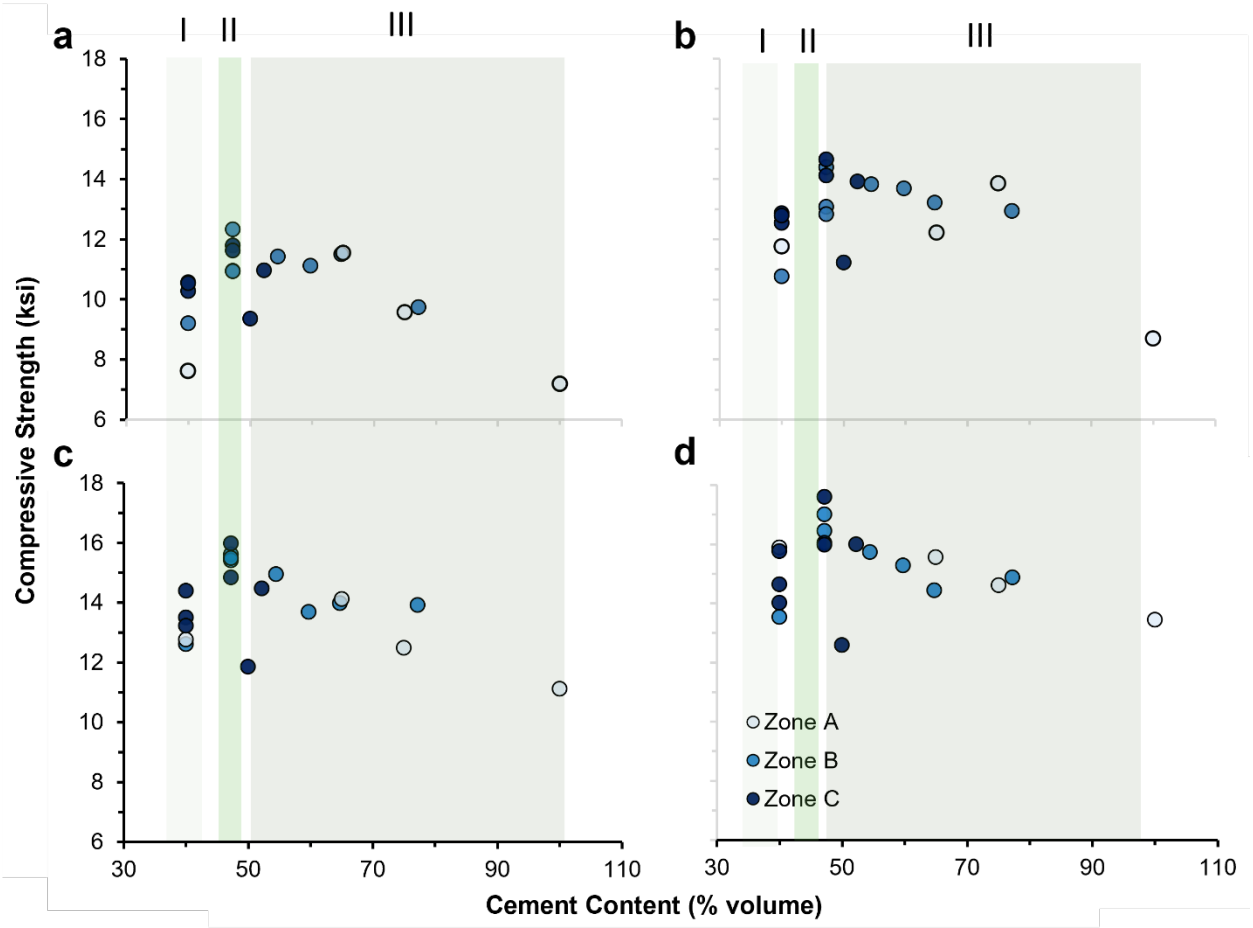

Figure 91. Graph. Variation of compressive strength of the UHPC mixes for an increase in cement content within the UHPC mix design.

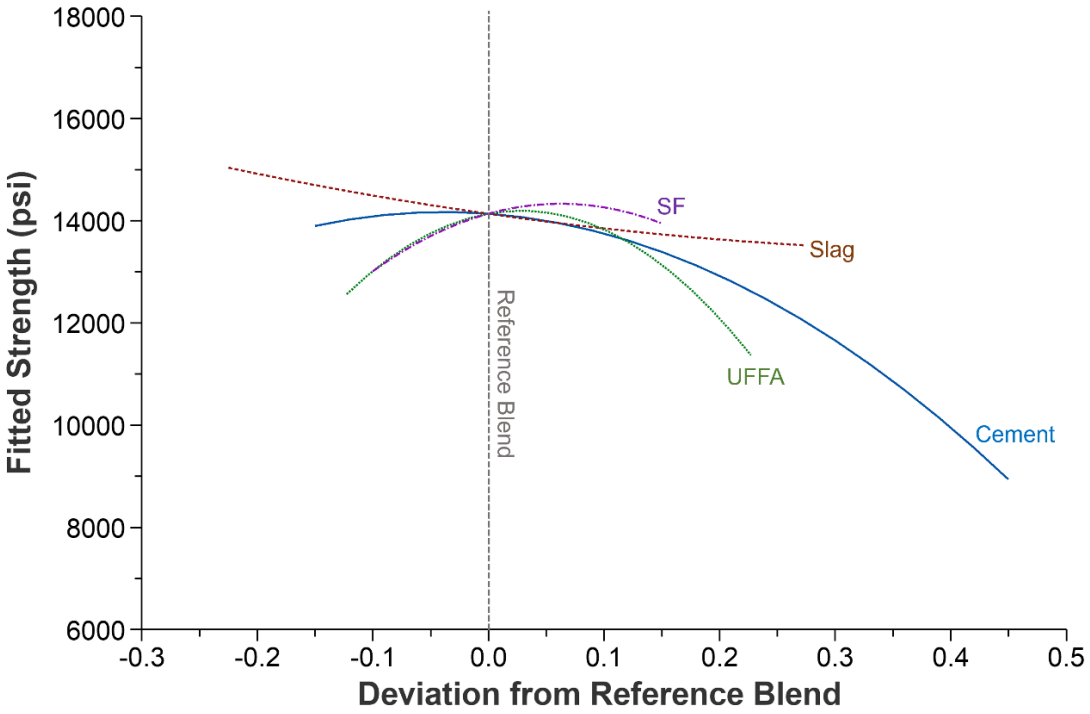

Figure 92. Graph. Sensitivity of the compressive strength of the UHPC mixes at 7 days of hydration for unit variation of different binder constituents.

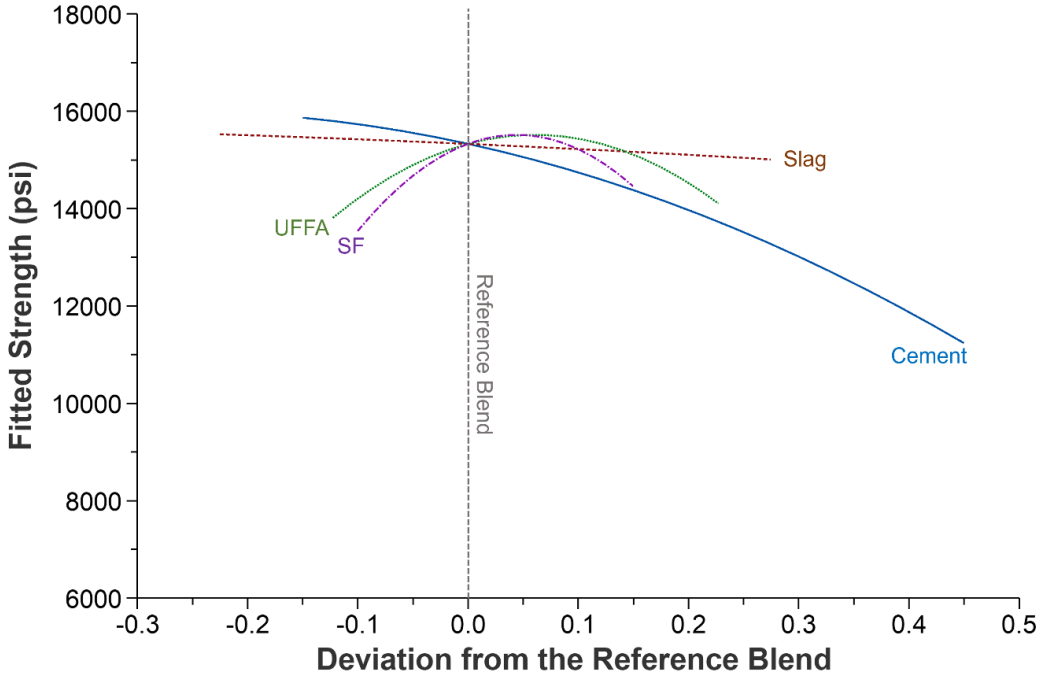

Figure 93. Graph. Sensitivity of the compressive strength of the UHPC mixes at 14 days of hydration for unit variation of different binder constituents.

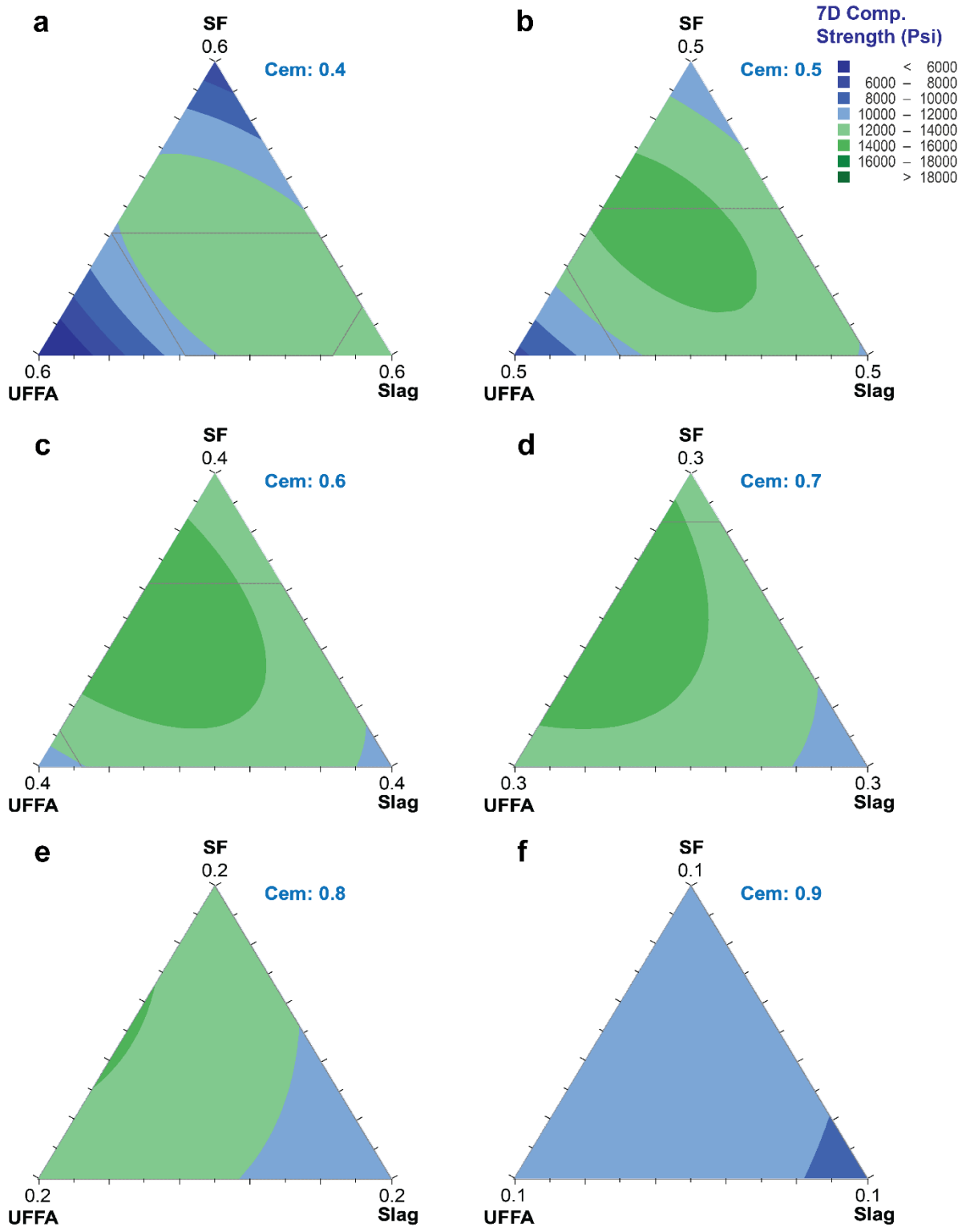

Figure 94. Graph. Ternary response plot showing the 7-days compressive strength of the UHPC mixes for compositional variation of the binder constituents used in the study.

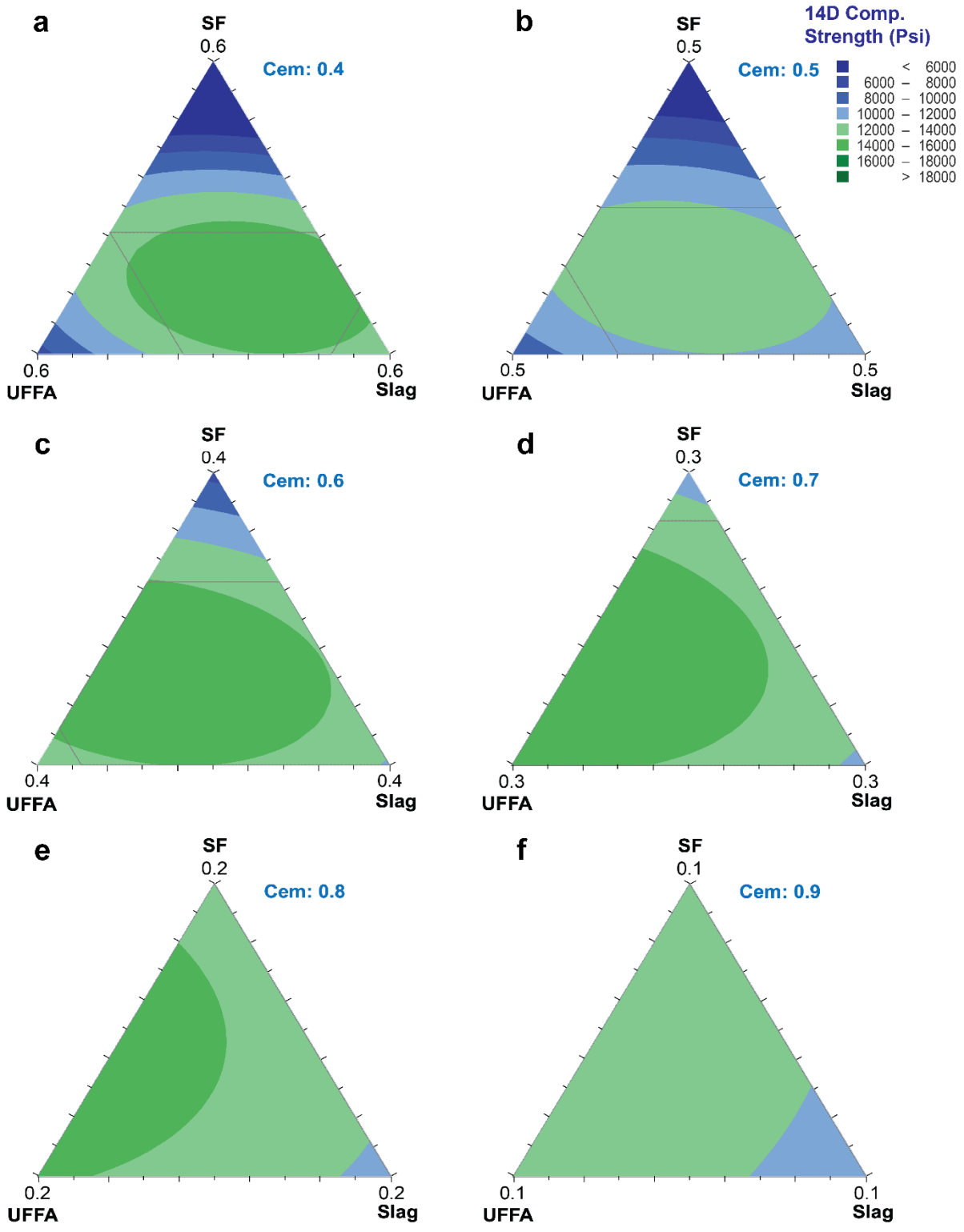

Figure 95. Graph. Ternary response plot showing the 14-days compressive strength of the UHPC mixes for compositional variation of the binder constituents used in the study.

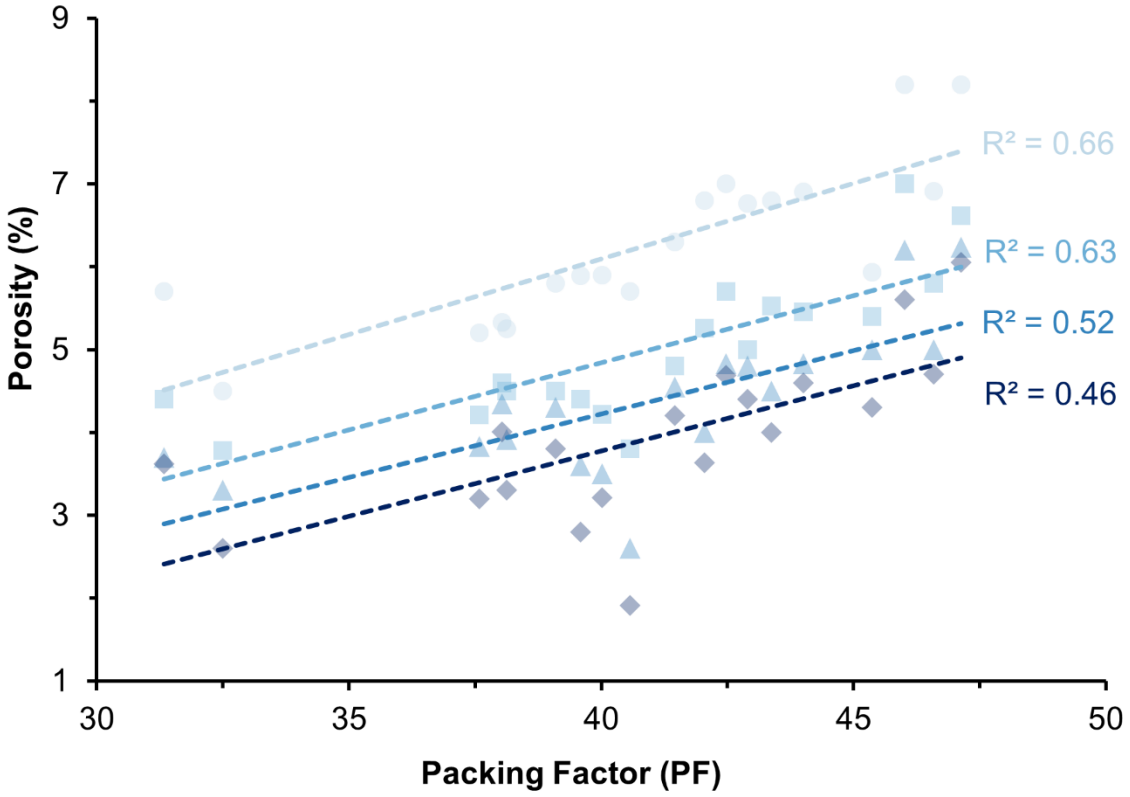

Figure 96. Graph. Correlation between the open porosity and packing factor for all the mixes combined regardless of the binder composition.

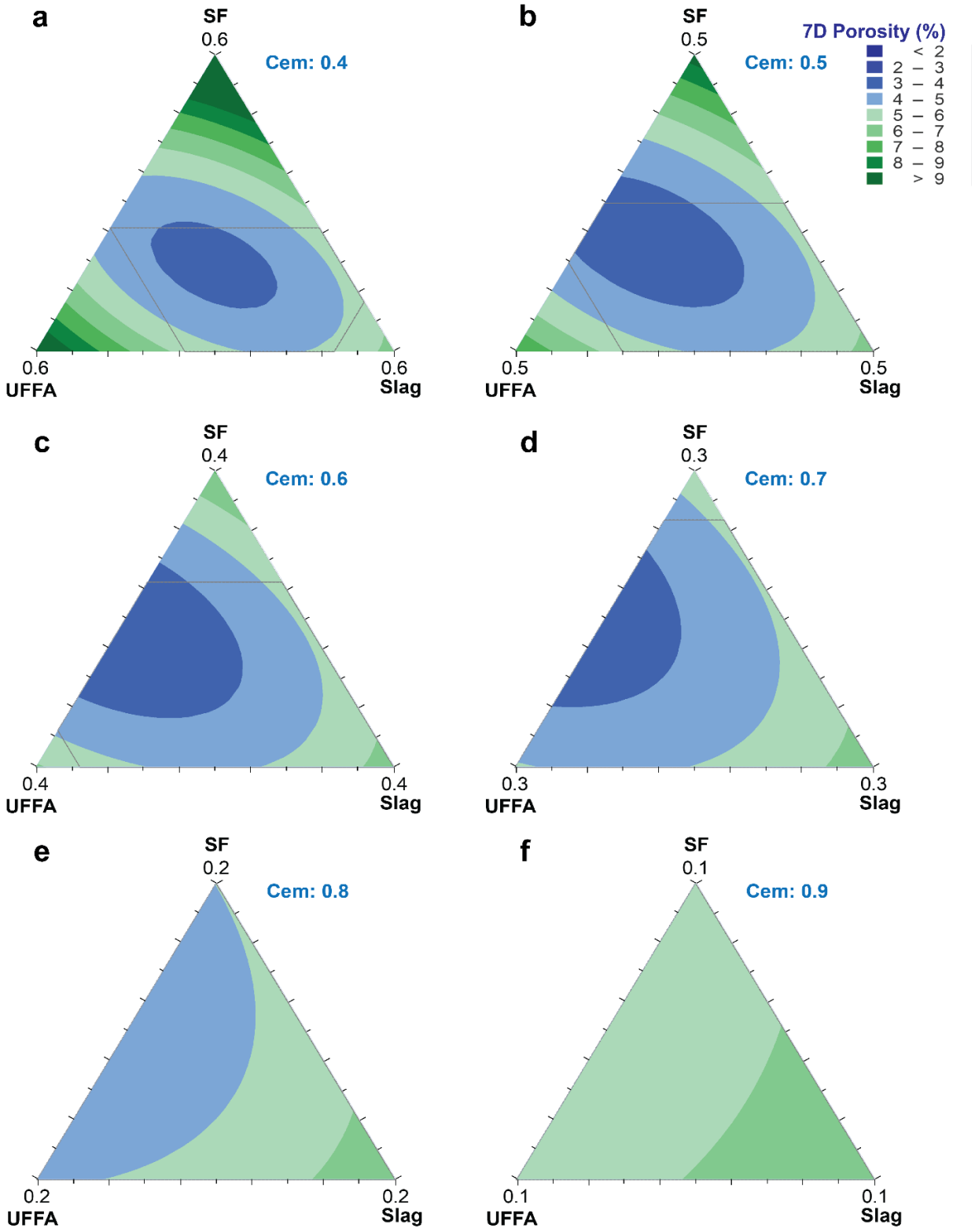

Figure 97. Graph. Ternary response plot showing the 7-days open porosity of the UHPC mixes for compositional variation of the binder constituents used in the study.

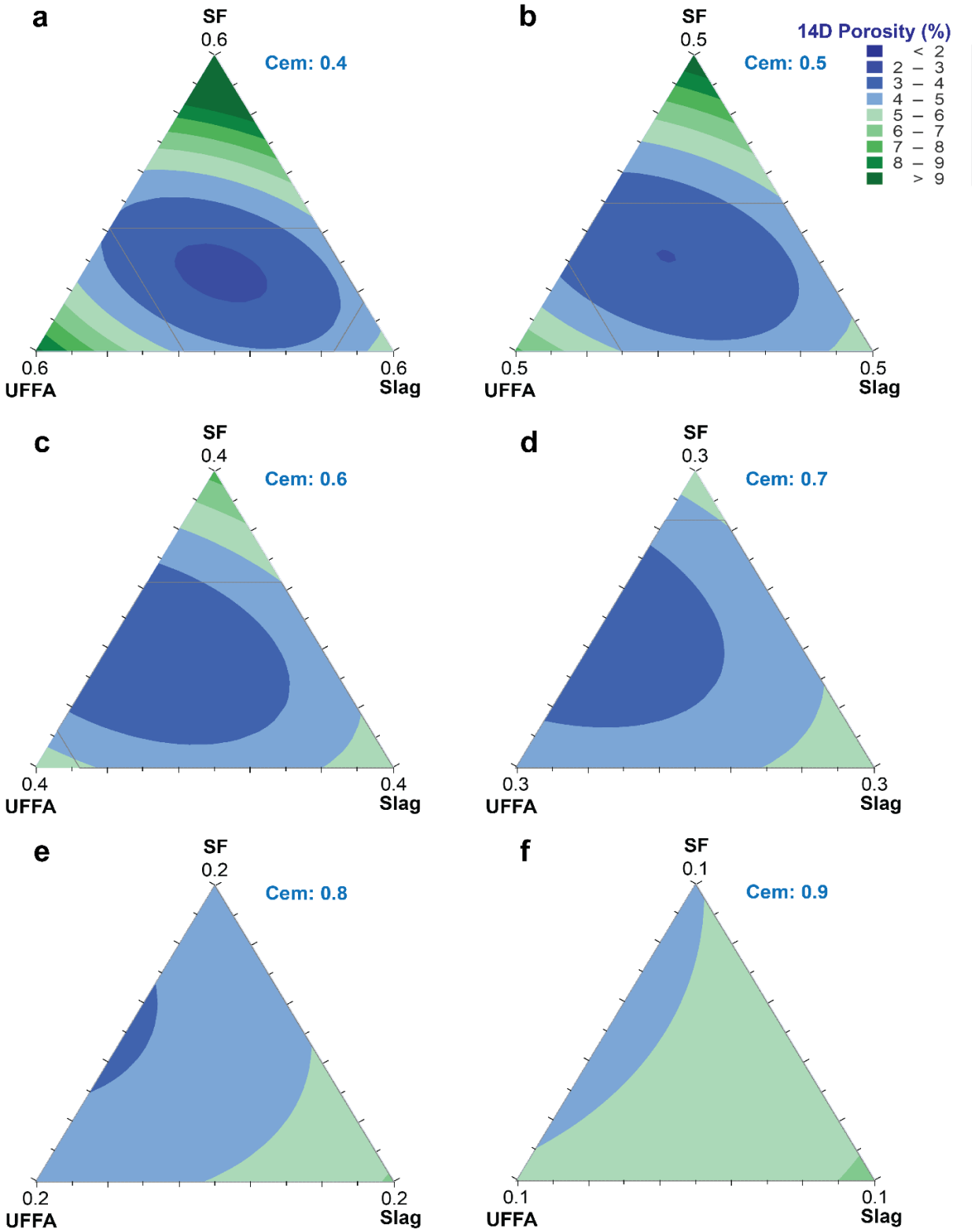

Figure 98. Graph. Ternary response plot showing the 14-days open porosity of the UHPC mixes for compositional variation of the binder constituents used in the study.

APPENDIX F: DRYING SHRINKAGE OF THE UHPC MIXES

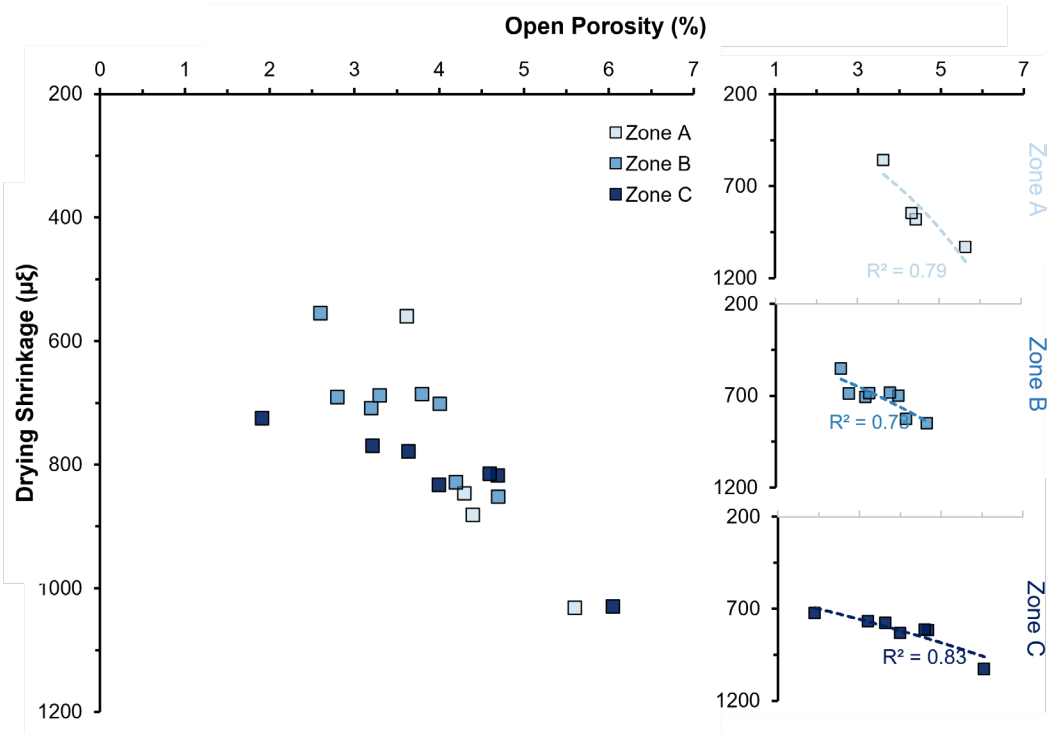

Figure 99. Graph. Correlation of 28-days drying shrinkage with the open porosity of the UHPC mixes.

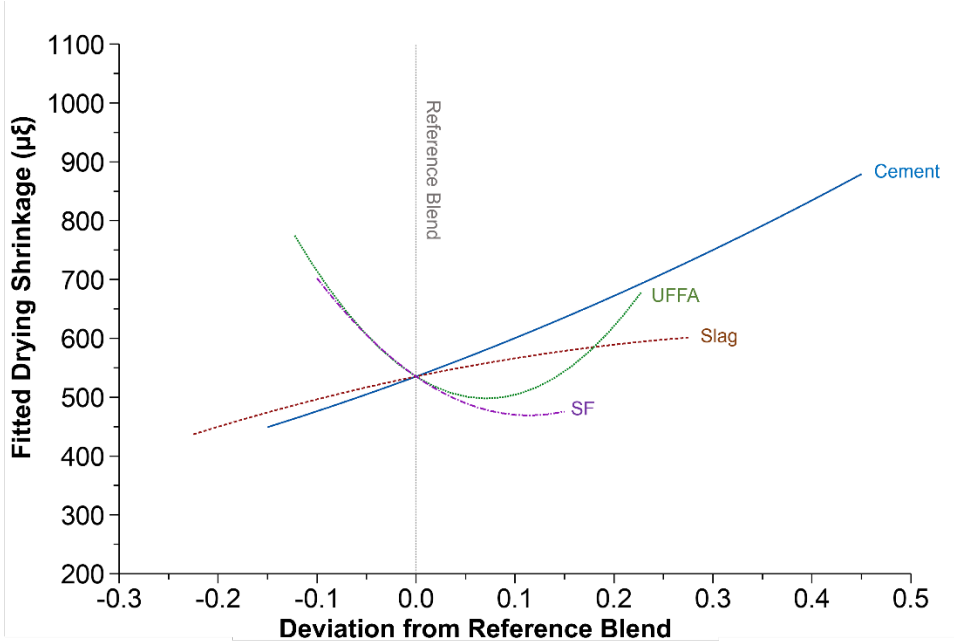

Figure 100. Graph. Sensitivity of the drying shrinkage of the UHPC mixes at 28 days of hydration for unit variation of different binder constituents.

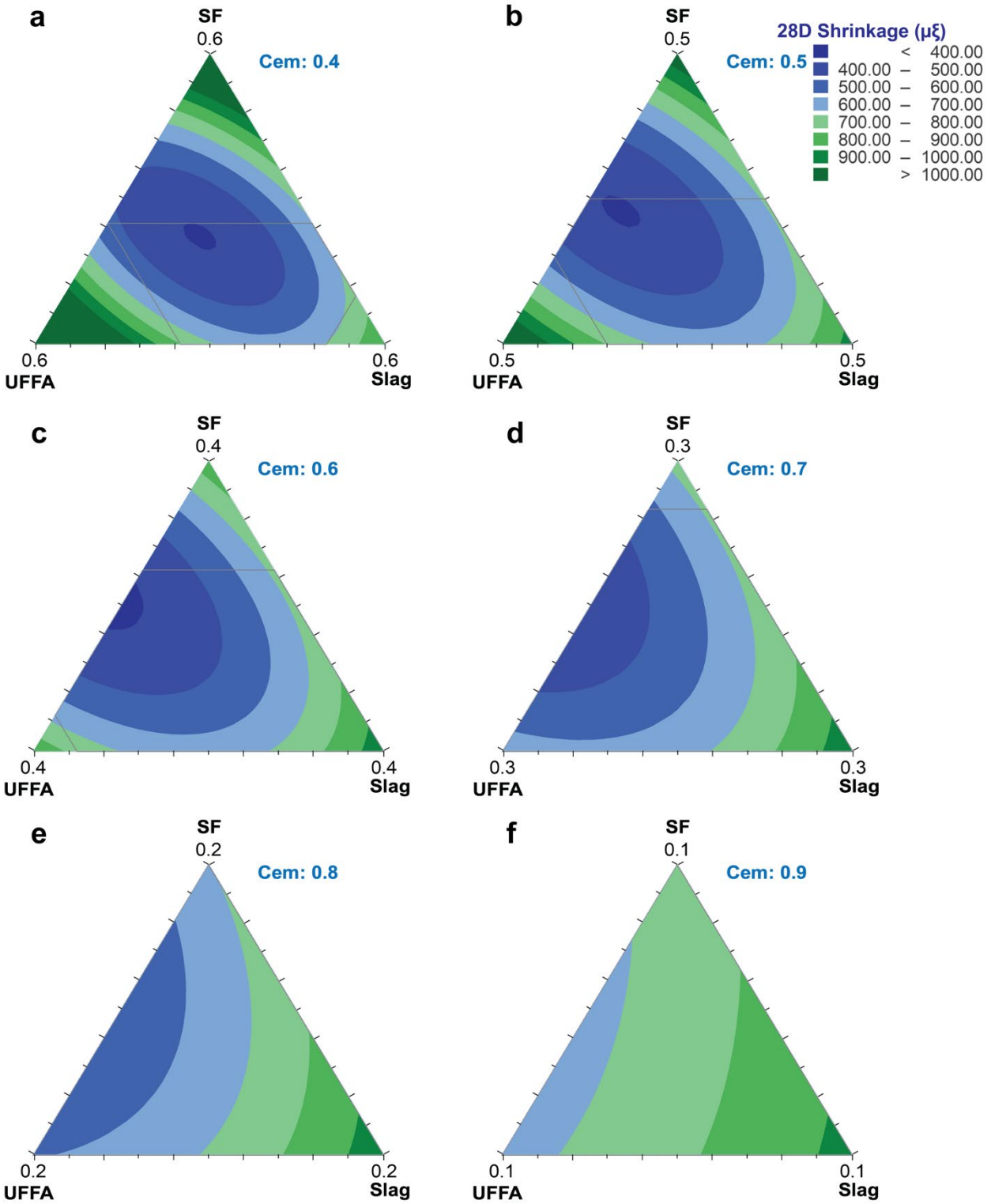

Figure 101. Graph. Ternary response plot showing the 28-day shrinkage of the UHPC mixes for compositional variation of the binder constituents used in the study.

APPENDIX G: MIX MODIFICATIONS

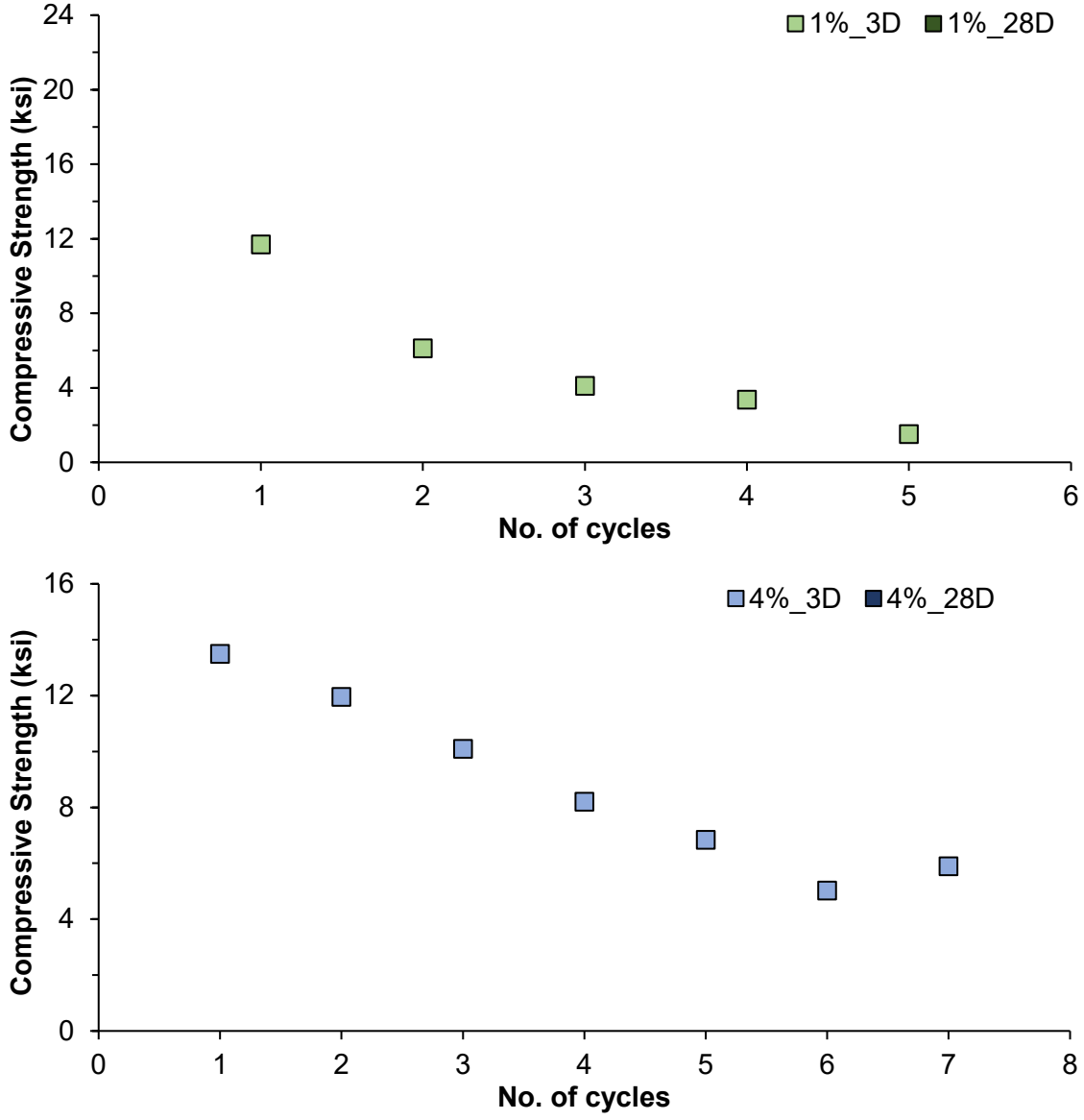

Figure 102. Graph. Residual strength development of UHPC mix M18 for steel fiber content of (a) 1% and (b) 4% by volume at a later age of 28 days.

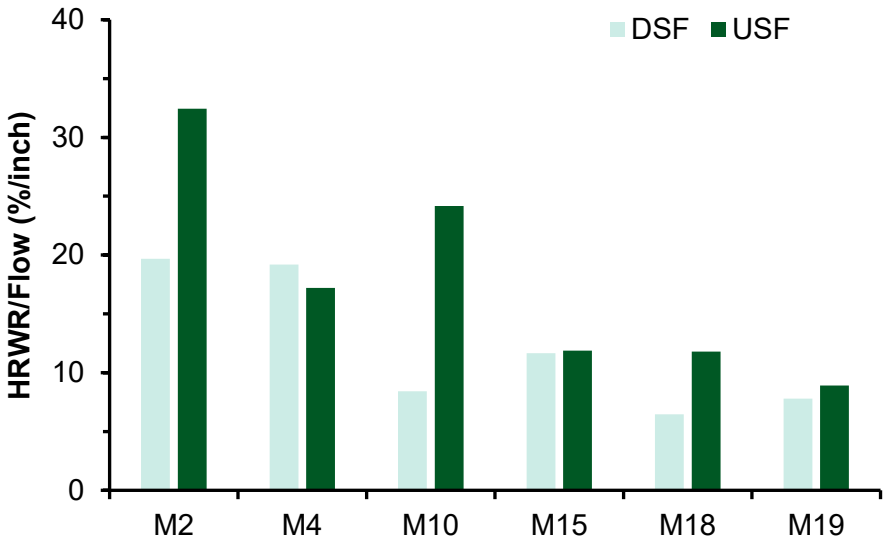

Figure 103. Chart. Effect of silica fume type on the HRWR/flow parameter of the UHPC mixes.

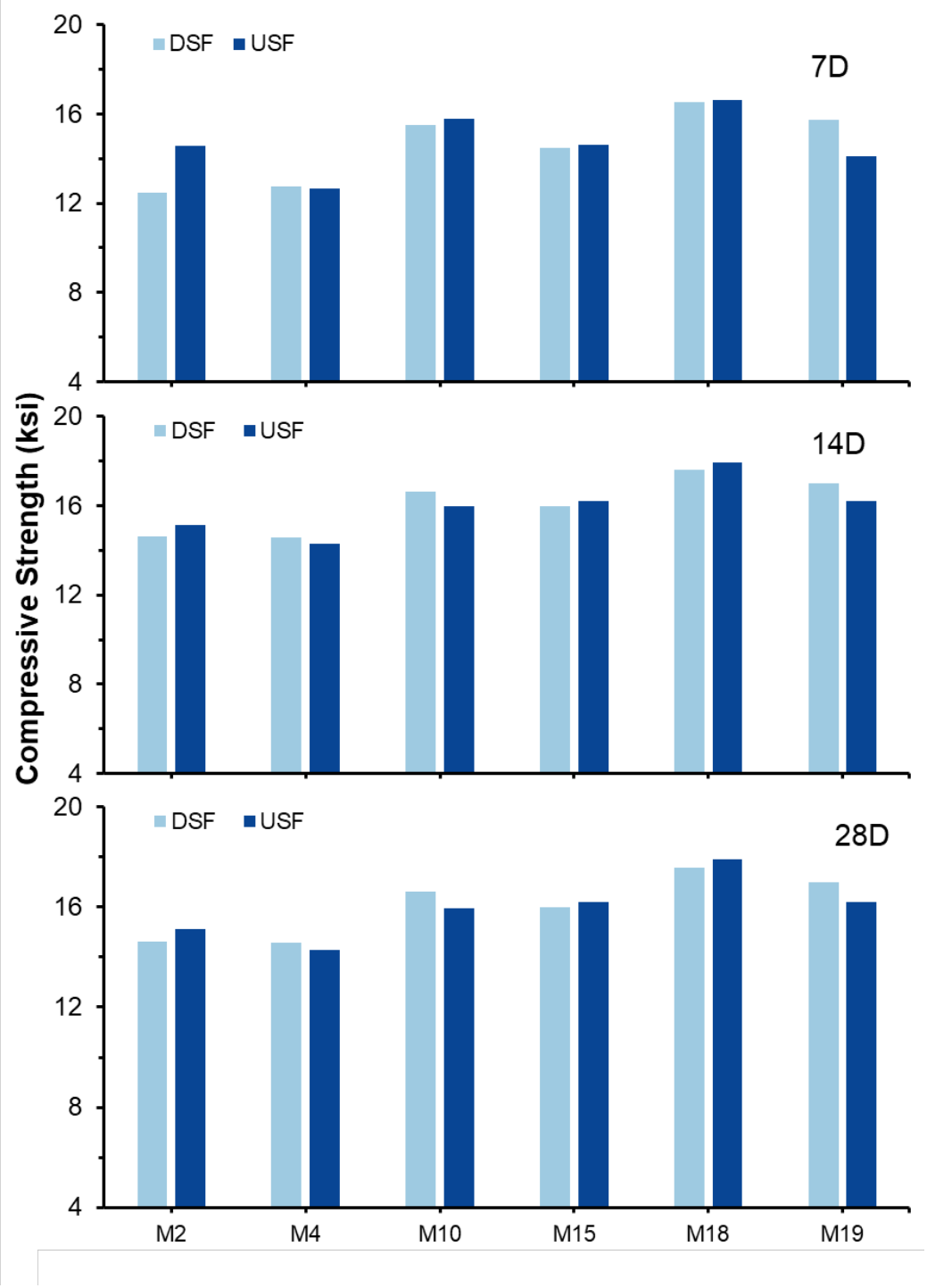

Figure 104. Chart. Effect of silica fume type on the 7, 14, and 28 days compressive strength of the UHPC mixes.

APPENDIX H: COST AND FEASIBILITY ANALYSIS

Table 19. Cost structure of the developed UHPC mixes

Mix ID	Cement	SF	UFFA	Slag	Sand	Water	HRWR	UHPC Cost (w/o fibers)	Fibers	Total Cost
M9	97.0	0.0	37.7	54.8	40.0	0.0	52.5	282.0	281.6	563.6
M3	157.7	0.0	37.7	0.0	40.7	0.0	73.1	309.1	281.6	590.7
M8	97.0	0.0	10.8	109.5	41.2	0.0	69.4	327.9	281.6	609.5
M19	114.5	30.0	25.7	52.9	40.3	0.0	113.1	376.5	281.6	658.1
M1	242.6	0.0	0.0	0.0	43.3	0.0	108.1	394.0	281.6	675.6
M5	121.3	0.0	0.0	109.5	41.9	0.0	125.6	398.4	281.6	680.0
M11	187.3	30.0	6.9	25.6	41.9	0.0	124.4	416.0	281.6	697.6
M15	126.7	30.0	6.9	80.3	41.2	0.0	139.6	424.6	281.6	706.2
M18	114.5	30.0	12.3	80.3	40.8	0.0	147.9	425.8	281.6	707.4
M6	97.0	63.5	0.0	109.5	40.6	0.0	117.3	428.0	281.6	709.6
M13	144.9	30.0	25.7	25.6	40.6	0.0	190.1	456.8	281.6	738.4
M16	114.5	61.8	6.9	80.3	40.6	0.0	158.5	462.6	281.6	744.2
M4	97.0	158.8	37.7	0.0	37.4	0.0	175.3	506.3	281.6	787.9
M10	132.1	60.0	13.8	51.1	40.5	0.0	221.1	518.5	281.6	800.1
M17	114.5	109.4	6.9	63.9	39.8	0.0	186.3	520.7	281.6	802.3
M14	114.5	109.4	25.7	25.6	39.0	0.0	212.8	527.0	281.6	808.6
M7	97.0	158.8	0.0	76.7	39.1	0.0	183.0	554.5	281.6	836.1
M12	157.0	109.4	6.9	25.6	40.3	0.0	251.3	590.4	281.6	872.0
M2	181.9	158.8	0.0	0.0	40.0	0.0	260.6	641.4	281.6	923.0

[All the cost values are noted in **$/m^3** of the UHPC mixes

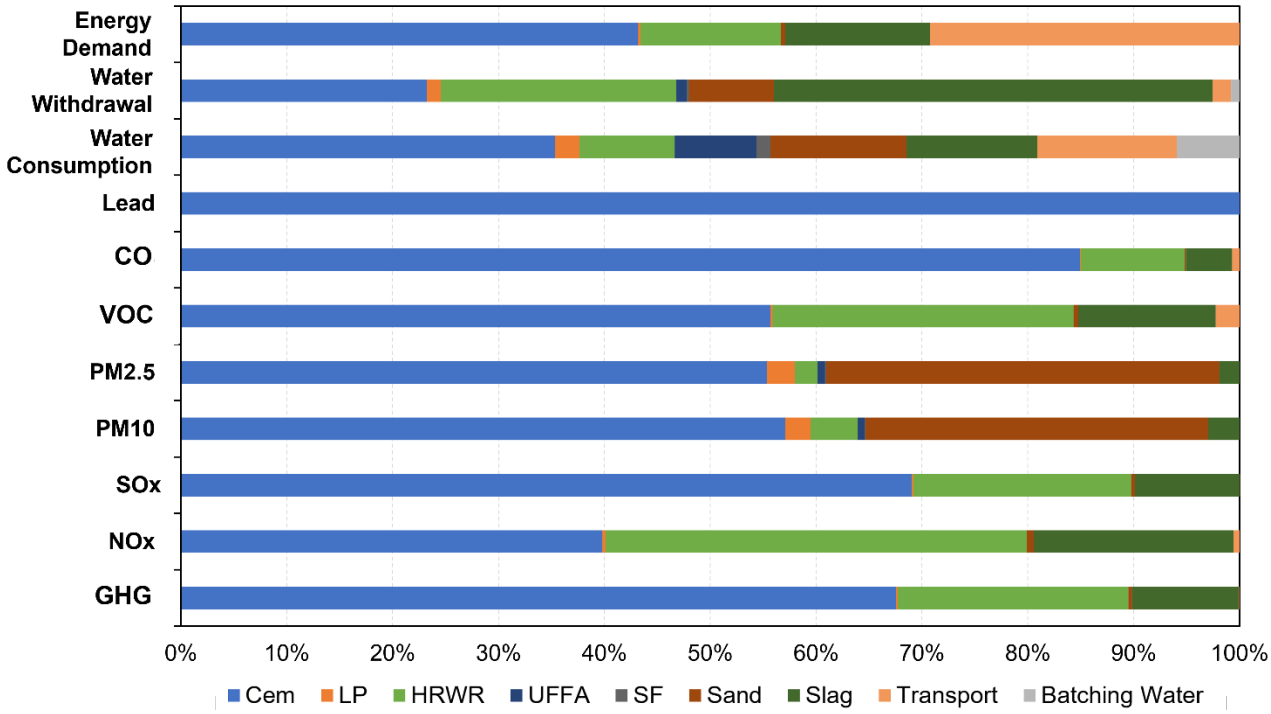

Figure 105. Chart. Environmental emissions for different contaminants for M19 obtained from the cradle-to-gate analysis using the Open Concrete LCA software.

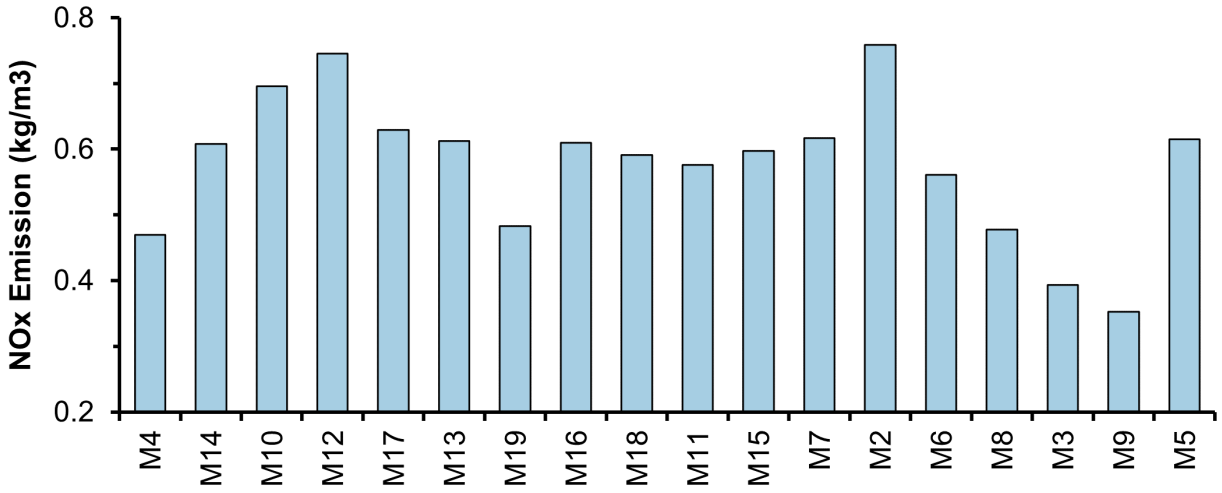

Figure 106. Chart. Summary of Nitrous Oxide (NO_x) emissions associated with the UHPC mix designs developed in this study.

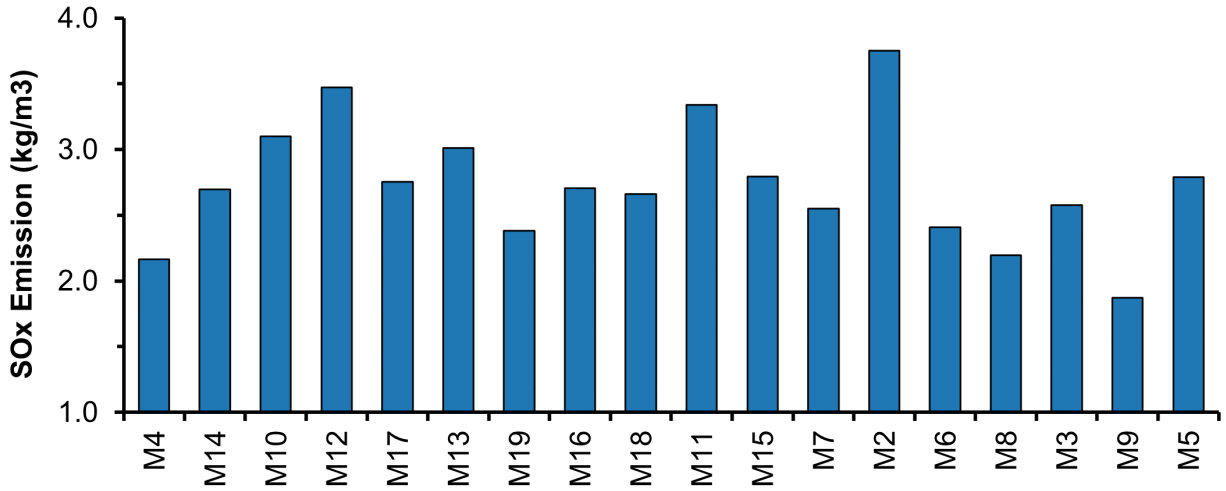

Figure 107. Chart. Summary of Sulphur Oxide (SO_x) emissions associated with the UHPC mix designs developed in this study.

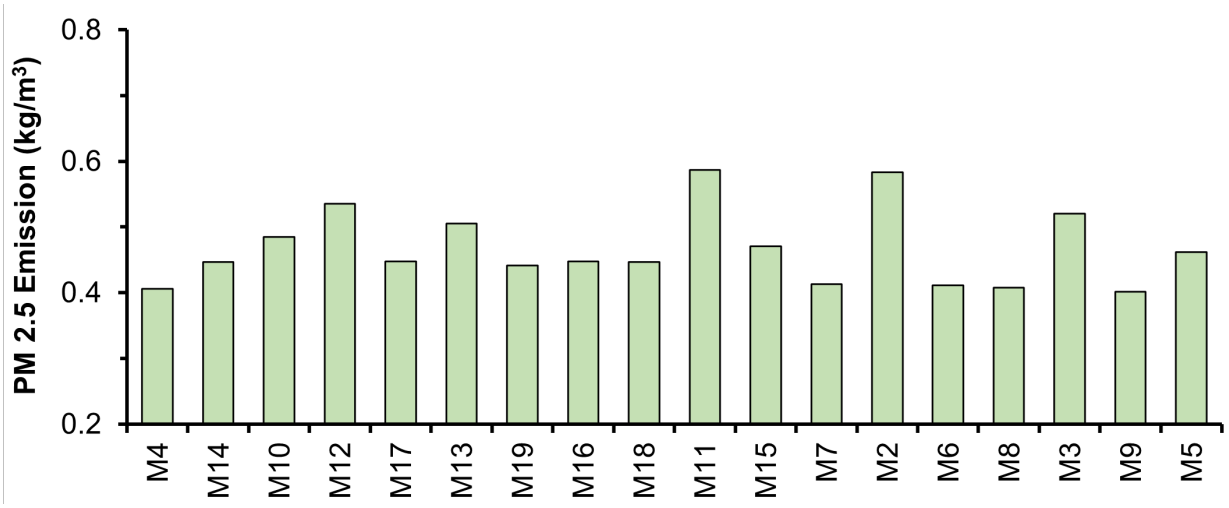

Figure 108. Chart. Summary of Particulate Matter ($PM_{2.5}$) emissions associated with the UHPC mix designs developed in this study.

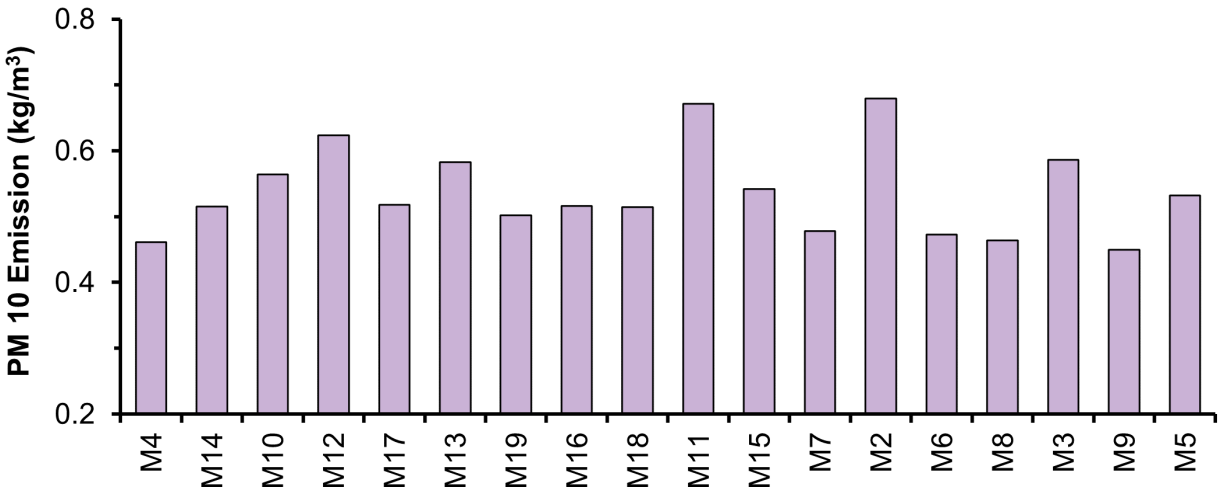

Figure 109. Chart. Summary of particulate matter (PM_{10}) emissions associated with the UHPC mix designs developed in this study.

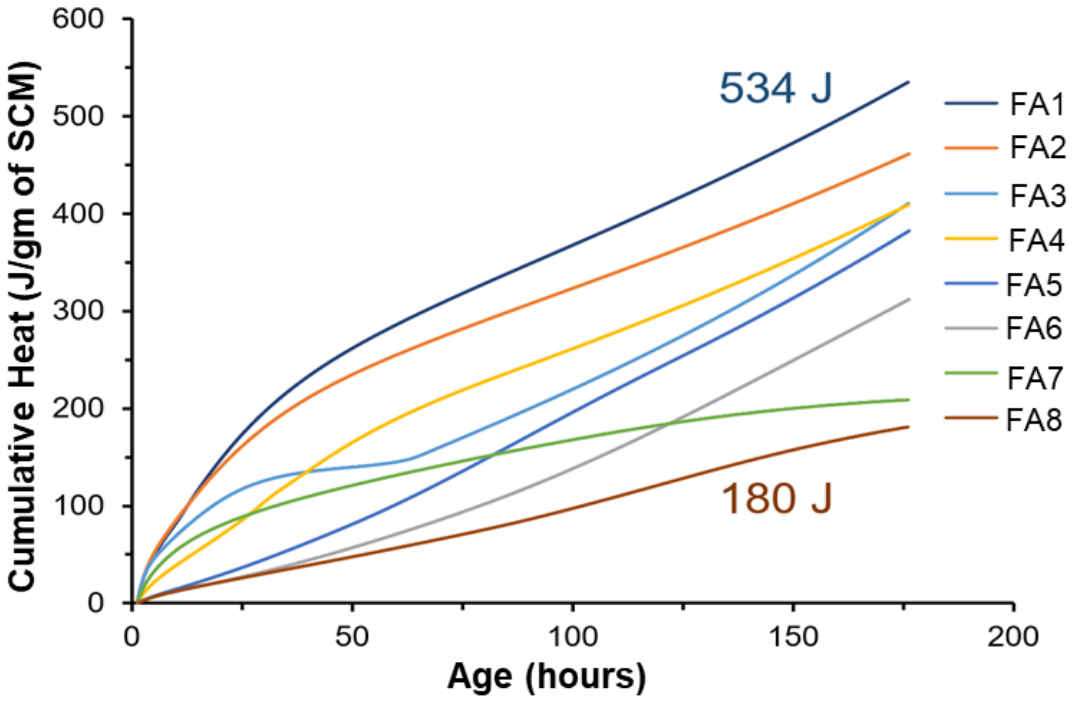

Figure 110. Graph. Cumulative heat produced from the modified R3 test performed on eight different fly ash samples (FA1–FA8) as a measure of their reactivity.

APPENDIX I: SUMMARY OF OPTIMUM MIX DESIGN RECIPE

I1 MATERIALS USED

- Cement: Type IL Portland Limestone Cement, in compliance with the IDOT-qualified list of approved cement producers.
- Granulated Blast Furnace Slag: Blast furnace Slag of Grade 100 with specific gravity and median particle size of 2.95 and 11.6 µm, respectively.
- Fly Ash: A finer version, ultra-fine fly ash (UFFA), conforming to class-F as per ASTM C816 with a median particle size of 3.4 µm.
- Silica Fume: Dry densified micro silica powder, complying to the specifications of ASTM C1240.
- Aggregate: Locally available masonry sand, complying to ASTM C144, with a spherical morphology and maximum particle size of 600 µm.
- High-Range Water Reducers: Polycarboxylate ether (PCE) based high range water reducer, AdvaCast 593, with dosage adjusted for a target flow of 8-11 inches.
- Steel Fibers: Striated steel fibers of 0.5 inch (13 mm) in length and 0.0078 inch (0.2 mm) in diameter with an aspect ratio of 65.

I2 OPTIMUM UHPC MIX COMPOSITION

The current study suggests two UHPC mix designs based on the range of the performance metric tested in this study, which are detailed below:

- Optimum Mix-1

Table 20. Composition of optimum Mix-1

Binder	% Volume	Weight, kg/m^3 (lb/yd^3)
Cement	50	788 (1328)
Silica Fume	5	55 (93)
Ultra Fine Fly Ash	10	131 (221)
Slag	35	516 (870)
Aggregate (Masonry Sand)		1325 (2233)
Water-Binder Ratio	0.18	
Sand-Binder Ratio	1.0	
Steel Fibers	2% by volume	
High Range Water Reducer (HRWR)	Adjusted as needed	

- Optimum Mix-2

Table 21. Composition of optimum Mix-2

Binder	% Volume	Weight, kg/m3 (lb/yd3)
Cement	50	788 (1328)
Silica Fume	5	55 (93)
Ultra Fine Fly Ash	20	261 (440)
Slag	25	369 (620)
Aggregate (Masonry Sand)		1325 (2233)
Water-Binder Ratio	0.18	
Sand-Binder Ratio	1.0	
Steel Fibers	2% by volume	
High Range Water Reducer (HRWR)	Adjusted as needed	

I3 MIXING PROTOCOL

The mixing of the UHPC mixes involves a step-by-step procedure which is listed below:

- **Initial Dry Mixing**: Sand and silica fume should be mixed dry for 5 minutes to break down agglomerates that may affect particle packing.
- **Incorporation of Dry Materials**: Cement, fly ash, and slag shall then be added and blended for an additional 5 minutes to ensure uniform dispersion, with care taken to prevent any material loss.
- **First Wet Mixing Phase**: 60% of the water, combined with high-range water reducer (HRWR), should be gradually introduced and mixed with the dry blend for 5 minutes to effectively disperse the polycarboxylate ether (PCE) particles.
- **Second Wet Mixing Phase**: The remaining water and HRWR shall be added, and mixing should continue until the mixture reaches the turnover time, transitioning the powders into a plastic state.
- **Steel Fiber Addition**: After achieving a plastic consistency, steel fibers should be gradually incorporated, ensuring uniform dispersion, with HRWR dosage adjustments made as necessary for the desired consistency.
- **Final Mixing**: The mix shall undergo 2 minutes of high-speed mixing, followed by 1 minute of slow-speed mixing, before proceeding to further testing.

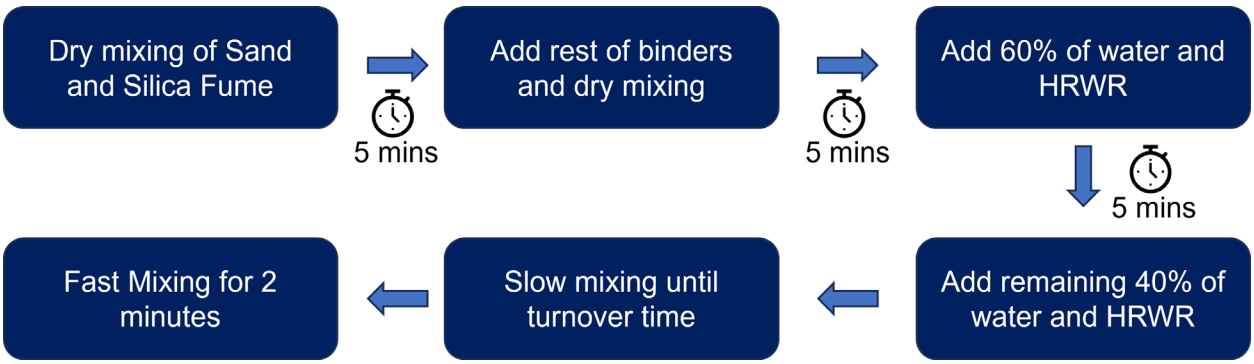

Figure 111. Mixing Regime of a typical UHPC mix.

I4. LIMITATIONS

The study considers the materials from a single source which was used throughout the optimization of the UHPC mixes at a smaller scale. Although the scalability section of the study considered materials from different sources, users should consider any potential variation in the binder composition and environmental factors for replication and/or further testing of the mixes.


Illinois Department
of Transportation


ILLINOIS